

RL-TR-96-100 (Volume II)
In-House Report
May 1996



PROCEEDINGS OF THE 1995 ANTENNA APPLICATIONS SYMPOSIUM

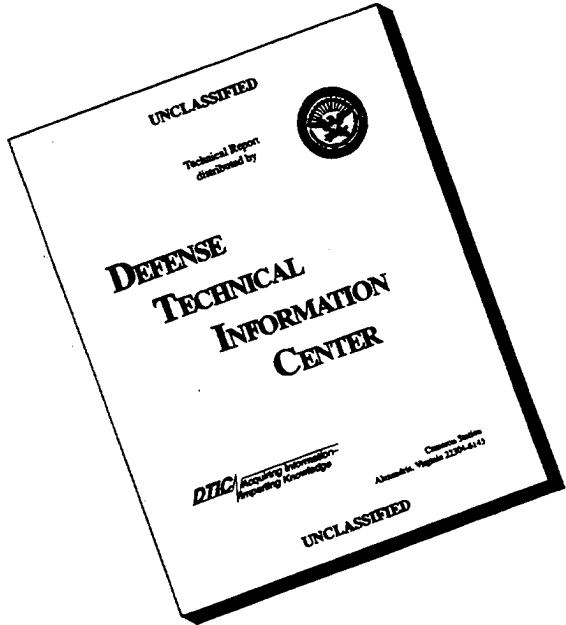
APPROVED FOR PUBLIC RELEASE; DISTRIBUTION UNLIMITED.

19960617 146

**Rome Laboratory
Air Force Materiel Command
Rome, New York**

DTIC QUALITY INSPECTED 1

DISCLAIMER NOTICE



**THIS DOCUMENT IS BEST
QUALITY AVAILABLE. THE
COPY FURNISHED TO DTIC
CONTAINED A SIGNIFICANT
NUMBER OF PAGES WHICH DO
NOT REPRODUCE LEGIBLY.**

Title of Report: PROCEEDINGS OF THE 1995 ANTENNA APPLICATIONS
SYMPOSIUM

PUBLICATION REVIEW

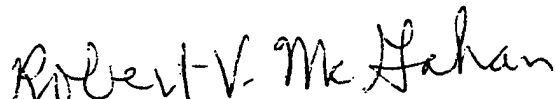
This report has been reviewed and is approved for publication.

APPROVED:



DANIEL J. JACAVANCO
Chief, Antennas & Components Division
Electromagnetics and Reliability Directorate

APPROVED:



ROBERT V. McGAHAN
Acting Director
Electromagnetics and Reliability Directorate

REPORT DOCUMENTATION PAGE

*Form Approved
OMB No. 0704-0188*

Public reporting burden for this collection of information is estimated to average 1 hour per response, including the time for reviewing instructions, searching existing data sources, gathering and maintaining the data needed, and completing and reviewing the collection of information. Send comments regarding this burden estimate or any other aspect of this collection of information, including suggestions for reducing this burden, to Washington Headquarters Services, Directorate for Information Operations and Reports, 1215 Jefferson Davis Highway, Suite 1204, Arlington, VA 22202-4302, and to the Office of Management and Budget, Paperwork Reduction Project (0704-0188), Washington, DC 20503.

1. AGENCY USE ONLY (Leave blank)	2. REPORT DATE	3. REPORT TYPE AND DATES COVERED	
	May 1996	Scientific Interim	
4. TITLE AND SUBTITLE			5. FUNDING NUMBERS
PROCEEDINGS OF THE 1995 ANTENNA APPLICATIONS SYMPOSIUM			PE: 62702F PR: 4600 TA: 460014 WU: 460014PP
6. AUTHOR(S)		8. PERFORMING ORGANIZATION REPORT NUMBER	
Daniel H. Schaubert, et al		RL-TR-96-100 Volume II	
7. PERFORMING ORGANIZATION NAME(S) AND ADDRESS(ES)		9. SPONSORING/MONITORING AGENCY NAME(S) AND ADDRESS(ES)	
Rome Laboratory/ERAA 31 Grenier Street Hanscom AFB, MA 01731-3010			
10. SPONSORING/MONITORING AGENCY REPORT NUMBER		11. SUPPLEMENTARY NOTES	
		Volume I consists of pages 1 through 351. Volume II consists of pages 352 through 671.	
12a. DISTRIBUTION/AVAILABILITY STATEMENT			12b. DISTRIBUTION CODE
Approved for Public Release; Distribution Unlimited			
13. ABSTRACT (Maximum 200 words)			
The Proceedings of the 1995 Antenna Applications Symposium is a collection of state-of-the-art papers relating to phased array antennas, multibeam antennas, satellite antennas, microstrip antennas, reflector antennas, HF, VHF, UHF and various other antennas.			
14. SUBJECT TERMS			15. NUMBER OF PAGES
Antennas Satellite Antennas Broadband Antennas			326
16. PRICE CODE			
17. SECURITY CLASSIFICATION OF REPORT		18. SECURITY CLASSIFICATION OF THIS PAGE	19. SECURITY CLASSIFICATION OF ABSTRACT
UNCLASSIFIED		UNCLASSIFIED	UNCLASSIFIED
20. LIMITATION OF ABSTRACT		SAR	

**PROGRAM FOR
1995 ANTENNA APPLICATIONS SYMPOSIUM**
WEDNESDAY, SEPTEMBER 20, 1995

I. MILITARY AND COMMERCIAL COMMUNICATIONS

		page #
1.	Keynote Address MMIC Array Demonstrations with the NASA Advanced Communications Technology Satellite (ACTS): Technology, Teamwork and Transition <i>C. Raquet</i> , NASA, Cleveland, OH.	*
2.	Triband Flyaway Antennas for Worldwide Communications <i>N. Moldovan</i> , Prodelin Corporation, Conover, NC.	1
3.	A Vehicular Antenna for Mobile Satellite Service <i>C.D. McCarrick and C.J. Mosher</i> , Seavey Engineering Associates, Inc., Cohasset, MA.	16
4.	Low Cost Millimeter Wave Phased Array Antenna <i>P. Pons and C. Renard</i> , Dassault Electronique, Saint Cloud, France.	26
5.	Performance Analysis for a Concealed Automobile Entertainment Radio Antenna Sub-System <i>A. Adrian</i> , Ford, Dearborn, MI.	36
6.	A Crossed-Slot Antenna with an Infinite Balun Feed <i>D.A. Paschen and S.C. Olson</i> , Ball Telecommunication Products, Broomfield, CO and <i>M.W. Schnetzer</i> , Qualcomm Inc., San Diego, CA.	66

* Not included in this volume.

II. REFLECTORS AND DF ANTENNAS

7.	Twist Reflector Seeker Antenna <i>J. Lane and R. Kliger</i> , Raytheon, Tewksbury, MA.	80
8.	Ka-Band Five Horn Feed <i>M. DelCheccolo and J. Lane</i> , Raytheon, Tewksbury, MA.	102
9.	A Rigorous Technique for Synthesis of Offset Three-Reflector Antennas <i>V. Oliker</i> , Emory University, Atlanta, GA.	126
10.	Monopulse Stick Phased Array <i>R. Kinsey</i> , Sensis Corporation, DeWitt, NY.	138
11.	Monopulse DF Antenna for Submarine ESM Applications <i>P. Eyring</i> , AIL Systems, Inc., Deer Park, NY.	168
12.	High Accuracy DF Antenna Using COTS Hardware <i>T.R. Holzheimer</i> , E-Systems, Inc., Greenville, TX.	187
13.	A Method of System and Sensor Sensitivity Improvement <i>T.R. Holzheimer</i> , E-Systems, Inc., Greenville, TX.	218

THURSDAY, SEPTEMBER 21, 1995

III. NEW TECHNIQUES AND CONCEPTS

		page #
14.	A Survey of Optical Beamforming Techniques <i>M.G. Parent</i> , Naval Research Laboratory, Washington, DC.	250
15.	Structurally-Integrated Optically-Reconfigurable Antenna Array <i>R. Gilbert, P. Hoefer, F. Hayes and D. Kopf</i> , Sanders, Nashua, NH, and <i>G. Pirrung</i> , Naval Air Warfare Center, Warminster, PA.	272
16.	The Design of Wire Antennas Using Genetic Algorithms <i>D.S. Linden and E.E. Altshuler</i> , Rome Laboratory, Hanscom AFB, MA.	292
17.	Isoimpedance Inhomogeneous Media in Antenna Applications <i>A. I. Knyaz</i> , Ukrainian Academy of Telecommunication, Ukraine, Russia.	307
18.	The Multifunction Mast Antenna for Submarines - Covering from VLF to L-band <i>J. Bryan, J. Blais and N.I. Herscovici</i> , Spears Associates, Inc., Norwood, MA.	313
19.	Tunable, Wide-Angle Conical Monopole Antennas with Selectable Bandwidth <i>P.E. Mayes and W. Gee</i> , Walter Gee and Associates, San Jose, CA.	352
20.	Photonic-Based Tuning and Control of Antenna Elements <i>T.L. Larry, C.J. Swann and M.L. VanBlaricum</i> , Toyon Research Corp., Goleta, CA.	382

IV. ANALOG AND DIGITAL BEAMFORMING

21.	Genetic Algorithm Array Pattern Synthesis <i>S. Santarelli, H. Southall and E. Martin</i> , Rome Laboratory, Hanscom AFB, MA and <i>T. O'Donnell</i> , ARCON Corp., Waltham, MA.	404
22.	Phase-Only Illumination Synthesis for Over-Sampled Phased Array Appertures <i>J.H. Pozgay</i> , Raytheon, Tewksbury, MA.	423
23.	Degree of Freedom Requirements for Sector Nulling of Errorred Antenna Patterns <i>P.R. Franchi</i> , Rome Laboratory, Hanscom AFB, MA.	446
24.	Techniques for Adaptive Array Pattern Control Using an Augmented Covariance Matrix <i>R.J. Mailloux</i> , Rome Laboratory, Hanscom AFB, MA.	459
25.	Digital and Adaptive Beamforming Techniques for Environmental Remote Sensing <i>C.D. Cherry, D.H. Schaubert, G. Hopcraft, J.B. Mead and R.E. McIntosh</i> , University of Massachusetts, Amherst, MA.	476

	page #
26. Neural Network Beam-Steering for Phased-Array Antennas <i>H. Southall, S. Santorelli and E. Martin</i> , Rome Laboratory, Hanscom AFB, MA, and <i>T. O'Donnell</i> , ARCON Corp., Waltham, MA.	495
27. Aircraft Motion Emulation by an Inverse Displaced Phase Center Antenna <i>H.M. Aumann and F.G. Willwerth</i> , Lincoln Laboratory, Lexington, MA.	506

FRIDAY, SEPTEMBER 22, 1995

V. ARRAY THEORY AND TECHNOLOGY

28. Leaky-Wave Scanning Antenna for W-Band <i>V. Manasson, L. Sadovnik, P. Shnitser, and R. Mino</i> , Physical Optics Corp., Torrance, CA and <i>L. Bui</i> , Laser Astronics, Santa Monica, CA.	527
29. Octave Bandwidth Microwave Scanning Array <i>P.G. Elliot</i> , APTI / E-Systems, Washington, DC.	537
30. Toward a Better Understanding of Wideband Vivaldi Notch Antenna Arrays <i>J. Shin and D.H. Schaubert</i> , University of Massachusetts, Amherst, MA.	556
31. Addition of a Polarimetric Capability to a Tactical SAR System <i>D. Collier, M. Greenspan, L. Orwig and H. Shnitkin</i> , Westinghouse Norden Systems, Inc., Norwalk, CT.	586
32. Measurement of Isolation Between Two Elliptically Polarized Antennas <i>H. Shnitkin and D. Collier</i> , Westinghouse Norden Systems, Norwalk, CT.	606
33. An Accurate Phase Alignment Procedure for Ultra Low Sidelobe Antennas Using Aperture Coupled Field Probe Techniques <i>G.E. Evans, D.T. Hotopp, G.L. Kempic, D.P. Parrish and K.G. Ramsey</i> , Westinghouse Electric Corp., Baltimore, MD.	615
34. E-3A Reflectionless Manifold Performance in the Presence of Mismatched Radiating Elements <i>D.P. Parrish, J.M. Vezmar and K.G. Ramsey</i> , Westinghouse Electrical Corp., Baltimore, MD.	638

TUNABLE, WIDE-ANGLE CONICAL MONPOLE ANTENNAS WITH SELECTABLE BANDWIDTH

Paul E. Mayes and Walter Gee
Walter Gee and Associates
1683 Cassiar Drive
San Jose, CA 95130-1514

Abstract: A single wide-angle conical monopole is inherently low profile and can be tuned to resonate at frequencies where the diameter of the structure is quite small compared to the wavelength. Tuning can be accomplished by varying the values of lumped elements that are connected across the radiating aperture. Continuously variable tuning is possible by using voltage-variable capacitors (varactors) as part of the tuning circuit. Since the element is a high-Q resonator, the match bandwidth is quite small, although adequate for some applications. When a wider match bandwidth is required, adding a second cone, nested inside the first, may supply it.

1. Introduction

It is well known that antennas made from conducting conical surfaces with apex angles (between the axis and generators of the cone) in the range from thirty to forty-five degrees have broad operating bandwidth [1]. For a single cone fed against a ground plane (monopole), the minimum slant height for low input reactance is approximately one-quarter wavelength ($\lambda/4$). For higher frequencies, where the slant height is larger than $\lambda/4$, the input reactance remains small and the input resistance is almost constant. The upper limit of the operating band for medium-angle conical monopoles is determined, not by the impedance, but by the directivity. Elevation-plane radiation patterns develop multiple

lobes when the monopole slant height exceeds one-half wavelength. Thus the operating band is approximately 2:1 [2].

Published data for conical antennas with apex angles near ninety degrees are sparse. An excellent review of conical antennas is given by Bevensee [3]. He presents data for both solid and hollow conical monopoles with apex angles as large as forty-five degrees. Other published works, even though the title may include the term "wide angle", consider mainly cases where the apex angle is less than forty-five degrees. An exception presents computed data for an apex angle of seventy degrees [4]. Another presents data for the apex angle of 50.6 degrees [5]. However, this author, as well as most others, considers only the case where the cones of a dipole are closed by spherical caps.

To achieve reduced visibility, mechanical ruggedness, safety, lower drag, etc., it is often desirable to use an antenna having a very small height. In those applications where an omnidirectional azimuthal pattern is required and where a suitable ground surface is available, using a conical monopole with a wide angle (near 90 degrees) will significantly reduce the antenna height in a way that provides some opportunities for reducing lateral dimensions as well. Nesting several wide-angle cones connected in series can increase the operating bandwidth. These benefits are not easily implemented with conventional thin, linear

monopole (whip) antennas. In some recent work on electronically tuned monopoles [6] some length reduction is achieved by using a helical element, but the reduction is not as great as that obtainable with a wide-angle cone. The tuning of the helical elements is by means of diodes that short circuit turns at various locations along the helix, making the helix resonant in the quarter-wavelength mode at the operating frequency. Since each resonance is of narrow bandwidth, numerous diodes and biasing circuits are required to adequately cover all frequencies in an extended band.

2. Wide-angle conical monopoles

The basic element is an open-ended conical monopole of very wide apex angle (between seventy-five and ninety degrees). In contrast to the medium-angle cones that have been used extensively in the past, the very-wide-angle conical monopole is a resonator with relatively narrow impedance bandwidth (relatively high Q). The cost of achieving reduced height is a decrease in the operating bandwidth. However, the smaller height provides opportunities to reduce other dimensions as well, and easily to add more conical elements to increase the impedance bandwidth.

Very wide apex angles make it feasible to connect lumped elements (loads) across the aperture between the edge of the cone

and ground. A resistive value of the input impedance can be achieved at a fixed frequency for a wide range of cone lengths by properly choosing the values of reactive loads. Thus it is not necessary for the generators of a cone to be almost one-quarter of the operating wavelength in order to achieve the first zero (lowest non-zero frequency) input reactance (resonance).

For inductance-loaded, very-wide-angle conical monopoles the first zero reactance condition occurs at a high value of input resistance. By adding a second cone nested inside the first cone to minimize the increase in size, and connecting the two so that the input terminals are effectively in series, a second, high-resistance, zero-reactance condition can be obtained at a frequency that is under the designer's control. When viewed on a Smith chart, the impedance locus is essentially circular for all frequencies between the two resonances. The diameter and location of the circle depend upon the separation between the resonances, upon the power dissipated within the structure, and upon the power radiated or dissipated at the aperture. However, for a wide range of radiated and/or dissipated power the center of the circle can be moved to a point near the center of the Smith chart by adding an impedance transformer at the input terminals. The magnitude of the input reflection coefficient (radius of the circular part of the impedance locus) is reduced by making the resonant frequencies

of the two cones closer together, consequently reducing the match bandwidth of the antenna. Thus, a trade-off exists between bandwidth and degree of match.

3. Equivalent circuit

The region between the tip and the aperture of a conical monopole can be represented by a transmission line. The length of the equivalent line will be equal to the radial distance from the tip to the aperture of the cone. If the line is terminated with a lumped impedance that correctly simulates the field beyond the aperture, the impedance at the input terminals of the line will be equal to the impedance observed at the tip of the cone. Since power will be radiated from the aperture of the conical monopole, the termination should have a resistive part that will dissipate power equal to that radiated. There will also be energy stored in the field near the aperture and this should be represented by a reactive part of the termination.

Values for the termination can be estimated from approximate theory and measurements. When lumped elements are connected across the aperture between the large ends of the cones, the accumulative value of those terminations will be paralleled with the effective resistive and reactive terminations of the open aperture. The equivalent circuit, although containing only

estimates for the values of some components, provides a simple, but adequate, approach for the design of wide-angle conical monopole antennas.

4. Experimental model

The structure of an experimental model is illustrated in Figure 1. A metallic cone with θ_1 (angle between axis of cone and its surface) of 80 degrees is supported by dielectric spacers so that the cone axis is perpendicular to the circular ground plane. The radius (distance from tip to edge) of the cone is 18.75 cm, one sixteenth of the wavelength at 100 MHz. A panel-mount coaxial connector is provided at the tip of the cone with a small hole in the ground plane to provide for attaching the pin of the connector to the cone tip.

From transmission line equations, or from the Smith chart, it is found that a high resistance, zero reactance resonance at 100 MHz can be achieved by loading the aperture with a normalized inductive reactance of 2.41. The characteristic impedance of the conical guide formed between the conducting cone (apex angle of θ_1) and ground is given by

$$Z_0 = 60 \ln \operatorname{ctn} \theta_1/2 \quad (1)$$

When $\theta_1 = 80$ degrees, the impedance is about 10 ohms. Thus the equivalent line should be terminated with a reactance of 24.1 ohms that would be realized by a single inductor with

$$L = \frac{X_L}{\omega} = \frac{24.1}{2\pi \times 10^8} = 38.4 \text{ nanohenries} \quad (2)$$

To maintain a high degree of azimuthal symmetry for the edge-loaded monopole this inductance could be achieved by placing four inductors with $L = 154$ nH spaced at 90-degree intervals around the periphery of the cone as indicated in Figure 1. The resonant frequency can be varied by changing the value of the terminating inductors. In the first model such changes were made by physically substituting inductors of various values.

Although a transformer can be used to improve the match to a lower resistance, the transformer is not required to demonstrate tuning of the antenna. As the inductance is reduced, the resonant frequency will increase. The upper limit of tuning in this way will be achieved when the cone radius is approximately one-quarter wavelength (400 MHz). This corresponds to a zero reactance termination which will not be quite achievable with inductors alone. Nevertheless, the antenna can be tuned over 4:1 band by simply changing the values of the terminating inductors.

5. Model for Design

As mentioned above, the approximate equivalent circuit for a terminated conical monopole is that shown in Figure 2. The transformer across the input improves the match to a low impedance, such as 50 ohms. When the resistance R simulates the effect of radiation, it has been determined empirically from measurements. Therefore, it is important to measure the input impedance of the antenna without the transformer in order to determine the optimum turns ratio for a transformer to be added later. The resistance R would also include any lumped resistors connected across the aperture to reduce the reflection there. Such resistive loading is generally not desirable since it reduces the efficiency and gain. However, for receiving applications at HF, where the noise is determined by factors external to the antenna, low efficiency may not be detrimental to system performance. The inductance L in the equivalent circuit is that which gives the effective aperture reactance of all inductors placed across the cone aperture. In this model the aperture reactance due to the energy stored in the field near the aperture is neglected.

The circuit of Figure 2 has been analyzed numerous times for various terminating inductors using the circuit simulation program

SuperStar Pro by Eagleware. The resistance R was computed from the formula

$$R = 10,500 \left(\frac{55}{f} \right)^{2.05} \quad (3)$$

where f is the frequency in MHz. This equation was determined from a fit to experimental data taken on an earlier model of a conical monopole that was tested at a lower frequency. Hence, it was expected to require revision after measurements were made on the current antenna.

Figures 3 and 4 give some results. The Smith chart plots illustrate the frequencies at which the zero-reactance points (resonances) occur for the various values of terminating inductance¹. The return loss curves show a narrow pass band that scans up in frequency as the value of the terminating inductor is decreased. To provide data for direct comparison with measurement, the same cases were run without the transformer. One result is shown in Figure 5. Measured data for these cases,

¹The marker frequencies are given in the row just below the line containing the file name and date. The first four frequencies apply to Markers 1-4 on the left-hand plot and the last four frequencies to Markers 5-8 on the right-hand plot. The next row gives magnitude of reflection coefficient at Markers 1-4 and the return loss in dB for Markers 5-8.

referenced to the upper surface of the ground plane, should agree fairly well with these computed values, particularly at 100 MHz. Data at the higher frequencies would permit one to fix more accurate parameters for Equation (3) for the terminating resistor R.

6. Physical Model

The cone was made from 0.030-in thick aluminum sheet metal and was formed into the conical shape by spinning on a lathe. The ground plane is 0.050-in aluminum, drilled and tapped to accept screws for affixing the panel-mount coaxial (SMA) connector. Dielectric shims ($\epsilon_r = 3.5$) serve to fix the cone in place relative to the ground plane. A RG-58 C/U 50-ohm cable was used to connect between the antenna and the HP8753C network analyzer.

Three sets of coils were wound to serve as the terminating inductors. Since the effects of interturn capacitance are considerable at the frequencies around 100 MHz, the inductors were measured independently before being attached to the antenna.

The inductances of the coils were also computed from the formula [7]

$$L = \frac{4\pi^2 N^2 r^2}{\ell} \left[K_n - \frac{\ell(a+b)}{\pi N r} \right] \quad (4a)$$

where

$$K_n = \left[1 + 0.9(r/\ell) - 0.02(r/\ell)^2 \right] \quad (4b)$$

$$a = 2.3 \log_{10} \left[1.73 \frac{wN}{\ell} \right] \quad (4c)$$

$$b = 0.336 \left[1 - \frac{2.5}{N} + \frac{3.8}{N^2} \right] \quad (4d)$$

L is the inductance in nanohenries, N is the number of turns, ℓ is the length of the coil in centimeters, r is the coil form and wire radius (mean turn radius) in cm, and w is the wire diameter in cm. Computed and measured inductances for the three different coils are summarized in Table 1.

Table 1
Computed and measured inductances for loading coils.

	Inductor dimensions	Inductance (comp)	Inductance (meas)
I	6.8 turns, $d=0.232"$ $\ell=0.36"$, $w=0.051"$	167 nH	162 nH
II	5.0 turns, $d=0.232"$ $\ell=0.36"$, $w=0.051"$	94 nH	101 nH
III	5.0 turns, $d=0.123"$ $\ell=0.42"$, $w=0.051"$	34 nH	38 nH

d = form diameter, ℓ = inductor length, w = wire diameter

Both input impedance and return loss data were recorded with each set of inductors. A Smith chart displaying the measured impedance is shown in Figure 6. The near circular locus predicted in Figures 3 and 4 is seen again in Figure 6. The expected shift in resonant frequency is observed as the inductance values are changed. A summary of the computed and measured resonant frequencies is given in Table 2. Although there is not a direct correspondence of the inductances between the computed and measured cases, the agreement obtained by interpolation is good.

Table 2
Resonant frequencies, measured and predicted

Case	Coil Ind. (nH)	f_r (MHz)	Model Ind. (nH)	f_r (MHz)
I	162	95.1	154	100
II	101	116.0	30	205
III	38	151.5	0.04	400

7. Second antenna model

The second experimental model consists of a single 80-degree cone with four series inductance/capacitance tuning circuits placed around its periphery. The same cone, ground plane, and connector were used. The terminating impedances are each an inductance and capacitance connected in series. Four such combinations were connected across the cone aperture at equally spaced intervals around the periphery. The value of the terminating impedance was

changed first by changing only the values of fixed capacitors while maintaining the same inductances. Later, the capacitance was changed by varying the bias voltage across varactors in series with the inductors. A bias tee connected to the coaxial input connector was used to supply the bias voltage from an external supply.

The equivalent circuit of Figure 2 was modified to include the effect of tuning capacitors in series with inductive terminations. It has been analyzed numerous times for various terminating inductors and capacitors. The computed return loss curves show a narrow pass band very similar to those shown in Figures 3 and 4. The pass band scans up in frequency as the capacitance is decreased. Without the transformer the return loss curves are like that of Figure 5, which is the type of plot expected for measurements made at the tip of the cone.

A high resistance, zero reactance resonance at about 400 MHz can be achieved by loading the aperture with four series combinations of a 46 nH inductor and a 3.5 pF capacitor. This capacitance corresponds to the minimum value for a particular varactor. As the bias voltage is reduced from 20 volts to 2.5 volts, the diode capacitance changes from 3.5 to 27 pF and the resonant frequency of the antenna would change from about 400 MHz to about 200 MHz. The computed resonant frequencies at the lower

and upper limits of the tuning range (216 and 397 MHz, respectively) have a ratio of 1.8. It is desirable to increase the tuning ratio to 2 or more. This can be done with a varactor that has capacitance that varies from about 2 to 16 pF. These varactors would be used with four 72 nH inductors.

8. Measured results

The first measurements were made with each one of four terminations consisting of a 100 nH inductor in series with a fixed capacitor. The Smith chart plots all have the same appearance as those of Figures 3 and 4. The frequencies of zero reactance for each value of capacitance are listed in Table 3.

Table 3
Frequencies of zero reactance versus terminating capacitance.

Capacitance (pF)	Freq. X=0 (MHz)
none	114.0
100	117.8
30	140.3
15	159.5
10	178.0
4.7	229.3

When the fixed capacitors were replaced with varactors and a voltage applied through a bias tee at the tip of the cone, the results were as expected. They are summarized in Figures 7 and 8

which show, respectively, the return loss measured for three different voltages and a plot of the resonant frequency versus bias voltage.

10. Wider Bandwidth Model

The first two experimental models demonstrated the capability to scan the match frequency of a wide-angle conical monopole. Since the element is a high-Q resonator, the match bandwidth is quite small. For applications where a wider match bandwidth is required, adding a second cone may supply it. The third experimental model consists of two cones, one with angle of 70 degrees and one with angle of 80 degrees, with four terminating inductors placed around the periphery of each cone.

A cross section of the antenna structure is illustrated in Figure 9. Metallic cones with θ_1 of 70 and 80 degrees are supported by dielectric spacers so that the cone axes are perpendicular to the circular ground plane. The radius (distance from tip to edge) of the lower cone is 18.75 cm, one sixteenth of the wavelength at 100 MHz. The upper cone has a radius of 17.2 cm (one-sixteenth of a wavelength at 108.8 MHz). To tune the antenna at approximately 100 MHz the values of each of the terminating inductors (not shown in Figure 9) should be approximately 154 nH, for the lower cone, and 148 nH, for the upper cone. Minor

adjustments in the values of the inductors should lead to a band-pass characteristic where frequencies contained in a loop on the Smith chart produce a band-pass characteristic with return loss that remains almost constant for those frequencies in the loop. By gradually reducing the sizes of these inductors, the passband can be increased to the vicinity of 400 MHz in much the same manner as was done previously.

11. Two-Resonator Model

The antenna of Figure 9 has two waveguiding regions that are each bounded on the sides by cones, excited at the small end by the incident wave on the coaxial cable, and open on the large end which allows radiation. If we associate an equivalent line with each conical guide, it is apparent that these lines must be connected in series, as shown in Figure 10, to properly represent the conditions in the feed region of the nested conical monopoles. That is, the output voltage of the transformer in Figure 10 is divided between the inputs to the transmission lines and, at the input, the current in the lower conductor of the upper line is equal to that in the upper conductor of the lower line. Hence, the two resonators, radiating conical guides in the antenna represented by terminated line sections in the equivalent circuit, are effectively connected in series at the input ends.

The circuit of Figure 10 has been analyzed for numerous sets of parameters. Typical results are shown in Figure 11. The presence of two resonators in the system produces two frequencies with zero reactance. When the two resonant frequencies are close together, in the band between them the impedance takes a circular locus on the Smith chart. The radius of the circle bounding the data becomes smaller as the resonant frequencies move closer together. The center of the near-circular part of the impedance locus can be shifted to the center of the chart by attaching a suitable transformer at the input as shown in the circuit of Figure 10. Consequently, the input SWR (and return loss) is very nearly constant over the band between the resonant frequencies as shown in the right-hand plot of Figure 11.

Some results of repeated analysis of the circuit of Figure 10 are summarized in Table 4. The frequencies f_1 and f_2 are the resonances and HPBW is the bandwidth between 3-dB points on the return loss plot.

Table 4

Model parameters and corresponding performance for a set of two nested conical monopoles (ℓ_1 and $\ell_2 = 22.5$ degrees at f_1 and f_2 , respectively).

L ₁ (nH)	L ₂ (nH)	f ₁ (MHz)	f ₂ (MHz)	HPBW(MHz)	Ret Loss(dB)	SWR
37.5	38.5	107	100	9.2	13	1.6
37.0	38.5	108.8	100	11.2	10	1.9
35.0	38.5	108.8	100	14.0	7	2.6

Notice the trade-off between the half-power bandwidth (HPBW) and the return loss in the passband. The bandwidth can be increased as the degree of impedance match is relaxed.

Data obtained by analyzing the circuit of Figure 10 without the transformer are shown in Figure 12. The inductance on the longer line was kept constant at 38.5 nH while the inductance on the shorter line was varied (35.0, 37.9, and 37.5 nH) for the three cases. As the second inductance approaches the first in value, the resonant frequencies move closer together and the size of the loop decreases. These computed data correspond to experimental data measured at the tip of the cone (no transformer). Note, however, that the size of the impedance loop is very sensitive to the value of the second inductance. Although this makes very difficult correlation between parameters of the model and those of the antenna, it is nevertheless possible to demonstrate the expected performance.

Figure 13 shows three cases of impedance taken with the physical version of the double-resonator antenna. First, eight coils were wound as identically as possible. Then, four of these coils were attached to each cone of the antenna and the inductances of the coils on the upper cone were progressively decreased by increasing the separation between the turns. In this way, it was possible to obtain the three sizes of impedance loops shown in Figure 13. This demonstrates that the bandwidth of a tunable system of nested conical monopoles can be adjusted to meet a wide variety of operational requirements.

12. Conclusions

For some applications it is desirable for the antenna to have vertically polarized, omnidirectional radiation in azimuth, but to be electrically small, particularly in height. Since small antennas usually have highly reactive input impedance, issues of impedance matching and bandwidth become all important. The input reactance of a small, wide-angle (75 - 90 degree) conical monopole is easily made zero (resonant) by attaching lumped inductances across the narrow radiating aperture. The resulting large resistance at the input can be converted to a useable lower value by means of a transformer.

The proper terminating reactance for a given frequency can also be obtained with series L-C circuits. Then, the frequency can be shifted by changing either the inductances or the capacitances. For continuous tuning the series capacitors can be replaced with varactors. The match frequency then depends upon the dc bias voltage that is supplied through a coaxial tee at the antenna input.

If the impedance bandwidth is not sufficient for a given application, it can be increased by introducing a second resonance with another conducting cone, nested with the first so that the overall height is not significantly increased. The proper transformer at the input produces a near-constant return loss over the band between the two resonances. A trade-off exists between the return loss and bandwidth.

13. Acknowledgments

This work was done under a Small Business Innovation Research contract.

14. References

1. H. J. Reich (ed), *Very High-Frequency Techniques*, Chapter Four, New York: McGraw-Hill, 1947.
2. Y. T. Lo and S. W. Lee, (eds), *Antenna Handbook: Theory, Applications, and Design*, p. 3-29, New York: VanNostrand Reinhold, 1988.

3. R. M. Bevensee, *Handbook of Conical Antennas and Scatterers*, New York: Gordon and Breach, 1973.
4. C. W. Harrison, Jr. and C. S. Williams, Jr., "Transients in Wide Angle Conical Antennas," *Trans. IEEE Antennas and Propagation Society*, vol. AP-13, p. 236, March 1965.
5. P. D. P. Smith, "The Conical Dipoles of Wide Angle," *Jour. Appl. Phys.*, Jan. 1948.
6. George Ploussios, "The Electronically Tuned Helix," *Proceedings of the Antenna Applications Symposium*, United States Air Force, the University of Massachusetts, and the University of Illinois, 1994.
- 7 A. Klappenberger; "RF Letters - Coil Inductors" *RF Design*, pp. 14-15, January, 1995.

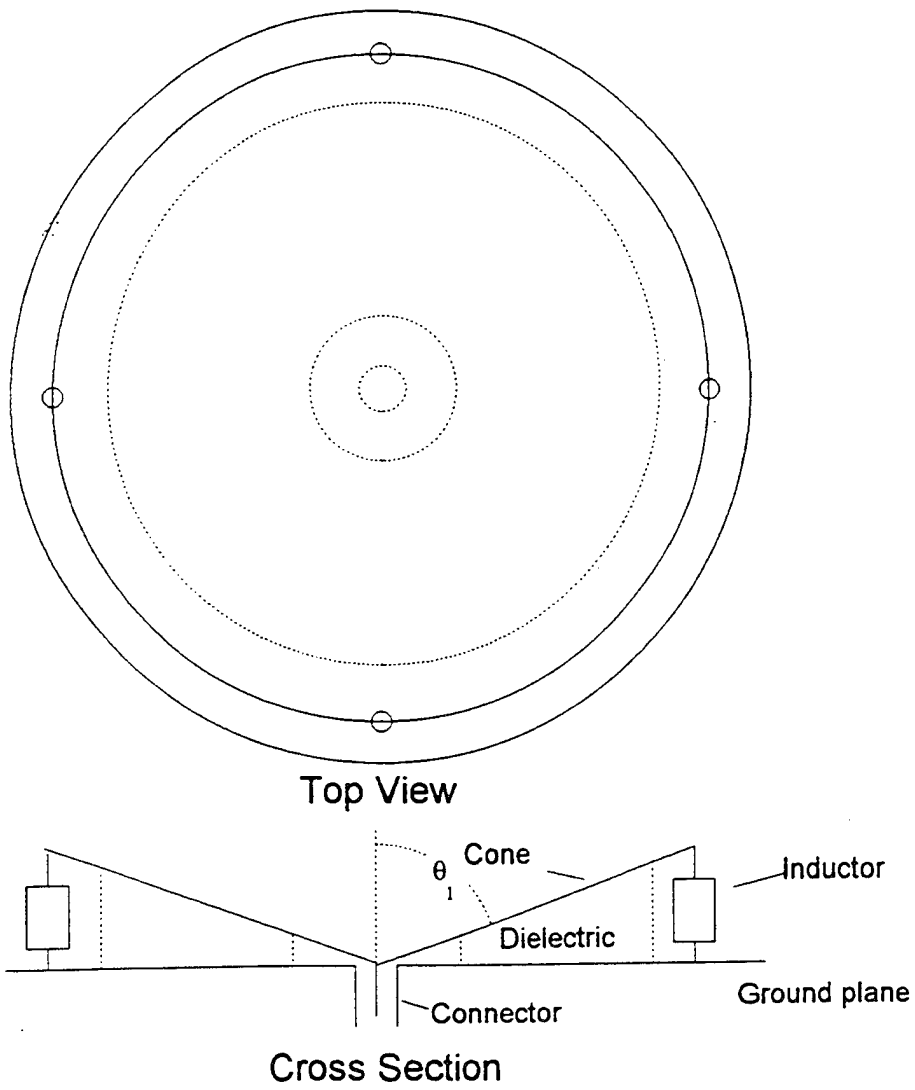


Figure 1. Inductance-loaded, wide-angle conical monopole.

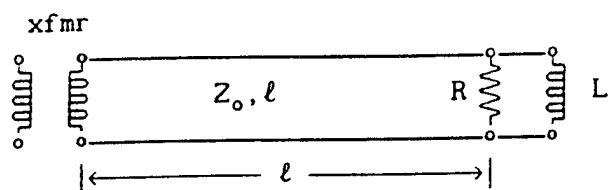
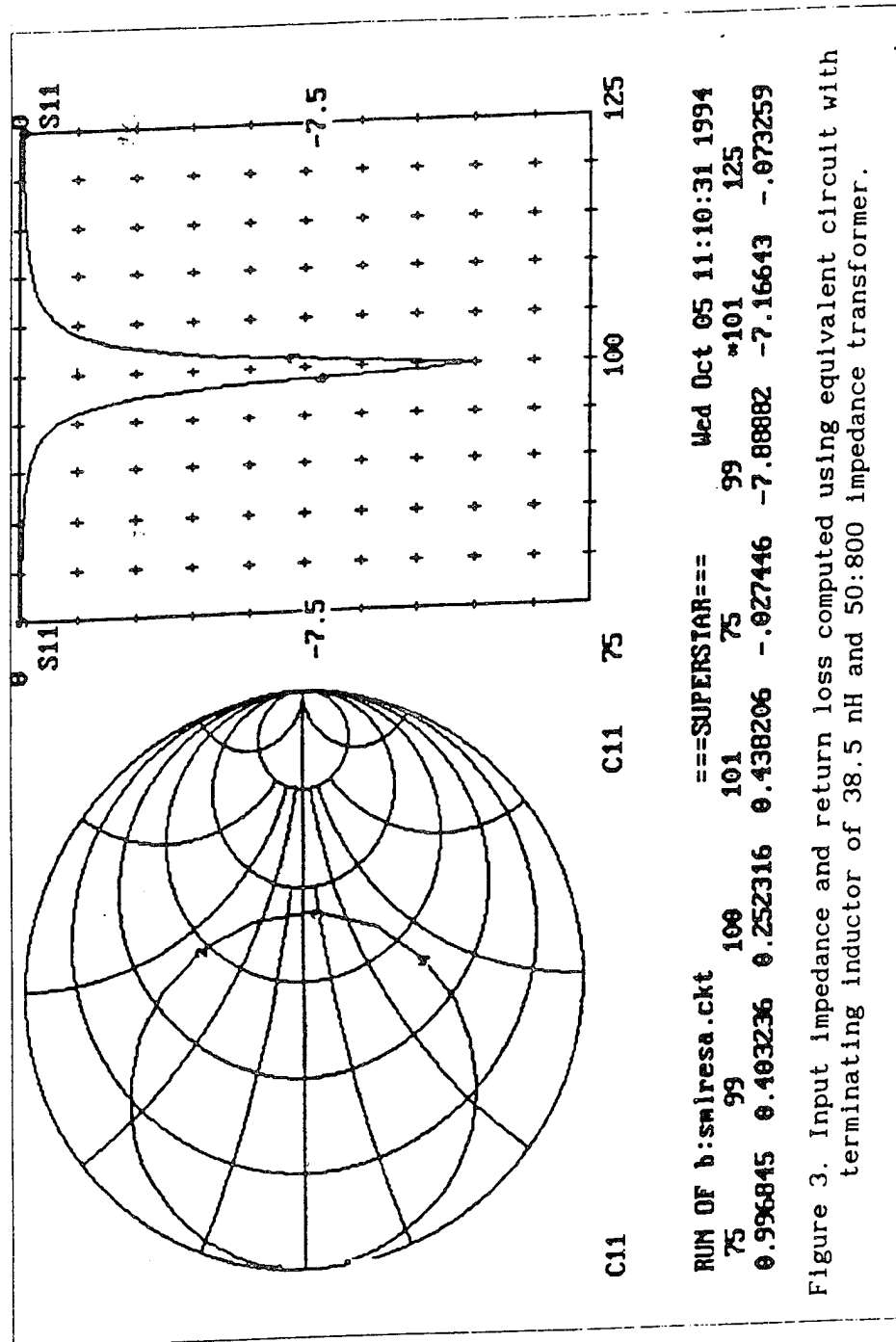
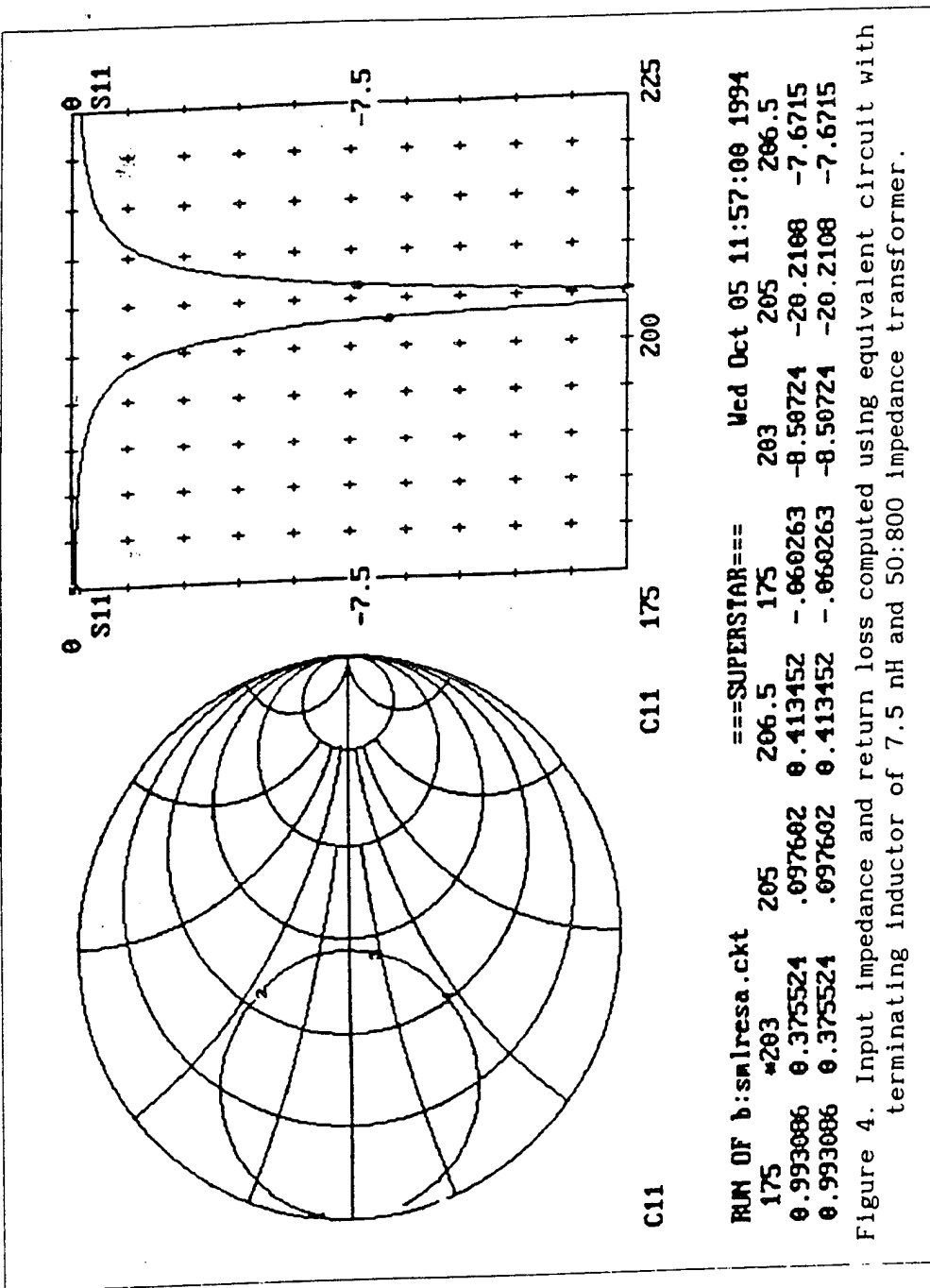
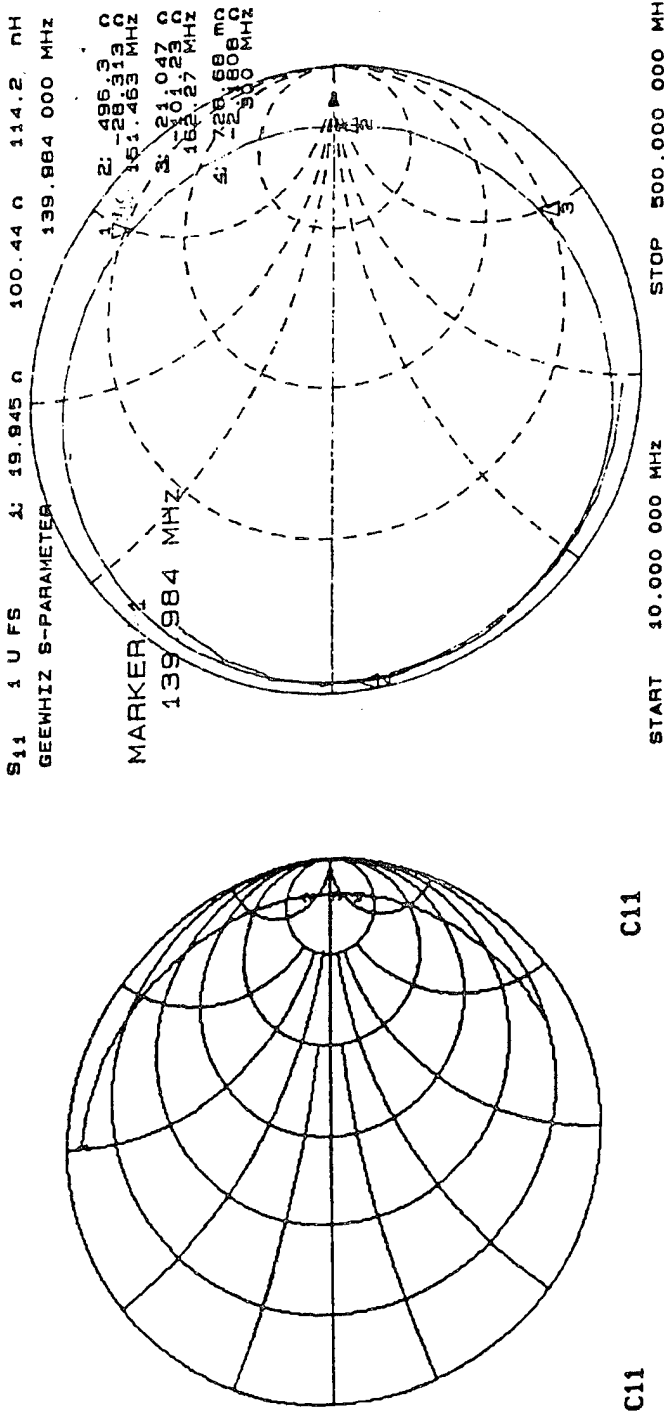


Figure 2. Equivalent circuit for impedance prediction of a conical monopole.







```

RUN OF b:s\iresa.ckt
  ===
175   293   205   206.5
0.946612 0.875183 0.872015 0.871632

```

Figure 5. Input impedance computed using equivalent circuit with terminating inductor of 7.5 nH and no transformer.

Figure 6. Measured input impedance for wide-angle conical monopole with four 38 nH inductors.

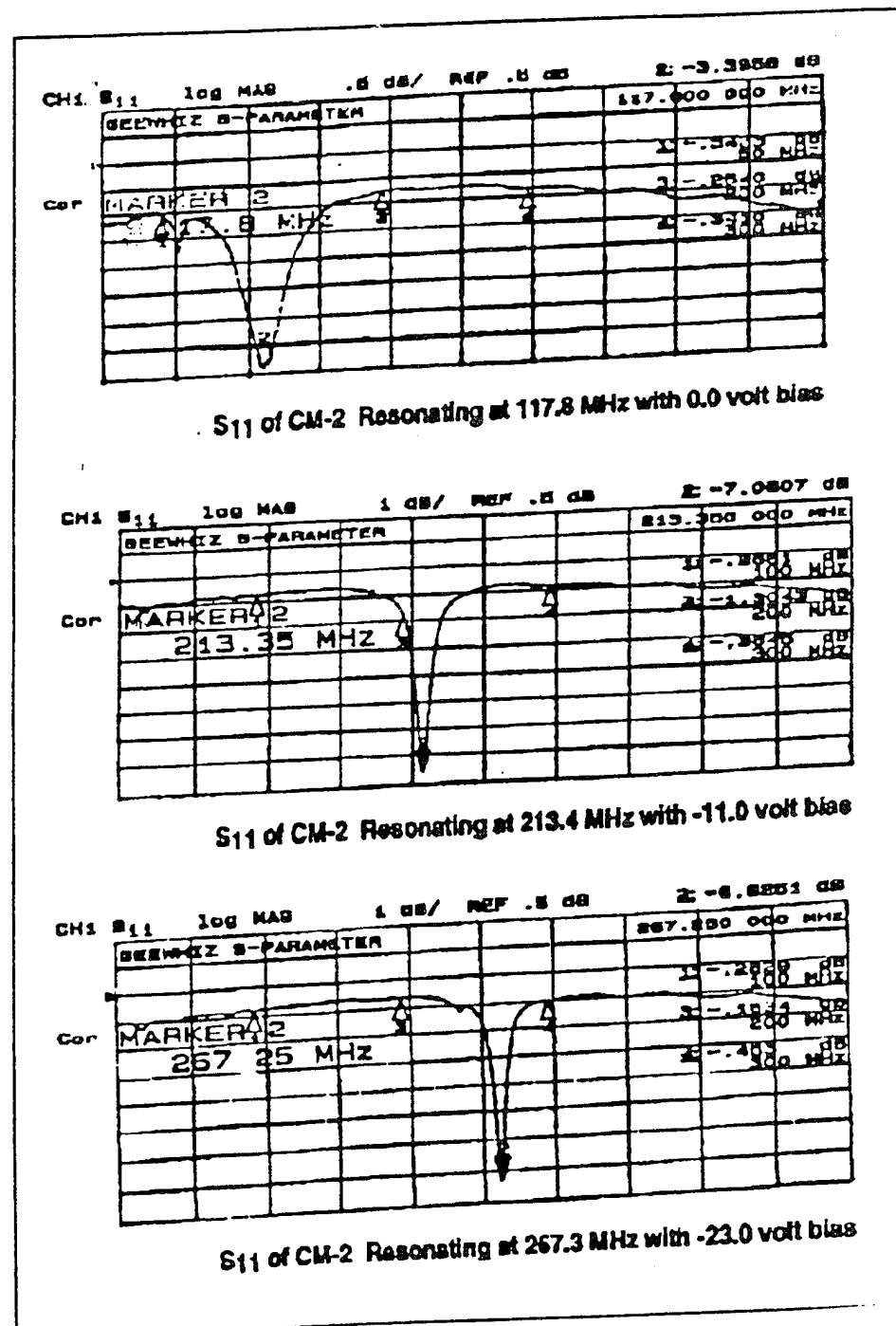


Figure 7. Magnitude of reflection coefficient as a function of varactor bias voltage.

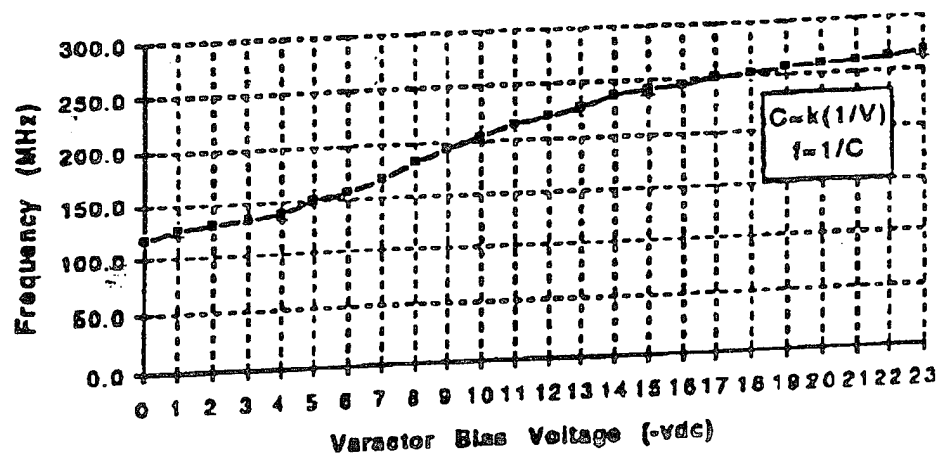
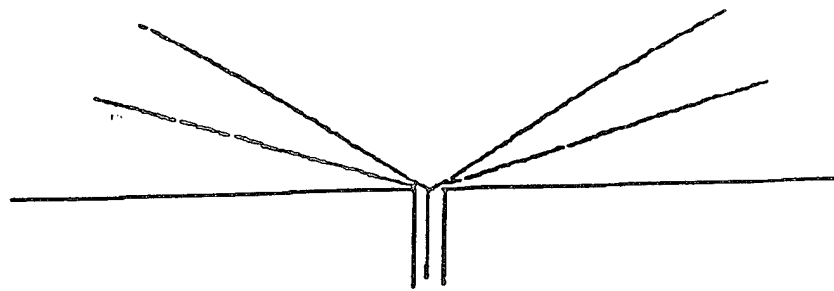


Figure 8. Resonant frequency versus varactor bias voltage.



CROSS SECTION

Figure 9. Two conical monopoles fed in series.

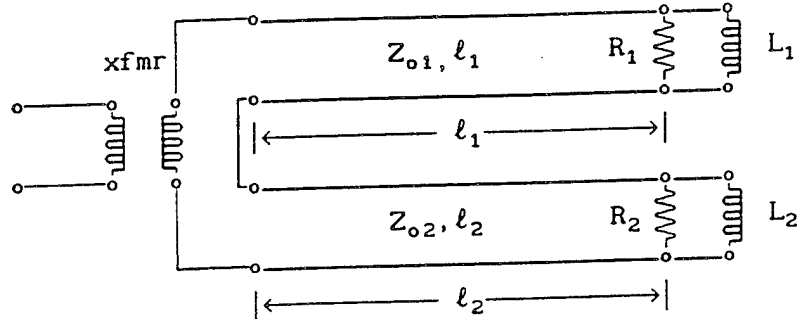
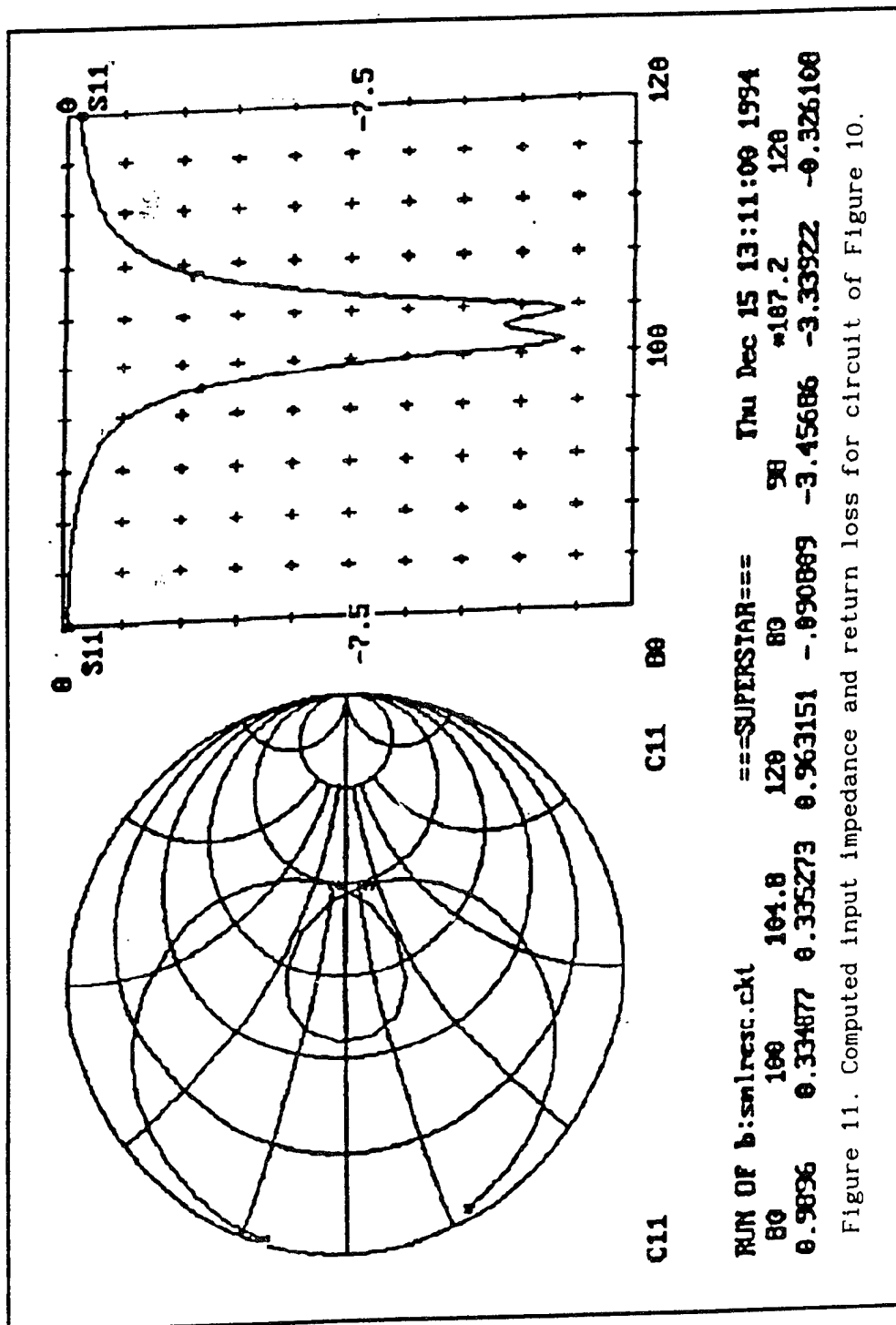


Figure 10. Equivalent circuit for impedance prediction for a set of two nested conical monopoles in series.



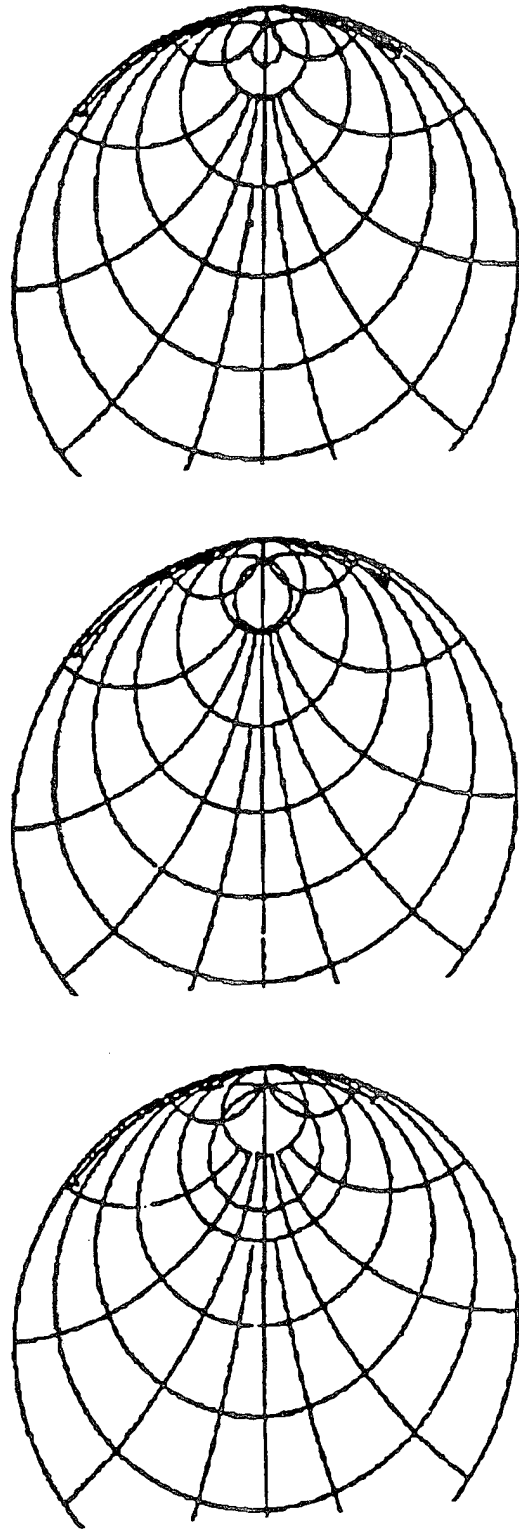


Figure 12. Computed input impedance for two-resonator system, one fixed and one varied by changing terminal inductance.

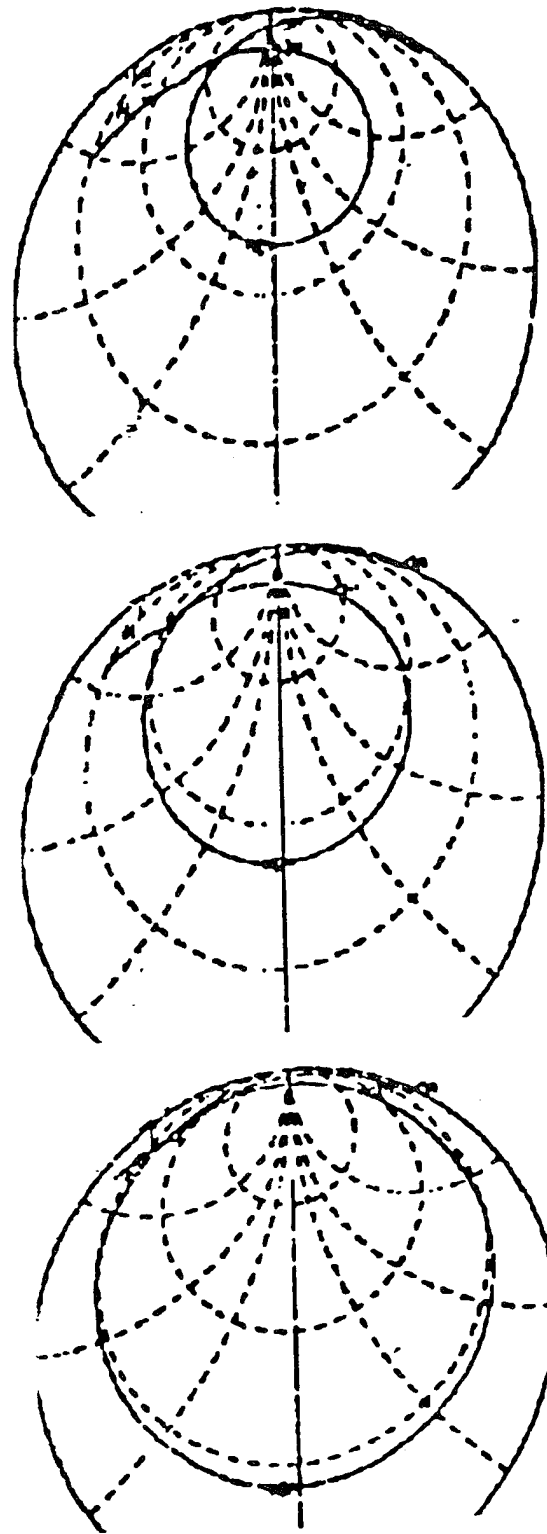


Figure 13. Measured input impedance for two-resonator system with three different values for terminal inductances on the upper cone.

PHOTONIC-BASED TUNING AND CONTROL OF ANTENNA ELEMENTS

Thomas L. Larry
Catherine J. Swann
Michael L. VanBlaricum
Toyon Research Corporation
75 Aero Camino, Suite A
Goleta, CA 93117

Abstract: There are many techniques for optically carrying an RF signal from an antenna element to its receiver, thereby optically isolating the antenna. However, if the antenna needs to be tuned or the matching network needs to be controlled, then it is desirable to perform that function optically as well. We show that an optically linked, electrically small loop can be tuned over almost an octave of bandwidth by using remote optical control via an optically variable reactance. Both theoretical and experimental results are presented.

Optically controlled reactive loads can be placed in the arms of an antenna element as a control device. We show that the antenna's radiation pattern can be steered by varying the reactive impedance value photonically. Theoretical examples are presented for a spiral antenna.

1. Introduction

Since the early 1980s, research groups have been investigating the use of photonic modulation devices connected to optical fiber systems for distribution of analog RF signals in antenna, phased array, and electromagnetic field sensor systems [1-4]. Potential applications include electromagnetic emissions monitoring, nuclear and lightning generated electromagnetic pulse measurements, anechoic chamber calibration and mapping, near-field probing, antenna remoting, direction finding, and radar systems, as well as, novel reconfigurable antenna and phased array feed designs.

In conventional systems, signals gathered by an antenna or array of antennas are usually fed to the receive electronics using metallic transmission lines or waveguides. These cables can inhibit the performance of the system response characteristics in a number of ways:

- 1) Directly perturbing the local field environment;
- 2) Attenuating and band-limiting the received signals through long cable runs;
- 3) Limiting low observability;
- 4) Allowing electromagnetic interference and crosstalk;
- 5) Adding weight to the antenna or antenna array system.

Metallic waveguide and cable problems can be avoided by replacing the feed system with a fiber-optical link and modulator system. Optical fiber and photonic devices offer many advantages to the antenna and sensor designer:

- Low transmission loss over long distances compared to conventional coaxial and waveguide feeds
- Light weight
- Small size
- Broad bandwidth
- Immunity from electromagnetic interference and crosstalk
- Low observability due to the dielectric nature of the fibers
- Non-interfering control lines

The RF attenuation in optical fiber is less than 0.5 dB / km compared to greater than 10 dB / km in coax or waveguide systems. The low dielectric constant of glass optical fiber reduces the RCS of the probe's feed system.

In a photonic-based antenna link, the RF signal from the antenna element drives an optical modulator which puts the RF signal on an optical carrier, **Figure 1**. The RF signal is then carried to the receiver via optical fiber. There are two types of optical

modulation schemes commonly used — direct and external modulation [5]. In direct modulation systems, the optical output of a laser at the RF source is directly modulated by applying the RF signal to the laser's bias current. This approach requires the laser and its power source to be located at the antenna. This precludes the direct modulation approach from being used in many antenna remoting systems. Externally modulated systems use a nominally-passive electro-optical modulator at the antenna to modulate the laser light which is delivered via optical fiber. In this approach, the optical source and the receive electronics can be collocated at a remote location. External modulation, the most common technique used in antenna links, is the technique used in this paper.

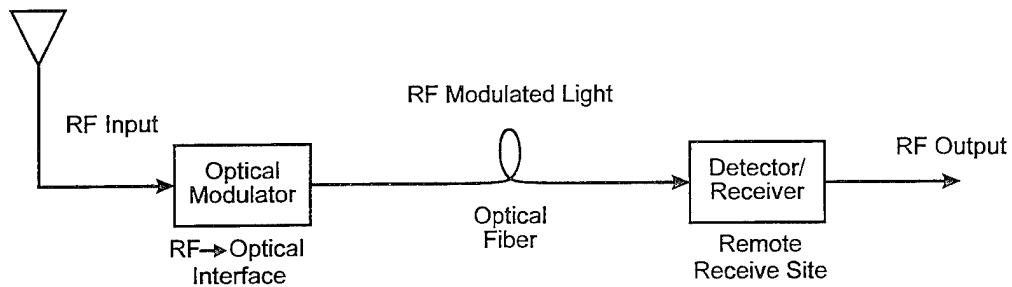


Figure 1. Photonic connection of an antenna element to a remote receiver.

Electro-optic modulators using the linear electro-optic (Pockel's) effect [6] are the principal devices used in external photonic-based antenna link systems. When an electric field is applied to a material exhibiting the Pockel's effect, the material's optical index of refraction changes in direct proportion to the applied field. If light is propagated through the material, the applied field modulates the phase of the optical signal.

In 1978, Bassen [7] patented the use of an integrated-optical amplitude-modulator as part of a remote antenna link. Since that time, several research groups have successfully used the integrated-optics (IO) Mach-Zehnder interferometer (MZI) as the modulating device in antenna link systems. An integrated optics MZI can be made by doping interferometer waveguides directly into a crystal (such as lithium niobate) or other materials (such as nonlinear optical polymers and III-V semiconductors) which exhibit Pockel's effect and then depositing electrodes on the surface as shown schematically in **Figure 2**.

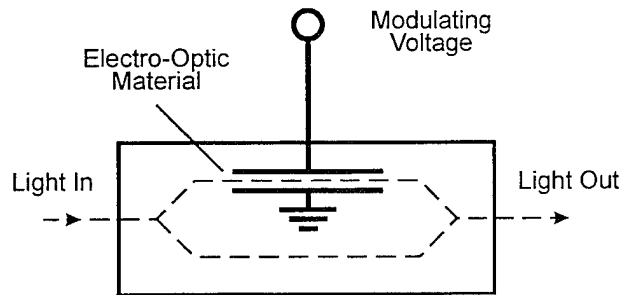


Figure 2. Typical layout for an integrated optics MZI modulator.

Coherent light entering the interferometer is split equally into the two arms. Along one arm of the interferometer, electrodes connected to the antenna element induce a voltage across the optical path. This voltage produces a phase change proportional to the voltage. This results in an output signal that is amplitude modulated when the two paths are combined in the output of the MZI. The resulting light intensity output is a function of voltage applied to the electrodes.

Figure 3 shows an equivalent circuit model for an MZI. The lumped element MZI behaves, to a good approximation, as a lead resistance in series with a parallel combination of the electrode capacitance and the dielectric resistance through the electro-optic material. In most cases, the leakage current through the electro-optic

material can be ignored so that the modulator impedance is represented as a resistor and capacitor in series. The input signal of concern is then the voltage developed across this capacitor.

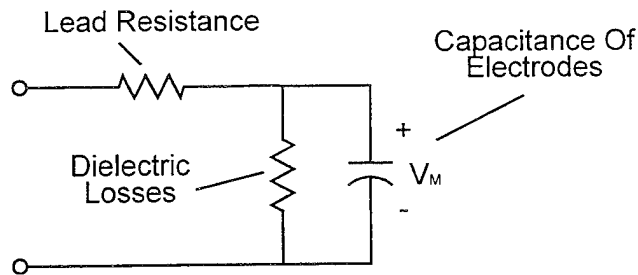


Figure 3. Equivalent circuit for the MZI device shown in **Figure 2**.

Commercially available modulators have demonstrated bandwidth performance up to 35 GHz [8]. The operating bandwidth of optically linked antenna systems is, however, generally limited by the frequency response of the antenna, matching network, and the electrodes feeding the optical modulator – not by the optics. For an increased bandwidth, traveling wave electrodes are used with integrated optical MZI systems in order to better match the optical wave velocity with the RF velocity. Bandwidths up to 60 GHz have been demonstrated using this approach.

Figure 4 shows the main components of an externally modulated, photonically linked antenna system. Conceptually, the system is very simple. A lightwave generated by the laser is transmitted through the fiber to the modulator where it is modulated by the RF output at the sensor antenna's matching network terminals. The modulated lightwave is then transmitted by optical fiber to an optical detector and converted back to an electrical RF signal. Separate fiber can be run to optically control the tuning of the antenna or control other parameters in the antenna element itself.

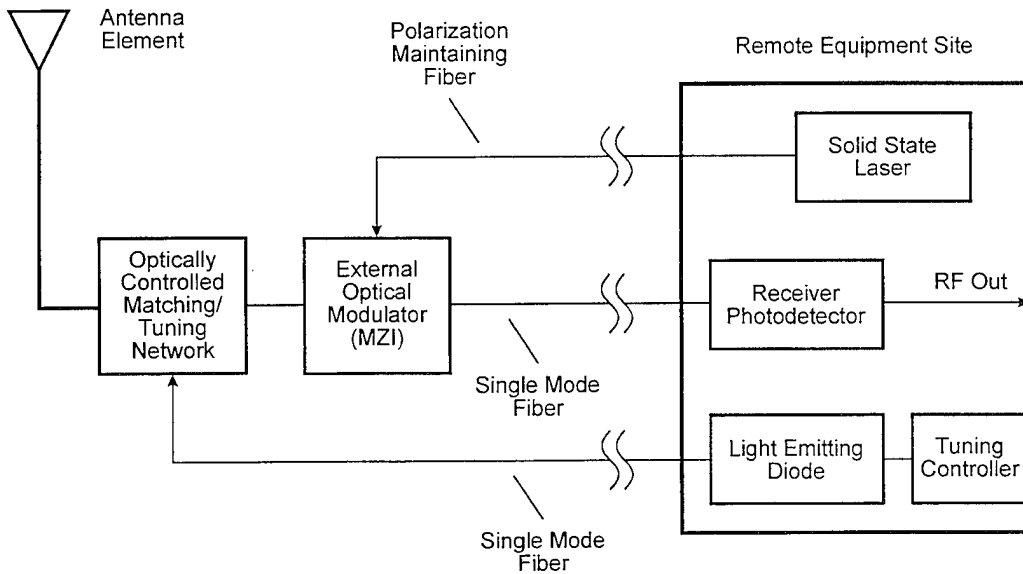


Figure 4. Simplified schematic diagram of main components of sensor system.

For the best performance, low-noise, high-power solid-state lasers operating in continuous-wave mode are used as the optical sources. At present, the input fiber from the laser to the MZI must be a polarization-preserving fiber. This is required by the polarization dependence of the MZI. The RF amplitude modulated laser light coming out of the MZI is sent down a single mode optical fiber where it is detected with an optical receiver consisting of a photodetector and a low-noise amplifier.

Dynamic range for a photonic link can be defined in several ways. A common way is to define the bottom of the range as the output noise level of the system and the upper end as the point where the third harmonic generated by the electro-optic modulator (an inherently nonlinear device) comes above the noise floor. Using this spurious-free distortion limit definition of dynamic range it is possible to obtain about 80 dB of dynamic range in a 100-kHz bandwidth if a low noise laser is used [9]. When interfering signals are not present (or at least not likely) the dynamic range can be defined as the maximum linear signal-to-noise ratio possible. This is

usually taken as the distance from the 1 dB compression point to the noise floor. This compression-limited dynamic range is typically as high as 150 dB.

2. Tuning of Photonically Linked Antennas

Connecting optical modulators and fiber optic links to an antenna allows flexibility in the system design beyond that available by conventional systems. This is due to two inherent properties of the optical links and modulators: 1) The bandwidth of optical modulators and optical links can be very broad; and 2) The effective impedance of the optical modulator is reactive with a very small (a few ohms) resistive component.

The broad bandwidth allows the potential for connecting a broadband antenna to the link and remoting the receiver electronics. For example, in a measurement one might connect a probe antenna with more than a decade of bandwidth (such as the cavity backed spiral antenna) to the optical link. Using photonic modulators and links for this provides broad bandwidth capability with low loss in the optical links. However, it has some drawbacks. It still uses conventional antennas which must be mechanically supported and can have a fairly large interaction with the antenna or system under test. A photonically linked system can provide a way around such drawbacks.

The highly reactive impedance of the MZI modulator allows one to construct a field sensor system that has high sensitivity but small physical size and electromagnetic cross section. As mentioned above, the MZI impedance is generally capacitive with some resistive losses due to the small diameter of the electrodes and their leads (see **Figure 3**). This difference in the load lends itself to narrow band matching with small antennas, such as short dipoles or small loops.

An electrically short dipole antenna or electrically small loop can be connected to an MZI with a matching / tuning circuit such that the overall circuit Q is very high and the voltage gain of the circuit can be 20 dB or more. This is possible because the resistive losses in an electrically short antenna due to radiation and attenuation are just a few ohms. Hence, the impedance of the antenna can be combined with the impedance of the MZI and a tuning circuit to form a series resonant circuit with only a few ohms of resistance. This resonant circuit can then be tuned over a large band by changing the capacitance of the tuning circuit. **Figure 5** presents a block diagram of this concept using a small loop antenna connected through a matching network to an optical modulator. **Figure 6** presents a schematic diagram for the antenna system of **Figure 5**.

Conventional approaches for tuning the antenna / matching network described above require electrical (hard wire) connectivity to the tuning circuit. This is not appropriate for optical-based sensor systems because it defeats the passive nature of the fiber optical link. However, with the use of Toyon's optically variable capacitor (OVCTM), it is possible to control the reactance of devices optically, while maintaining the all-dielectric characteristic of the link. The capacitance can be varied over almost a decade. Tuning circuits have been built that allow an antenna's resonance to be swept over nearly an octave of bandwidth by changing the intensity of light incident on the tuning circuit.

To test the complete photonic link and control of a loop antenna as shown in **Figure 5**, we built a half-loop antenna above a ground plane and reactively matched (See **Figure 6**) it to a MZI modulator using an OVCTM. The diameter of the loop was 1.5 cm. A half loop antenna was used because we planned to illuminate it in a TEM (Crawford) cell [10] and needed to feed it against a ground plane.

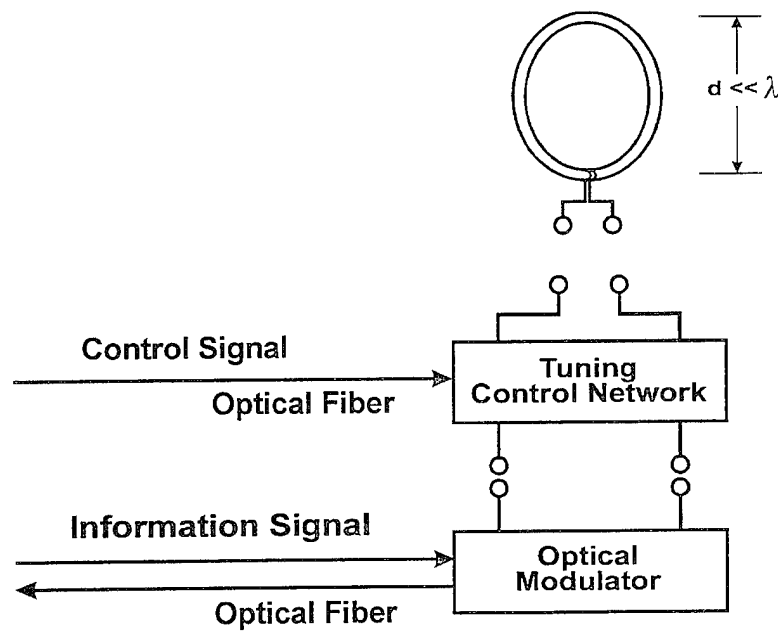


Figure 5. Block diagram of a photonically connected and controlled electrically small loop antenna.

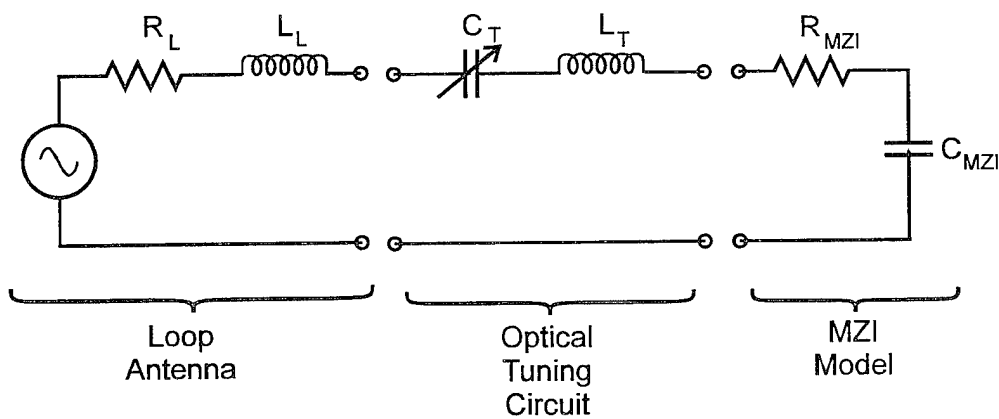


Figure 6. Schematic diagram of the equivalent circuit for the photonically connected antenna of **Figure 5**.

Before performing the measurements, we modeled the entire system in our PHLASH™ code. PHLASH™ is a PC/Windows-based system engineering tool for predicting the performance of sensor and antenna systems which include a fiber optic link in their architecture. This particular link included an MZI with a V_π of 5.6 volts. The link was driven with only 6 mW of laser power. Hence, the link was not designed for optimal link gain or sensitivity. **Figure 7** shows the predicted link gain values for the two extreme values of our OVC™. For the dark case the capacitance was 19 pF and the loop was tuned to 248 MHz. For the case of maximum light on, the OVC™ produced a capacitance of 3 pF and the loop was tuned to 408 MHz.

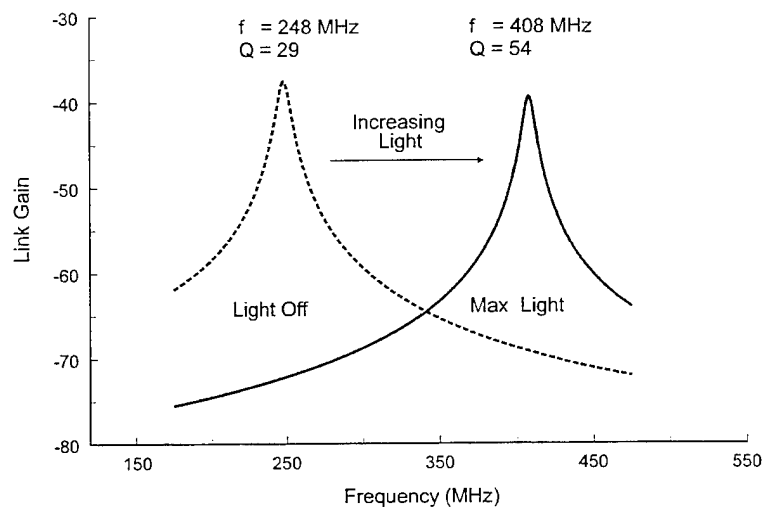


Figure 7. Predicted link gain for the 1.5-cm diameter half-loop antenna reactively matched to the MZI-based link. The two extreme states of the OVC™ tuning capacitor are shown.

Figure 8 shows the measured gain for the tuned half-loop link. The measured gain is uncalibrated because of the TEM cell measurements. The tuning range and the Q values were of principal interest to us. From **Figure 8** the tuning range is seen to go from 242 MHz to 413 MHz or 71% which is greater than that which we had predicted. The measured Q is seen to be fairly close to the predicted value.

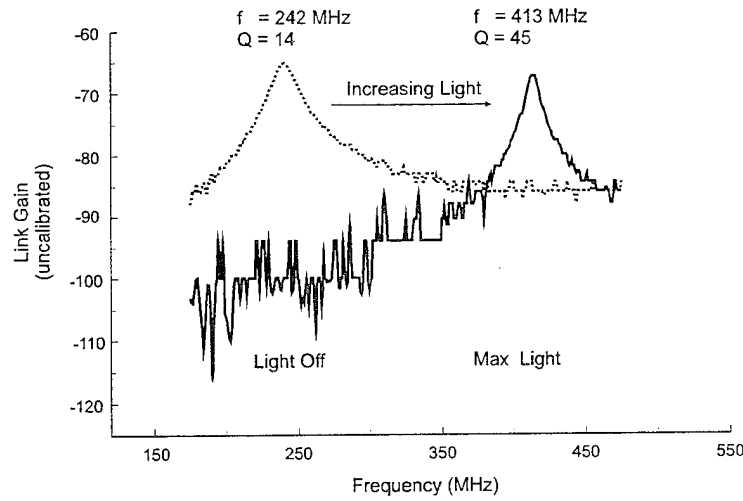


Figure 8. Measured link gain (uncalibrated) for the 1.5-cm diameter half-loop antenna reactively matched to the MZI-based link.

The above test was not optimized for link sensitivity. It was done to prove that a small antenna could be tuned and connected photonically. Subsequent to this test, we used PHLASH to predict what the link gain and sensitivity for a loop antenna with a 4-cm loop diameter. We optimized the photonic link parameters to reflect the state-of-the-art available today. We used a MZI with a V_π of 0.75 volts and a laser with 150 mW of output power.

Figure 9 presents the predicted link gain for the 4-cm loop and optimized link. In this study, the same OVC™ was used. The larger antenna caused the tuning range to be lowered to 180 to 300 MHz. The tuning bandwidth was 66%, which is the same as that predicted with the smaller antenna. However, in this case, the link power gain is predicted to be about 22 dB. **Figure 10** shows that this translates into a minimum detectable field of less than 10 μ V/meter at the tuned value. It is interesting to note, for the light-off case, the minimum sensitivity stays lower than 100 μ V/meter from below 100 MHz to above 350 MHz.

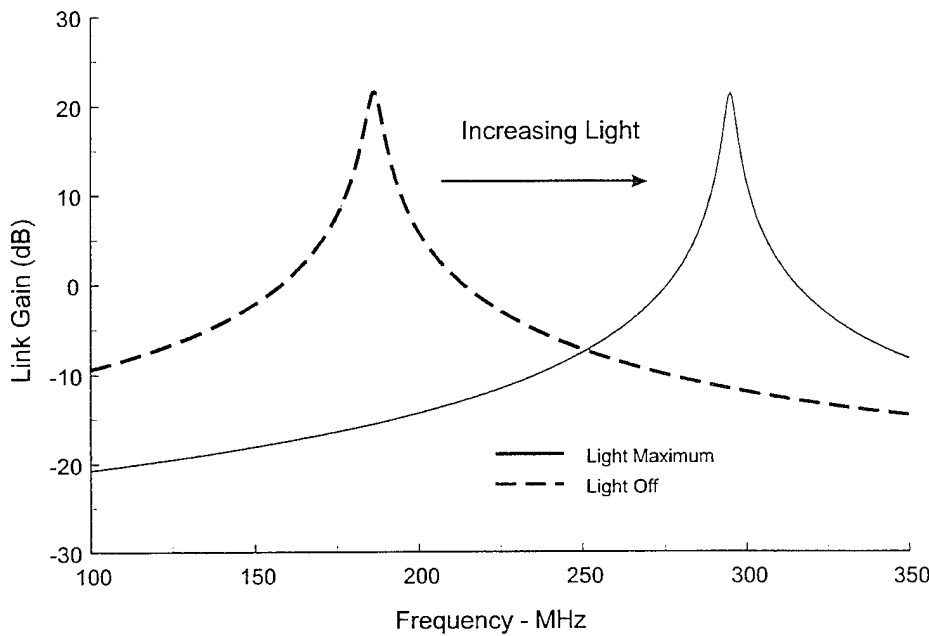


Figure 9. Predicted link gain for a 4-cm diameter loop antenna reactively matched to an optimized MZI-based photonic link. The gain is shown for the two extreme settings of the OVC™ capacitor.

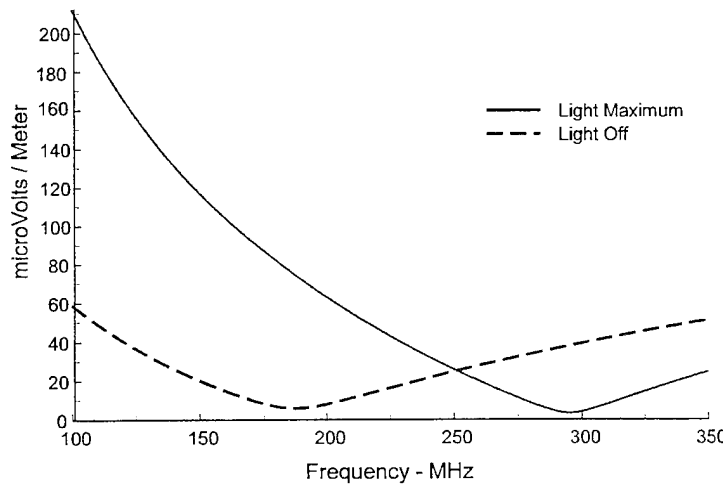


Figure 10. Predicted minimum detectable electric field for the 4-cm diameter loop antenna reactively matched/tuned to an optimized MZI-based photonic link.

Figure 11 presents the predicted dynamic range in a 10-kHz bandwidth for this system. The spurious-free dynamic range (SFDR) is nearly 90 dB everywhere except at the point of maximum link gain. The dynamic range, as it is calculated for the photonic link, is:

$$\begin{aligned} SFDR &= \frac{2}{3} (IP3 - P_{o, mds}) \\ &= \frac{2}{3} (IP3 + 174 \text{ dBm} - NF - 10 \log(B) - G_a) , \end{aligned}$$

where IP3 is the third order intercept point for the MZI, $P_{o, mds}$ is the minimum detectable signal at the output of the link, NF is the link noise figure, G_a is the link gain, and the $-174 \text{ dBm} = kT$.

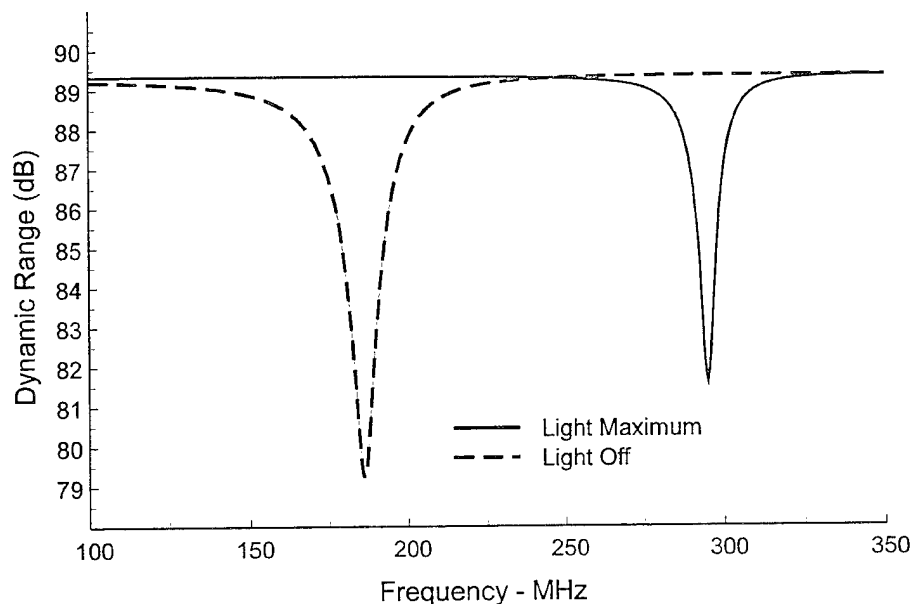


Figure 11. Predicted dynamic range for the 4-cm diameter loop antenna reactively matched/tuned to the optimized MZI-based photonic link.

The minimum detectable signal at the output of the link is defined as:

$$P_{o,mds} \text{ (dBm)} = -174 \text{ dBm} + 10 \log B + NF + G_a$$

From the expression for SFDR, it is clear that as the link gain goes up, the dynamic range goes down. Hence, design tradeoffs can be performed to maximize dynamic range at the expense of link gain.

3. Antenna Pattern Control

In the previous section, we looked at optical control within the RF link of an antenna for the purpose of matching and tuning the antenna feed. This was accomplished by placing a circuit with a variable capacitor between the antenna terminal and the modulator. We now theoretically examine the idea of placing variable lumped loads in the arms of the antenna itself. Each load circuit could contain an optically variable capacitor which would be used to alter the load impedance. This has the effect of changing current distributions on the antenna and, hence, the antenna characteristics. This is illustrated in **Figure 12**. Such an alteration of antenna properties is referred to as photonically-controlled reconfiguration and it is accomplished without any geometric change in the antenna. Also, the use of optical control to reconfigure the antenna along with a photonic link provides complete RF isolation.

Figure 13 presents an equivalent circuit diagram for the system shown in **Figure 12**. Both the antenna impedance, Z_A , and the antenna length, L_A , are variable since they depend on the choice of the capacitance values for the control elements within the lumped load circuits. The capacitor values in turn depend upon the optical power delivered to each of them. This can be expressed as:

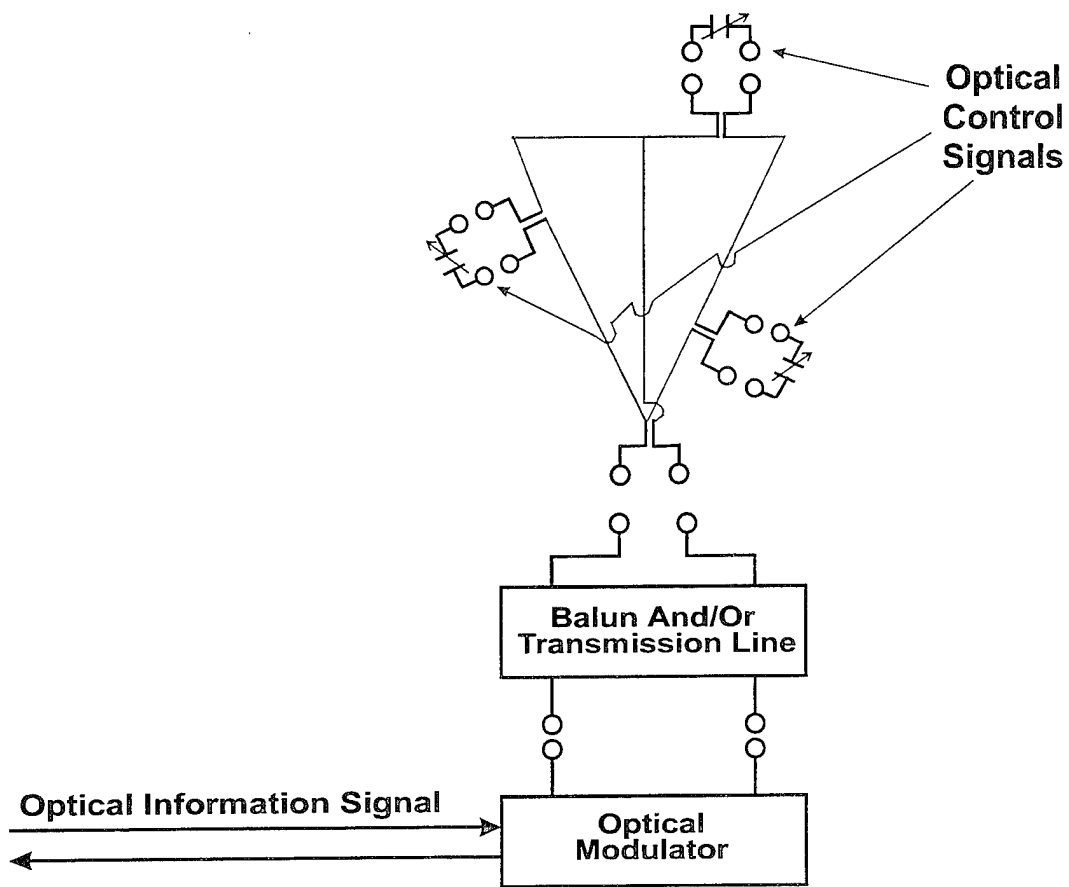


Figure 12. Photonically-controlled reconfigurable antenna.

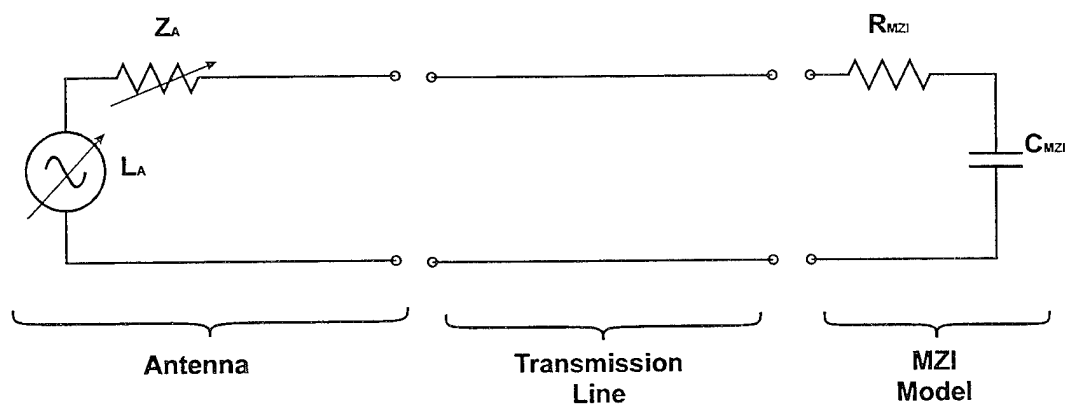


Figure 13. Equivalent circuit of antenna/reconfigurable external photonic link.

$$Z_A = Z_A(f; P_1, P_2, \dots)$$

$$L_A = L_A(f, \Omega, v; P_1, P_2, \dots)$$

where (Ω, v) refer to the direction and polarization of the source and P_n is the optical power in the control signal being delivered to the nth optically variable capacitor. The values of P_1, P_2, \dots can be optimally chosen to give Z_A and L_A desirable properties. This must be done in such a way so that each P_n does not exceed a saturation value.

To illustrate the idea of a photonically reconfigurable antenna, we performed a numerical analysis with the planar spiral antenna shown in **Figure 14**. The antenna element is a 15-cm diameter two-arm spiral located 2 cm above a ground plane. This antenna is basically an extension of the center conductor of a coax feed. The feed point is at the ground plane. This provides a natural balance between the current flowing to the antenna and the current flowing in the ground plane. The Z_A and L_A values are referenced to this feed point. Photonically variable capacitors were located along the spiral arms as shown. In the study we chose P_1, P_2, \dots, P_8 to maximize the RHCP gain for different directions at 2.6 GHz. Any direction could be chosen, but we limited ourselves to the vertical plane containing the line of capacitors shown in **Figure 14**. We could also have optimized the efficiency of the antenna by matching Z_A to the load impedance at the feed. This would have accomplished the same thing as the more conventional approach of matching the feed to the antenna. The difference here is that the antenna would have been reconfigured to match the feed. In a practical implementation of such an antenna this would be an important condition to maintain while steering the gain pattern for different directions.

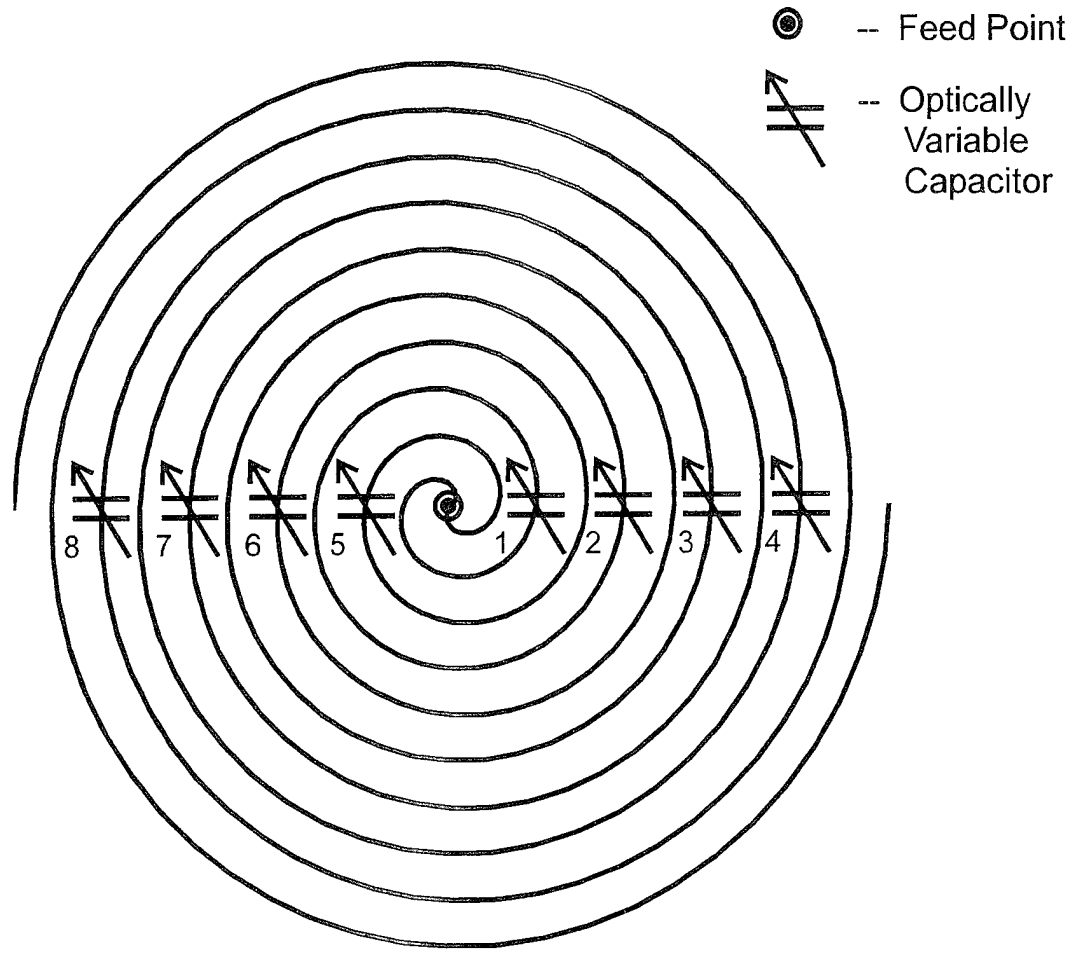


Figure 14. Archimedean spiral antenna; 2 arms, 5 turns each.

The antenna gain is given as,

$$G(\Omega, v) = (\pi \zeta / \lambda^2) |L_A|^2 / R_A$$

where $\zeta = 377$ ohms and R_A is the resistive component of Z_A . For this problem we chose v to correspond to RHCP and Ω was restricted to a single vertical plane. The gain G was maximized for several different elevation angles by choosing an appropriate set of P_1, P_2, \dots, P_8 values for each direction. For each case the resulting

gain patterns were plotted across the 2.5 to 2.7 GHz band. Samples of these are shown in this paper.

Figure 15 shows the RHCP gain pattern (dBic) as a function of elevation in the vertical plane. In this case there were no control loads along the spiral arms. This serves as a baseline case that can be used for comparison to see the effect on gain of reconfiguring the antenna. **Figures 16 through 19** show reconfigured gain patterns. The antenna element is being steered by appropriately varying the optically controlled capacitors. **Figure 16** shows the gain pattern that resulted from choosing the capacitances to optimize the gain at 45° of elevation. For **Figure 17** the gain was optimized for 60°. For **Figures 18 and 19**, the gain was optimized for 75° and 90°, respectively. For each of these cases the maximum gain was 5 to 6 dBic across the band.

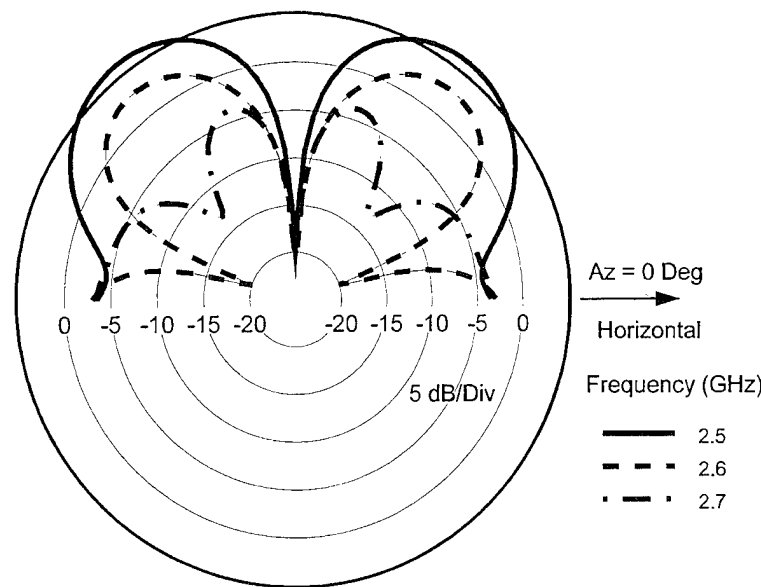


Figure 15. Gain (dBic) in elevation plane; no control loads.

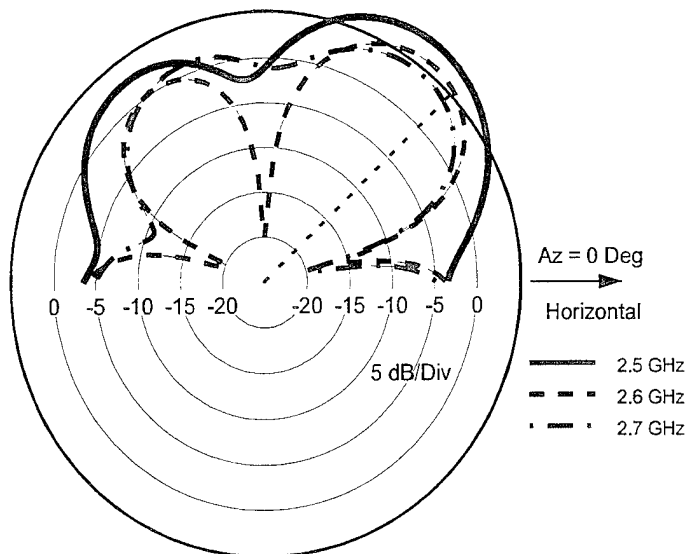


Figure 16. Gain (dBic) in elevation plane; capacitors chosen for 45° .

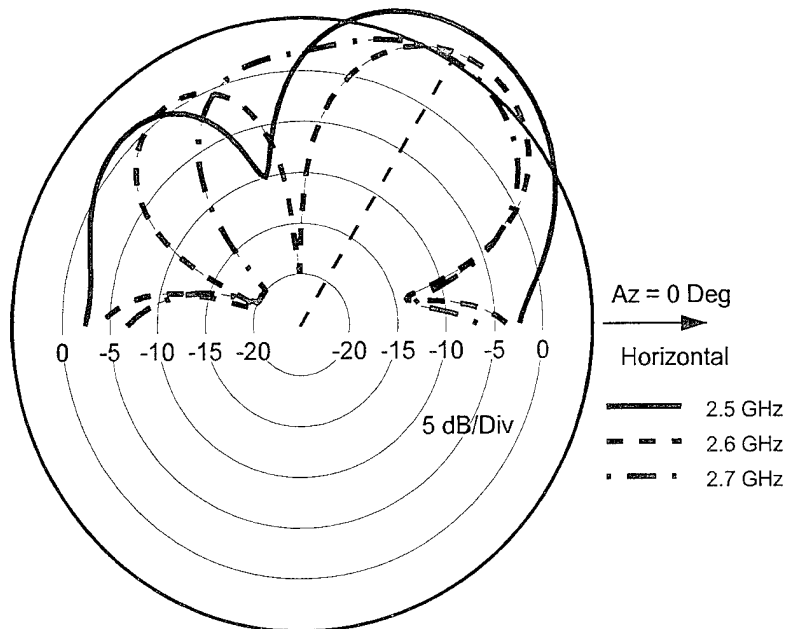


Figure 17. Gain (dBic) in elevation plane; capacitors chosen for 60° .

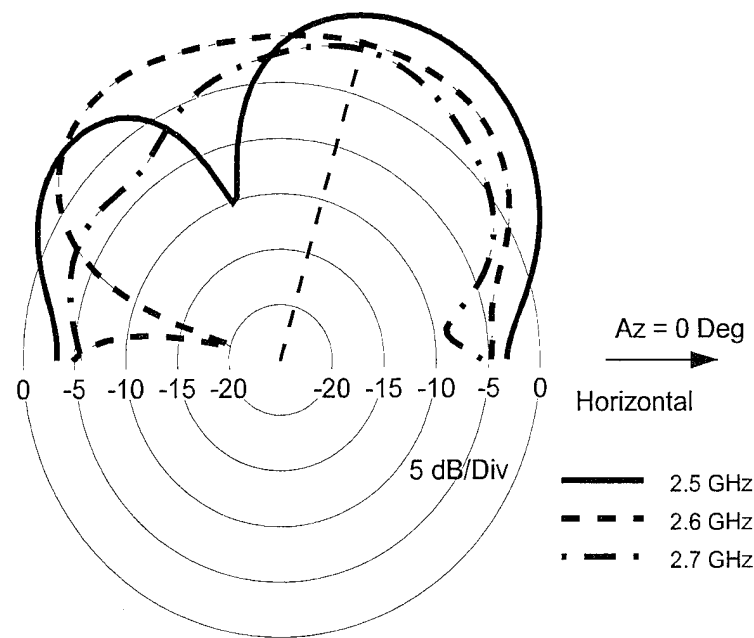


Figure 18. Gain (dBic) in elevation plane; Capacitors chosen for 75° .

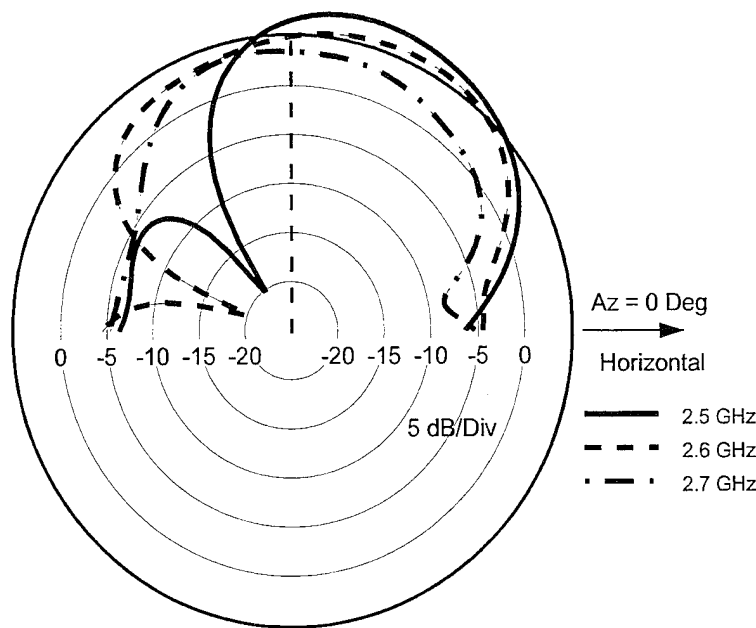


Figure 19. Gain (dBic) in elevation plane; Capacitors chosen for 90° .

5. Summary

In this paper we presented experimental data demonstrating that an photonically linked, electrically small loop antenna can be tuned over a 71% bandwidth using an optically variable capacitor. This technique can potentially give a very sensitive small receive antenna that is completely isolated optically. This bodes optimistically for building antenna chamber or near field probes that do not greatly perturb the fields they are measuring.

We also presented a theoretical study demonstrating that optically variable capacitors, when placed in the arms of a spiral antenna, can be used to beam steer a single antenna element. A number of interesting applications can be envisioned for photonically reconfigurable antenna elements. They can be rapidly and/or adaptively steered non-mechanically. The fact that the antenna can be tuned to the feed has the potential of simplifying feed designs. The use of optical fibers both for control as well as carrying the signal permits antenna remoting as well as RF isolation.

6. References

- [1] A.S. Daryoush, E. Ackerman, N.R. Samant, S. Wanuga, and D. Kasement, "Interfaces for High-Speed Fiber-Optic Links: Analysis and Experiment," *IEEE Transactions on Microwave Theory and Techniques*, Vol. 39, No. 12, December 1991, pp 2031 - 2044.
- [2] C. H. Cox III, "Analog Fiber-Optic Links with Intrinsic Gain", *Microwave Journal*, Vol. 35, No. 9, September 1992, pp 90-99.
- [3] T. Sueta and M. Izutsu, "Integrated Optic Devices for Microwave Applications," *IEEE Transactions on Microwave Theory and Techniques*, Vol. 38, No. 5, May 1990, pp 477-481.
- [4] R.G. Walker, I. Bennion, and A.C. Carter, "Low-Voltage, 50Ω , GaAs/AlGaAs Travelling-Wave Modulator with Bandwidth Exceeding 25GHz," *Electronics Letters*, Vol. 25, No. 23, pp. 1549-1550, 9 Nov. 1989.
- [5] C.H. Cox III, G. E. Betts, and L. M. Johnson, "An Analytic and Experimental Comparison of Direct and External Modulation in Analog Fiber-Optic Links," *IEEE Transactions on Microwave Theory and Techniques*, Vol. 38, No. 5, May 1990. pp 501-509.
- [6] R. Simons, *Optical Control of Microwave Devices*, Artech House, Boston, 1990.
- [7] H. Bassen and R. Petersen, "Antenna with electro-optic modulator", U.S. Patent 4 070 621, January, 1978.
- [8] R.G. Walker, "High Speed III-V Semiconductor Intensity Modulators", *IEEE Journal of Quantum Electronics*, 27(3), 1991, pp. 654-667.
- [9] G.E. Betts, L.M. Johnson, C.H. Cox III, and S.D. Lowney, "High-Performance Optical Analog Link Using External Modulator," *IEEE Photonics Technology Letters*, Vol. 1, No. 11, November 1989, pp404-406.
- [10] M.L. Crawford, "Generation of Standard EM Fields Using TEM Transmission Cells," *IEEE Transactions on Electromagnetic Compatibility*, Vol. EMC-16, No. 4, Nov. 1974, pp 189-195.

GENETIC ALGORITHM ARRAY PATTERN SYNTHESIS

Scott Santarelli, Hugh Southall, and Edward Martin

USAF Rome Laboratory

Electromagnetics and Reliability Directorate

RL/ERAS, 31 Grenier Street

Hanscom AFB, MA 01731

Terry O'Donnell*

ARCON Corporation

260 Bear Hill Road

Waltham, MA 02154

Abstract

We are currently experimenting with the use of genetic algorithms (GAs) to solve for the unknown transfer function of low cost or degraded antenna arrays. We develop adaptive array software which can learn to synthesize patterns and form beams with non-ideal arrays in imperfect environments. Our goal is to reduce the costs of phased arrays by any means possible, while maintaining acceptable array performance. This effort, which can have enormous cost benefits to the warfighter, is part of a larger "neural beamforming" project [1]. Results from the GAs will be used as training points for a neural network which will learn to generalize beam-steering control of the array [2].

In this paper, we present a genetic algorithm which determines the attenuator and phase-shifter settings required to create a desired beam. We describe the structure of the chromosome which we designed, and the genetic encodings and operators which have proven most successful at solving this beamforming problem. We present results showing how the genetic algorithm solves the beamforming problem with simulated antenna models. We also present experimental results applying the genetic algorithm to an eight element linear array. This array, which only has phase control, uses Reggia-Spencer phase shifters which are nonlinear and adversely coupled with the elements' attenuation. The GA will be used with this antenna to find the optimal beam steered patterns at several azimuthal angles

*Work performed under USAF Contract #F19628-92-C-0177.

1 Introduction

Our overall goal is to solve for the unknown transfer characteristics of low cost or degraded antenna arrays. Many manufactured arrays contain elements with nearly identical transfer characteristics, and compensation for these small differences is accomplished via a near field or far field calibration. A “degraded” antenna array, on the other hand, may possess any combination of the following properties: nonlinear phase shifters and attenuators, degraded performance as a result of prolonged exposure to unfavorable environmental conditions, and “dead” elements that can not be easily replaced because of the remote location of the array.

Although the transfer characteristics of such arrays inhibit the use of traditional beam-forming algorithms, a one-to-one mapping from input to output may still exist. Once the transfer function of the system is established, we can steer the main beam of the antenna pattern for real time applications. We plan to implement a strategic combination of neural networks, fuzzy logic, and genetic algorithms to accomplish this task.

An adaptive radial basis function (ARBF) neural network is able to perform function approximation when provided with appropriate training data [3, 4]. In our example, the function that we wish to approximate is the transfer function of a degraded array. “Training data” are points that are experimentally known to lie on the transfer function curve. For example, if we know the phase-shifter settings that form a main beam at broadside, then this is considered a training point. The phase-shifter settings that form a beam at 10° is another training point, and so on.

Now suppose that we have access to the phase-shifter settings that form beams from -90° to 90° in 10° increments for a total of 19 training points. The ARBF neural network should be able to generalize between training points after it is properly trained. In essence, the algorithm and architecture of the network “learn” the transfer function of the array between the training points, as well as at these points themselves. Hence, the network should provide the phase-shifter settings for any specified angle between -90° and 90° , despite the fact that only a finite number of data points are experimentally known [2].

Yet, how does one obtain the initial training points? If the phase-shifters and attenuators on the array are linear, and if all of the individual elements are identical, then the phase-shifter settings that correspond to a particular main beam angle can be solved by traditional methods. With such an ideal antenna, of course, all beam positions could be calculated analytically and we wouldn’t need a neural network. If the phase-shifters and attenuators behave nonlinearly, however, and if the individual elements are nonuniform, then the problem is unsolvable by analytical means. In addition, the mathematical space containing all possible phase-shifter and attenuator setting combinations is too immense to search exhaustively for an exact or optimal solution.

For these reasons we propose to use a genetic algorithm (GA) to solve for the phase-shifter settings. GAs are capable of finding optimal solutions to problems that possess large solution spaces. Convergence is achieved through a directive search method that relies largely on stochastic operators.

In this paper, we first briefly introduce the underlying concepts pertaining to GAs. Next, we illustrate these ideas with a simple array pattern synthesis problem simulated in MATLAB. Finally, we describe the experiment in which we synthesize several array patterns using GAs on a non-ideal antenna.

2 Genetic Algorithms

Genetic Algorithms (GAs), as the name implies, are modeled after Charles Darwin's theory of "survival of the fittest". Applications of these programs already exist in many areas, including marketing analysis, VLSI technology, and music generation [5]. Recently, genetic algorithm solutions have been proposed to electromagnetics problems as well. [6, 7, 8].

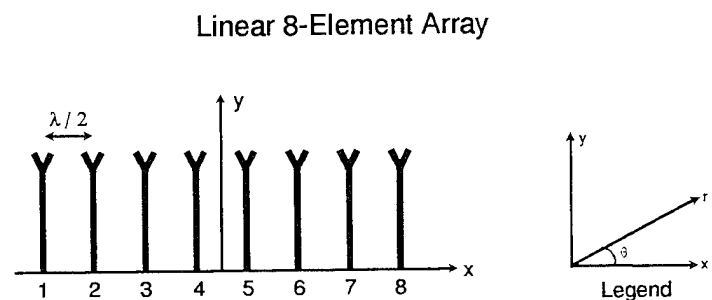
To apply a GA, you first represent the problem as a string of characters. Traditionally, binary format is used in which the characters are restricted to be either a "1" or "0". Initially, you create random strings to form the first population. This is the starting point of the evolution process. Each string is analogous to an individual confined to a particular environment in which only the strongest members will survive and procreate. In reality, the string represents one possible solution to the defined problem. The binary information contained on the string is processed and then compared with the desired or ideal solution to determine how "fit" the string is to remain in the environment and reproduce some of its genetic material. The most fit strings produce offspring while the weaker individuals are eliminated. After several generations, a string is produced that represents an optimal solution to the specified problem, and the algorithm is completed.

Perhaps the best way to demonstrate the power of these algorithms, as well as highlight the important concepts, is to step through an example from beginning to end. In the next several paragraphs we will describe our initial simulated experiment.

3 GA Pattern Synthesis

Consider an ideal, linear, eight-element, isotropic array with half-wavelength spacing between adjacent elements as shown in Figure 1. Each element has a three-bit attenuator and a three-bit phase-shifter. The problem is to find the attenuator and phase-shifter settings that will produce a broadside pattern, using a genetic algorithm.

As stated previously, the first step in this procedure is to represent the problem as a string



- Isotropic Elements
- Half wavelength spacing between adjacent elements
- Origin at Center of Array

Figure 1: Problem description for simulation.

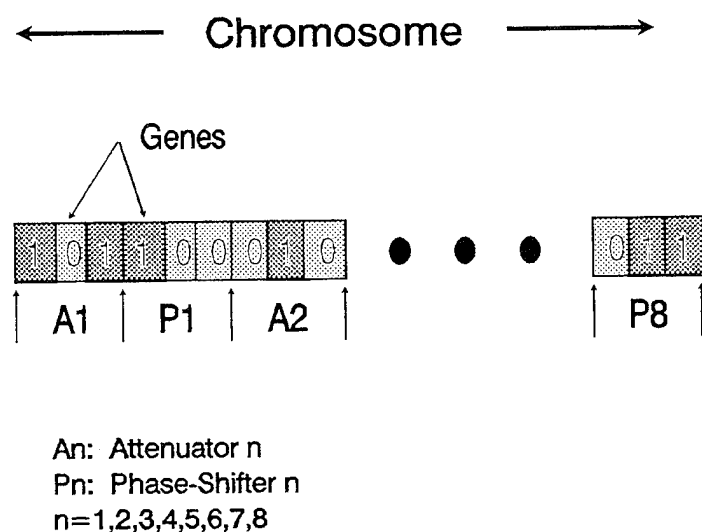


Figure 2: Problem representation for simulation.

of 1's and 0's. Arbitrarily, we chose the representation shown in Figure 2. The first three bits of the string represent the attenuator setting of element 1. The next three bits represent the phase-shifter setting of element 1. The following three bits represent the attenuator setting of element 2. And so this scheme is continued for all eight elements.

We could have encoded all of the attenuators first, followed by the phase-shifter bits rather than this "amplitude-phase" ordered pair structure. Many other string representations could also have been used. The point that we want to emphasize is that the GA is oblivious to the particular encoding one uses. The actual GA operator that most influences the convergence rate is the "fitness function" which will be discussed shortly. Depending on the particular problem, certain encodings may achieve convergence faster than others [5].

Thus, in this case, the total string length is $48 (6 \frac{\text{bits}}{\text{element}} \times 8 \text{ elements})$. The string itself is called a chromosome, and the individual bits are denoted as genes. Each chromosome represents a unique antenna pattern. The information for the attenuators and phase-shifters can be extracted from the chromosome, and the corresponding antenna pattern can be generated. For example, attenuator 1 in Figure 2 has an amplitude of 5 (binary 101 = decimal 5). Note that the amplitude values in this problem range from 0 to 7 because of the three-bit accuracy of the attenuator. The phase values have the same range, but must be multiplied by 45° since this is the angular resolution of the three-bit phase-shifters. So in Figure 2, the phase-shifter setting of element 1 is $4 \times 45^\circ = 180^\circ$.

After selecting the problem encoding, the next step is to select a random starting point for the GA search. We generate an arbitrary number of chromosomes which we use as the parents of the first generation. In this experiment, ten random strings of length 48 were created using a random number generator.

The ten initial random chromosomes are mated to produce the first population of strings. The chromosomes in our simulation are sex-less and can mate with any other individual chromosome. Although there are several ways to mate two chromosomes, we used *crossover*, which is one of the simplest methods. During crossover, two individual chromosomes are split at the same, randomly chosen, location in the bit string, and the head of one chromosome is attached to the tail of another to produce a new chromosome (see Figure 3).

We also perform a mutation operation on each new chromosome. This involves randomly toggling bits in each string, based on a mutation probability which usually lies anywhere from 0.001 to 0.05. A probability below 0.001 will have no noticeable effect on the algorithm while a probability greater than 0.05 will begin to destroy the useful genetic information contained in the chromosome. In our research, we found that a mutation probability of 0.02 worked well for this problem.

Note that the purpose of mutation is to give access to "lost genetic information" [5]. For example, the chromosome that corresponds to the optimal solution of the actual problem

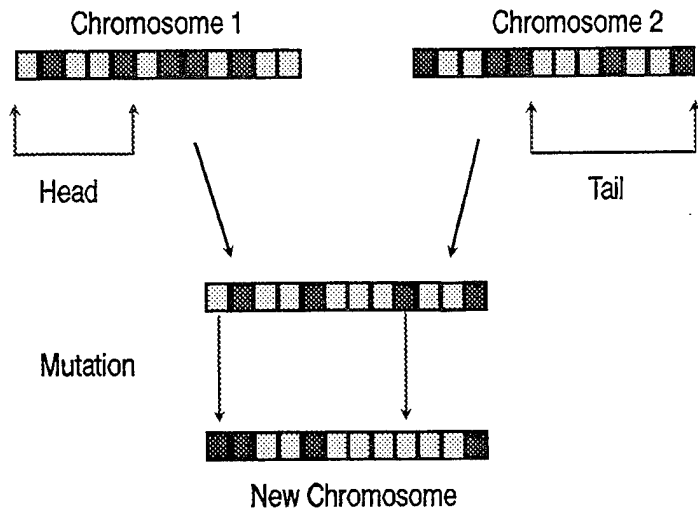


Figure 3: The crossover mating scheme.

may require a “1” in the first gene, but it is entirely possible that none of the initial randomly generated chromosomes have a “1” as their first bit. No matter how many times new chromosomes are created with the above mating scheme, a “1” will never occur in the first gene, and, hence, the algorithm will never converge upon the optimal solution. Therefore, mutation is a necessary ingredient in any genetic algorithm.

In this experiment, we mate each chromosome with every other one, thus creating 90 new chromosomes. This technique covers a broad area of the solution space. We also keep the original 10 “parent” strings to preserve the best solutions to date. In our experiment, this forms a total population of 100 chromosomes.

Each chromosome in the population is then tested against the environment to determine how “fit” the chromosome is to survive and produce offspring. In this experiment, the “fitness environment” is simply the desired antenna pattern, as shown in Figure 4. Each string generates an antenna pattern according to the information it contains about the attenuators and phase shifters (remember Figure 2). We compare each pattern to the desired pattern and calculate an error value, for this chromosome, based on how closely the patterns match.

Figure 5 helps to illustrate these ideas. Each of the two plots shows the antenna pattern represented by a particular chromosome compared to the ideal broadside case. Figure 5 (a) shows very little correlation between the chromosome-generated pattern and the ideal case, so this chromosome would be assigned a large error value. However, in Figure 5 (b), the chromosome pattern more closely resembles the ideal pattern and, hence, this string would be assigned a smaller error value. The actual numerical error value is computed by squaring

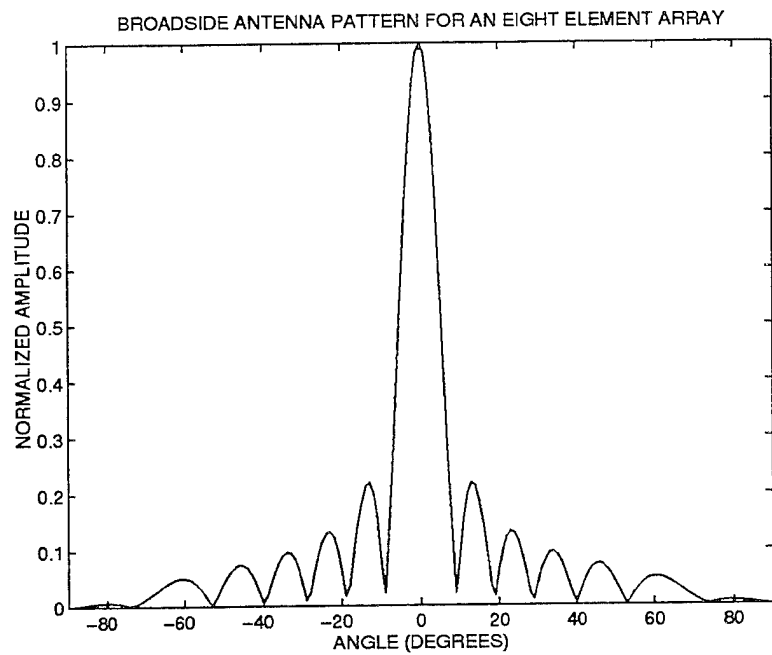


Figure 4: Environmental fitness function for simulation.

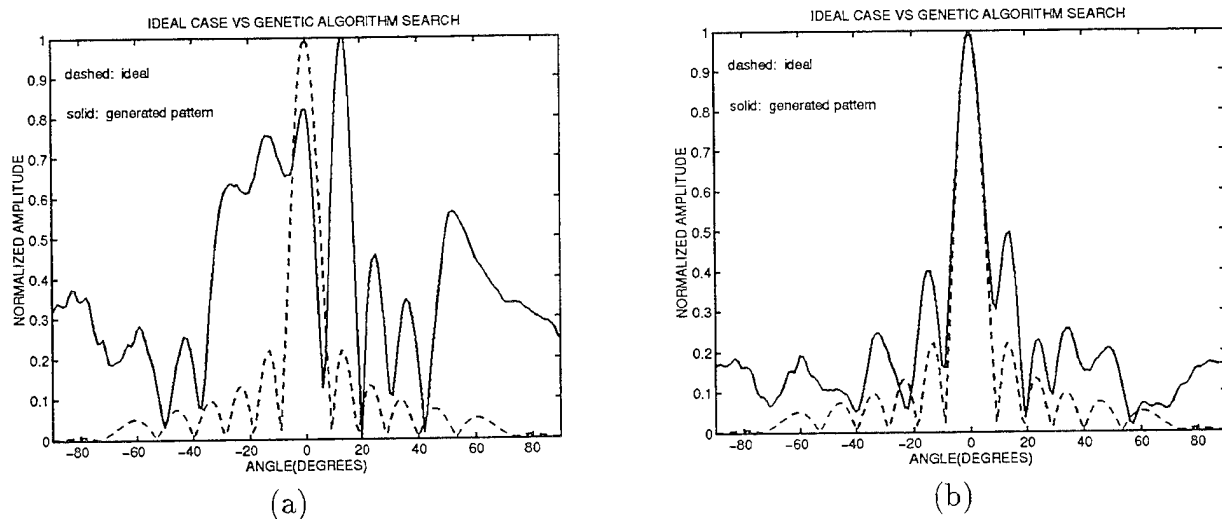


Figure 5: (a) Example of a chromosome with a large error value. (b) Example of a chromosome with a smaller error value.

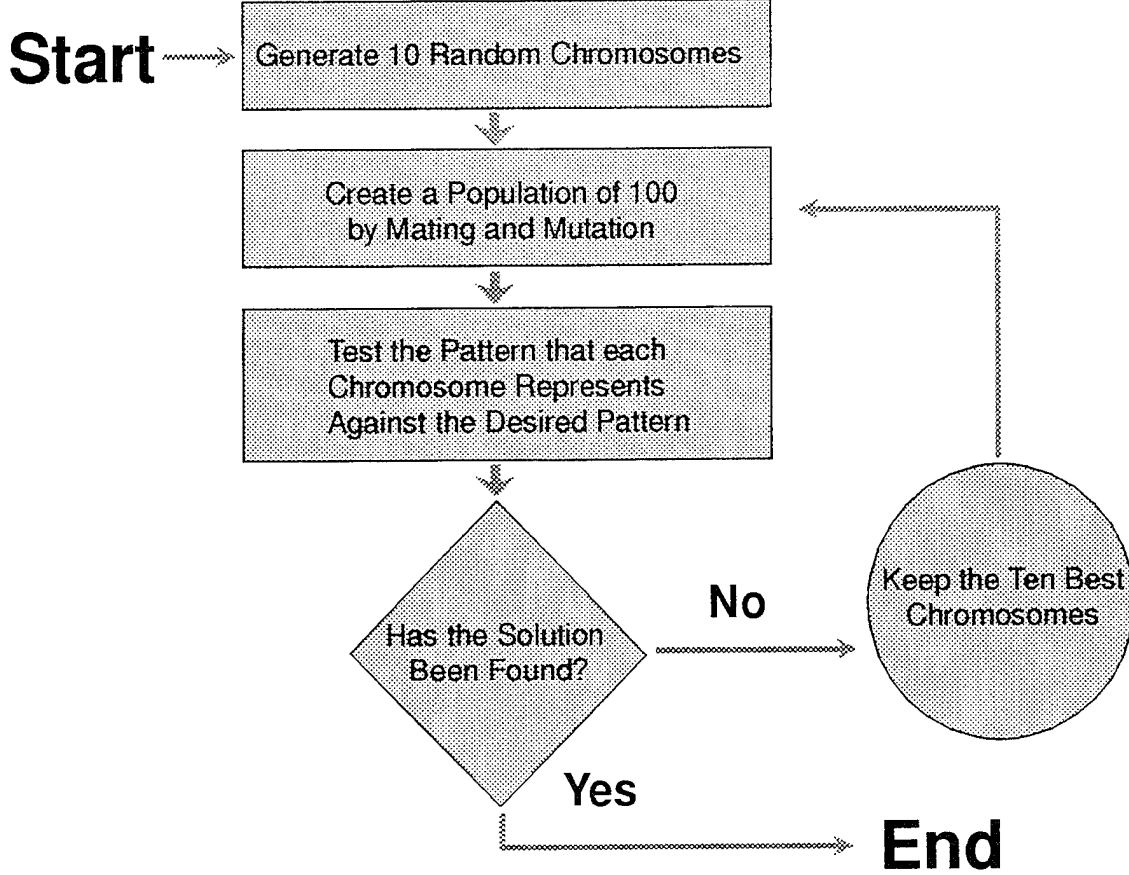


Figure 6: Flowchart representation of the GA used in the simulation.

the difference between the two patterns, point by point, and obtaining a sum; i.e.

$$\sum_{\theta=-90}^{90} (P_{a\theta} - P_{d\theta})^2 \quad (1)$$

where θ represents angular pattern points at 1° increments from -90° to $+90^\circ$, P_a is the chromosome-generated pattern, and P_d is the desired pattern.

Once each chromosome is assigned an error value, the strings are ranked from best to worst. The top 10 chromosomes are saved while the other 90 are discarded, and the mating process begins again. The algorithm continues to iterate through several generations until convergence upon the exact or optimal solution is reached. Figure 6 is a flowchart representation of the entire process. In many cases, an “exact” solution is unobtainable and one must be content with an optimal solution. More will be said about this in the next section.

Figure 7 shows the results of this simple experiment. Figure 7 (a) was plotted immediately after the first population (iteration) in the simulation. The dashed curve is the desired

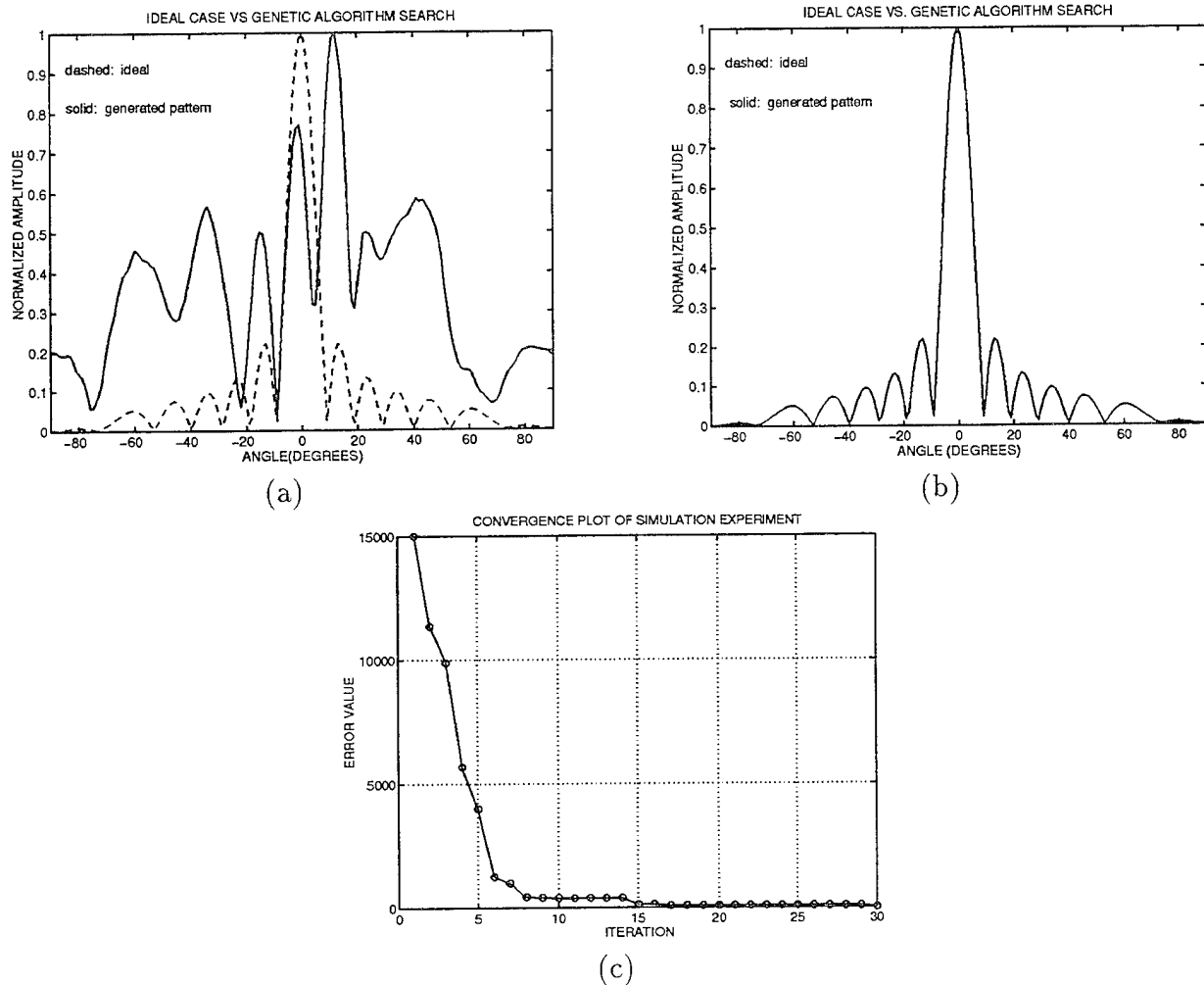


Figure 7: (a) GA simulation results after the first iteration. (b) GA simulation results after approximately 30 iterations. (c) Decreasing pattern error during GA convergence.

broadside pattern for an eight element array, while the solid curve represents the best chromosome solution available at that time. Approximately 30 iterations/populations later, one can see that the solid curve in Figure 7 (b) completely overlays the dashed curve, signifying that an exact solution was found. Figure 7 (c) shows the error between the desired pattern and best chromosome pattern for each population. It is worth noting that for a string length of 48, there are a possible 281 trillion combinations of 1's and 0's, and this algorithm was able to find an exact solution by only testing 3,000 of those strings.

The purpose of conducting this simplistic experiment was to determine whether a GA approach could solve the antenna pattern synthesis problem for a simulated, ideal antenna. In the next section, we apply this GA approach to the more practical problem of synthesizing a pattern from a physical, imperfect linear array.

4 Experiment

Figure 8 shows a front view photograph of the eight element array that was used for this experiment, and Figure 9 is a block diagram of the experimental setup. The individual elements are open ended waveguides, each connected to a Reggia-Spencer 8-bit digital phase-shifter. Although there is no amplitude control available, the amplitude of each element is, unfortunately, a function of the digital setting of the phase-shifter. An example of this phenomenon is depicted in Figure 10 in which the antenna was pointed in the broadside direction relative to the source. The x-axis represents the digital state of the phase-shifter, and the y-axis represents the corresponding phase in (a) and amplitude in (b). It is interesting to note that the amplitude varies by as much as 6 dB depending on the digital state of the phase-shifter! Plot (c) is the measured element pattern of element 1 for an arbitrary phase setting.

The transmitting horn radiates at a frequency of 7.1 GHz., and the distance between elements is approximately 1.3 inches; this translates to an element spacing of $.7815\lambda$. The primary reason for using this frequency rather than one that could provide us with half wavelength spacing, is the fact that the phase-shifters are unable to represent a complete 360 degree cycle at lower frequencies. For example, instead of digital phase-shifter states 0 through 255 covering a complete 360 degrees, they may only cover 0 to 240 degrees or some other number depending on the radiating frequency. This high frequency of 7.1 GHz, however, causes grating lobes as the main beam is scanned to angles far away from broadside. Since the main purpose of this experiment was to use a GA to find the optimal phase-shifter settings to steer the main beam, the fact that a grating lobe exists is secondary.

As shown in Figure 9, our experimental setup satisfies the far field approximation, and, in addition, the radiating horn contains a lens that acts to further “flatten out” the incoming

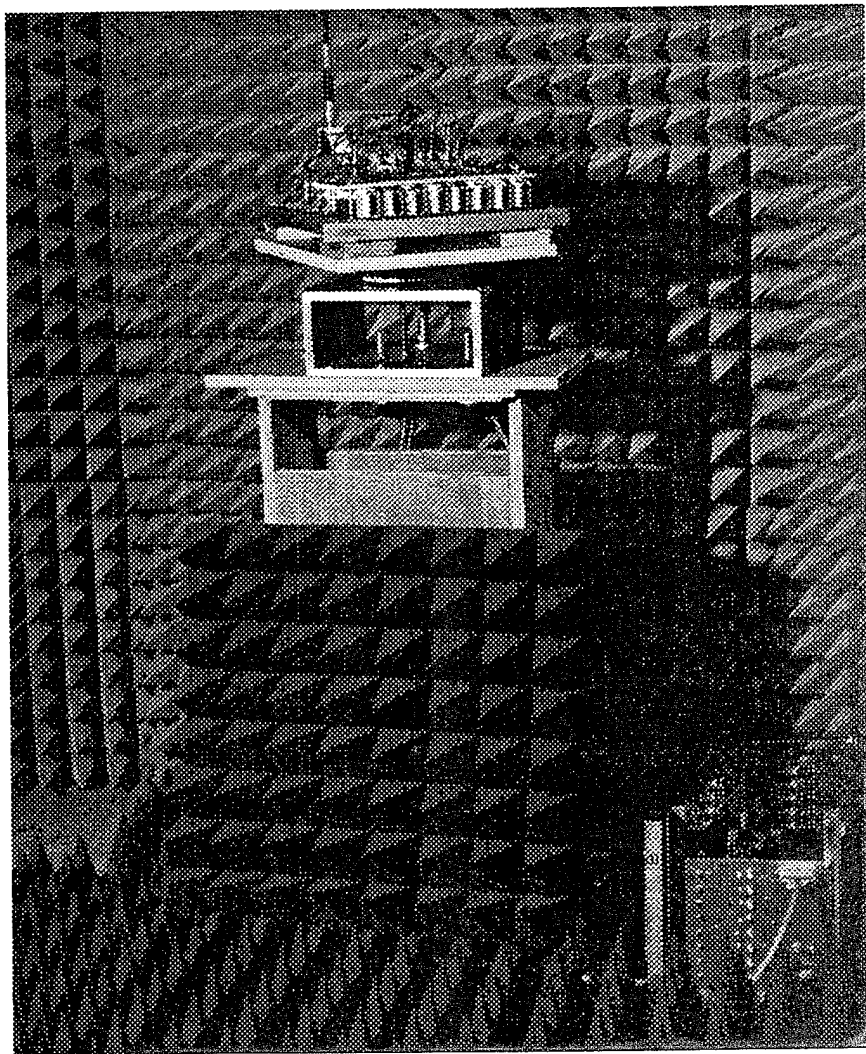


Figure 8: Front view of the experimental array.

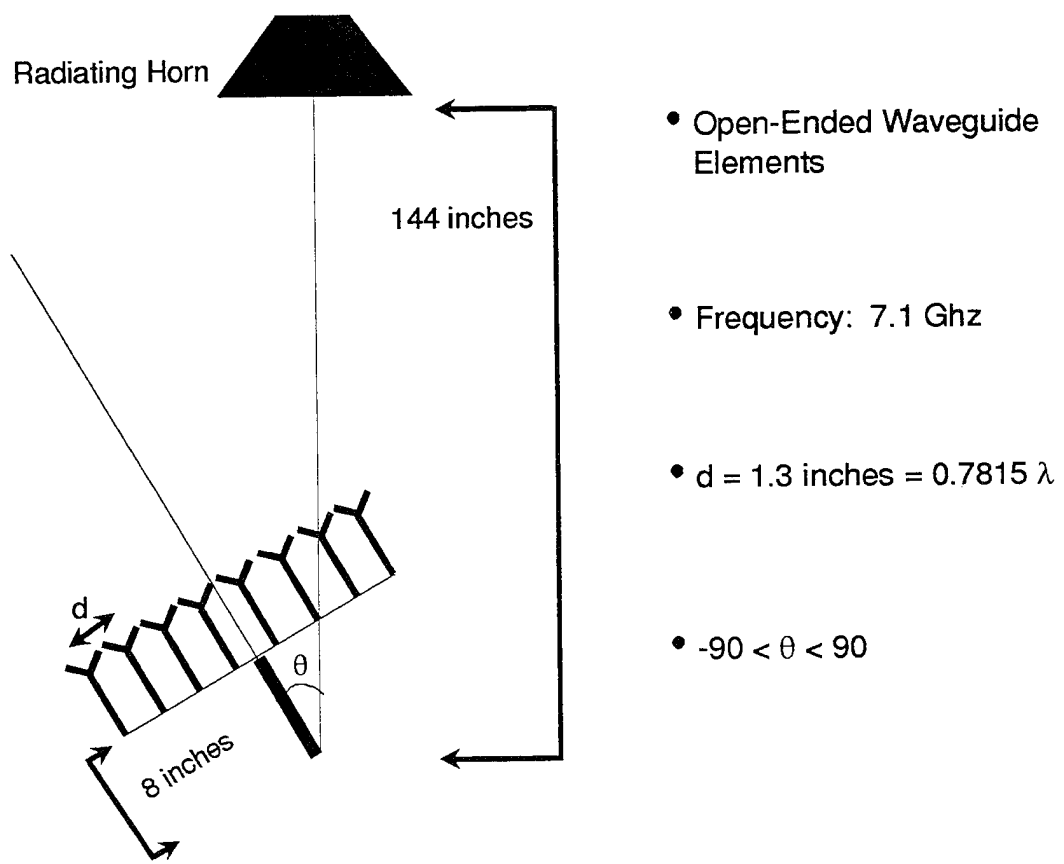


Figure 9: Block diagram of experimental setup.

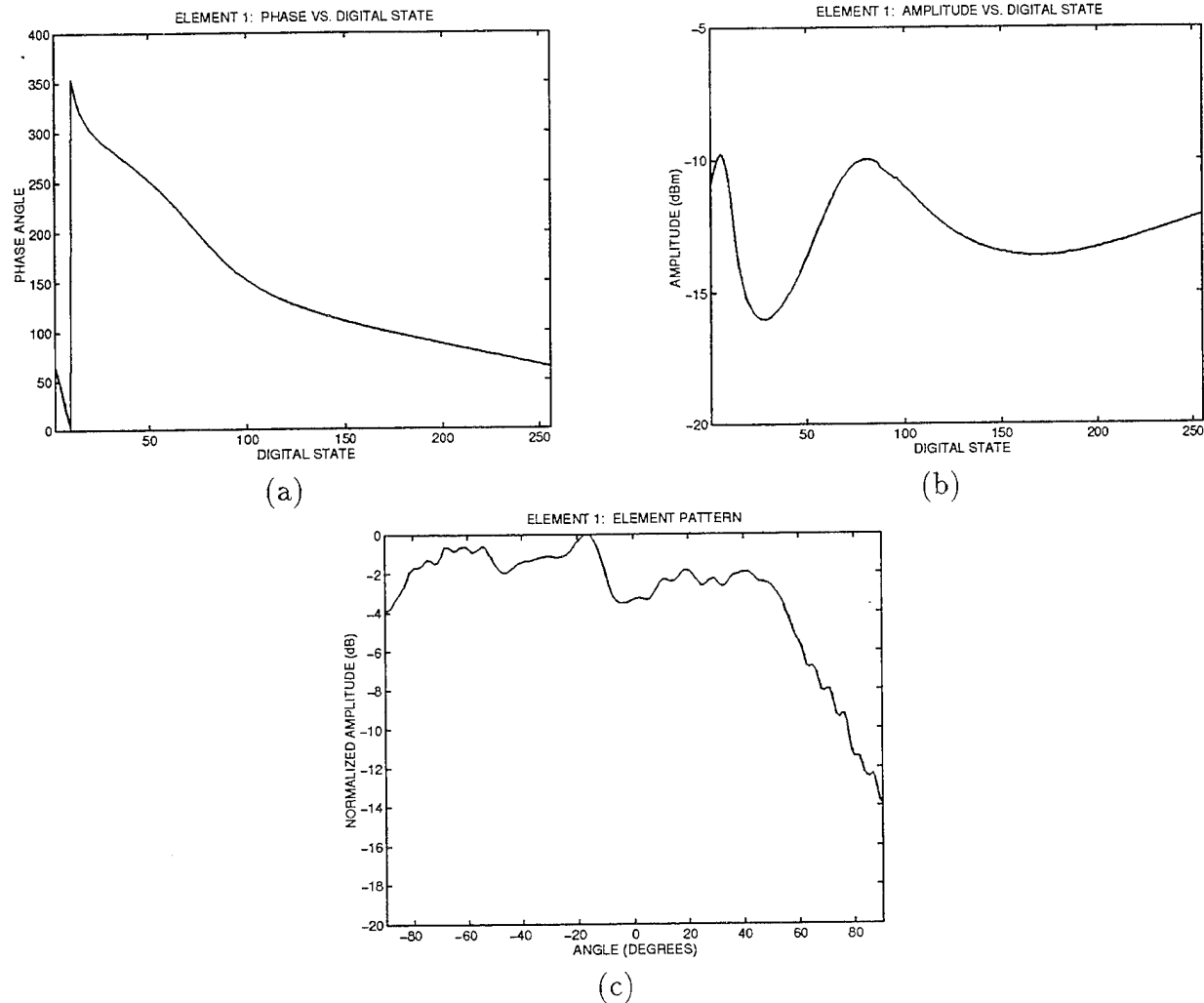
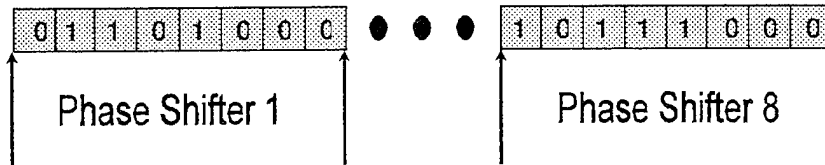


Figure 10: (a) Phase angle vs. digital phase-shifter state for element 1. (b) Amplitude vs. digital phase-shifter state for element 1. (c) Element pattern for element 1.

Problem Representation



- Eight 8-bit Phase Shifters

Figure 11: Problem representation for experiment.

radiation to approach an ideal plane wave. In order to apply a GA to this particular system, we simulated the phase, amplitude, and element pattern characteristics of all eight elements as measured at broadside. Note that no calibration of the array was needed since the GA doesn't rely on analytical methods to steer the beam. It was able to steer the main beam in a specified direction simply by finding the optimal phase-shifter settings of the elements. Because the elements possess nonlinear amplitude and phase behavior, as well as non identical element patterns, this array is a prime candidate for GA array pattern synthesis.

5 GA Pattern Synthesis

The first step is to represent the problem as a string of 1's and 0's. Unlike our first experiment, this problem has no attenuators to model. We have eight phase-shifters that each have eight-bit accuracy. Therefore, our string length is 64, and we arbitrarily chose the chromosome representation in Figure 11.

Again, we generate 10 chromosomes as our starting point. Our mating scheme, however, has a slight twist. Instead of the simple head-tail crossover reproduction method, we decided to use a "circular" mating operator. Depicted in Figure 12, this particular mating scheme involves picking two random points in the string length (which is represented as a circle with

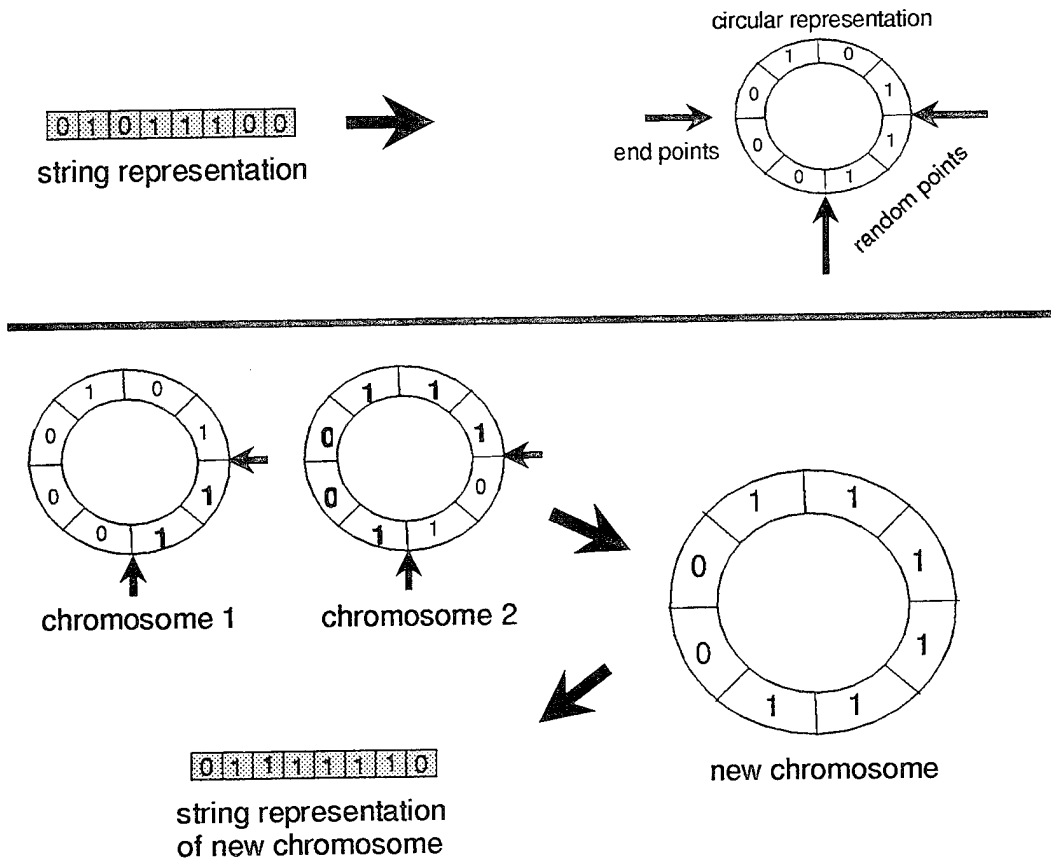


Figure 12: Circular mating scheme.

no defined end points) and then extracting the corresponding sections from the two mating chromosomes to form an offspring. This technique eliminates any biases on the string ends that are present in the simple crossover mating scheme [5].

We chose a mutation probability of 0.05 and, as before, we created 90 new chromosomes in each generation for a total population of 100. Again, each of the 10 chromosomes are mated with every other one in order to explore as much of the solution space as possible.

In the simulated experiment we used the ideal array pattern as our environmental fitness function since we knew that there existed an exact solution. It is highly unlikely, however, that we will achieve an exact solution given the quality of the antenna system with which we are working. In this case an “optimal solution” will suffice, and we will tailor our environmental fitness function to emphasize the characteristics of the pattern that we feel are the most important.

We would like to find a solution in which the main beam is directed towards the desired angle, the width of the main beam approaches the ideal case, and the maximum sidelobe

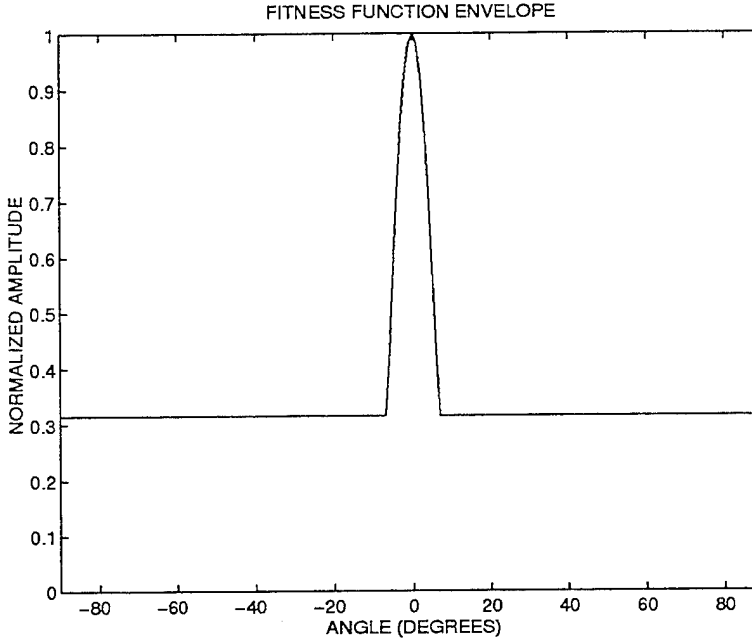


Figure 13: Environmental fitness function for experiment.

level is at least 10 dB below the height of the main beam, if physically realizable. These requirements are pictured in Figure 13 for the broadside case. When we calculate our numerical error value, we are only concerned that these standards are met, rather than attempting to replicate the ideal case.

6 Results

GAs are perfect candidates for parallelization. Running several sessions in parallel, all with different random number “seeds”, allows one to explore more of the solution space in a minimal amount of time. Without access to parallel computing resources, we ran the algorithm ten times for each angle, and the best solution was used to verify the results experimentally. We coded our GA simulation in MATLAB and ran the program on a single CPU of a Sun SparcServer 1000. It took approximately one 24 hour day to obtain all the data for each beam steered angle, and 9 days to run the entire simulation. It only took one day to verify the simulation results experimentally.

We used a GA to solve for the optimal phase settings for beams steered from 0° to -40° in 5° decrements. Figure 14 (a) shows the simulation results for a beam steered to -10° . When these phase settings were used in the actual experiment the pattern of Figure 14 (b) was created. The patterns are quite similar, signifying that the GA was able to successfully form beams and steer the array.

The simulated results for all of the beam steered angles are shown in Table 1, and the

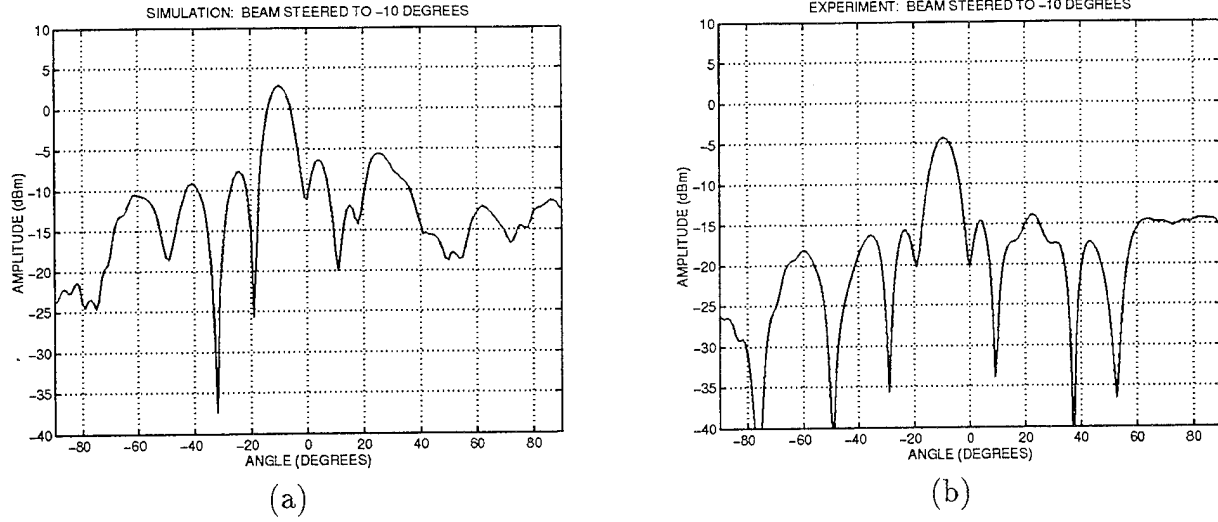


Figure 14: (a) Simulation results for steering main beam to -10° . (b) Experimental results for steering main beam to -10°

Simulated Antenna Results				
Test #	Desired Angle	Experimental Angle	Error	Maximum Sidelobe Level
1	0°	0°	0°	-5.98 dB
2	-5°	-6°	1°	-6.71 dB
3	-10°	-10°	0°	-8.40 dB
4	-15°	-16°	1°	-8.60 dB
5	-20°	-21°	1°	-5.22 dB
6	-25°	-25°	0°	-7.49 dB
7	-30°	-30°	0°	-8.03 dB
8	-35°	-34°	1°	-9.02 dB
9	-40°	-40°	0°	-7.77 dB

Table 1: Pattern synthesis results using genetic algorithm with simulated antenna model.

experimental results can be found in Table 2. In all cases, the mainbeam was never more than one degree different from its desired steering angle. The sidelobe levels may appear to be quite high, ranging from -4.31 dB to -9.88 dB. For example, one would expect a maximum sidelobe level of approximately -13 dB for a broadside beam. We repeat here that GAs don't supply an exact solution to the problem but, rather, an optimal one. In other words, the GA is only as good as the equipment with which you are working. We believe that the high sidelobe levels were caused by the amplitude fluctuations of the individual elements versus the digital setting of the phase shifters (as shown in Figure 10), rather than the failure of the GA to find a "good" solution. This conjecture is supported by other experiments with this physical antenna [2], which also result in patterns with high sidelobe levels.

Measured Antenna Results				
Test #	Desired Angle	Experimental Angle	Error	Maximum Sidelobe Level
1	0°	0.0°	0.0°	-5.87 dB
2	-5°	-4.1°	0.9°	-5.18 dB
3	-10°	-9.1°	0.9°	-9.51 dB
4	-15°	-14.6°	0.4°	-6.10 dB
5	-20°	-19.1°	0.9°	-7.40 dB
6	-25°	-25.0°	0.0°	-4.31 dB
7	-30°	-29.1°	0.9°	-7.89 dB
8	-35°	-35.0°	0.0°	-7.56 dB
9	-40°	-40.0°	0.0°	-9.88 dB

Table 2: Pattern synthesis results using genetic algorithm with experimental antenna.

7 Conclusion

We have introduced GA concepts and operators, and have shown how they were successfully applied to the synthesis and steering of a pattern with a non-ideal phased array antenna. Our experiment demonstrates that a GA was able to steer beams to a set of specified angles with very little error. In the future we will experiment with different cost functions in an attempt to lower sidelobe levels and, perhaps, even eliminate grating lobes. We will also be including the antenna gain as part of the cost function calculation.

References

- [1] T. H. O'Donnell, J. A. Simmers, H. L. Southall, and T. J. Klemas. Neural Beamforming for Signal Detection and Location. In *1994 IEEE MILCOM Conference Record*, volume 2, pages 326–330. IEEE, October, 1994.
- [2] H. Southall, S. Santarelli, E. Martin, and T. O'Donnell. Neural Network Beam-Steering for Phased-Array Antennas. In *Proceedings of the 1995 Antenna Applications Symposium (Robert Allerton Park)*, University of Illinois, Griffiss AFB, NY, September 1995. USAF Rome Laboratory.
- [3] T. Poggio and F. Girosi. Networks for Approximation and Learning. *Proceedings of the IEEE*, 78(9):1481–1496, September 1990.
- [4] M. J. D. Powell. Radial Basis Functions for Multivariable Interpolation: A Review. In J. C. Mason and M. G. Cox, editors, *Algorithms for Approximation*, pages 143–167. Clarendon Press, Oxford, 1987.

- [5] M. Srinivas and L. M. Patnaik. Genetic Algorithms: A Survey. *Computer*, 27(6):17–26, June 1994.
- [6] M. Shimizu. Determining the Excitation Coefficients of an Array Using Genetic Algorithms. In *IEEE Antennas and Propagation Society International Symposium 1994 Digest*, volume 1, pages 530–533. IEEE, 1994.
- [7] R. L. Haupt, J. J. Menozzi, and C. J. McCormack. Thinned Arrays Using Genetic Algorithms. In *IEEE Antennas and Propagation Society International Symposium 1993 Digest*, volume 2, pages 712–715. IEEE, 1993.
- [8] R. L. Haupt. An Introduction to Genetic Algorithms for Electromagnetics. *IEEE Antennas and Propagation Magazine*, 37(2):7–15, April 1995.

PHASE-ONLY ILLUMINATION SYNTHESIS FOR OVER-SAMPLED PHASED ARRAY APERTURES

Jerome H. Pozgay
Raytheon Electronic Systems
50 Apple Hill Drive
Tewksbury, MA 01876

Abstract: A new class of aperture illumination distributions has been developed. These distributions produce low pattern sidelobes through application of systematically derived and defined phase-only algorithms. The algorithm defining the phase distributions is quite general, but is strictly applicable only to rectangular format apertures with smaller than $\lambda/2$ spacing, as for wideband active aperture array configurations.

In a mathematical sense, the phase-only functions demonstrate a previously unknown relationship that can exist between the discrete Fourier transforms of two-dimensional real and complex functions. A transformation has been discovered which maps a real function into complex space in such a fashion that, above a noise level which is inversely proportional to the number of samples, and only weakly dependent on sample spacing, the discrete Fourier transforms of the functions are identical, at least in a practical context. For the phased array antenna designer, this simply means that a phase-only pattern shaping algorithm will produce higher rms sidelobe levels than its amplitude distribution counterpart.

1. Introduction: A new class of aperture illumination distributions has been developed which produce low pattern sidelobes by phase rather than amplitude tapering. These phase taper illuminations meet numerous low sidelobe requirements in the same fashion that a variety of amplitude distributions are available.

Array sidelobe control for pencil beams is conventionally achieved by underilluminating the aperture such that the radiator excitation amplitude (or amplitude den-

sity) monotonically decreases with distance from the aperture center. Illumination distributions are held symmetric in order to maintain deep pattern nulls. With the exception of applying linear phase progressions across the aperture for beam steering, the desired aperture phase distribution is uniform. The shape of the amplitude taper determines the systematic characteristics of the pattern produced: That is, the 3 dB and null widths of the main beam, the sidelobe spacing and levels, and the pattern directivity gain. For an active aperture array, the shape of the amplitude illumination also determines the total power available for radiation, and an amplitude tapered active aperture antenna will produce significantly lower ERP than its uniformly illuminated counterpart, independent of whether the taper is achieved by amplifier gain distribution shaping, aperture thinning or signal attenuation at the input to the active device.

It was with the prospect of simultaneously achieving higher ERP with lower sidelobes that these studies were first undertaken. What was achieved was a very efficient means of removing variable attenuators in wideband active aperture array configurations: the architecture and control logic are considerably simplified while providing low sidelobe receive patterns.

2. The Phase Taper Algorithm: The relative far field produced by a planar array of N identical I mode multimode radiators lying in the xy -plane can be expressed as:

$$\mathbf{E}(\mathbf{u}) = \sum_{n=1}^N \mathbf{f}_n(\mathbf{u}) \sum_{i=1}^I v_n(x_i) \exp(jk\mathbf{u} \cdot \mathbf{x}_i) \quad (1)$$

where bold characters are used to represent vector quantities. In equation (1), \mathbf{u}

is the vector defining an angular position in the hemisphere forward of the aperture, $\mathbf{f}_n(\mathbf{u})$ is the vector Fourier transform of the m^{th} modal aperture field distribution, $v_n(\mathbf{x}_i)$ is the modal excitation of the m^{th} mode in the i^{th} radiator, and \mathbf{x}_i is the location of the i^{th} radiator with respect to a suitably chosen reference. The direction to the observation point is embodied in the vector \mathbf{u} , defined by:

$$\begin{aligned}\mathbf{u} &= \mathbf{x}_0 \sin\theta \cos\phi + \mathbf{y}_0 \sin\theta \sin\phi \\ &= \mathbf{x}_0 u + \mathbf{y}_0 v\end{aligned}\tag{2}$$

and \mathbf{x}_i is defined by:

$$\mathbf{x}_i = \mathbf{x}_0 \mathbf{x}_i + \mathbf{y}_0 \mathbf{y}_i\tag{3}$$

The angles θ and ϕ are defined in Figure 1, and are specifically related to the Cartesian system unit vectors \mathbf{x}_0 , \mathbf{y}_0 and \mathbf{z}_0 as shown.

For discussion of illumination synthesis, it is customary to assume that the modal element pattern is broad relative to the achievable beamwidth for a given array aperture - *i.e.*, the array consists of many radiators. Furthermore, the array radiator is typically driven only in a single mode: normally the device's dominant mode. Higher mode excitation coefficients are generated by interaction at the aperture plane. As a result, it is customary to examine only the pattern characteristic produced by active excitation of hypothetically isotropic (in the forward half space) radiators. The patterns are known as the array factor and embody only the geometrical relationship of radiator phase centers, relative active excitation of the phase centers, and the operating frequency. A general expression for the array factor is:

$$E(\mathbf{u}) = \sum_{i=1}^I v(\mathbf{x}_i) \exp(jk\mathbf{u} \cdot \mathbf{x}_i) \quad (4)$$

Note that the modal subscript has been dropped for the excitation coefficient and that the field is now treated as a scalar. In general, the dominant mode excitations are complex, and have the form:

$$v(\mathbf{x}_i) = |v(\mathbf{x}_i)| \exp(j\phi_i) \quad (5)$$

Let us suppose, now that $|v(\mathbf{x}_i)| = 1$ for all i and that the phase of the excitation at the i^{th} radiator, ϕ_i , takes the form:

$$\phi_i = \varepsilon_i - k\mathbf{u}_0 \cdot \mathbf{x}_i \quad (6)$$

where $k\mathbf{u}_0 \cdot \mathbf{x}_i$ represents the uniformly sloping phase distribution required to maximize the collimated phased array response at \mathbf{u}_0 . Substitution of equation (6) into equation (4) produces

$$E(\mathbf{u}) = \sum_{i=1}^I \cos(\varepsilon_i) \exp(jk\mathbf{U} \cdot \mathbf{x}_i) + \sum_{i=1}^I \sin(\varepsilon_i) \exp(jk\mathbf{U} \cdot \mathbf{x}_i) \quad (7)$$

Here, $\mathbf{U} = \mathbf{u} - \mathbf{u}_0$. If the angle ε_i is restricted to the right half plane ($-\pi/2 \leq \varepsilon_i \leq \pi/2$), then the first summation is similar in form to equation (4). More specifically, if a

one-to-one correspondence between $|v(x_i)|$ and $\cos(\varepsilon_i)$ can be established, then the first summation in equation (7) is *identically* equation (4). An obvious assignment is therefore:

$$\varepsilon_i = \cos^{-1}(|v(x_i)|) \quad (8)$$

If the assignment in equation (8) makes the second summation in equation (7) very small relative to the first, for all values $|U| \leq 1$, then the phase distribution, ε_i , produces patterns nearly identical to those produced by the prototype amplitude distribution $|v(x_i)|$.

The assignment in equation (8) does not generally result in a small value for the second summation relative to the first unless ε_i is itself restricted to small angular values. Such a restriction would limit the assignment in equation (8) to prototype amplitude distributions for which the array edge is heavily excited. It is evident then that simple examination of equation (7) can provide no further insight into the problem of generating low sidelobes using phase-only tapers.

Suppose, however, that the array is two-dimensional, and arrayed such that any grid location in one quadrant has images in the other three quadrants. then each resulting phase excited quadrupole produces the pattern:

$$E^q(u) = \sum_{i=1}^2 \exp(jkUx_i) \sum_{l=1}^2 \cos(\varepsilon_{i,l}) \exp(jkVy_l) \\ + j \sum_{i=1}^2 \exp(jkUx_i) \sum_{l=1}^2 \sin(\varepsilon_{i,l}) \exp(jkVy_l) \quad (9)$$

Here, the form of summation has been collapsed about the $u=0$ and $v=0$ axes, taking advantage of the correspondence between quadrupole and spatial geometries. From this form, a novel phase excitation can be inferred which produces patterns that are essentially identical to those produced by arbitrary prototype amplitude distributions. If the quadrupole is geometrically centered such that:

$$x_2 = -x_1 = -x \quad (10)$$

$$y_2 = -y_1 = -y \quad (11)$$

and

$$\varepsilon_{i,l} = (-1)^{i+l} |\varepsilon_{i,l}| = (-1)^{i+l} \varepsilon \quad (12)$$

then equation (9) reduces to:

$$E^q(u) = 4\cos(\varepsilon)\cos(kUx)\cos(kVy) - 4j\sin(\varepsilon)\sin(kUx)\sin(kVy) \quad (13)$$

The real term in equation (13) has major lobes at:

$$u = u_0 + n\lambda/(2x), n = 0, \pm 1, \pm 2, \dots \quad (14)$$

$$v = v_0 + m\lambda/(2x), m = 0, \pm 1, \pm 2, \dots \quad (15)$$

whereas the imaginary term has major lobes at:

$$u = u_0 + (2n'-1)\lambda/(4x), n' = 0, \pm 1, \pm 2, \dots \quad (16)$$

$$v = v_0 + (2m'-1)\lambda/(4x), m' = 0, \pm 1, \pm 2, \dots \quad (17)$$

The resulting quadrupole pattern therefore appears to be produced by the superposition of two arrays - an array with spacing $(2x, 2y)$ and an array with spacing $(4x, 4y)$. The effective array with smaller spacing (the real term in equation (9)) has a filled grating lobe pattern such as is found for a conventionally excited regular grid. However, the effective array with larger spacing has a sparse grating lobe diagram. That is lobes which should reside in the $u = u_0$ and $v = v_0$ planes are cancelled, and the nearest lobes are typical of a smaller spacing. For example, if $x = y = d/2$, then the nearest real term lobes are in the $u = u_0$ and $v = v_0$ planes at λ/d from the main lobe ($n = m = 0$), while the nearest imaginary term lobes are located in the 45 degree planes relative to the pointing direction (u_0, v_0) at a distance $\lambda/(d\sqrt{2})$.

From the foregoing, it is evident that an array of radiators, on a rectangular grid, and possessing no central rows of columns can be phase excited to produce patterns which are essentially identical to those produced by any of the standard separable amplitude tapers. That is, if:

$$\begin{aligned} v_{i,l} &= g(x_i)h(y_l) \\ &= g_i h_l \end{aligned} \quad (18)$$

is a particular prototype product illumination, then the phase excitation:

$$\epsilon_{i,l} = (-1)^{i+l} \cos^{-1}(g_i h_l) \quad (19)$$

should produce essentially identical patterns provided the grating lobe and its ridges of sidelobes remain well out of real space. Or, more specifically, if the grid is square, the maximum scan angle is θ_m and the uniformly excited array null width is $2\theta_n$, then the phase excitation given by equation (19) will produce patterns nearly identical to those produced by the corresponding amplitude excitation if:

$$d/\lambda \leq 0.707(1 + \sin\theta_m + \sin\theta_n)^{-1} \quad (20)$$

where d is the interelement spacing. As an example, a 900 element phase tapered square array on 0.325 in. spacing will be grating lobe free out to 60 deg scan up to approximately 13.2 GHz: an amplitude tapered array would be grating lobe free to approximately 18.8 GHz.

The above characteristics of phase tapering become more apparent when applied to large rectangular or elliptical apertures of rectangular grids when the far electric field is expanded in row/column form as follows. If the array has N columns (N even) and the n^{th} column has R_n radiators (R_n even), then the electric field is proportional to:

$$E(u,v) = \sum_{n=1}^N \exp(jkux_n) \sum_{r=1}^{R_n} \exp(j\phi_{n,r}) \exp(jkv_y_r) \quad (21)$$

Let

$$x_n = nd_x - (N+1)d_x/2 \quad (22)$$

$$y_r = rd_y - (R_n + 1)d_y/2 \quad (23)$$

$$\phi_{n,r} = \varepsilon_{n,r} - k\mathbf{u}_0 \cdot \mathbf{x}_i \quad (24)$$

Then

$$E(u,v) = K_1 \left\{ \sum_{n=1}^N g_n \cos(knUd_x) K_n \sum_{r=1}^{R_n} h_r \cos(krVd_y) \right. \\ \left. - j \sum_{n=1}^N \sin(knUd_x) K_n \sum_{r=1}^{R_n} [1 - g_n^2 h_r^2] \sin(krVd_y) \right\} \quad (25)$$

where

$$K_1 = \exp[-jkU(N+1)d_x/2] \quad (26)$$

$$K_n = \exp[-jkV(R_n+1)d_y/2] \quad (27)$$

For comparison, the far electric field produced by the prototype amplitude taper $g_n h_r$ is:

$$E_a(u,v) = K_1 \sum_{n=1}^N g_n \cos(knUd_x) K_n \sum_{r=1}^{R_n} h_r \cos(krVd_y) \quad (28)$$

Hence,

$$E(u_0, v) = E_a(u_0, v) \quad (29)$$

and

$$E(u, v_0) = E_a(u, v_0) \quad (30)$$

Equations (29) and (30) are valid, independent of operating frequency, and one can conclude that for a reasonably large array (say 900 radiators), that the phase taper algorithm in equation (19) produces patterns which are substantially identical to those produced by the prototype amplitude taper $g(x)h(y)$.

3. Phase Taper Examples: The phase taper illumination has been applied to a square array of 900 elements on 0.325 in. square grid. The array is assumed to be comprised of wideband notch radiators operating over 6 to 18 GHz and providing 60 deg cone half angle scan coverage over the full frequency range. Two prototype amplitude distributions have been examined. These are separable cosine and separable linear Taylor taper with $n = 5$ and 35 dB sidelobe level (35 dB SLL). Full forward hemisphere contour patterns have been obtained at three frequencies, *viz.* 6, 12 and 18 GHz for each illumination and for both the phase and amplitude tapers. All patterns are presented with the peak gain set to 0 dB.

For reference, Figure 2 shows the pattern of the uniformly excited array at 6 GHz. The representational floor in this pattern, as well as all others, is 45 dB below the pattern peak. Contour intervals are 5 dB. In the following, the element pattern is assumed to be half-space isotropic.

Figures 3 through 18, inclusive, demonstrate pattern performance with phase tapering or amplitude tapering, assuming no phase quantization errors. A cursory examination of these patterns shows that, to the 45 dB level, the phase tapered

array, and its prototype amplitude tapered array have nearly indistinguishable pattern characteristics provided the phase tapered array grating lobes and grating lobe sidelobes reside outside real space.

4. Patterns with Errors: A major concern in the consideration of phase tapering is the stability of the pattern in the presence of errors. To examine this issue, in at least a cursory fashion, the phase taper has been evaluated for quantized phase shift of 3, 4 and 5 bits. The results are shown for 6 GHz in Figures 19 through 21, inclusive. As the number of bits increases, the pattern approaches the shape of the prototype pattern - 5 bits is clearly sufficient here. As the pattern uniformly evolves with increasing number of bits, it is concluded that the phase taper algorithm is not a supergain result, and is therefor physically realizable.

5. Mutual Coupling Considerations: When it first became apparent that simple phase taper algorithms could provide excellent sidelobe control in wideband active aperture systems, the focus immediately turned to the issue of whether low active aperture transmit sidelobes and high system efficiency could be achieved simultaneously. On the basis of detailed mutual coupling analyses at the aperture of an oversampled array, we concluded that the optimum achievable performance is obtained with all radiators identically matched as if for an infinite array environment. With such a matching condition for the phase tapered and amplitude tapered apertures, it was found that the ERPs of the two active configurations differed insignificantly. Figure 22 shows an example of the pattern control that can be achieved in the coupled environment for a 10×10 array of loaded rectangular waveguide radiators on a square grid. Then objective peak sidelobe level was -23 dB: the prototype amplitude distributions is indicated on the figure.

6. Conclusions: The new class of illumination functions will produce stable antenna pattern performance. Although there does not appear to be an ERP advantage associated with the use of phase taper illuminations, their application in active aperture systems can lead to reduced parts counts and a significant reduction in the complexity of T/R modules and their controllers.

7. Acknowledgments: The work reported here was supported entirely under Raytheon IR & D programs.

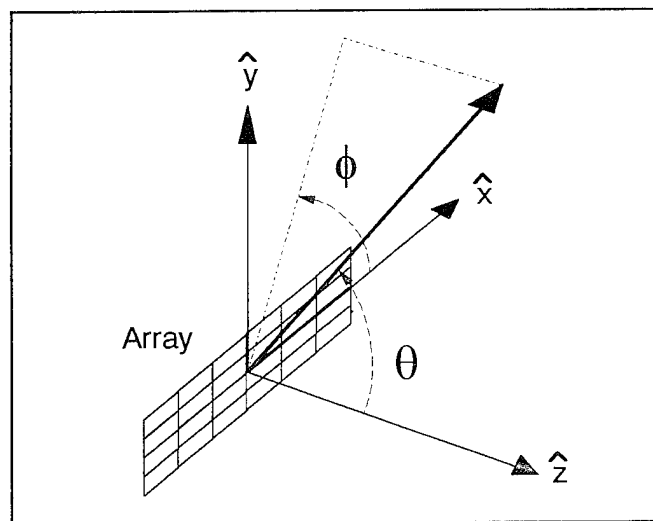


Figure 1. Array Geometry

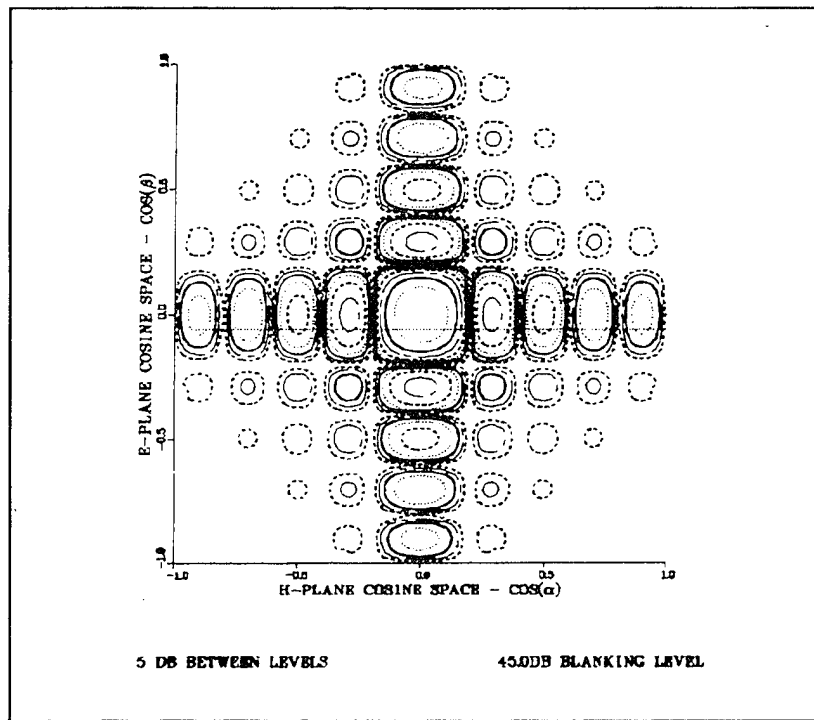


Figure 2. Pattern of Uniformly Excited Array
 $u_0 = 0.0, v_0 = 0.0, f = 6 \text{ GHz}$

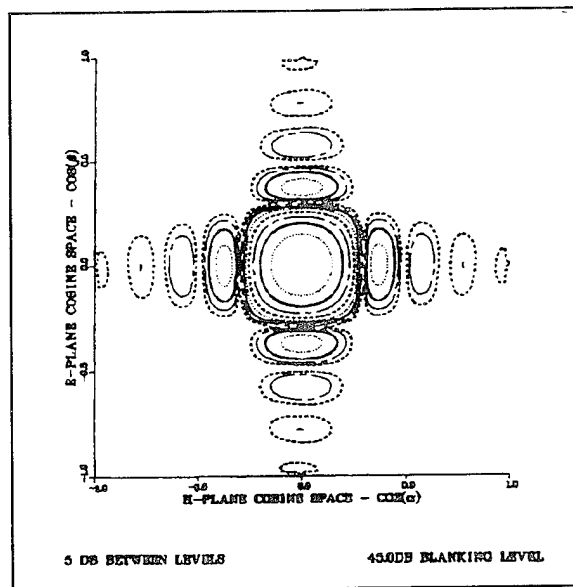


Figure 3. Pattern of Phase Tapered Array
 $u_0 = 0.0, v_0 = 0.0, f = 6 \text{ GHz}$
 Prototype Amplitude Illumination: Separable Cosines
 Phase Quantization: None

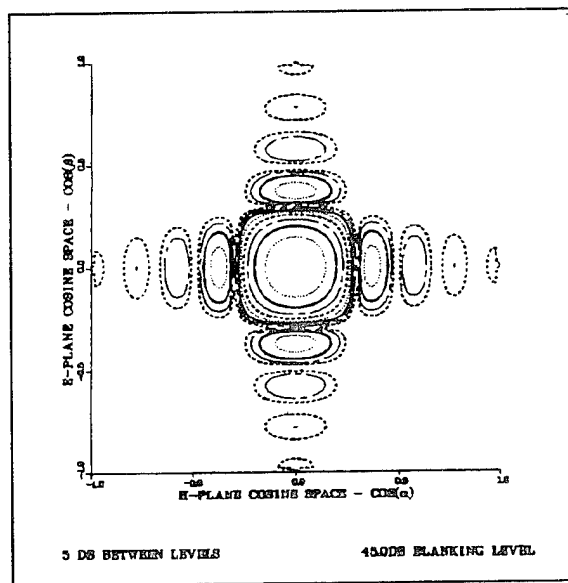


Figure 4. Pattern of Amplitude Tapered Array
 $u_0 = 0.0, v_0 = 0.0, f = 6 \text{ GHz}$
 Taper: Separable Cosines

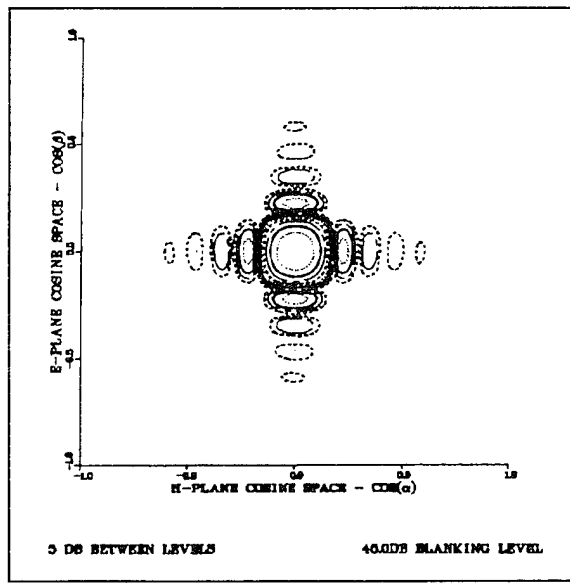


Figure 5 Pattern of Phase Tapered Array
 $u_0 = 0.0, v_0 = 0.0, f = 10 \text{ GHz}$
 Prototype Amplitude Illumination: Separable Cosines
 Phase Quantization: None

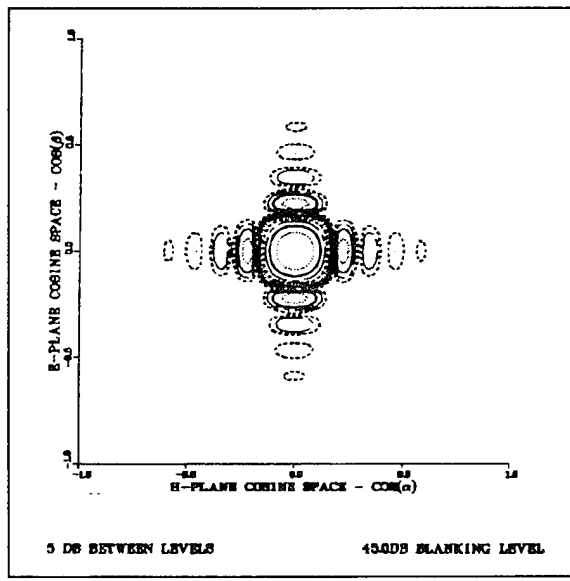


Figure 6. Pattern of Amplitude Tapered Array
 $u_0 = 0.0, v_0 = 0.0, f = 10 \text{ GHz}$
 Taper: Separable Cosines

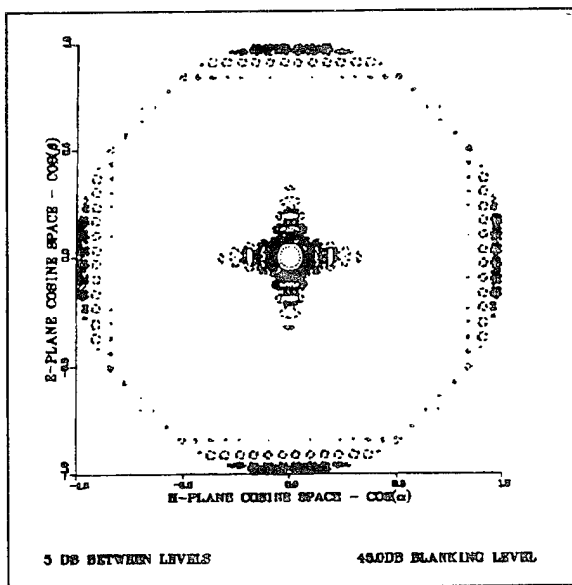


Figure 7. Pattern of Phase Tapered Array
 $u_0 = 0.0, v_0 = 0.0, f = 18 \text{ GHz}$
 Prototype Amplitude Illumination: Separable Cosines
 Phase Quantization: None

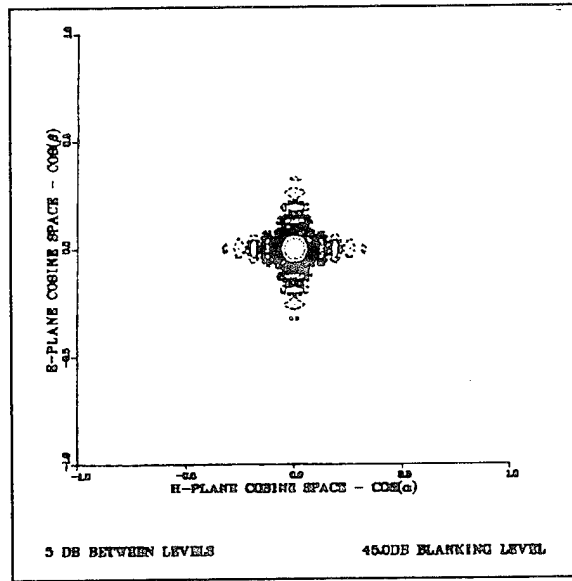


Figure 8. Pattern of Amplitude Tapered Array
 $u_0 = 0.0, v_0 = 0.0, f = 18 \text{ GHz}$
 Taper: Separable Cosines

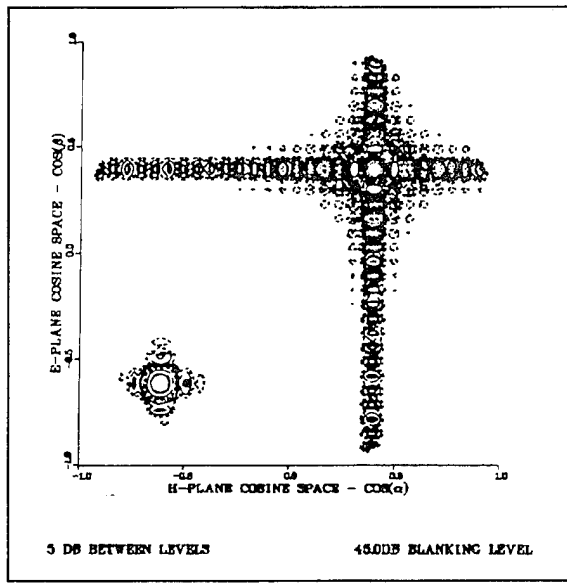


Figure 9. Pattern of Phase Tapered Array
 $u_0 = v_0 = -0.61$, $f = 18$ GHz
 Prototype Amplitude Illumination: Separable Cosines
 Phase Quantization: None

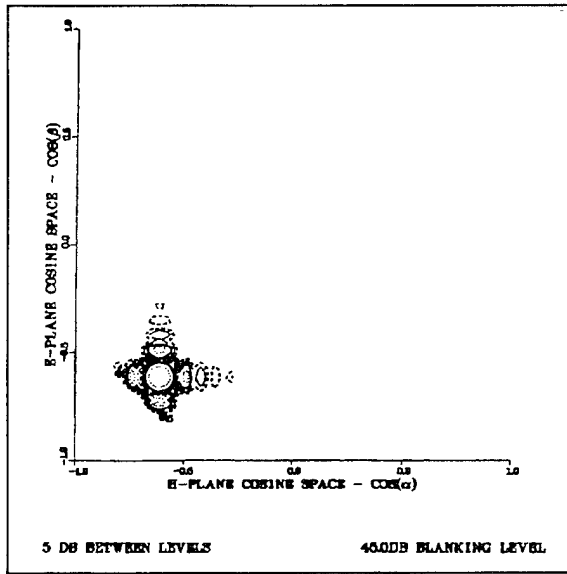


Figure 10. Pattern of Amplitude Tapered Array
 $u_0 = v_0 = -0.61$, $f = 18$ GHz
 Taper: Separable Cosines

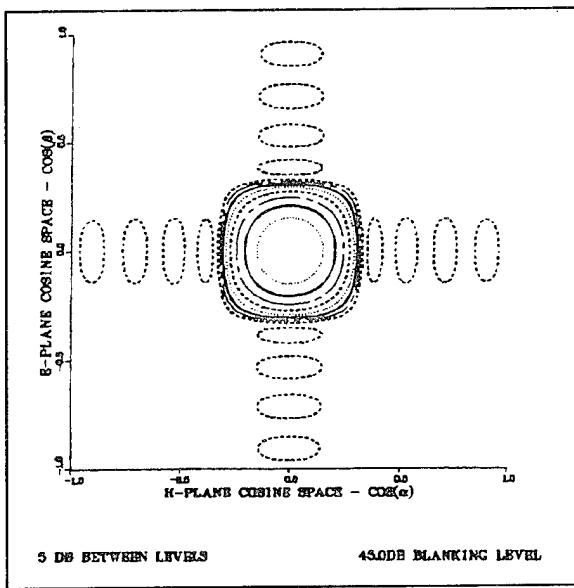


Figure 11. Pattern of Phase Tapered Array
 $u_0 = 0.0, v_0 = 0.0, f = 6 \text{ GHz}$
 Prototype Amplitude Illumination: Separable Taylors
 Phase Quantization: None
 Taylor Parameters: $n = 5, \text{SLL} = 35 \text{ dB}$

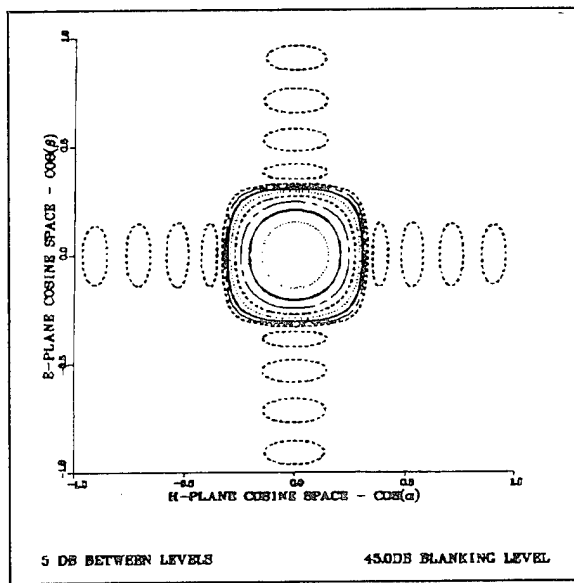


Figure 12. Pattern of Amplitude Tapered Array
 $u_0 = 0.0, v_0 = 0.0, f = 6 \text{ GHz}$
 Taper: Separable Cosines
 Taylor Parameters: $n = 5, \text{SLL} = 35 \text{ dB}$

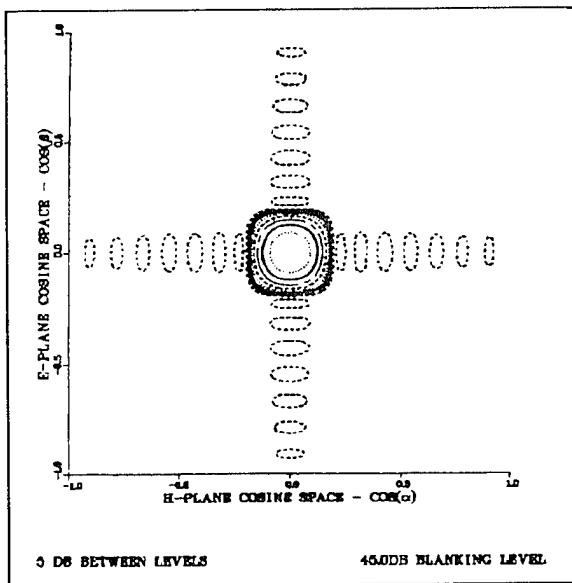


Figure 13. Pattern of Phase Tapered Array
 $u_0 = 0.0, v_0 = 0.0, f = 10 \text{ GHz}$
 Prototype Amplitude Illumination: Separable Taylors
 Phase Quantization: None
 Taylor Parameters: $n = 5, \text{SLL} = 35 \text{ dB}$

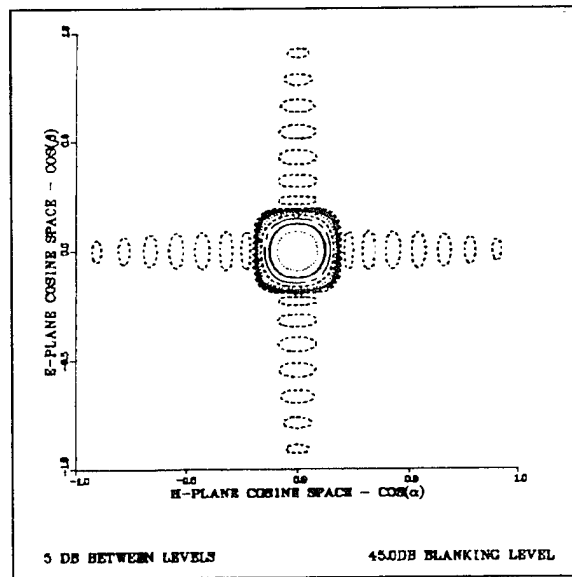


Figure 14. Pattern of Amplitude Tapered Array
 $u_0 = 0.0, v_0 = 0.0, f = 10 \text{ GHz}$
 Taper: Separable Cosines
 Taylor Parameters: $n = 5, \text{SLL} = 35 \text{ dB}$

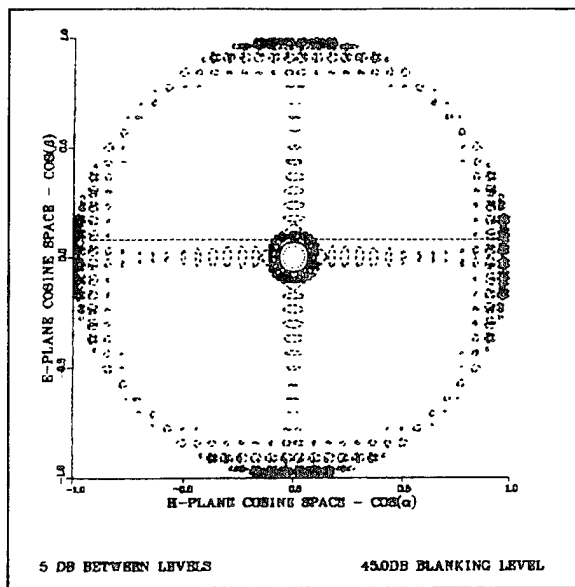


Figure 15. Pattern of Phase Tapered Array
 $u_0 = 0.0, v_0 = 0.0, f = 18 \text{ GHz}$
 Prototype Amplitude Illumination: Separable Taylors
 Phase Quantization: None
 Taylor Parameters: $n = 5, \text{SLL} = 35 \text{ dB}$

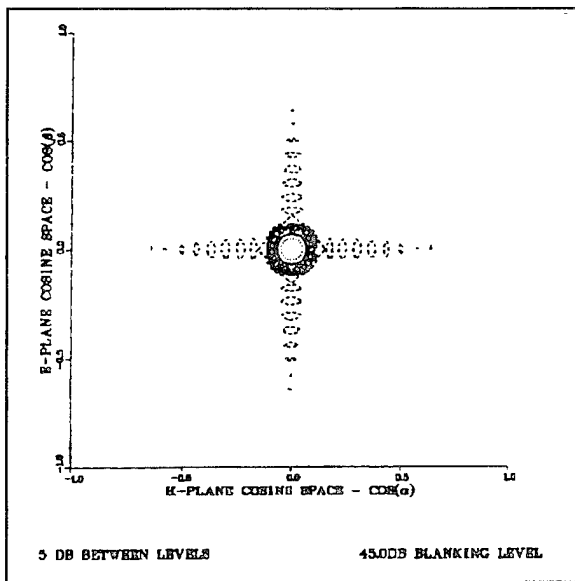


Figure 16. Pattern of Amplitude Tapered Array
 $u_0 = 0.0, v_0 = 0.0, f = 18 \text{ GHz}$
 Taper: Separable Cosines
 Taylor Parameters: $n = 5, \text{SLL} = 35 \text{ dB}$

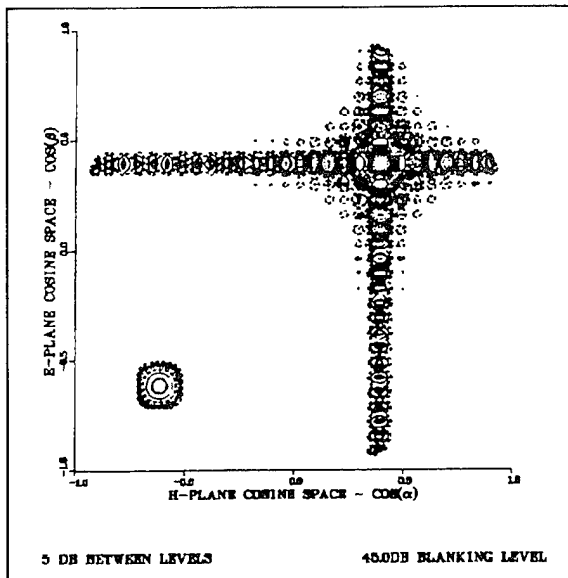


Figure 17. Pattern of Phase Tapered Array
 $u_0 = v_0 = -0.61$, $f = 18$ GHz
 Prototype Amplitude Illumination: Separable Taylors
 Phase Quantization: None
 Taylor Parameters: $n = 5$, SLL = 35 dB

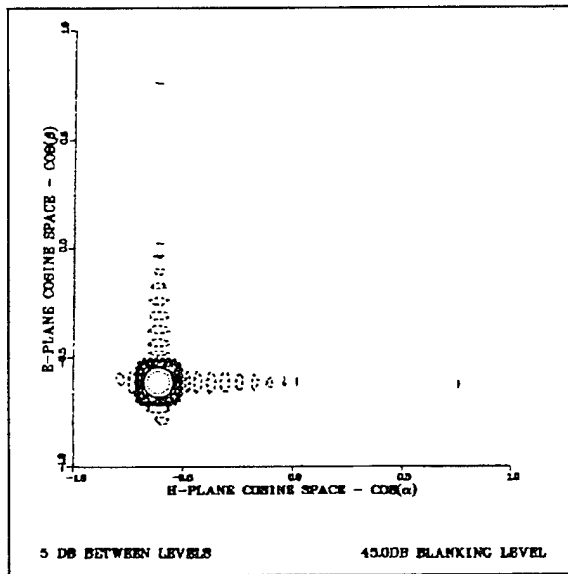


Figure 18. Pattern of Amplitude Tapered Array
 $u_0 = v_0 = -0.61$, $f = 18$ GHz
 Taper: Separable Cosines
 Taylor Parameters: $n = 5$, SLL = 35 dB

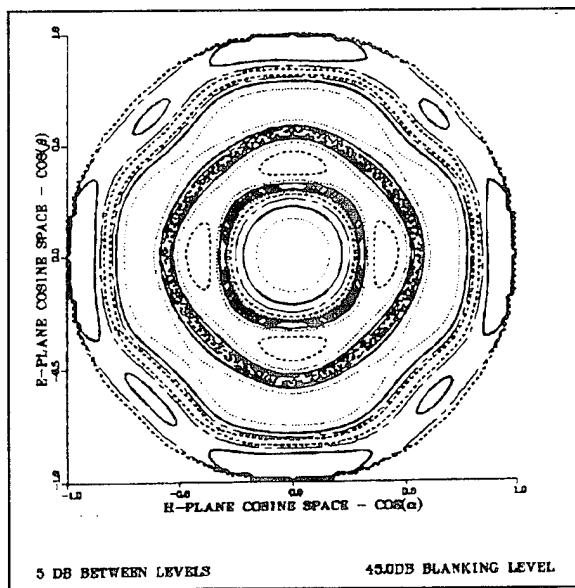


Figure 19. Pattern of Phase Tapered Array
 $u_0 = 0.0, v_0 = 0.0, f = 6 \text{ GHz}$
 Prototype Amplitude Illumination: Separable Cosines
 Phase Quantization: 3 bits

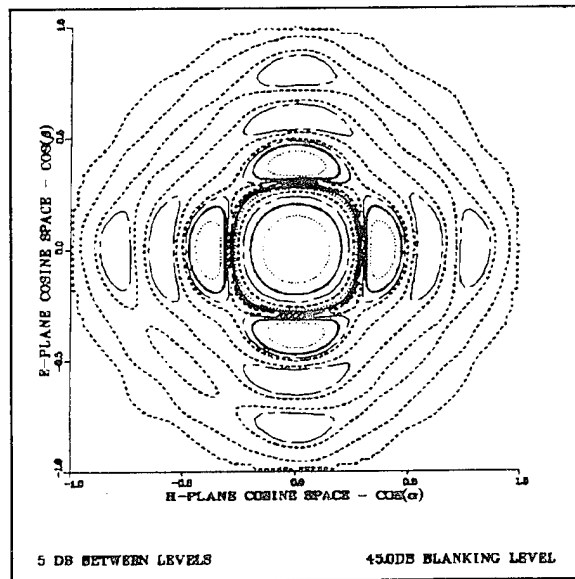


Figure 20. Pattern of Phase Tapered Array
 $u_0 = 0.0, v_0 = 0.0, f = 6 \text{ GHz}$
 Prototype Amplitude Illumination: Separable Cosines
 Phase Quantization: 4 bits

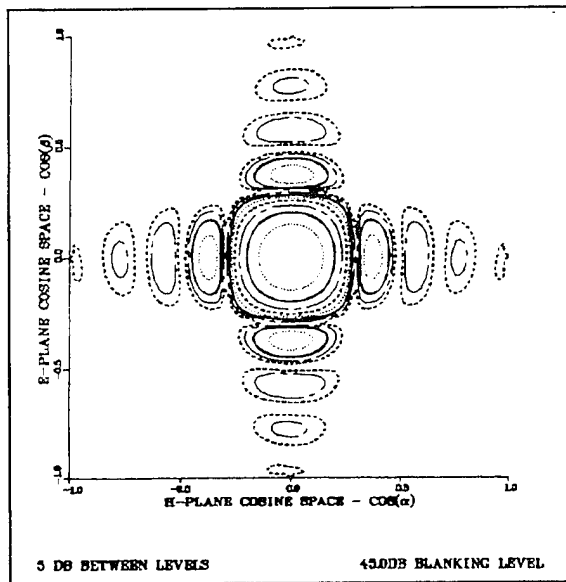


Figure 21. Pattern of Phase Tapered Array
 $u_0 = 0.0, v_0 = 0.0, f = 6 \text{ GHz}$
 Prototype Amplitude Illumination: Separable Cosines
 Phase Quantization: 5 bits

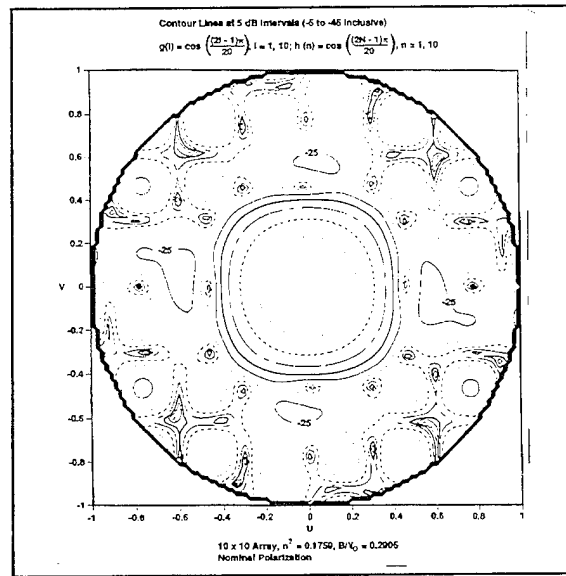


Figure 22. Pattern of Phase Tapered 10×10 Array
 $u_0 = 0.0, v_0 = 0.0, f = 6 \text{ GHz}$, Mutual Coupling Modeled
 Prototype Amplitude Illumination: Separable Cosines
 Phase Quantization: None

DEGREE OF FREEDOM REQUIREMENTS FOR SECTOR NULLING OF ERRORED ANTENNA PATTERN

Peter R. Franchi
Rome Laboratory
Antenna Technology

ABSTRACT

Several papers in recent years have established the number of degrees of freedom required to null a specific angular width of a theoretical pattern down to some desired level. The problem of field patterns for antennas with errors has not been addressed. Since patterns with some finite error is the normal situation, the deficiencies of the earlier works are addressed in this paper. In general, less degrees of freedom are required for the errored patterns than are required for the theoretical patterns. With the ratio of actual sidelobe level to the ideal sidelobe level introduced as a new parameter along with the old ones of null depth, sector width, and required degrees of freedom, a closed form solution is found. This solution can be simplified to convenient rule of thumb answer for many cases. The limits on the simplified approximation are easily derived.

I. INTRODUCTION

For many adaptive nulling applications, the degree of freedom requirements should be accurately estimated by the systems designers initially to determine feasibility and complexity of competing approaches. Prior work has given estimates for degrees of freedom requirements for arbitrary null depth and sector widths, but only for ideal or theoretical quiescent patterns. Since the actual patterns are usually distorted by errors in the array, this earlier work will often give an inaccurate

degrees of freedom estimate. By adding the generally known or estimated quantity, the amount the actual pattern (with errors) is higher than the theoretical or ideal pattern, to the null depth required and the null width required, a new derivation for the degrees of freedoms needed is found.

A very rough ‘rule of thumb’ currently used is that the degrees of freedom required is just the number of beamwidths (λ/D) contained within the angular sector to be nulled, $\Delta\mu$ (in $\sin\theta$ space), or the degrees of freedom $N = \Delta\mu/(\lambda/D)$. This approximation is generally inadequate for accurate null depth estimations. An accurate closed form solution is found in this paper, as well as a second rule of thumb results that simply ties the prior null depth based on ideal patterns to the actual null depths required and the added sidelobe levels due to errors. This paper will contain a short review of the prior ideal pattern results, a section connecting the added sidelobe level due to errors to the general Schelkunoff polynomial deviations from the ideal and then the null depth determination from which the ‘rule of thumb’ equation emerges.

II. PRIOR RESULTS

Earlier work was based on the degree freedom requirements for sector nulling of theoretical or ideal patterns. The simplest of this early work, equally spaced nulls, is repeated here for continuity. The equal amplitude nulled region is

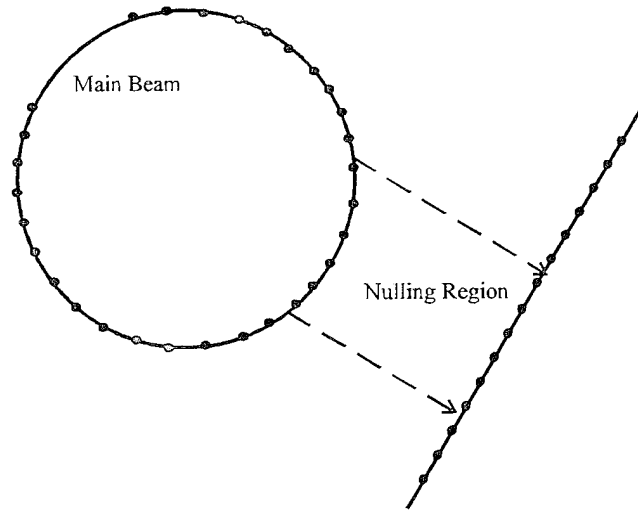


Figure 1. An illustration of a straight line approximation of the null region

too lengthy to be repeated here. Only three quantities are involved in this derivation: the normalized angular width M , the nulled region depth ΔSLL and N the required degrees of freedom. M is $\Delta\mu/(\lambda/D)$ with $\Delta\mu = \sin\theta_1 - \sin\theta_2$ (the width of the null region), λ the wavelength and D the length of the array. Two conditions are imposed for this derivation. First, the array must be large and second, the nulled region must be far from the main beam. Because of these two conditions and the additional fact that only a small local region is changed, that local region can be treated as a straight line rather than a section of Schelkunoff unit circle (Figure 1).

From Schelkunoff, the field pattern $f(\theta)$ is given by

$$f(\theta) = \sum_{i=0}^{n-1} a_i e^{j k i d \cos(\theta)} \quad (1)$$

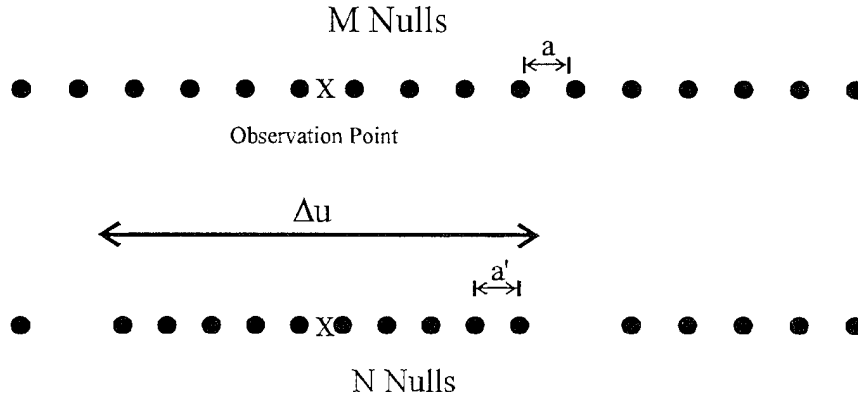


Figure 2. Nulled region comparison with quiescent pattern nulls.

This can be written as the Schelkunoff polynomial

$$f(\theta) = \prod_{i=1}^{n-1} (c - c_i) \quad (2)$$

where c_i are the zeros of the far field pattern. This expression shows that the field at any angle given by c is proportional to the product of the distance from that point to all the nulls in the pattern.

In Figure 2, a , the spacing between nulls is λ/D and a' is the reduced spacing in the nulled pattern. Thus, the original sidelobe level, SLL_0 is given by

$$SLL_0 \propto \left(\frac{a}{2}\right)^4 \left(\frac{3a}{2}\right)^4 \left(\frac{5a}{2}\right)^4 \dots \quad (3)$$

For the center lobe in the nulled region, the new sidelobe level is SLL_1 given by

$$SLL_1 \propto \left(\frac{a'}{2}\right)^4 \left(\frac{3a'}{2}\right)^4 \left(\frac{5a'}{2}\right)^4 \dots (2N-1)^4 \left(\frac{a'}{2}\right)^4 (2N+1)^4 \left(\frac{a}{2}\right)^4 \dots \quad (4)$$

The sidelobe reduction ΔSLL_o is then given by

$$\Delta SLL = \frac{SLL_1}{SLL_0} = \left(\frac{a'}{a} \right)^{2N} \quad (5)$$

Since $Ma = \Delta\mu$ and $a' = \Delta\mu$

$$\frac{a'}{a} = \frac{M}{N} \quad (6)$$

and

$$\Delta SLL = \left(\frac{M}{N} \right)^{2N} \quad (7)$$

This is basically the same result found in [5] with a modified definition of sector width.

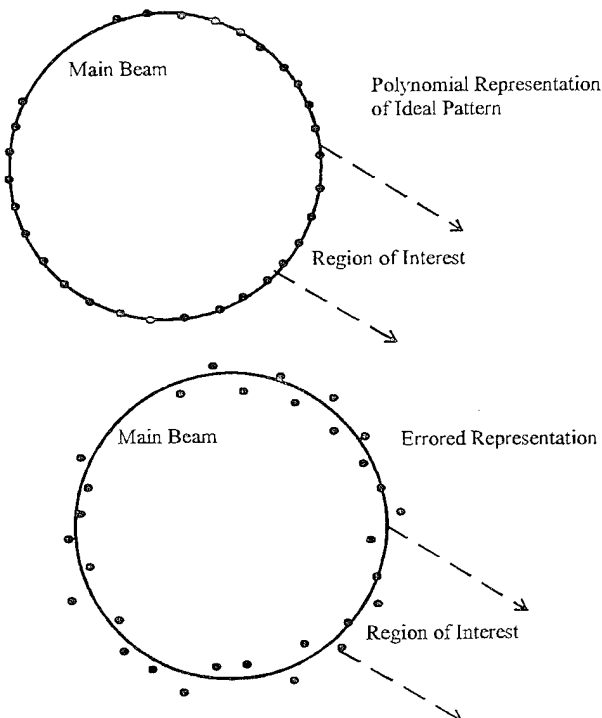


Figure 3. Comparison of errored Schelkunoff circle with unerrored Schelkunoff circle

III. ESTIMATED SIDELOBE LEVEL WITH ERRORS

For the case of an antenna pattern with errors, the roots of the Schelkunoff polynomial are displaced off the unit circle. The greater the distance off the circle the higher the sidelobes above the theoretical levels.

In order to analyze the case of an actual pattern with errors, a fourth variable must be introduced in addition to M, N, and ΔSLL . This quantity is the relative height of the actual patterns sidelobe to the theoretical sidelobes at the region. It will be symbolized by ΔSLL_o .

$$SLL_E \propto \prod_{n=1}^{\infty} (x_n^2)^2 \quad (8)$$

where x_n is defined as the distance between the observation point and the off-circle null (Figure 4).

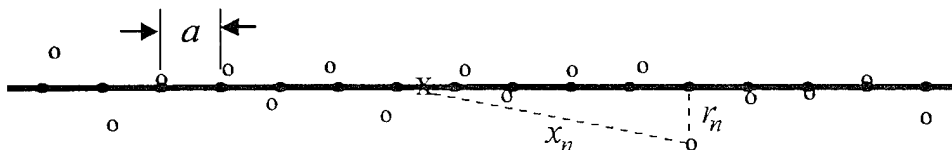


Figure 4. Displacement of the errored nulls off the unit circle.

For the ideal pattern,

$$SLL_o \propto \prod_{n=1}^{\infty} \left(\left(\frac{a}{2} \right)^2 (2n-1)^2 \right)^2 \quad (9)$$

$$\bar{x}_n^2 = \int_0^{2\pi} \int_0^b (d_n^2 + r_n^2 - 2d_n r_n \cos(180 - \theta)) P(r_n) P(\theta) dr d\theta \quad (10)$$

where

$$\begin{aligned} d_n &= \frac{a}{2}(2n-1) \\ P(\vartheta) &= \frac{1}{2\pi}, \quad 0 < \vartheta < 2\pi \\ P(r) &= \frac{1}{b}, \quad 0 < r < b \end{aligned}$$

Therefore,

$$\bar{x}_n^2 = \frac{a^2}{4}(2n-1)^2 + \frac{b^2}{3} \quad (11)$$

and so,

$$\begin{aligned} \Delta SLL_o &= \frac{SLL_E}{SLL_o} = \frac{\prod_{n=1}^{\infty} \left(\frac{a^2}{4}(2n-1)^2 + \frac{b^2}{3} \right)^2}{\prod_{n=1}^{\infty} \left(\frac{a^2}{4}(2n-1)^2 \right)^2} \\ &= \prod_{n=1}^{\infty} \left(1 + \frac{4}{3} \frac{b^2}{a^2 (2n-1)^2} \right)^2 \quad (12) \end{aligned}$$

Using the identity

$$\cosh(\gamma) = \prod_{n=1}^{\infty} \left(1 + \frac{\left(\frac{2}{\pi}\gamma\right)^2}{(2n-1)^2} \right), \quad \left(\frac{2}{\pi}\gamma\right)^2 < \infty$$

and if $\gamma = \frac{\pi}{\sqrt{3}} \frac{b}{a}$, then

$$\Delta SLL_o = \cosh^2 \frac{\pi}{\sqrt{3}} \frac{b}{a} \quad (13)$$

Furthermore,

$$\frac{b}{a} = \frac{\sqrt{3}}{\pi} \cosh^{-1} (\Delta SLL_o^{1/2}) \quad (14)$$

This equation ties the known or estimated quantity ΔSLL_o and a which is simply λ/D to b , the rms deviation of the zeros off the Schelkunoff circle. This equation is an approximation because the distances to the far nulls do not cancel as they did for the nulled region calculations, but for large arrays it is, nevertheless, a very good approximation.

IV. SECTOR NULLING ON PATTERN WITH ERRORS

If N nulls from the Schelkunoff circle displaced an average distance b from the ideal null location are now moved back onto the circle over a region $\Delta\mu$ with a spacing between nulls at a'

$$Na' = \Delta\mu$$

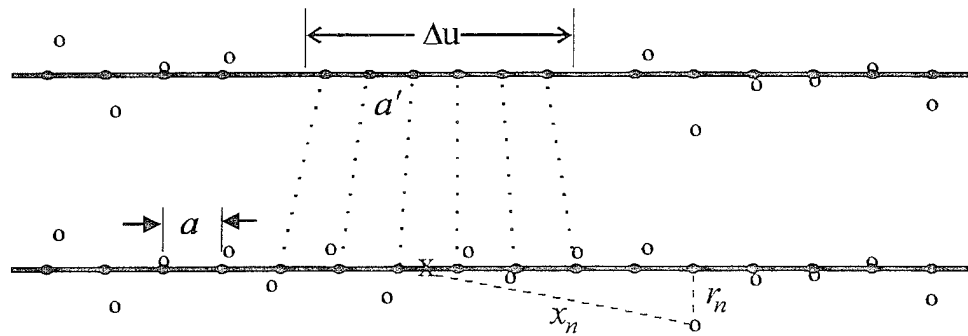


Figure 5. Comparison of nulled pattern with quiescent pattern

Far from the main beam and for large arrays, the regions of interest is approximated by an infinite radius of curvature, and so can be treated as a straight line (Figure 5).

As before,

$$SLL_N \propto \left(\frac{a'}{2}\right)^4 \left(\frac{3a'}{2}\right)^4 \left(\frac{5a'}{2}\right)^4 \dots \bar{x}_n^2 \bar{x}_{-n}^2 \bar{x}_{n+1}^2 \bar{x}_{-(n+1)}^2 \dots \quad (15)$$

$$SLL_E \propto \bar{x}_1^2 \bar{x}_{-1}^2 \bar{x}_2^2 \bar{x}_{-2}^2 \dots \bar{x}_n^2 \bar{x}_{-n}^2 \dots \quad (16)$$

So,

$$\begin{aligned} \frac{SLL_N}{SLL_E} &= \frac{\left(\frac{a'}{2}\right)^4 \left(\frac{3a'}{2}\right)^4 \left(\frac{5a'}{2}\right)^4 \dots (N-1)^4 \left(\frac{a'}{2}\right)^4}{\left(\frac{a^2}{4} + \frac{b^2}{3}\right)^2 \left(\frac{3^2 a^2}{4} + \frac{b^2}{3}\right)^2 \dots \left(\frac{(N-1)^2 a^2}{4} + \frac{b^2}{3}\right)^2} \\ &= \left(\frac{a'}{a}\right)^{2N} \frac{1}{\prod_{n=1}^{N/2-1} \left(1 + \frac{4b^2}{3a^2(2n-1)^2}\right)^2} \end{aligned} \quad (17)$$

Since $\Delta\mu/a=M$, $a=\lambda/D$, and $\Delta\mu/a'=N$,

$$\Delta SLL = \left(\frac{M}{N}\right)^{2N} \frac{1}{\prod_{n=1}^{N/2-1} \left(1 + \frac{4b^2}{3a^2(2n-1)^2}\right)^2} \quad (18)$$

This is the basic solution. It can also be written in a form that includes the known quantity ΔSLL_o

$$\Delta SLL = \left(\frac{M}{N}\right)^{2N} \frac{1}{\prod_{n=1}^{N/2-1} \left(1 + \frac{4}{\pi^2} \frac{\left(\cosh^{-1}(\Delta SLL_o)^{\frac{1}{2}}\right)^2}{(2n-1)^2}\right)^2} \quad (19)$$

This general form can be simplified for many cases to give a reasonable rule of thumb equation.

Recall that

$$\Delta SLL_o = \prod_{n=1}^{\infty} \left(1 + \frac{4}{3} \frac{b^2}{a^2(2n-1)^2}\right)^2$$

Substituting into equation number (18), we obtain

$$\Delta SLL = \left(\frac{M}{N}\right)^{2N} \frac{1}{\Delta SLL_o} \prod_{n=\frac{N}{2}}^{\infty} \left(1 + \frac{4}{3} \frac{b^2}{a^2(2n-1)^2}\right)^2 \quad (20)$$

So for large N and small b/a, we get

$$\Delta SLL = \left(\frac{M}{N} \right)^{2N} \frac{1}{\Delta SLL_o} \quad (21)$$

since

$$\prod_{n=\frac{N}{2}}^{\infty} \left(1 + \frac{4}{3} \frac{b^2}{a^2 (2n-1)^2} \right)^2 \approx 1$$

This approximate answer states that the total null depth achieved is simply the product of the null depth below the ideal pattern level (with this depth determined by the earlier equations) and the ratio of the actual patterns with errors to the ideal. This rule of thumb equation breaks down for small N and large error sidelobes.

If a 3 dB tolerance is permitted then

$$\prod_{n=\frac{N}{2}}^{\infty} \left(1 + \frac{4}{3} \frac{b^2}{a^2 (2n-1)^2} \right)^2 \leq 2$$

Therefore, we can use this approximation when

$$N \geq \frac{1}{2} \left(\cosh^{-1} \left(\Delta SLL_o \right)^{\frac{1}{2}} \right)^2 + 1 \quad (22)$$

For example, if $\Delta SLL_o = 100$ (20dB), then $N > 6$.

V. SUMMARY

Prior analysis dealt only with sector null depths for ideal antenna patterns, but the actual antenna patterns are nearly always higher than the ideal because of array errors. This increased sidelobe level is usually known from measurements or estimated from equations describing error sidelobe. This increase, ΔSLL_o , together with the normalized sector depth, ΔSLL , gives the degrees of freedom required, N .

Two related equations are obtained, an ‘exact’ equation provided $N > M$ and a rule of thumb formula for large N and small ΔSLL_o . This latter equation is very useful because of its simplicity. It states that the required null depth is just the product of $1/\Delta SLL_o$ and the null depth predicted from the theoretical null equation. As an example, if a total null depth of 30 dB were desired and the actual sidelobes are 20 dB above the ideal then N could be determined from the theoretical formula for a 10 dB null and not 30 dB.

REFERENCES

1. Shore, R. A. and Fante, R. L., "Sector Sidelobe Nulling", RADC-TR-81-32, In House Report, Nov 1981
2. Steyskal, H., "Wideband Nulling Performance Versus Number of Pattern Constraints for an Antenna Array, IEEE Transaction on Antennas and Propagation, 83 Jan
3. Tseng, F. I., "Design of Array and Line-Source Antenna for Taylor Patterns with a Null", IEEE Transaction on Antennas and Propagation, 79 July, pp 479-479
4. Collin, R. E., and Zucker, F. J., "Antennas Theory Part I", Inter-University Electronics Series, pp 158-160
5. Franchi, P. R., "Constraints on Nulling Bandwidth", Proceedings of the 1982 Antenna Application Symposium, Urbana-Champaign, IL, September 22-24, 1982

TECHNIQUES FOR ADAPTIVE ARRAY PATTERN CONTROL USING AN AUGMENTED COVARIANCE MATRIX

R.J. Mailloux

Electromagnetics and Reliability Directorate
Rome Laboratory
31 Grenier St.
Hanscom AFB, MA 01778-3010, USA

Abstract

ABSTRACT: An adaptive technique is presented that produces array pattern troughs in response to discrete sources of interference. The technique is implemented by a simple modification of the measured covariance matrix, and can be used to form troughs in both the near and far zones. A related technique is shown to allow placing simple nulls (or troughs) at locations displaced from the measured source locations. This feature could null a moving source of interference with fewer updates than necessary with conventional nulling.

1.0 INTRODUCTION

Conventional methods of adaptive array control use sample matrix inversion to optimize the signal to noise ratio by multiplying the quiescent array weights by the inverse of the measured covariance matrix. For strong, narrow band sources of interference, this amounts to placing individual nulls at the source locations. Broadband sources result in adapted array patterns that have deep troughs that span the source frequency band, and appear as appropriately wide troughs in the angle domain. There are times when it would be advantageous to be able to produce broad angular pattern troughs in anticipation of interference signal behavior. Such cases include discrimination against interference sources that frequency hop, or whose apparent location changes rapidly because of reflection from clutter, or receiver platform motion or vibration.

Treating such sources with conventional adaptive techniques increases the signal processing load as well as the time devoted to obtaining covariance matrix updates.

This paper presents a particularly simple method for producing near or far field trough-like array patterns in place of simple adapted nulls. The method involves very little extra processing to form an augmented covariance matrix and is here shown to produce patterns that are almost identical to what would be obtained by clustering a group of sources around each measured source. The technique is adaptive, and so requires no information about source location or source strength.

The adaptive array optimizes signal-to-noise using the measured noise covariance matrix. The signal-to-noise ratio is given in terms of the signal and noise covariance matrices as:

$$\frac{S}{N} = \frac{\overline{E_s^* E_s}}{\overline{E_N^* E_N}} = \frac{W^\dagger M_s W}{W^\dagger M_N W} \quad (1)$$

where the superscript \dagger means conjugate transpose, and the overbar indicates a time average. M is the covariance matrix of the signal or noise as indicated by the subscript, and E is the weighted sum of the signals received from any sources and receiver channel noise. The covariance matrix is given in terms of the column vectors of received signals "e" as:

$$M = \overline{e^* e^T} \quad (2)$$

2.0 ADAPTIVE FAR FIELD TROUGH PATTERNS FOR A ONE DIMENSIONAL ARRAY

The method is most simply presented by considering a line array with arbitrarily spaced elements.

Assuming that the noise terms are not correlated with the incident waves, and the incident waves are not correlated with each other, the terms in the noise covariance matrix M_N for a one dimensional array are:

$$m_{nm} = N_n \delta(n, m) + \sum_j P_j e^{j \frac{2\pi}{\lambda_j} (x_m - x_n) u_j} \quad (3)$$

The sum is performed over all interfering sources with averaged power P_j and direction cosines $u_j = \sin \theta_j$ for θ_j measured from the array normal. The numbers x_m are the element locations, N_n is the receiver noise in the n'th channel and $\delta(n, m)$ is the Kronecker delta function. The sources of interference are here shown to be at monotonic frequencies, but are more likely to be narrow band uncorrelated sources.

For strong sources at discrete angles, the array will place a null at every source. If instead of that one source P_j there were a cluster of ' n_0 ' equal strength incoherent sources arranged in a line centered about each original interference source, the pattern would have troughs centered at each source. For the linear array with interference sources at angles u_j , these new sources are at:

$$u = u_j + q\delta \quad (4)$$

for

$$-(\frac{(n_0 - 1)}{2}) \leq q \leq (\frac{(n_0 - 1)}{2}) \quad (5)$$

Choose $\delta = \frac{W}{n_0 - 1}$ where W is the trough width between outermost nulls.

In this case the additional sources can be summed in closed form, as a geometric sum, and the covariance matrix term becomes;

$$M_{nm} = N_n \delta(n, m) + \sum_j \frac{\sin(n_0 \Delta_j)}{\sin(\Delta_j)} P_j e^{j \frac{2\pi}{\lambda_j} (x_m - x_n) u_j} \quad (6)$$

for

$$\Delta_j = \frac{\pi}{\lambda_j} (x_m - x_n) \delta \quad (7)$$

Notice that for the off-diagonal terms, the components of the new covariance matrix are just the original terms multiplied by the sinc function. There is no angle dependence in the sinc functions, and so the same factor multiplies each source term.

The measured covariance matrix has noise in the diagonal terms, and so it is not possible to exactly duplicate the expression above by multiplying the measured matrix coefficients by the sinc functions. The off diagonal terms are

exactly reproduced, but the diagonal terms have the noise contribution multiplied by n_0 . Thus, in place of equation 6, the augmented covariance matrix produced by simply multiplying the measured covariance matrix by the sinc factors has coefficients of the form:

$$M_{nm} = m_{nm} \frac{\sin(n_0\Delta)}{\sin(\Delta)} \quad (8)$$

for m_{nm} given in equation 3. Notice that in this expression we have replaced the individual Δ_j terms by Δ , assuming some average wavelength λ in place of the λ_j . This approximation simply scales the width of the trough region at each frequency.

The net change to the covariance matrix is to diagonally load the matrix by adding noise (here specifically by multiplying the channel noise by n_0), while otherwise producing a trough of scaled width W_j at each interference location. In effect, each source appears like ' n_0 ' equally spaced sources, and the channel noise is multiplied by n_0 . The diagonal loading itself does not necessarily decrease the signal to noise of the array, and some cases may improve it, or [1] reduce the array sensitivity to errors in the measured estimate of the matrix.

Figure 1 shows the pattern of a 64 element array with a 20dB Taylor pattern ($\bar{n} = 8$). The array has equally spaced elements with 0.5 wavelength spacing. The array is subject to two interfering sources of the same amplitude, and located at $u_j = 0.3$ and 0.8 . The interfering sources are taken as 30dB larger than the channel noise. The pattern without augmentation of the covariance matrix is not shown, but does have narrow nulls at the locations of

the interfering sources. The array covariance matrix is modified as indicated in equation 8 to produce trough shaped regions centered at these two locations by using $n_0=7$ and $W=0.1$. The resulting pattern shows the two trough regions with enough detail to observe the individual nulls making up each trough.

Although this example used a periodic array, the analysis does not rely upon periodicity, and could as well pertain to an arbitrarily spaced array.

3.0 MATRIX FOR A TWO DIMENSIONAL ARRAY:

The augmented matrix for a two dimensional array is readily obtained in the same manner as the one dimensional array. In this case it is desired to produce a rectangular grouping of ' n_0 ' by ' m_0 ' equal sources at each interference.

The result is :

$$M_{nm} = m_{nm} \frac{\sin(n_0\Delta_x)}{\sin(\Delta_x)} \frac{\sin(m_0\Delta_y)}{\sin(\Delta_y)} \quad (9)$$

For Δ_x and Δ_y as defined in equation 7 based upon the trough widths in each plane, and using:

$$m_{nm} = N_n \delta(n, m) + \sum_j P_j e^{j \frac{2\pi}{\lambda} [(x_m - x_n) u_j + (y_m - y_n) v_j]} \quad (10)$$

Figures 2 and 3 show contour plots of the pattern of an array of 16 columns and 16 rows, with half wave spacing on a square grid. The array taper is the separable product of the same Taylor pattern as the linear array, and so produces the principal plane ridges shown in Figure 2 for the quiescent pattern. Principal plane sidelobes are at the -20dB level, and so the contours

chosen are at dB levels of -3,-15,-30,-45, etc.. The channel noise and interfering sources are in the same -30dB ratio. Although not shown, a contour plot for the adaptive array response to the original covariance matrix had a simple narrow null at each interference location. Figure 3 was chosen to illustrate a fairly extreme broadening of the pattern subject to two interfering sources at $(u,v) = (0.42,0.0)$ and $(0.0,0.42)$. The chosen trough width is 0.2 in both planes, and both n_0 and m_0 were 11. This forced the resulting pattern to be the response to 121 interfering sources at each trough region, and shows two contoured regions (darker line) of the correct size with all sidelobes below -75 dB. The trough regions are not rectangular because the interference has a diagonal symmetry.

4.0 ADAPTIVE NEAR FIELD TROUGHS

A similar formulation can produce wide troughs in the near field of an array. In this case, unlike the case of far field pattern troughs, the method applied to form a trough at one area does not necessarily form useful troughs at every other area, because the near field behavior is far more complex. In this case one can form a single near field trough, using one noise source, and the behavior at other near or far field sources will be modified, but not necessarily caused to have deep troughs.

The signal and noise received at element 'n' of an array is given as it receives radiation from far field sources $j=1$ to J_F and near field sources $j = J_{F+1}$ to J_{F+J_N} .

$$e_n = n_n + \sum_{j=1}^{J_F} A_j e^{+jk_j \hat{\rho}_j \cdot \bar{r}_n} + \sum_{j=J_F+1}^{J_F+J_N} A_j \frac{e^{-jk_j R_{jn}}}{R_{jn}} \quad (11)$$

In this expression the array element center coordinates \bar{r}_n , and far field source direction unit vector $\hat{\rho}_j$ are:

$$\bar{r}_n = \hat{x}x_n + \hat{y}y_n + \hat{z}z_n \quad (12)$$

$$\hat{\rho}_j = \hat{x}u_j + \hat{y}v_j + \hat{z}\cos\theta$$

The wave number $k_j = \frac{2\pi}{\lambda_j}$ and the constants A_j are referenced to the various incident waves. The near field sources of interference are located at (x_j, y_j, z_j) and the discrete R_{jn} given by

$$R_{jn} = [(x_j - x_n)^2 + (y_j - y_n)^2 + (z_j - z_n)^2]^{1/2} = |\bar{r}_j - \bar{r}_n| \quad (13)$$

The covariance matrix corresponding to this set of incident waves has the matrix coefficients

$$m_{nm} = N_n \delta(n, m) + \sum_{j=1}^{J_F} P_j e^{jk_j (\bar{r}_m - \bar{r}_n) \cdot \hat{\rho}_j} + \sum_{j=J_F+1}^{J_F+J_N} P_j \frac{e^{-jk_j (R_{jm} - R_{jn})}}{R_{jm} R_{jn}} \quad (14)$$

In deriving this expression it is assumed that all jamming sources are uncorrelated , which may not necessarily be so if the near field sources are scattered from nearby platform scatterers. A similar relation is readily derived for the correlated case.

To create a three dimensional trough in the near field, in the neighborhood of some one near field source location \bar{r}_j , one adds additional sources of power amplitude P_j at locations \bar{r}'_q in a coordinate system centered at \bar{r}_j , so that the sources are at

$$(x, y, z) = (\bar{r}_j + \bar{r}'_q). \quad (15)$$

The distance from this q'th source at the n'th element is given exactly and approximately by the following equations.

$$R_{qn} = | -\bar{r}_n + \bar{r}_j + \bar{r}'_q | \quad (16)$$

$$\doteq R_{jn} + \bar{r}'_q \cdot \left(\frac{\bar{r}_{jn}}{R_{jn}} \right)$$

this ratio $\frac{\bar{r}_{jn}}{R_{jn}}$ is the unit vector that points from the n'th element to the j'th source.

Superimposing 'Q' of these sources, each at some different location \bar{r}'_q , one obtains a new covariance matrix for an idealized system that has troughs at every near field source.

$$M_{nm} = N_n \delta(n, m) + \sum_{j=1}^{J_F} P_j e^{jk_j(\bar{r}_m - \bar{r}_n) \cdot \hat{r}_j} + \sum_{j=J_F+1}^{J_F+J_N} P_j \frac{e^{-jk_j(R_{jm} - R_{jn})}}{R_{jm} R_{jn}} \sum_{q=1}^Q S_{jnm}^q \quad (17)$$

where

$$S_{jnm}^q = e^{-jk_q \bar{r}'_q \cdot [\frac{\bar{r}_{jm}}{R_{jm}} - \frac{\bar{r}_{jn}}{R_{jn}}]} \quad (18)$$

With this new covariance matrix, the array pattern will have trough regions centered about the defined near field sources.

Unfortunately, using the measured covariance matrix due to a number of real sources, it will not be possible to make modifications that correspond to the idealized configuration above. The best one can do is to pick one near field location, $\bar{r}_j = \bar{r}_J$, and form the augmented covariance matrix with terms:

$$M_{nm} = m_{nm} \sum_{q=1}^Q S_{Jnm}^q \quad (19)$$

This new matrix places the desired trough at the one selected location, and places modified trough regions around the other near field sources. It retains the point far field nulls and adds distorted trough regions about each far field source. Figures 4 and 5 show an example of this technique for broadening near field nulls. Figure 4 shows the near and far field patterns of a 32 element linear array adapted by sample matrix inversion to discriminate against two sources of interference, a far field source at $u=0.3$, and a near field source at location $(x,y,z) = (-5,0,20)$, with all dimensions normalized to wavelengths. The array is centered at the origin of the coordinate system, and extends along the x-axis, with elements one half wavelength apart. The far field pattern is derived from a quiescent -20 dB Taylor pattern, and displays the expected null at $u=0.3$. The near field pattern of Figure 4 is calculated along a line from $x=-25$ to 25 , with $y=0$ and $z=20$, and shows the near field null at $x=-0.5$. Figure 5 shows the corresponding far and near field patterns obtained with the augmented covariance matrix, using 10 virtual sources, spread out over a trough width of 5, centered at -5. The matrix was created to widen the near field null in Figure 5, and it does, but the figure also shows broadening of the far field null in this case. These figures confirm that the augmented covariance matrix technique has utility for near field control as well as far field control.

5.0 AUGMENTED COVARIANCE MATRIX TO IMPROVE THE ADAPTIVE RESPONSE TO A MOVING SOURCE

Giving a single interfering source at the far field source direction $\hat{\rho}_j$, moving in any general direction, one would need to update the noise covariance matrix periodically in order to keep the pattern continually nulled in the direction of the interference. If the source motion can be estimated, this processing burden can be relieved by modifying the noise covariance matrix to force the formed pattern null to follow the motion of the source.

The covariance matrix for the noise source at $\hat{\rho}_j$ has terms:

$$m_{nm} = N_n \delta(n, m) + P_j e^{jk_j (\bar{r}_m - \bar{r}_n) \cdot \hat{\rho}_j} \quad (20)$$

Using this measured covariance matrix as basis, one can modify the matrix to correspond to one for a source at $\hat{\rho}'$ where

$$\hat{\rho}' = \hat{\rho}_j + \Delta\hat{\rho} \quad (21)$$

The resulting covariance matrix has terms:

$$M_{nm} = N_n \delta(n, m) + P_j e^{jk_j (\bar{r}_m - \bar{r}_n) \cdot (\hat{\rho}_j + \Delta\hat{\rho})} \quad (22)$$

As before, this augmented covariance matrix is obtained by multiplying the terms of the measured covariance matrix by the known factor, to result in:

$$M_{nm} = m_{nm} e^{jk_j \Delta\hat{\rho} \cdot (\bar{r}_m - \bar{r}_n)} \quad (23)$$

which is the same as the previous expression for M_{nm} .

This result shows that as long as the motion of an interfering source can be anticipated, the adapted pattern using the augmented covariance matrix obtained for the original location can be made equal to what it would be if it adapted to the new location. This feature should be a significant advantage in terms of required signal processing, since it is accomplished by an extremely simple algorithm.

6.0 CONCLUSION

This paper has introduced a simple technique to produce adaptive trough patterns and other generalized pattern changes in response to discrete sources of interference. The technique is useful for linear or planar arrays with arbitrary spacing, can produce near and far field troughs, and displace pattern nulls in accord with pre-set rules. Each of these alterations can be implemented with very little processing.

ACKNOWLEDGEMENT:

The author is grateful to the Air Force Office of Scientific Research for sponsoring this work.

REFERENCES

1. B.D. Carlson, "Covariance Matrix Estimation Errors and Diagonal Loading in Adaptive Arrays" IEEE Trans. on Aerospace and Electronic Systems, Vol. 24, No.4, July 1988

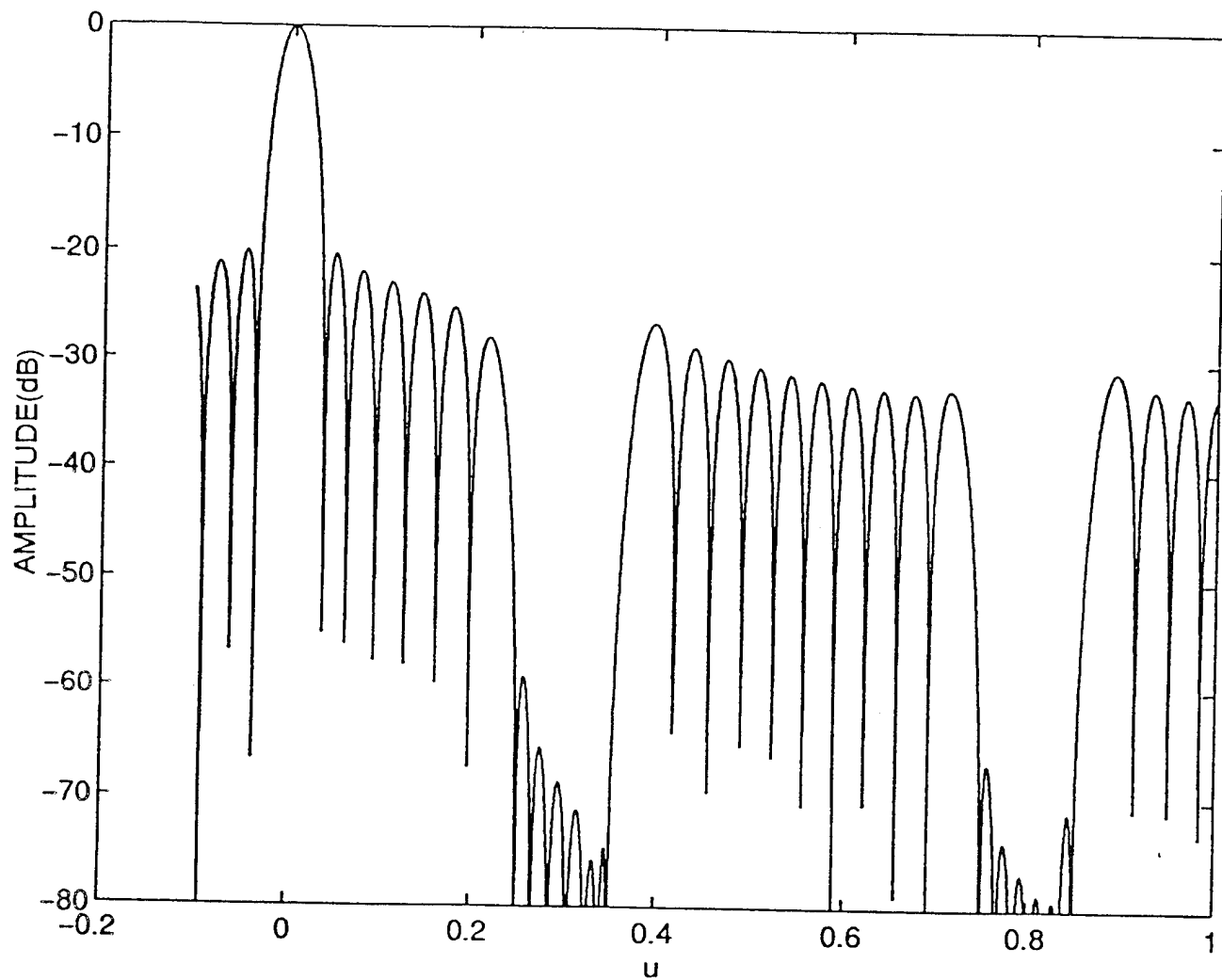


Figure 1. Pattern of linear 16 element broadside array with augmented covariance matrix and interfering sources at $u = 0.3$ and 0.8

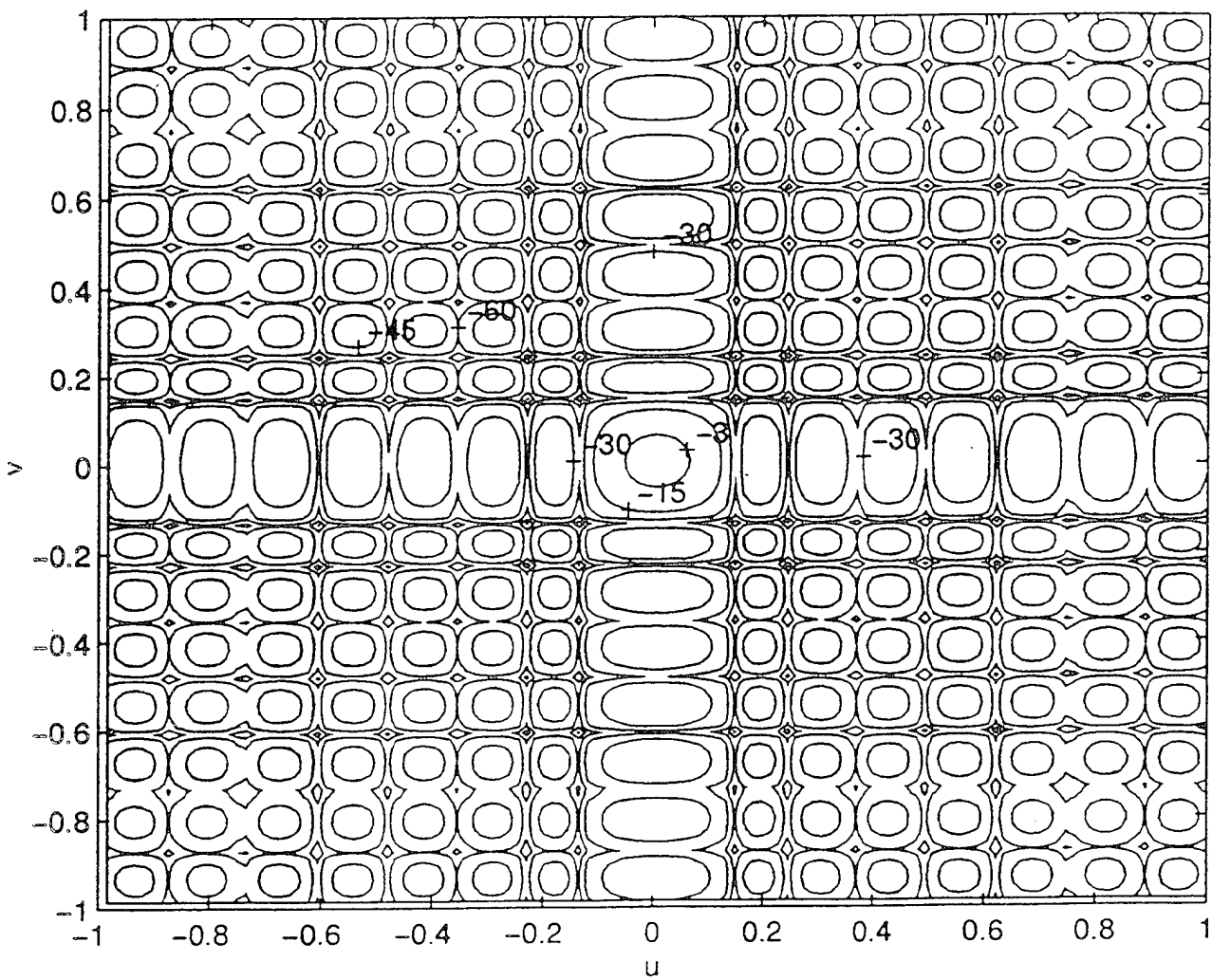


Figure 2. Quiescent contour pattern of 16 by 16 element array with broad-side separable Taylor illumination.(Note: Pattern is restricted by "real space" limits $u^2 + v^2 \leq 1$)

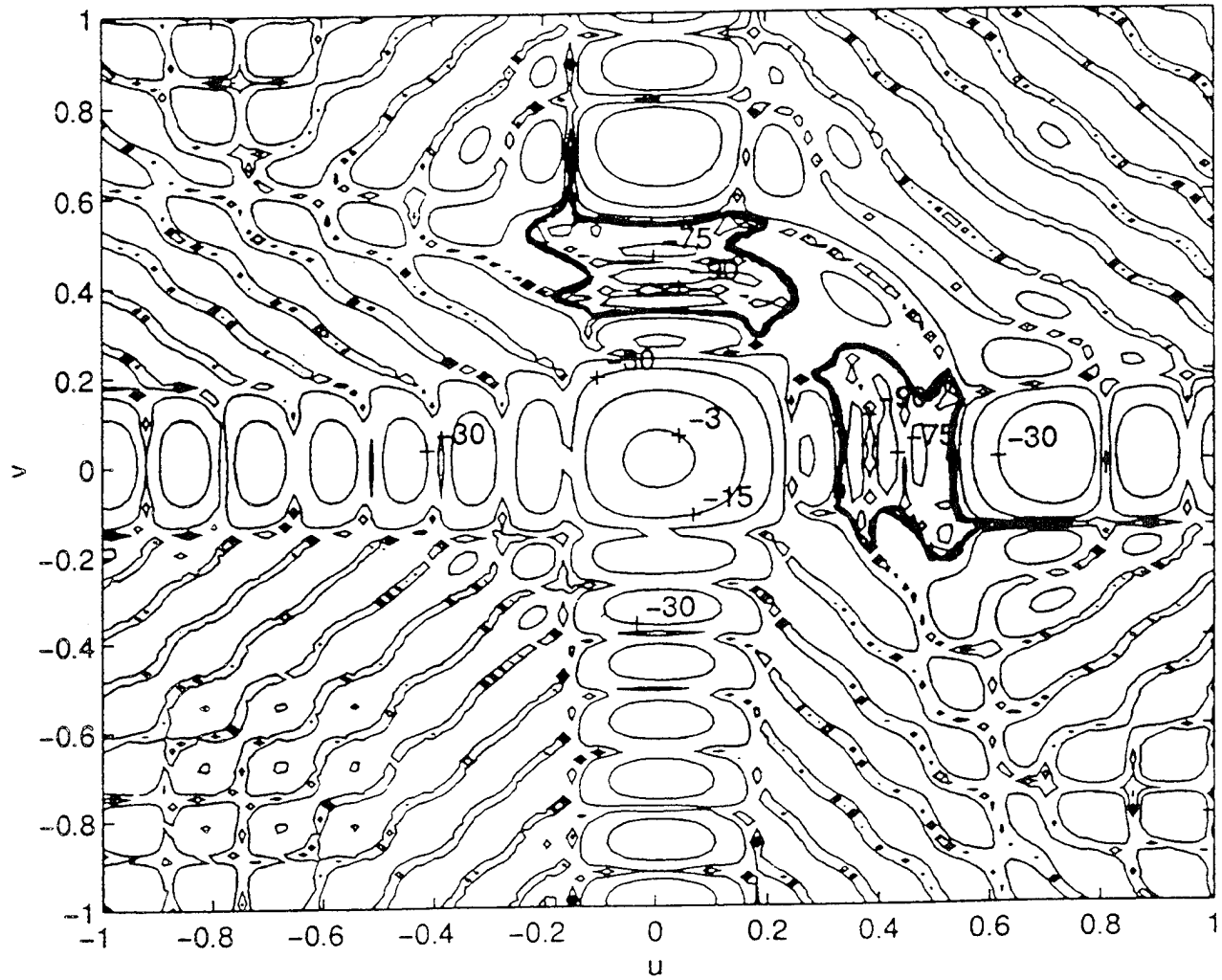
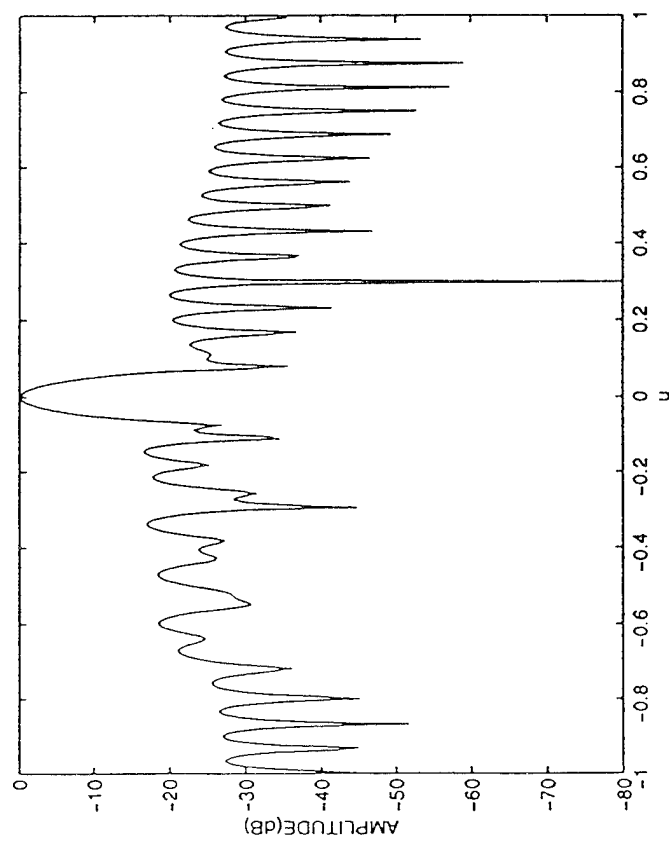
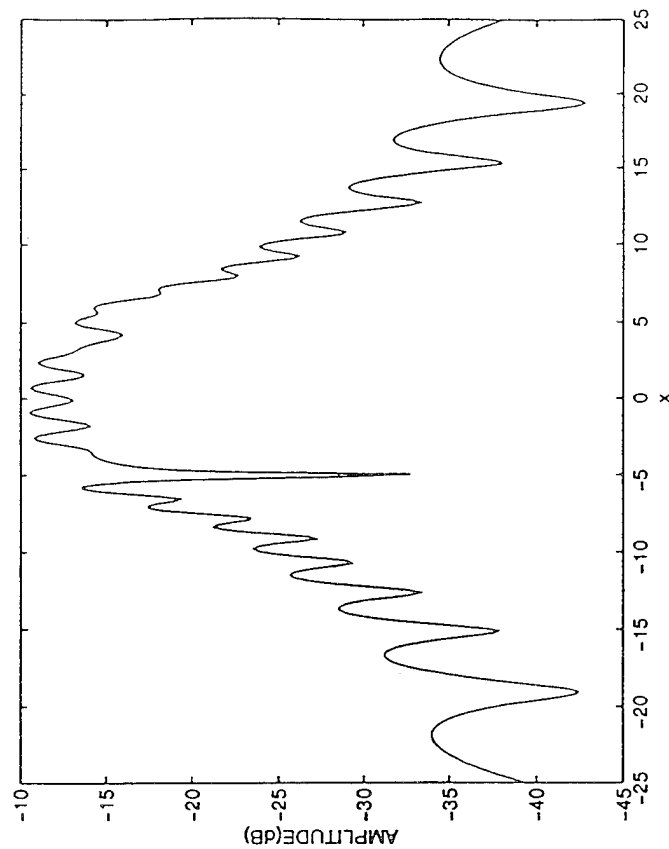


Figure 3. Contour pattern of 16 by 16 element array with augmented covariance matrix ($m_0 = n_0 = 11$, $W=0.2$ in both planes, and interfering sources at $(u,v) = (0.42, 0)$ and $(0, 0.42)$ (Note: Pattern is restricted by "real space" limits $u^2 + v^2 \leq 1$)

PATTERNS FOR ONE NEAR FIELD AND ONE FAR FIELD INTERFERENCE



FAR FIELD PATTERN



NEAR FIELD PATTERN

Figure 4. Far field and near field patterns of a 32 element array with point sources of interference at $u=0.3$ in the far field, and $(x,y,z) = (-5,0,20)$ in the near field. The near field pattern is calculated along the line $x=-25$ to $+25$, $y=0$, $z=20$

PATTERNS FOR ONE NEAR FIELD AND ONE FAR FIELD INTERFERENCE
(WITH 10 SOURCE THROUGH FORMED IN NEAR FIELD)

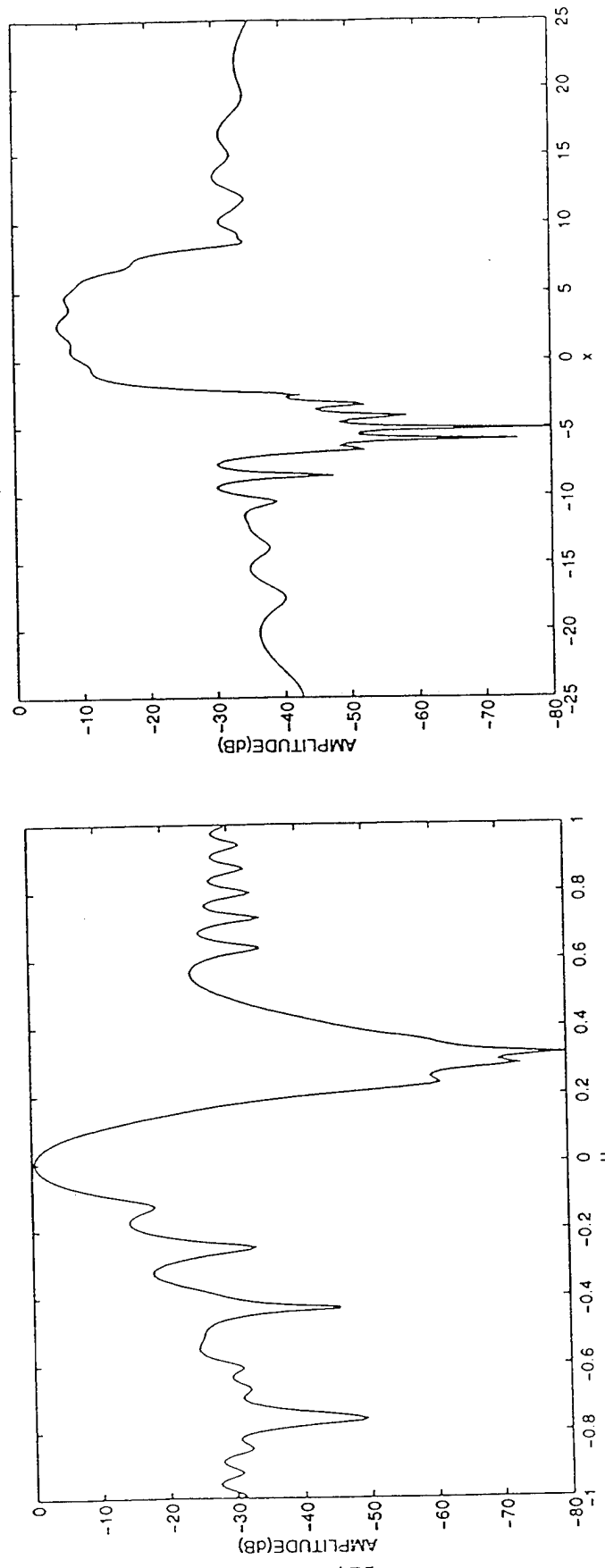


Figure 5. Far field and near field patterns of a 32 element array as stated in Figure 4, but assuming 10 near field sources from $x=-7.5$ to $x=2.5$.

**DIGITAL AND ADAPTIVE BEAMFORMING TECHNIQUES
FOR ENVIRONMENTAL REMOTE SENSING**

Christopher D. Cherry*, Daniel H. Schaubert,
Geoffrey Hopcraft, James B. Mead, Robert E. McIntosh
University of Massachusetts
Antenna Laboratory / Microwave Remote Sensing Laboratory
Amherst, MA 01003

Abstract

This paper will detail some of the digital beamforming and adaptive array processing work taking place at the University of Massachusetts Microwave Remote Sensing Laboratory (MIRSL). Data from both linear and planar imaging array radar systems are considered, and they are combined with theoretical results to evaluate the performance of common algorithms operating in signal environments typical of remote sensing radars.

1. Introduction

Imaging radar systems rely heavily on their antenna systems for spatial filtering as the ability of a system to separate signals arriving from different directions significantly affects the accuracy with which a target or region of interest can be imaged in the presence of interfering signals. This is particularly true of radars used in remote sensing of environmental targets as the ‘target’ and ‘interference’ signals often have nearly identical temporal spectra, making the use of doppler filtering techniques (e.g. MTI) difficult or impossible. It is highly

desirable, therefore, to optimize the spatial frequency response of the antenna system such that the total interference return is minimized.

The Microwave Remote Sensing Laboratory at the University of Massachusetts is fortunate to have two functional digitally beamformed imaging array radars. The first (FOPAIR [1]) is an X-band linear array (Figure 1) that is used for studying ocean wave phenomena. The second ,TEP [2] (Figure 2), is an L-band planar array for imaging clear-air turbulence in the atmospheric boundary layer. Each of these systems experiences interference problems differently, and the two systems serve as a test-bed for evaluating the potential performance gains that are obtainable through adaptive or optimum beamforming.

2. Linear Array Studies Using the FOPAIR System

2.1 Brief Description of the FOPAIR System

The Focused Phased Array Imaging Radar (FOPAIR) uses a 128-element linear array to form images of the ocean surface at near grazing angles. The system functions as a pulse-doppler radar, illuminating a large swath of the ocean surface (+/- 16 degrees about array broadside) with a single transmit antenna and measuring the scattered return coherently at each of the 128 receive antennas. These complex signals are digitized and used to form a large number of simultaneous beams at each range gate, breaking the image up into pixels.

A typical returned intensity image formed by this system has a fairly limited dynamic range. However, several cases arise in which the returned intensity is such that image distortions occur. The first case of interest is when a large scatterer such as a boat or a buoy is present in the image. These objects present a large return to the array (with respect to the ocean-scattered return), and ‘paint’ onto other pixels in the same range gate through sidelobe leakage (Figure 3a). A similar effect may be seen when breaking waves are present in the image, and the specular reflection from the wave face produces an impulsive response at the array (i.e. a “sea spike”). The breaking wave response is often simultaneously present over several beamwidths in the image, making cancellation a difficult problem. Finally, even when the intensity image does not show significant degradation due to interference, the pulse-pair processing used by the FOPAIR system to estimate mean doppler velocity can be highly biased by interference leaking though the sidelobes of the array.

In all of these situations, the dynamic range of the system is being fundamentally limited by the array sidelobes. When the scene generates returns with a larger dynamic range than the peak sidelobe level of the array response, significant degradation of the image may result. By using adaptive or optimum array processing instead of conventional weight-and-sum type beamforming, it is

hoped that the array's degrees of freedom can be more efficiently utilized, and the dynamic range of the system can be increased.

An important limitation that is immediately evident when attempting to apply adaptive processing techniques to FOPAIR data is the fact that the scene changes fairly rapidly, so only 32 to 128 independent samples are available at each pixel before the ocean structures move through the pixel. Since the fastest adaptive algorithms require a number of samples greater than twice the number of degrees of freedom, it clear that a fully adaptive processor is not practical, and sub-optimal techniques must be considered.

2.2 *Outline of Processing Steps*

The basic problem is to chose a limited number of the available degrees of freedom and, assuming that this limited set of signals adequately represents the dominant interference sources, to adapt the array response such that the interference return is minimized. The flow diagram of the algorithm that we have implemented is shown in Figure 4, and it represents a beamspace partially adaptive nulling routine[3]. A number, N (N =number of array elements), of simultaneous beams are formed using a simple FFT processor. From these beams, we choose the M beams with largest intensity for adaptive processing. The number M is chosen to be approximately 1/3 the number of available samples to ensure

convergence. The algorithm then proceeds as a constrained power minimization problem [4] and can be represented as follows:

Denote the complex adaptive beam weights as the column vector

$$\mathbf{w} = [w_1 \quad w_2 \dots \quad w_M]^T$$

and the associated complex beam outputs can be written as:

$$\mathbf{b} = [b_1 \quad b_2 \dots \quad b_M]^T.$$

The output of the desired beam and its associated (and fixed) weighting coefficient are given respectively as:

$$\begin{aligned} b_o &= \text{desired beam output} \\ w_o &= \text{desired beam weight} \end{aligned}$$

In these equations, the superscript ‘T’ denotes transpose, ‘*’ denotes conjugate, and ‘H’ denotes conjugate transpose.

The output of this processor is then given by the complex scalar

$$y = w_o^* \cdot b_o + \mathbf{w}^H \cdot \mathbf{b}$$

The total output power, the expected value of $|y|^2$, is then minimized subject to the constraint that the desired beam coefficient, w_o , is held constant. The solution to this problem is a common result [3] and is given by

$$\mathbf{W}_{\text{opt}} = -\mathbf{R}_{bb}^{-1} \cdot \mathbf{r}_o \cdot w_o,$$

where \mathbf{R}_{bb} is the $M \times M$ correlation matrix of the M complex beam outputs,

$$\mathbf{R}_{bb} = E[\mathbf{b} \cdot \mathbf{b}^H],$$

and r_o is defined as

$$\mathbf{r}_o = E[\mathbf{b} \cdot b_o].$$

A simple block average in time is used to estimate \mathbf{R}_{bb} , and the SMI technique[5] is then used to compute the optimum weight vector. The beamwidth of the FOPAIR array is quite narrow ($\sim 0.25^\circ$), and the single main beam constraint is usually all that is necessary to maintain well formed main beams in the majority of the pixels. This is true mainly because the interference is present only in the sidelobe regions of most of the beams, well away from the steering direction of the desired beam. Multiple linear constraints are easily implemented [4] to improve main beam shape for beams with interference near to the steering direction.

Care must be taken when adapting beams near to strong interference sources, as strong desired returns may leak into neighboring beams. This leakage may be used by the processor to cancel part of the desired signal. Although it has not been implemented as an entirely automated process, we have used analysis of the spatial covariance matrix \mathbf{R}_{bb} to help identify this problem and to aid in a better selection of adaptive beams. In cases where the dominant interferers are nearly point-source in nature, the eigenvalues of \mathbf{R}_{bb} will correspond to the powers of the individual interference sources. If it is suspected that desired signal is leaking into the adaptive beams, one could examine the eigenvalues of the $M-1 \times M-1$

covariance matrices formed using all combinations of $M-1$ of the M beams chosen for adaptation. By determining how the eigenvalues change with varying choice of adaptive beams, one may determine which beams are contributing to which eigenvalues, and therefore which beams are being influenced most strongly by which interference sources. This information can be used in turn to allow a better utilization of the adaptive degrees of freedom. For example, consider an 64-element fully adaptive beamspace processor with a single narrowband interference source incident on the array from 3 degrees from the broadside direction (to account for the issue of orthogonal beams). Uncorrelated white noise is also assumed present at each element. Figure 5 plots the eigenvalues associated with the 63×63 covariance matrix formed by removing one beam at a time from the processor. The x-axis represents the removed beam, and the y-axis represents the magnitude of the eigenvalues. Each plot on this graph represents the variation of the one of the eigenvalues with respect to the choice of adaptive beams. Although there is only one source present, it is clear that the beams around the broadside direction contribute to the dominant eigenvalue due to the interference source leaking into these other beams through their sidelobe responses. These beams may have been chosen for adaptation on the basis of their received power, but will all be used to null a single interference source. On the basis of the previous eigen-decomposition, however, we can remove these beams from the processor, and

permit them to be used for other interference sources, if necessary. The work in [3] is similar to this in that it uses a threshold on the eigenvalue magnitudes to decide if they are true interference contributions or leakage and noise contributions. A pseudo-inverse technique is then used to form R_{bb}^{-1} using only the dominant eigen-components. We have found that this threshold is difficult to set accurately when the data contains multiple strong interference sources of varying power. Choosing a threshold based on the largest source's leakage potential (for example, 10dB below the peak received power) may filter out significant, but smaller, sources. On the other hand, choosing a lower threshold to permit smaller source contributions may permit the leakage from the larger source to use up degrees of freedom unnecessarily. We are continuing to work on a more automated way of implementing these ideas.

2.3 *Typical Results*

The above techniques were applied to experimental data from the FOPAIR system, and typical image results are shown in Figure 6a and Figure 6b. Figure 6a is an intensity plot produced using a FFT beamformer with a 30dB Taylor weighting applied to the aperture. Ocean wave structure is evident in the lower right portion of the image, while three dominant sources (returns from a measurement tower and buoys) are located near the top left of the scene. The

sidelobe leakage into other azimuthal bins around these sources has significantly degraded the image. Figure 6b illustrates the adaptively beamformed version of the same data set. Significant improvement has been made by using only 8 adaptive beams and 32 samples. The dominant sources are now well localized, and the remainder of the image is no longer distorted. Figure 7 examines in detail the range gate with the largest source. The adaptive processing retains the details of the scene, and permits a significantly larger dynamic range in the scene than that obtainable through conventional beamforming.

2.4 *Comments*

As a final note, it should be pointed out that the techniques described thus far are not truly optimal. The question of which beams are chosen for adaptive weighting was answered by using a simple threshold detector based on the received power, and the problem of how to optimally chose a limited number of adaptive degrees of freedom from a fully adaptive set remains largely unanswered. This is particularly true if one additionally includes a limitation on the number of available independent sample that are available to the algorithm. The work in [6] and [7] represents important contributions to resolving this issue, but both approaches require more information or assumptions about the signal environment than can be practically satisfied. Also, the present implementation of the processing requires significant operator intervention to identify signal cancellation

and similar phenomena. Comparison of the adaptive nulling results to simple FFT images and associated array patterns yields important clues for the operator, and use of the eigen-structure of the covariance matrix is a useful tool (see also [3]), but, again, these are non-optimal solutions and are certainly not efficient to implement. These kinds of issues are fundamental to the application of adaptive nulling techniques to real systems, and provide interesting (and challenging) problems for future work in the area.

3. Planar Array Studies Using the TEP System

3.1 Brief Description of the TEP System

The Turbulent Eddy Profiler (TEP) (Figure 2) uses a 90-element hexagonal array operating at 915 MHz to form images of clear air turbulence in the atmospheric boundary layer. The system functions as a pulse-doppler radar, illuminating a large conical volume looking straight up from the ground (+/- 12.5 degrees about array broadside) with a single transmit antenna and measuring the scattered return coherently at each of the 90 receive antennas. These complex signals are digitized and used to form approximately 50 simultaneous beams at each of 64 range gates, breaking the image up into pixels roughly 30 x 30 x 30 m at a range of 500m.

The returned signal from the atmosphere is very small in magnitude, and is easily dwarfed by returns from ground clutter, particularly at lower range gates. Furthermore, the small doppler velocity typical of the atmospheric return often results in the target and interference temporal spectra overlapping. Thus, frequency filtering is a problem, and we must rely heavily on spatial information to act as a discriminant between signals.

3.2 Processing Overview

Several difficult problems are presented to the signal processor by the interference environment experienced by TEP. Ground clutter is inherently a distributed phenomenon, implying that we would like the array to produce a low-sidelobe response over broad angular regions. In the TEP application, the interference is incident on the array from near endfire from a wide range of azimuth angles. The TEP receive array is nearly 25 wavelengths across, but the ultimate receiver bandwidth (+/- 100Hz at baseband) is extremely narrow, and bandwidth is not expected to be an issue for this adaptive processor [8].

Information particular to the TEP system can be used to mitigate some of these issues, however. First, we will assume that the ground clutter has a zero-mean temporal spectra. We can therefore implement a digital filter to eliminate all zero-doppler signals (e.g. returns from fixed object such as buildings), before

doing adaptive beamforming. This allows the adaptive processor to focus on moving clutter, such as wind driven vegetation. Second, we know that the ground clutter of interest is moving, but generally fixed in location (e.g., trees). Therefore, we can obtain a large number of independent samples of the interfering signals without worrying about any migration of the sources in range. The entire array can therefore be used for adaptation. Finally, the interference environment is not likely to change significantly in time, so the adaptive weights can be generated once and used for the remainder of the imaging time, essentially implementing a clutter map.

The derivation of the adaptive weight vector follows exactly that of Section 2, except that we may now allow the number of adaptive degrees of freedom (M) to equal the total number of beams (N). (Note that an N -element array can be combined to produce at most N independent beams).

3.3 *Sample Results*

The TEP system is undergoing final engineering tests this summer, and the calibration of the large, upward-looking receive array has not yet been adequately validated. Experiments are currently underway to improve our understanding of the system and the practical limitations that it may place on the adaptive processor.

Preliminary application of the techniques described above to simulated data has demonstrated only limited success ($\sim 2\text{-}3\text{dB}$ improvement in clutter rejection over conventional beamforming techniques). Clutter that is distributed all about the array in azimuth decorrelates quickly from element-to-element, and appears as uncorrelated noise in the covariance matrix estimate. The array therefore has a difficult time nulling the clutter even though it is present over only a small range of elevation angles.

Assuming zero bandwidth signals and that signals from different directions are mutually uncorrelated, the element-space spatial correlation matrix is given by

$$R_{m,n} = \int_{\phi_1}^{\phi_2} \int_{\theta_1}^{\theta_2} P(\theta, \phi) \cdot \exp(j \cdot 2\pi \cdot k \cdot (\mathbf{S}_m - \mathbf{S}_n) \bullet \boldsymbol{\alpha}) \cdot d\theta \cdot d\phi$$

Where

$P(\theta, \phi)$ = Angular distribution of clutter power

\mathbf{S} = element position vector = $\mathbf{a}_x \cdot \mathbf{X}_{\text{element}} + \mathbf{a}_y \cdot \mathbf{Y}_{\text{element}}$

$\boldsymbol{\alpha}$ = spatial projection vector = $\mathbf{a}_x \cdot \sin(\theta)\cos(\phi) + \mathbf{a}_y \cdot \sin(\theta)\sin(\phi)$

k = propagation constant = $2\pi / \lambda$.

The clutter is assumed to be distributed over the region given by

$$\theta_1 \leq \theta \leq \theta_2 ; \phi \leq \phi \leq \phi_2 .$$

Except in the case of uniformly distributed clutter ($P(\theta, \phi) = \text{constant}$), this expression can be difficult to evaluate analytically, so we have proceeded with Monte-Carlo type simulations.

Figure 8 illustrates some of the performance limits of the proposed processing for clutter distributed over a fixed region of elevation angles and varying ranges of azimuth. Clutter was simulated [9] for a single range gate using a large number (~ 1000) of independent clutter scatterers distributed about the array in azimuth, and the clutter was permitted to have a small doppler spread consistent with measured ground clutter results. The plot shown is an average of 100 trials, and shows the ratio of total received clutter power received by a 30dB Taylor weighted array to that of an adaptively weighted array. It is clear that only small performance gains are achieved when the clutter is distributed over a large number of resolution cells.

We are continuing to investigate the use of adaptive techniques for nulling of distributed clutter. Although initial results do not demonstrate sufficient improvement relative to non-adaptive techniques to warrant the additional computation time, the potential for significantly improved system performance through adaptive clutter suppression motivates further study on this topic.

4 Summary

The data presented here represent a first effort at applying adaptive array processing to actual imaging radar data for the Microwave Remote Sensing Laboratory at the University of Massachusetts. Preliminary results are encouraging and demonstrate that the potential benefit of adaptive beamforming to

actual systems can be significant in some situations. We have shown that practical systems impose many constraints on the processor, however, and many of the classic adaptive nulling techniques must be revisited and reworked with these limitations in mind. The ability to optimally configure a partially adaptive processor based on a limited number of independent samples of the scene remains as a difficult problem. Also, the ability of an adaptive system to deal with large regions of distributed clutter has not been fully investigated and is particularly applicable to ground based imaging radars such as TEP. These issues form the basis for the continuing adaptive array processing work at the University of Massachusetts.

Acknowledgements

The authors gratefully acknowledge the help of Dr. Steve Frasier and Delwyn Moller of the MIRSL at UMass for generously supplying this research with quality experimental data, and for their help in deciphering the contents of some rather large data files.

References

- [1] R.E. McIntosh, S.J. Frasier, and J.B. Mead, "FOPAIR - A Focused Array Imaging Radar for Ocean Remote Sensing", IEEE Trans. Geo. and Remote Sensing, v 33, n 1, Jan. 1995.
- [2] R.E. McIntosh and C.T. Swift, TEP Grant Proposal, July 1991.
- [3] K. Takao and K. Uchida, "Beamspace Partially Adaptive Antenna", IEE Proceedings, Vol. 136, Pt. H, No. 6, December 1989.
- [4] R.A. Monzingo and T.W. Miller, *Introduction to Adaptive Arrays*, Wiley Interscience, New York, 1980.
- [5] I.S. Reed, et. al., "Rapid Convergence Rate in Adaptive Arrays", IEEE Trans. on Aerospace and Electronic Systems, AES-10, n 6, Nov. 1974.
- [6] S. Haykin and A. Steinhardt, *Adaptive Radar Detection and Estimation*, Chapter 4, Wiley Interscience, New York, 1992.
- [7] J. Goldstein and D. Williams, "Optimal Partially Adaptive Sensor Array Processing", IEEE Ant. and Prop. Symposium Digest, 1995.
- [8] R. Compton, Jr, *Adaptive Antennas*, Prentice Hall, New Jersey, 1988.
- [9] R. Mitchell, *Radar Signal Simulation*, Artech House, Massachusetts, 1976.

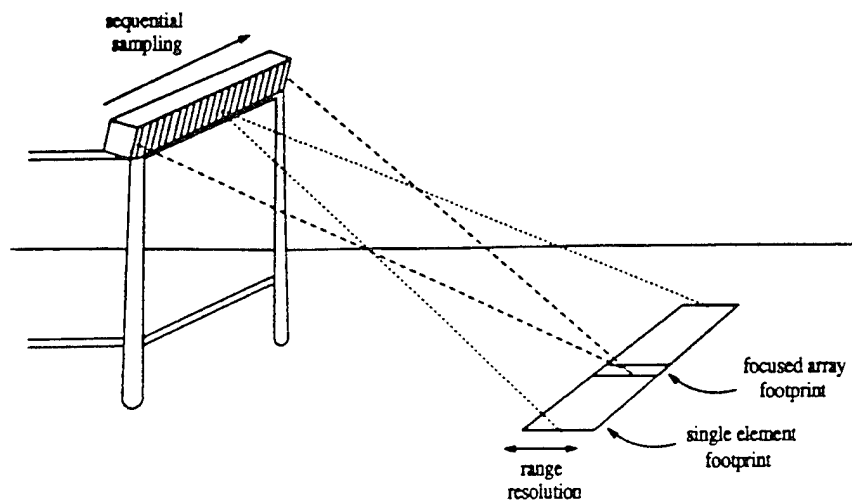


Figure 1. Conceptual diagram of the FOPAIR system [1]

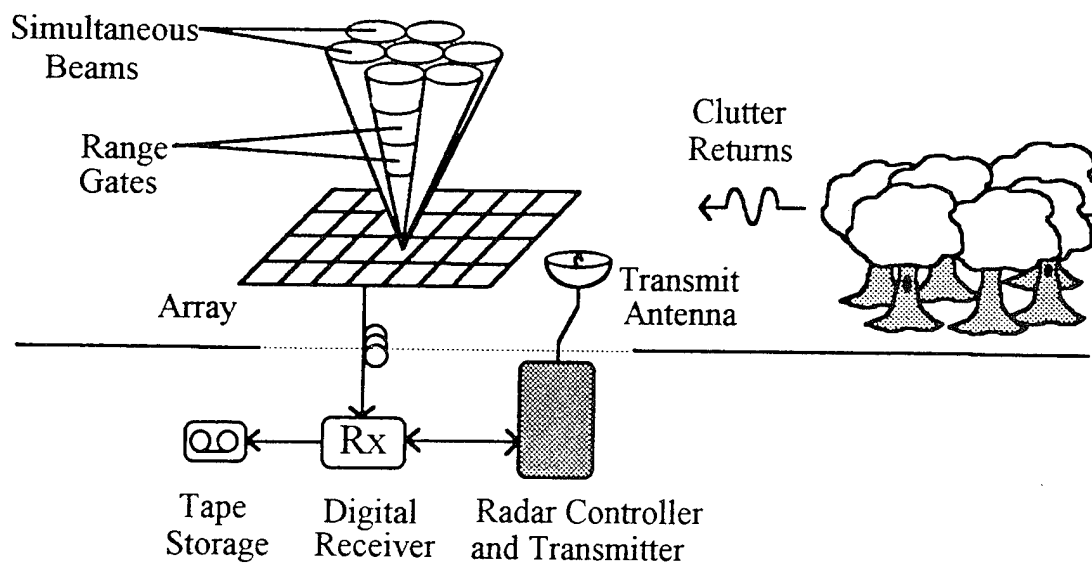


Figure 2a. Conceptual diagram of the TEP System

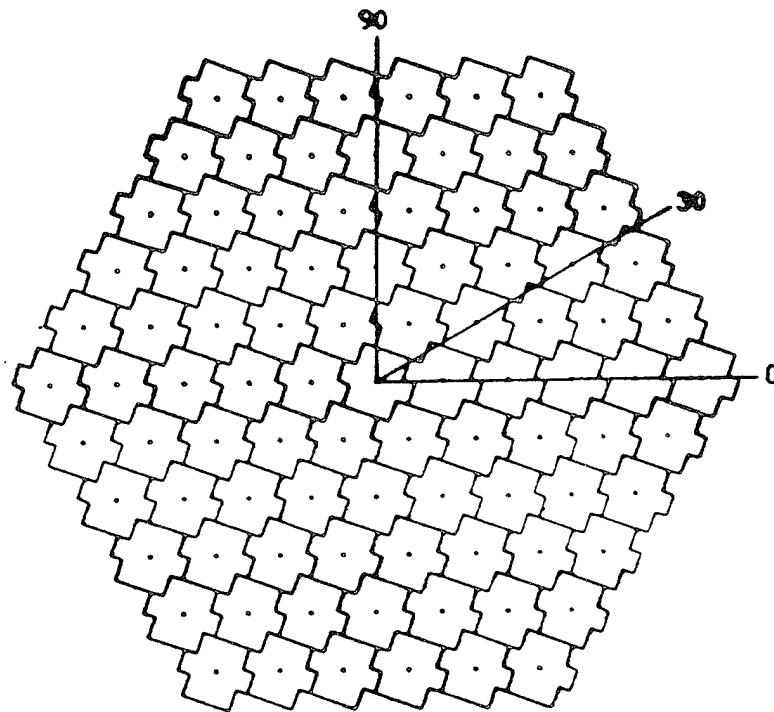


Figure 2b. 91-Element TEP Phased Array Layout

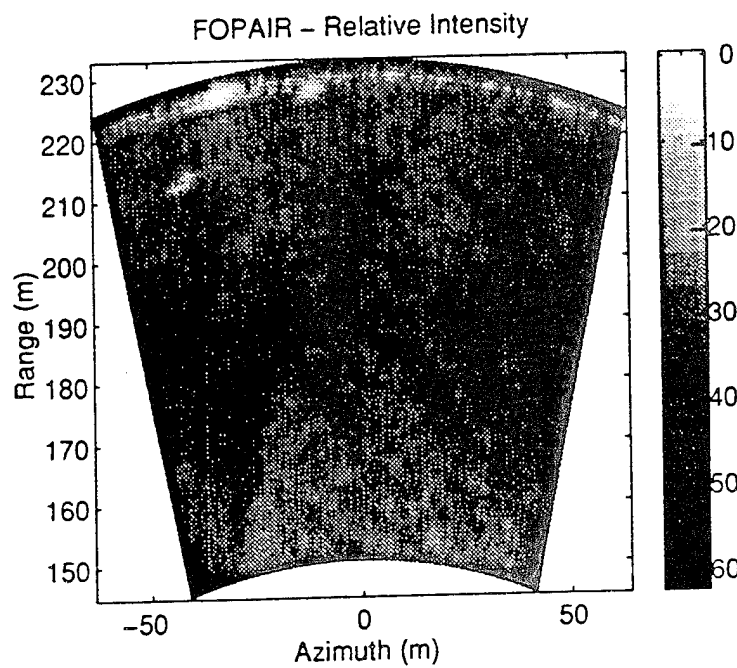


Figure 3. Typical FOPAIR Intensity Image - Point interference in top left of image

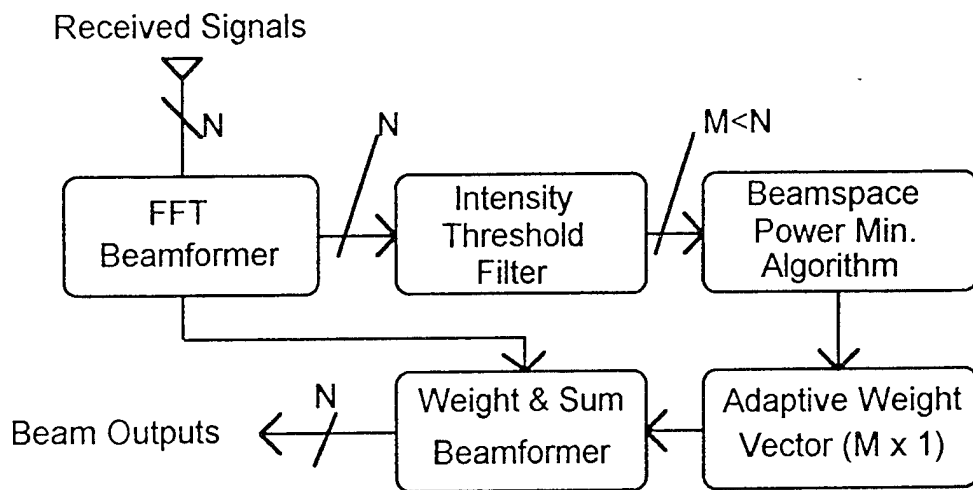


Figure 4. Adaptive Processing Flow Diagram (FOPAIR Application)

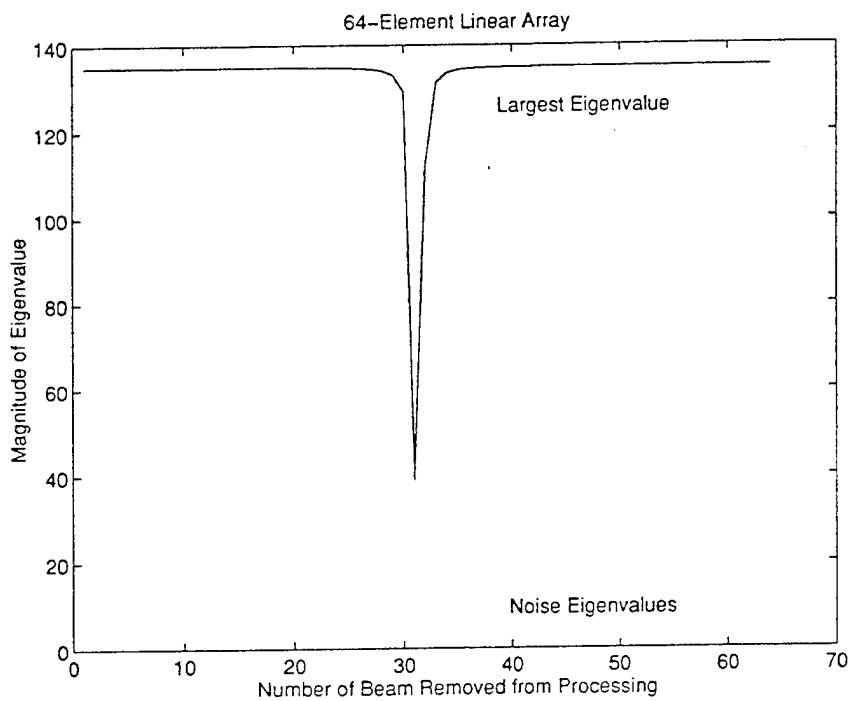


Figure 5. Eigenvalue plot - 64 element linear array, 0.5 w.l. spacing
Single jammer present at 3 degrees off broadside (SNR=40dB)

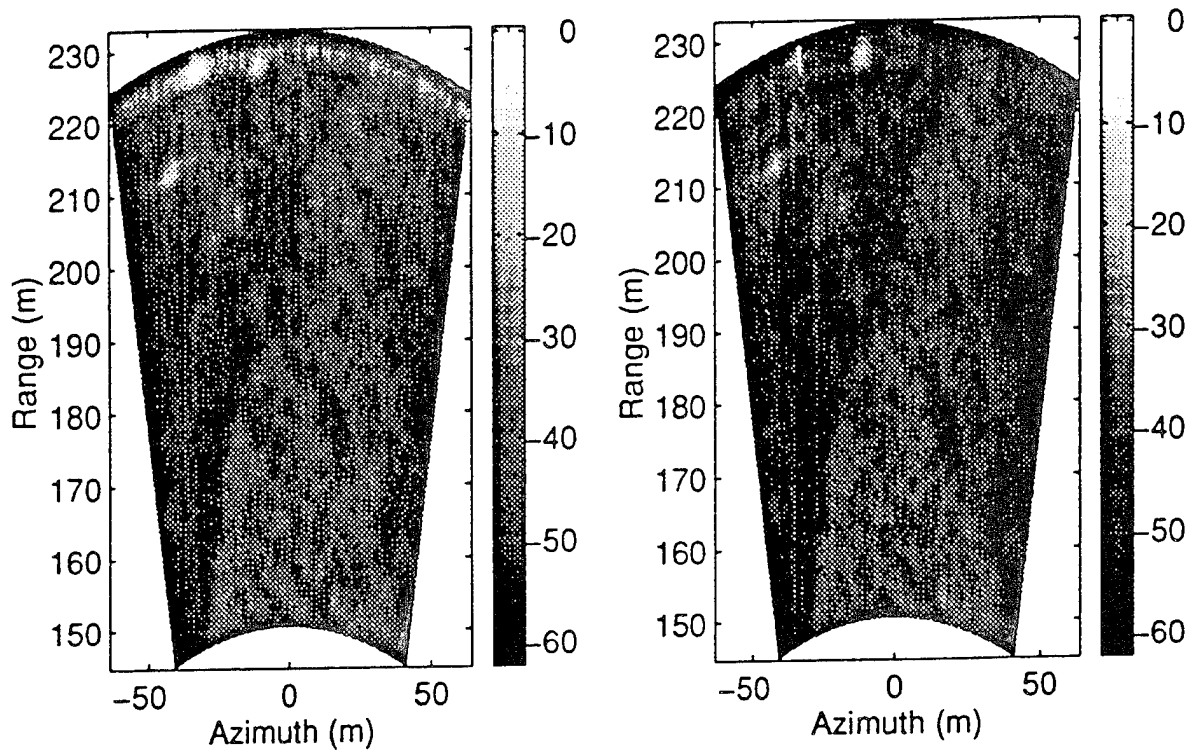


Figure 6a/b. FOPAIR Intensity Images
 6a) 30dB Taylor weighted array response 6b) Adaptively weighted response

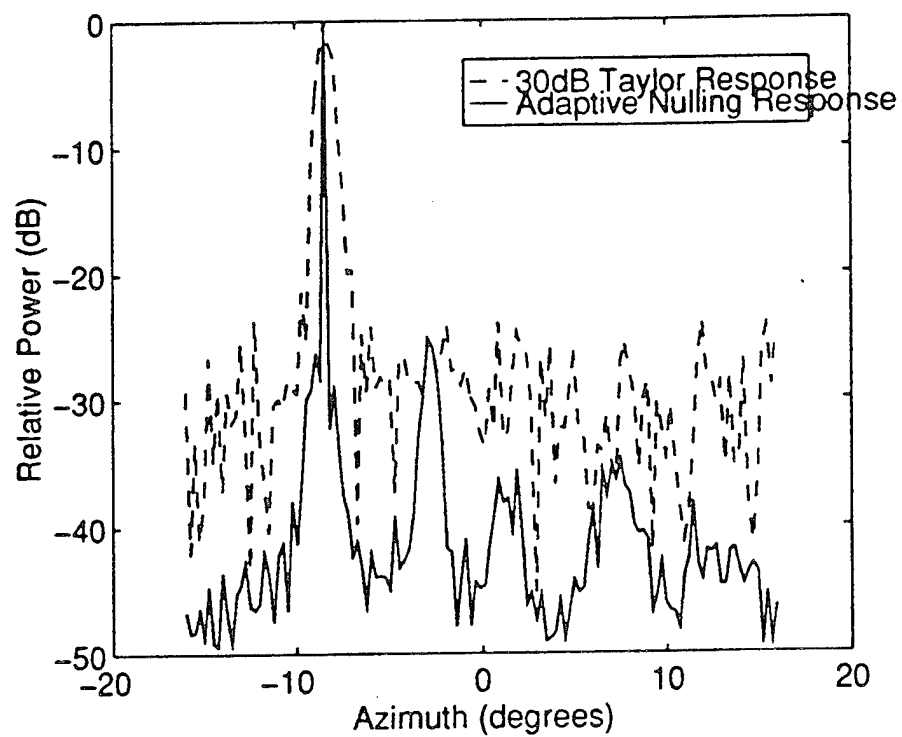


Figure 7. Detail of range gate #55 from Figure 6.

Neural Network Beam-Steering for Phased-Array Antennas

Hugh Southall, Scott Santarelli and Edward Martin

USAF Rome Laboratory

Electromagnetics and Reliability Directorate

RL/ERAA, 31 Grenier Street

Hanscom AFB, MA 01731

Terry O'Donnell*

ARCON Corporation

260 Bear Hill Road

Waltham, MA 02154

Abstract

A radial basis function (RBF) artificial neural network was developed with output nodes which set phase shifters to steer the main beam of an eight element, linear, phased-array antenna. Each element is an open-ended waveguide with a ferrite phase shifter which is set by an eight bit digital word. The neural net is trained at discrete angles within the antenna field of view. We present experimental results and theoretical predictions.

1 Introduction

Previously, we described RBF neural beamformers for single source direction finding (DF) [1, 2, 3, 4] and detection [5]. Current research is on the control of the radiation pattern of a phased-array antenna using neural network techniques (reported here) and genetic algorithm techniques (reported in a companion paper [6] in this proceedings). In the present paper, we describe a neural network which computes the element phases required to steer the array main beam to any angle in the antenna field of view (typically $-60^\circ \leq \theta \leq +60^\circ$). This relatively simple, but useful, task is a first step in developing intelligent control algorithms for phased-array antennas, including operation with degraded or failed elements, conformal geometries and non-ideal environments with near field scattering.

*Work performed under USAF Contract #F19628-92-C-0177.

The paper begins with a description of the experimental antenna. Next, we describe the network architecture and training technique. Finally, we present theoretical and experimental results and conclude.

2 Description of the Experimental Phased-Array Antenna

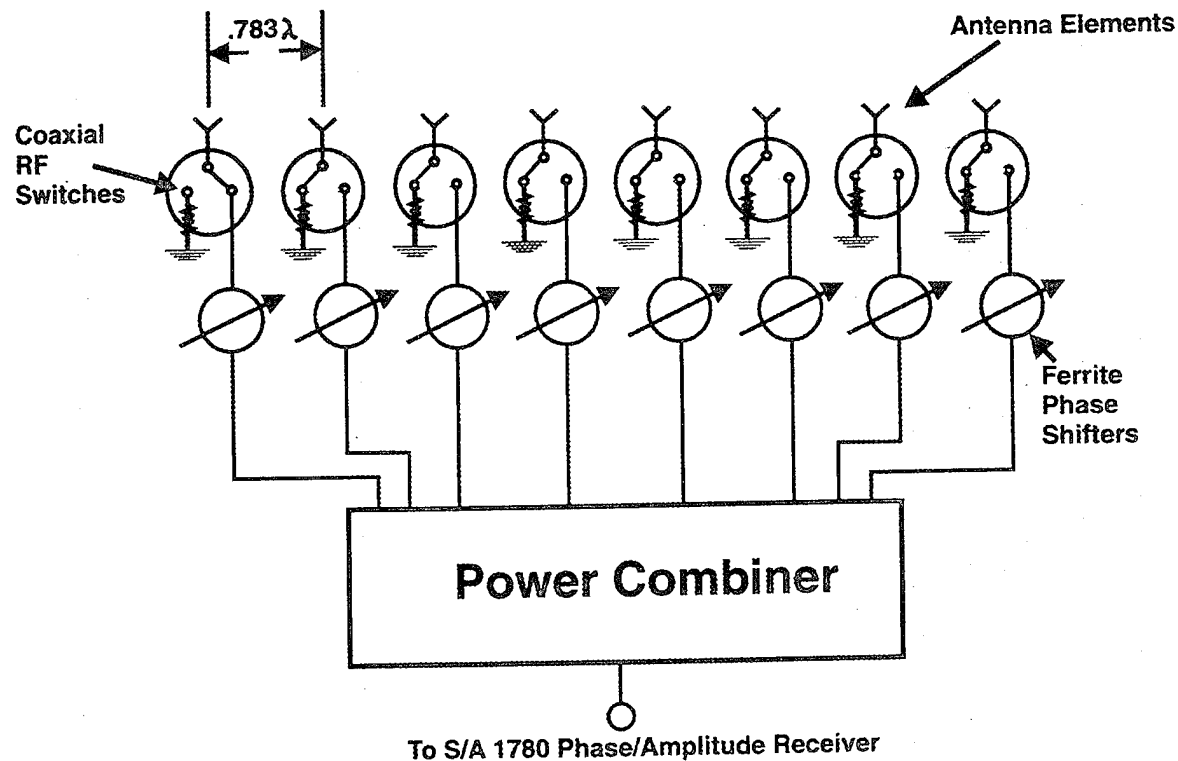


Figure 1: Array architecture

Our experimental antenna is a C-band (7.1 GHz), eight element, linear array of open-ended waveguides with ferrite phase shifters as shown in Figure 1. Due to mechanical considerations, the elements had to be separated by 0.783λ . Measurements were taken with the array in an anechoic chamber as shown in Figure 2. The array rotates in front of a stationary source horn located 12 feet away.

With all eight coaxial RF switches connected to the antenna elements, the feed is an analog beamformer with a single output port going to a Scientific Atlanta 1780 phase/amplitude receiver. We can then measure array patterns. Individual elements are connected to the receiver as shown in Figure 1 where the left-most element is connected. We can then measure element patterns. The phase and amplitude response of each element (including the cumulative effects of coaxial feed lines and the power combiner) is measured as the array rotates

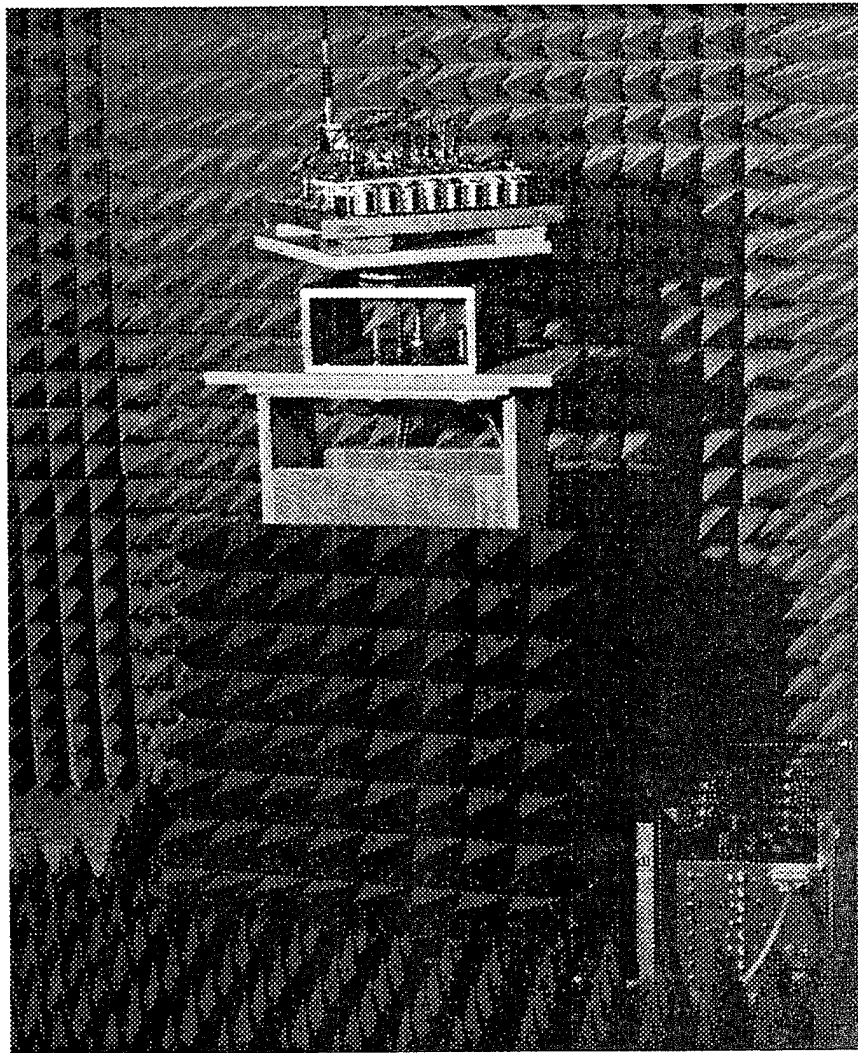


Figure 2: Experimental phased-array antenna in the anechoic chamber. The phase shifter drivers are in the box in the lower right.

from -90° to $+90^\circ$. Measured element phase is the useful information for training our neural network to perform the beam-steering function.

We control only the phase shift in each element channel. The phase shifters are axial-field, ferrite phase shifters (see Figure 3) and, at 7.1 GHz, provide 360° of insertion phase. The amount of phase shift is determined by the current through the magnetic coil which is set by the voltage output from a digital to analog (D/A) converter in the phase shifter driver. An eight bit word is sent to the D/A from our PC controller, therefore, we can set 256 states (0 to 255) corresponding to insertion phases between 0° and 360° .

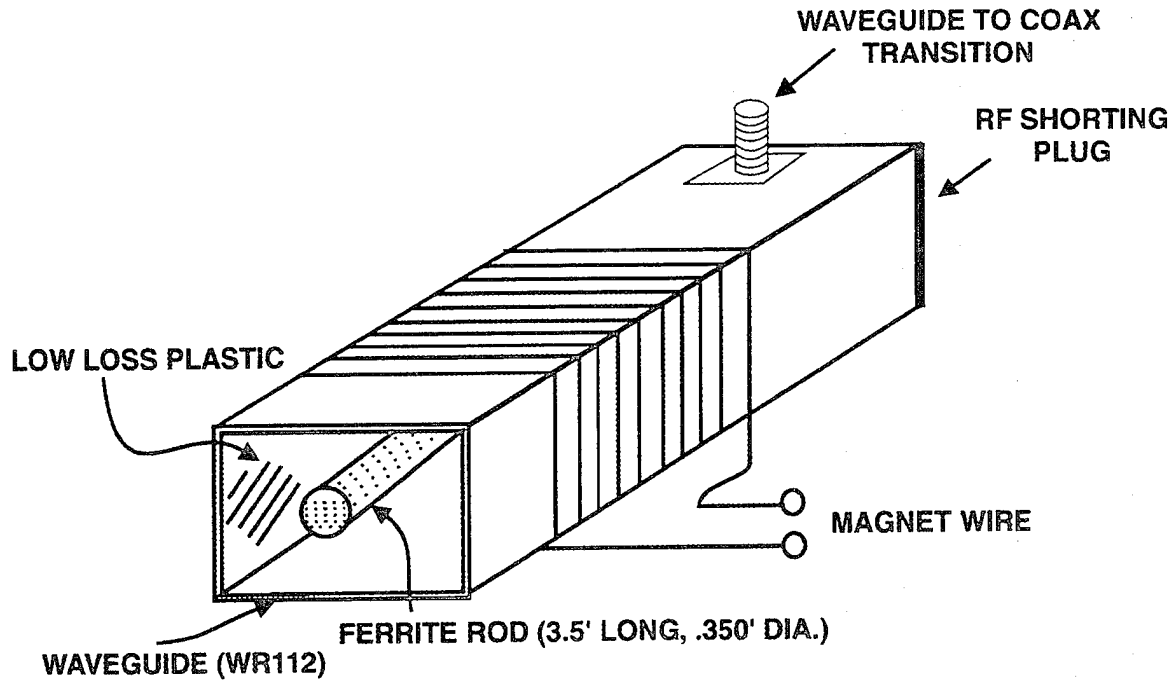


Figure 3: C-band Reggia-Spencer type, axial-field, reflective ferrite phase shifters

3 Neural Network Beam-Steering

The architecture of the neural network beam-steering system is shown in Figure 4. The network input is the commanded beam-steering (or scan) angle. The Gaussian RBF nodes have centers in the input space of commanded steering angles. Network outputs are phase differences. Postprocessing automatically converts the phase differences to eight digital states (eight bit words) to set the phase shifters to steer the main beam to the commanded angle.

The role of the network is function approximation [7, 8]. To effectively perform its task, the network is trained using a process called supervised learning. We present the network with beam-steering angles and corresponding “target” or “desired” output vectors. Each target vector consists of the negative of the seven measured phase differences. Negative values are used so we can apply the conjugate phase gradient. The network is “trained” at these angles to output the target vector, and, hopefully, has learned to generalize and accurately steer the beam between training angles.

The RBFs used in the hidden layer nodes (nodes with RBF centers indicated in Figure 4) are Gaussians. The output of the i th Gaussian for steering angle θ is

$$\phi_i(\theta) = e^{-\frac{(\theta-\theta_i)^2}{2\sigma^2}}, \quad (1)$$

for $i = 1, 2, \dots, t$. There are t training angles in the input space. The θ_i are the Gaussian centers in the input space, and σ is the RBF spread parameter.

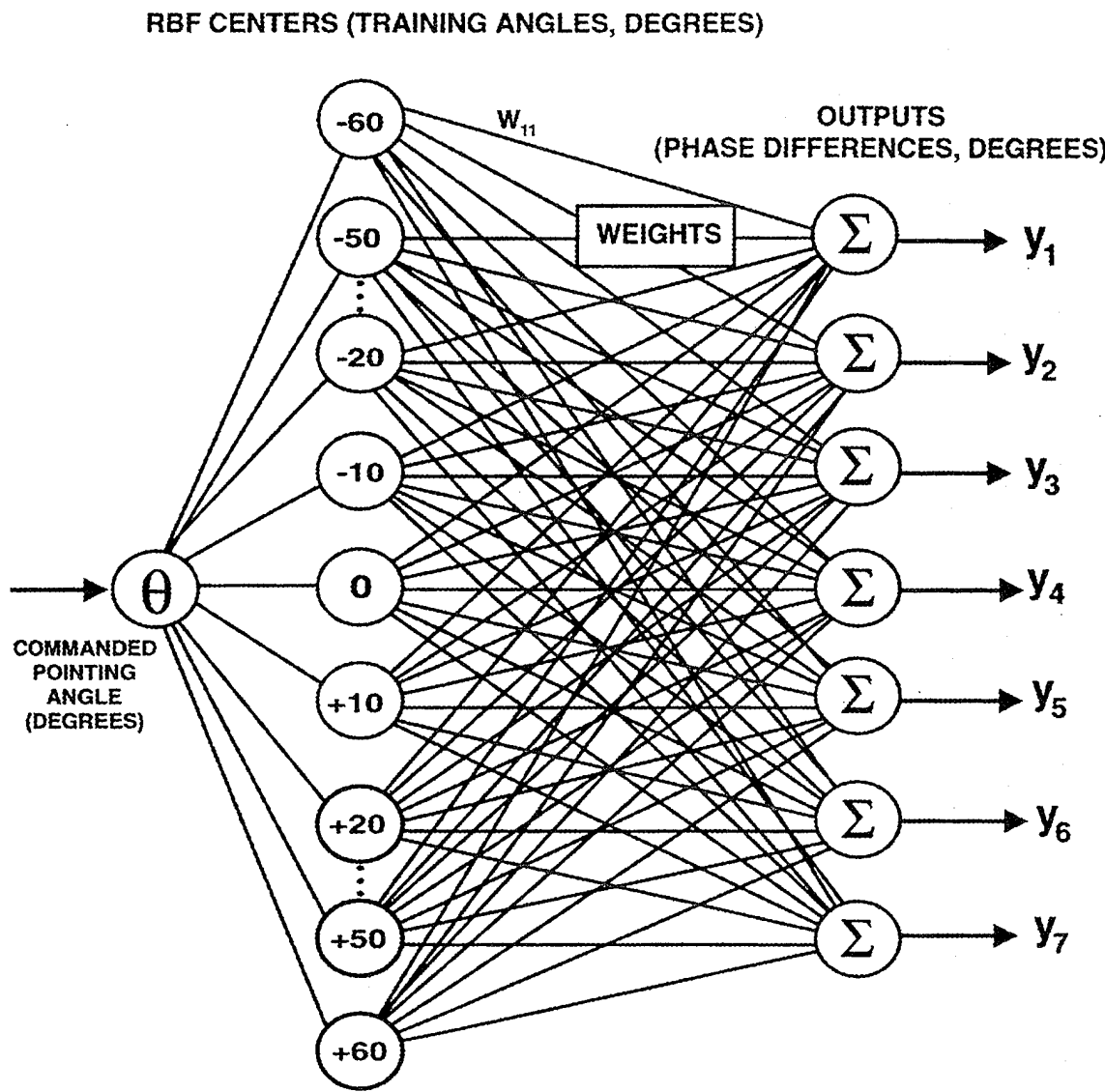


Figure 4: RBF Neural network architecture

A general rule of thumb for determining σ is that it should not be much smaller than the distance between training angles, nor should it be very much larger than this distance. In other words, the Gaussians should overlap sufficiently for generalization between training points, but not be so broad that their responses are the same and the capability for generalization is lost. The j th component of the output vector, y_j , for $j = 1, 2, \dots, 7$, is computed as a weighted sum of hidden layer node outputs, i.e.

$$y_j = \sum_{i=1}^t \phi_i(\theta) w_{ij}. \quad (2)$$

To solve for the network weights, w_{ij} , we define an interpolation matrix, Φ , whose elements are given by

$$\phi_{ki} = e^{-\frac{(\theta_k - \theta_i)^2}{2\sigma^2}}, \quad (3)$$

where k and $i = 1, 2, \dots, t$. Next, define a “desired” output matrix Y_d whose rows are the target output vectors. We can write the relation between Y_d , Φ , and the matrix of network weights W as a linear system.

$$Y_d = \Phi W \quad (4)$$

In our case, Φ is square and positive definite (invertible), therefore, we can solve for the weights from

$$W = \Phi^{-1} Y_d \quad (5)$$

to complete the training process. The network has then learned the function and we can calculate predicted output vectors for any N commanded scan angles θ_n , for $n = 1, 2, \dots, N$. We now define a performance matrix $\tilde{\Phi}$ whose elements are calculated from

$$\tilde{\phi}_{ni}(\theta_n) = e^{-\frac{(\theta_n - \theta_i)^2}{2\sigma^2}}, \quad (6)$$

where $i = 1, 2, \dots, t$. Note that θ_n must be within the antenna field of view, or, in neural network parlance, the trained region. Output matrix, Y , is calculated from

$$Y = \tilde{\Phi} W, \quad (7)$$

where the n th row of Y is the network output vector corresponding to commanded scan angle θ_n .

4 Results

To train the network, we obtain training vectors by measuring the phase response of each element as described earlier. This data is shown in Figure 5 without the $\pm\pi$ transitions introduced by the receiver. The phase data has been unwrapped using our Matlab data analysis software, making it easier to see phase differences between elements. For example, to find the seven phase differences at a -60° training angle, just draw a vertical line up from -60° and find the difference in phase between successive elements. Note that to the left of

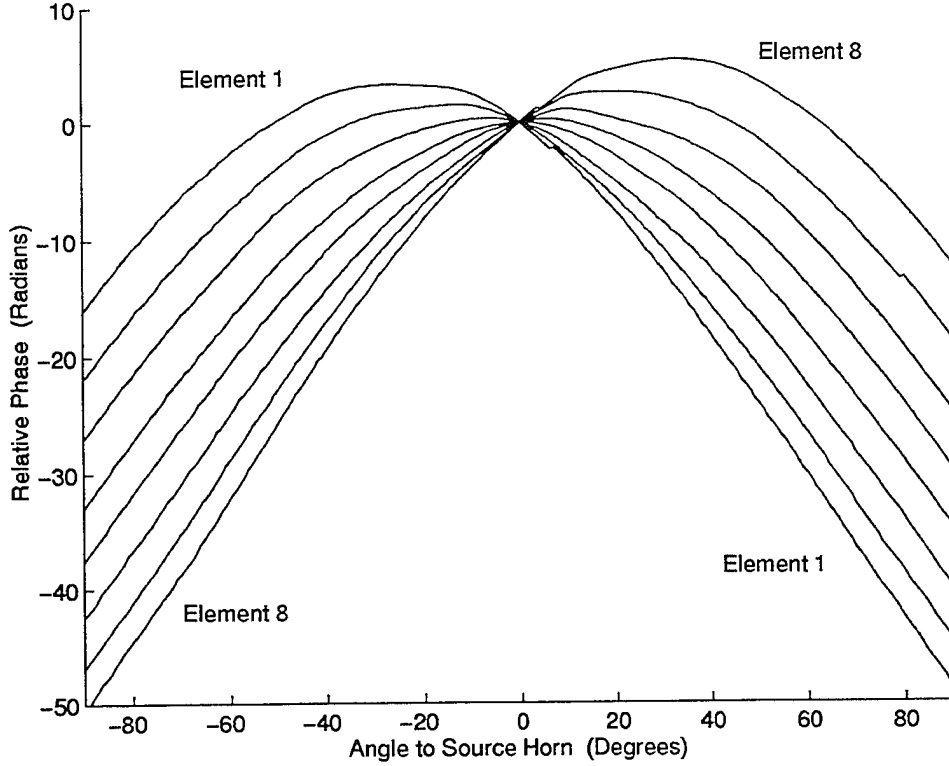


Figure 5: Measured element phases in radians (unwrapped). Note that element numbers are sequential 1 to 8 from top to bottom on the left and sequential 8 to 1 from top to bottom on the right.

0° , the phase difference between elements 7 and 8 is smallest, while to the right, the phase difference between elements 1 and 2 is smallest. Phase differences are negative to the left of 0° and positive to the right. We define phase difference as the phase of element $m + 1$ minus the phase of element m . Also, note that the seven phase differences are not the same for a given far field angle as would be the case for a plane wave hitting an ideal array of identical elements.

The phase differences are zero at 0° since the plane wave from the source horn hits the array broadside. However, this condition occurs only after we remove the measured broadside phases (which we call “offset” or correction phases) due to the insertion phases in the different coaxial line lengths and the power combiner in each of the eight element channels. For this commercial power combiner, typical phase imbalance is $\pm 12^\circ$. Phase imbalance due to line lengths are much larger, since no special attention was paid to phase-matching.

After we removed the offset phases with the phase shifters, we measured an antenna pattern and obtained the broadside beam shown in Figure 6(a). The higher sidelobes for the measured pattern are due to the amplitude taper induced by setting the phase shifters. The received amplitude as a function of phase state is highly nonlinear and can vary by as

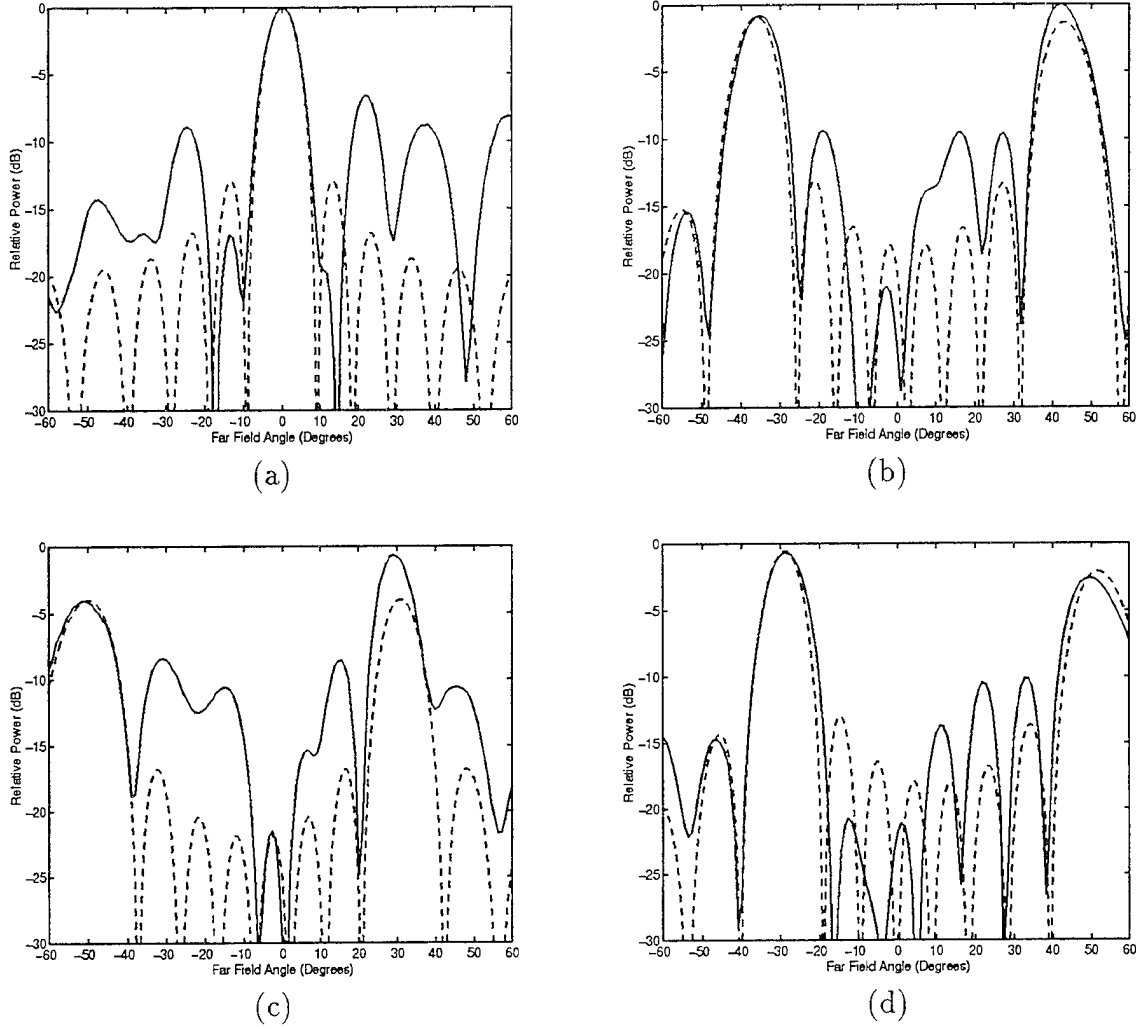


Figure 6: Scanned antenna patterns: (a) Broadside with offset phases removed. (b) Training angle, -36.37° . (c) Training angle, -50° . (d) Network-predicted angle between training angles, -29.1° . Patterns for an ideal, uniformly-illuminated array with linear phase progression for beam-steering are shown as dashed curves. The peak of the ideal main beam has been normalized to be the same as the peak of the measured main beam.

much as 8 dB over the 256 states of a single element and by more than this from element to element. We have no control over this and simply set phase shifters for beam-steering and let amplitudes fall where they may. The genetic algorithm approach [6] attempts to optimize antenna patterns using both phase settings and the induced amplitude changes.

We steer the beam by applying the conjugate phase gradient at the commanded steering angle. To accomplish this, the network outputs the negative of the seven measured phase differences at the training angles. Between training angles, the network produces an approximation based on its generalization capability. In postprocessing, the phase differences are converted to element phases (modulo- 2π) by making element one the Reference (zero phase).

These “beam-steering” element phases are combined with the offset phases on an element by element basis to obtain total phase at each element. Care must be taken in combining the two phases. In particular, the two phases must be summed at each element for positive steering angles and subtracted for negative ones.

To obtain the digital state to send to the phase shifter driver, we use a calibration look up table of digital state (0 to 255) versus phase shift (0° to 360°) for each element. The digital state versus phase shift is a highly nonlinear function for our phase shifters. To illustrate the process, suppose element three requires 57° of phase shift. Postprocessing finds the calibration table for element three and looks up the digital state giving a phase shift closest to 57° , with a typical accuracy of $\pm 2^\circ$.

In the remainder of Figure 6, we show scanned antenna patterns for three commanded steering angles. The main beam is always to the left of 0° , while the right beam is a grating lobe due to the large element spacing. The scan angles in Figure 6(b) and (c) are for training angles of -36.37° and -50° . Figure 6(d) shows a pattern for a scan angle of -29.1° which is between training angles. Measured steering angles agree with the commanded angles within one degree. Angles used for training were approximately every 5° starting at -59.09° and ending at -0.01° . We trained the network on only half the field of view since we only wanted to demonstrate the concept. The angles are not integers because a stepper motor was used to rotate the array and each step turned out to be slightly less than a degree to obtain equal steps from -90° to $+90^\circ$.

Finally, we investigate network performance as σ and the number of training angles are varied. Once the network architecture has been selected, these are the only parameters left to adjust. In Figure 7, we plot the RMS beam-steering error normalized by the broadside 3 dB beamwidth ($\theta_{3dB} \approx 8.1^\circ$). The RMS error is calculated for steering angles from -60° to 0° in 2° increments. The error is the difference between commanded and network-predicted steering angles. There are too many scan angles in this computation to set phase shifters and measure patterns. Therefore, we use element phases predicted by the neural network and mathematically transform to the far field to obtain predicted steering angles. Based on comparisons with measured patterns, steering angles obtained in this manner should be reasonably accurate. Note that there is an optimum σ for each set of training data. For the 5° set, σ_{opt} is about 1.6 times the separation between training angles, and slightly more than twice the separation for the 10° set.

5 Conclusions

We developed a neural network which computes phase shifter settings to perform the beam-steering function. This can be useful where the settings cannot easily be determined, for

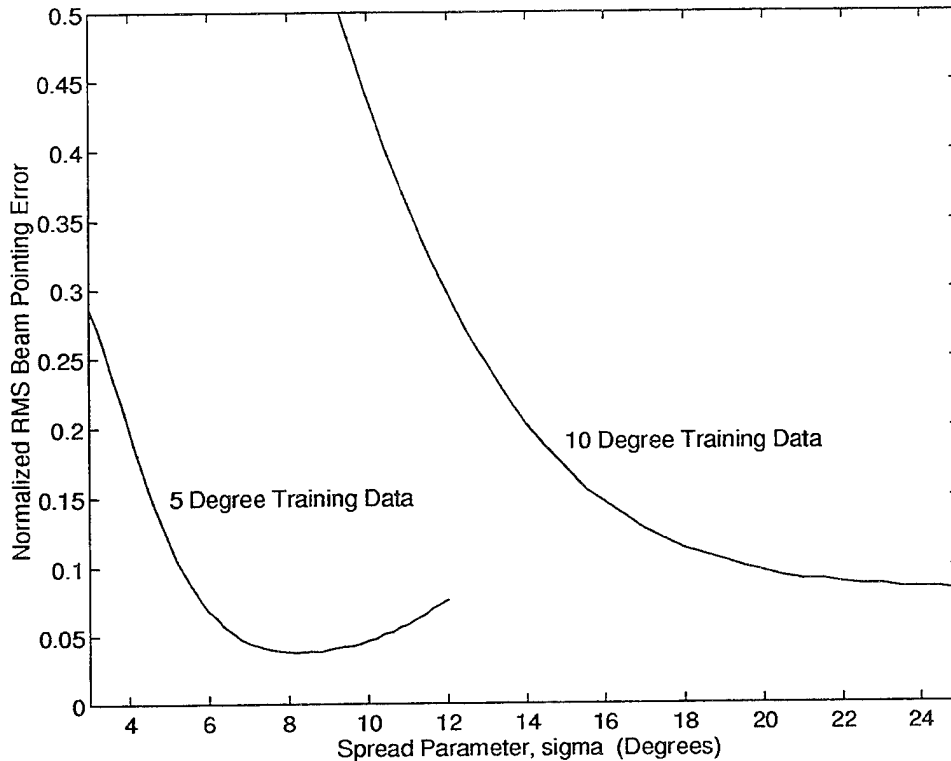


Figure 7: RMS beam-pointing error normalized by θ_{3dB} as a function of σ for two sets of training data. For the 5° data set, there are 14 training angles over the input space and for the 10° data set, there are 7 training angles over the input space.

instance, conformal arrays with near field scattering, or for arrays with degraded or failed elements. The concept was demonstrated experimentally by showing that the network can generalize and accurately scan the beam between training angles. An optimum network spread parameter for a given set of training data was determined. With a normalized RMS steering error of about .04 (see Figure 7), gain loss is less than .02 dB.

6 Acknowledgments

We would like to acknowledge the many helpful discussions with Peter Franchi and Livio Poles of Rome Laboratory concerning array scanning and phase references. The antenna was fabricated by Ed Martin, also of Rome Laboratory. We also acknowledge the software and construction support of Alex Kittenplan of ARCON Corporation and the technician support of Senior Airman Jim Rouse of Rome Laboratory. This research was supported under the Adaptive Optics and Beamforming initiative of the Air Force Office of Scientific Research (AFOSR), Bolling AFB, DC.

References

- [1] J. A. Simmers and T. O'Donnell. Adaptive RBF Neural Beamforming. In *Proceedings of the 1992 IEEE Mohawk Valley Section Command, Control, Communications, and Intelligence (C3I) Technology & Applications Conference*, pages 94–98. IEEE, June, 1992.
- [2] T. O'Donnell, J. Simmers, and D. J. Jacavanco. Neural Beamforming for Phased Array Antennas. In *Proceedings of the 1992 Antenna Applications Symposium (Robert Allerton Park)*, Griffiss AFB, NY, September, 1992. USAF Rome Laboratory.
- [3] J. Simmers, H. L. Southall, and T. O'Donnell. Advances in Neural Beamforming. In *Proceedings of the 1993 Antenna Applications Symposium (Robert Allerton Park), University of Illinois*, Griffiss AFB, NY, September, 1993. USAF Rome Laboratory.
- [4] H. L. Southall, J. A. Simmers, and T. O'Donnell. Phased Array Antennas with Neural Network Signal Processing. In *Proceedings of the 1994 Antenna Applications Symposium (Robert Allerton Park), University of Illinois*, Griffiss AFB, NY, September, 1994. USAF Rome Laboratory.
- [5] T. O'Donnell, J. Simmers, H. Southall, and T. Klemas. Neural Network Antenna Processing for Detection and Direction Finding. In *The Record of the IEEE 1995 International Radar Conference*, pages 213–218. IEEE, May 1995.
- [6] S. Santarelli, H. Southall, E. Martin, and T. O'Donnell. Genetic Algorithm Array Pattern Synthesis. In *Proceedings of the 1995 Antenna Applications Symposium (Robert Allerton Park), University of Illinois*, Griffiss AFB, NY, September 1995. USAF Rome Laboratory.
- [7] M. J. D. Powell. Radial Basis Functions for Multivariable Interpolation: A Review. In J. C. Mason and M. G. Cox, editors, *Algorithms for Approximation*, pages 143–167. Clarendon Press, Oxford, 1987.
- [8] T. Poggio and F. Girosi. Networks for Approximation and Learning. *Proceedings of the IEEE*, 78(9):1481–1496, September 1990.

AIRCRAFT MOTION EMULATION BY AN INVERSE DISPLACED PHASE CENTER ANTENNA

Herbert M. Aumann
Francis G. Willwerth
MIT Lincoln Laboratory
244 Wood Street
Lexington, MA 02173

Abstract: In an airborne radar, the aircraft motion causes stationary ground clutter to be spread over a significant part of the Doppler spectrum, potentially masking the Doppler return from a target. It is difficult to verify the performance of clutter suppression algorithms in such a radar without expensive flight testing. A cost effective technique is presented for producing an airborne radar clutter environment from a stationary, ground-based site.

Displaced phase center antennas have been used on aircraft to synthetically arrest aircraft motion. The present application uses an inverse displaced phase center antenna (IDPCA). By electronically moving the phase center forward, Doppler sidelobes are created that match the sidelobe structure observed by an airborne radar.

A new UHF phased array antenna is described whose phase center can be electronically moved by a switching matrix. Switching is controlled by a stationary surveillance radar. For a 16-pulse coherent processing interval, the array length and column spacing result in clutter returns that span the Doppler space. Examples of emulated clutter motion observed from a mountain top site are presented. The technique's effectiveness was verified by comparing emulated clutter data with data collected by an aircraft flying over the same terrain.

1. Introduction

Without a doubt, successful deployment of an advanced airborne radar will require a great deal of system testing. Since flight testing is very expensive, as much system testing as possible should be carried out on the ground. In this paper an implementation of a ground based aircraft motion emulation will be presented

which is based on an inverse displaced phase center antenna.

The motion emulation goal is to develop a practical, affordable and timely technique for generating signals with the spatial and temporal characteristics of an airborne radar, except that the signals are to be generated from a fixed, land-based site. The ultimate objective is to provide the means for developing and evaluating space-time adaptive signal processing techniques [1, 2] that would be used in a future advanced airborne radar system.

2. Airborne Radar Doppler Spectrum

In order to size the motion emulation task it is necessary to make some assumptions about the airborne radar antenna size and the aircraft motion. One might expect the aircraft motion during a pulse repetition interval (PRI) to be about 0.5 feet, or about a quarter wavelength at UHF, and the aircraft motion during a coherent processing interval (CPI) is of the order of the antenna length, that is about 20 feet. Of course, this length will have a direct impact on the cost of the motion emulation.

It is well known that in an airborne radar, the clutter Doppler return received through the sidelobes may compete with the target Doppler return received through the main lobe [2]. A two-dimensional, spatial and temporal (Doppler) power spectrum provides a convenient way of illustrating this effect. Assume that the transmit and receive antenna consist of an M -element phased array aligned with the aircraft motion. The corresponding antenna patterns, $T(\theta)$ and $P(\theta)$, are given by

$$T(\theta) = \sum_{m=1}^M \exp\left(j \frac{2\pi m}{\lambda} D \sin \theta\right) \quad (1)$$

$$P(\theta) = \sum_{m=1}^M \exp\left(j\frac{2\pi m}{\lambda} D \sin \theta\right), \quad (2)$$

where D is the element spacing, λ the radar wavelength, and θ the angle normal to the flight direction. Furthermore, assume that the aircraft moves a distance d during a PRI. As a result of this aircraft motion, the n -th two-way return from uniform and omnidirectional clutter is proportional to

$$s(\theta, n) \propto \left[T(\theta) \exp\left(j\frac{\pi n}{\lambda} d \sin \theta\right) \right] \left[P(\theta) \exp\left(j\frac{\pi n}{\lambda} d \sin \theta\right) \right]. \quad (3)$$

A discrete Fourier transform (DFT) of N returns yields the Doppler spectrum

$$S(\theta, k) = \sum_{n=1}^N T(\theta) P(\theta) \exp\left[j2\pi n \left(\frac{2d}{\lambda} \sin \theta - \frac{k}{N}\right)\right]. \quad (4)$$

Clutter distributed uniformly over all angles appears as a ridge in an azimuth-Doppler plot [2]. Figure 1 illustrates the situation for a stationary radar. Shown in the azimuth dimension is the main beam and sidelobe structure. Space and time are uncorrelated for a stationary radar. Hence, except for any residue of the weighting function, there are no sidelobe features in the Doppler dimension.

For a moving radar the situation is quite different. Figure 2 illustrates that as a result of the aircraft motion, the same angle sidelobes will now also show up in Doppler space. Neglecting elevation effects, the sidelobe clutter ridge has a normalized Doppler frequency

$$f(\theta) = \frac{2d}{\lambda \text{ PRF}} \sin \theta. \quad (5)$$

In Figure 2, the aircraft motion and pulse repetition frequency (PRF) were chosen so that the maximum clutter Doppler is unambiguous. In other words, the maximum phase shift from pulse to pulse due to aircraft motion is $\pm\lambda/2$ wavelength.

For most radar systems, the Doppler sidelobes are much lower than the angle sidelobes. For example, for an array with uniform illumination on transmit and a 40 dB Chebyshev taper on receive, the angle sidelobes would be about 60 dB down. Doppler sidelobes are usually set by transmitter stability. It would not be very difficult to achieve -80 dB Doppler sidelobes. When the array is stationary, the Doppler sidelobe floor is set by this weighting function. When the array is moving, the angle sidelobes will show up in Doppler space as indicated in Figure 3(a). Since the angle sidelobes are 20 dB higher, the angle sidelobes will degrade the performance of standard moving target indicator (MTI) techniques [3].

The aircraft motion has several effects on the clutter Doppler spectrum. Depending on the antenna pointing angle, the Doppler peak might be shifted. This effect can be compensated by shifting the local oscillator frequency of the transmitter or receiver by an equal amount in the opposite direction. There will be a widening of the mainlobe. This effect can be emulated by using a heavier weighting function. The spreading of the angle sidelobes into Doppler space is not easily compensated. For the development of space-time processing techniques, our concern is primarily with the emulation of sidelobe clutter effects.

3. Doppler Sidelobe Spectrum Emulation

There are a variety of techniques by which the clutter spectrum seen by an airborne radar could be emulated. For example, we could inject artificial clutter into the radar receiver system. However, since clutter is very much environment dependent, it is unlikely that synthetic clutter can be generated to everyone's satisfaction. Various airborne and ground based clutter repeaters were considered. These were rejected for reasons of either cost or lack of realism. Mechanical means of emulating the aircraft motion were rejected for the same reason. Only

some form of electronic emulation of antenna motion appear to be practical.

A displaced phase center antenna (DPCA) is common to all electronic emulation techniques considered. Displaced phase center antennas are commonly used in airborne radar for clutter cancellation [3]. In such a radar, the phase center is moved electronically backwards in order to arrest the aircraft motion. Reception of two radar returns from the same location allows cancellation of stationary clutter and moving target detection. In an inverse displaced phase center antenna (IDPCA) the phase center of the antenna is electronically moved forward in order to create the aircraft motion.

There are several options for implementing an IDPCA antenna. The most straight forward option is to electronically move both the transmit and receive apertures. Obviously, the antenna has to be made much longer. Its length should be at least the length of the actual aperture plus the aircraft motion during a CPI. For the above stated motion assumptions, this could well double the array antenna cost. Furthermore, this option requires very precise matching of antenna patterns. Matching antenna patterns for DPCA purposes has been examined in the past [4]. Experience has shown that pattern matching is practical down to the -40 dB level. However, Figure 3(a) indicates that sidelobes at the -60 to -80 dB level need to be controlled for an accurate emulation of an airborne radar scenario.

Since it is not practical to simulate the entire clutter Doppler spectrum from the peak of the mainbeam down to the Doppler sidelobe level, the proposed emulation technique concentrates on emulation only the Doppler characteristics of sidelobe clutter. This is achieved by adding to the Doppler spectrum of the stationary antenna under test in Figure 3(a), the Doppler spectrum of an electronically movable auxiliary transmit aperture in 3(b). When combined as shown in 3(c), there is very

close agreement between the emulated and actual Doppler sidelobe characteristics.

An implementation of the IDPCA concept is depicted in Figure 4. Except for the addition of an auxiliary transmit antenna, no changes need to be made to the stationary radar under test. The auxiliary aperture consists of a linear array of column radiators connected to a switching matrix. In synchronism with the radar under test, columns of this array will sequentially radiate at an appropriate power level. The number of columns in the auxiliary array has to be equal to the number of pulses in a CPI, and the column spacing must be chosen to create the desired aircraft motion.

The motion emulation turns out to be velocity independent because the auxiliary array switches through successive columns at the radar's pulse repetition frequency. The spacing d^* between adjacent columns will determine how much of the available Doppler space will be covered by clutter. Assume that all auxiliary array columns have identical transmit patterns, $T_A(\theta)$ with the phase center at the origin. For a column located a distance nd^* from the origin, the transmit pattern is given by

$$T_A^*(\theta) = T(\theta) \exp(j \frac{2\pi}{\lambda} nd^* \sin \theta). \quad (6)$$

When used in conjunction with the stationary test array, as shown in Figure 4, the emulated clutter spectrum is

$$\begin{aligned} S^*(\theta, k) = & \sum_{n=0}^{N-1} T(\theta) P(\theta) \exp \left[-j \frac{2\pi nk}{N} \right] + \\ & \sum_{n=0}^{N-1} T_A(\theta) P(\theta) \exp \left[j 2\pi n \left(\frac{d^*}{\lambda} \sin \theta - \frac{k}{N} \right) \right]. \end{aligned} \quad (7)$$

Now the motion emulation parameters can be chosen. The first term in Eq.

(7) is due to the stationary radar. With sufficiently heavy weighting, it should not significantly contribute to the Doppler sidelobes. In the sidelobe region, the second term in Eq. (7) can be made approximately equal to Eq. (4) by letting

$$T_A(\theta) = T(\theta). \quad (8)$$

This means that the power-aperture product of a column of the auxiliary array has to approximately match the power-aperture product in sidelobes of the radar antenna. Furthermore, to match the Doppler spread, the auxiliary array column spacing has to be

$$d^* = 2d. \quad (9)$$

That is, the auxiliary array column spacing should be twice the desired platform motion during a PRI. Hence the length of the auxiliary array has to be at least twice the aircraft motion during a CPI. It is interesting to note that the emulation will fill the unambiguous Doppler space exactly once when

$$d^* = \frac{\lambda}{2}. \quad (10)$$

4. Inverse Displaced Phase Center Antenna Implementation

The motion emulation concept was first demonstrated with an ultralow sidelobe radar antenna [5] and a simple IDPCA antenna [6]. For a radar system with higher azimuth transmit sidelobes, a more powerful and capable IDPCA antenna was required. The characteristics of the new IDPCA antenna are given in Figure 6 and 7. The antenna is about 5 feet by 21 feet in size, and contains 72 horizontally polarized patch radiating elements spaced 0.47λ apart. It operates at UHF with a 10 MHz instantaneous bandwidth. Perhaps a somewhat unique feature of the

array are the rolled edges which were intended to reduce edge diffraction effects.

Some typical column antenna patterns are shown in Figure 8. There is still about 0.3 dB rms of edge diffraction ripple. Since such ripple creates spurious Doppler sidelobes, we prefer to use three-column subarrays. The three-column subarray patterns in Figure 9 are more directive and considerably smoother.

Several IDPCA operating modes are illustrated in Figure 10. The active part of the antenna consists of either one 4-element column, or a subarray of three columns. Either an 8-pulse or a 16-pulse CPI motion emulation can be implemented. That is, the active area can be electronically shifted to the right or to the left in either one-column or two-column increments.

The peak power of the IDPCA antenna in the three-column mode is 2400 watts. This resulted in a power-aperture product that is consistent with a sidelobe motion emulation. That is, the IDPCA power-aperture product is about 20 dB down from the that of the radar itself. In the one-column mode the peak power is only 800 watts.

A block diagram of the IDPCA system is shown in Figure 11. Electrically, the array is organized as four identical rows of 18 elements. Each row contains three 200 watt power amplifiers and nine high power switches. This arrangement is very efficient, but requires commutation of the power amplifiers in the three columns as indicated in Figure 10. The twelve power amplifier were matched to 0.1 dB in amplitude and 2.7 deg. rms in phase. Small but periodic amplitude and phase differences will produce a Doppler modulation. The modulation effects can be reduced, in part, by phase shifters, and by post mission calibrations.

Proper emulation of airborne radar sidelobe clutter effects requires an additional,

antenna scan angle dependent Doppler correction. In Figure 2, the radar was pointing broadside to the direction of aircraft motion. In that case, the mainbeam Doppler is zero, regardless of whether the radar is moving or not. Normally, the radar will be pointing in some other direction. Consequently, the main beam clutter Doppler will not be zero. Many radar systems employ some technique for shifting the main beam Doppler back to zero [3]. One such technique is known as TACCAR (Time-average clutter coherent airborne radar).

We will assume that the main beam clutter Doppler has been shifted back to zero by TACCAR as illustrated in Figure 5(a). This is convenient because the main beam clutter return for the stationary radar is already at zero. However, Figure 5(b) indicates that the auxiliary array generates moving sidelobe clutter that still has to be shifted back to zero Doppler. This requires shifting the phase of the signal transmitted by the auxiliary array on a pulse-by-pulse basis by an amount that compensates for the radar main beam pointing. It is accomplished by the three phase shifters shown in Figure 11. As a result of real-time phase control, the emulated and actual Doppler spectrum in 5(c) will be nearly identical, even if the radar is pointing in a direction other than broadside.

5. Experimental Results

The new IDPCA antenna was installed on North Oscura Peak at the White Sands Missile range in New Mexico. Figure 12 shows an experimental surveillance radar [5] and the IDPCA antenna overlooking the desert floor some 3000 feet below. In the distance, 50 to 100 nmi away, were several mountain ranges with radar cross-sections exceeding 60 dBsm.

The data collected by the radar with the IDPCA antenna can be represented as a

data cube of V samples from N receiver channels, M PRI's and R range cells. The radar antenna itself consists of an array of 14 column antennas uniformly spaced a distance 0.48λ apart. Each column is connected to a receiver channel. A typical data cube contained 16 CPI's and up to 1000 range samples. Assuming uniform weighting, the radar return from a specific direction is given by

$$P(\theta) = \sum_{n=0}^{N-1} V \exp\left(j \frac{2\pi n}{\lambda} D \sin \theta\right). \quad (11)$$

By substituting

$$k = \frac{ND \sin \theta}{\lambda}, \quad (12)$$

Eq. (11) takes on the form of a direct Fourier transform

$$P(k) = \text{DFT}(V). \quad (13)$$

Doppler processing of M PRI's by another DFT, and averaging over all range samples yields a two-dimensional azimuth-Doppler power density function (PDF)

$$\overline{\text{PDF}} = \frac{1}{R} \sum |\text{DFT}^2(V)|. \quad (14)$$

Such average PDF's are used to demonstrate the motion emulation capability of the auxiliary array.

Although the motion emulation technique assumes that the radar and the IDPCA antenna are both transmitting, the effects of motion emulation are most clearly evident when only the IDPCA antenna is transmitting. Figure 13 shows an average PDF for a 16-pulse CPI, with the IDPCA in the 3-column mode, and with the motion emulation inhibited. Figure 14 shows that when emulation is enabled in the one column / PRI motion, a diagonal clutter ridge is created that nearly spans the azimuth-Doppler space. In Figure 15, an example is given of the one-column

mode with two-column / PRI motion. The resulting Doppler clutter ridge is folded over.

At certain ranges the radar clutter return has characteristics of a point scatterer. Such a scatterer, as shown in Figure 16, can be used to establish a performance bound on the motion emulation. For the particular scatterer, Figure 17 indicates that the average azimuth sidelobes are 28 dB down, and the average Doppler sidelobes are at least 32 dB down. The actual sidelobes due to IDPCA implementation errors may be lower.

For comparison of an emulated with an actual airborne radar clutter Doppler spectrum, a test was carried out with only the radar receiver and a small, 100 watt transmitter on an airplane. The aircraft flight path was parallel to IDPCA antenna axis. Synchronization with the radar receiver on the ground was achieved by transmitting a coded waveform and detecting the direct path signal. When comparable radar parameters are chosen, the azimuth-Doppler plot in Figure 18 is remarkably similar to that in Figure 14 generated by the IDPCA motion emulation.

An example of the radar and IDPCA antenna working together is given in Figure 19. The Doppler sidelobes of the stationary array are about 75 dB down. The Doppler spectrum created by the IDPCA antenna operating in the one-column mode raised the Doppler sidelobes to -55 dB.

6. Conclusions

Ground testing of a space-time processor for an airborne radar application requires a mountain top test site and a motion emulation technique. A suitable motion emulation technique is described in this paper.

The motion emulation technique is based on an inverse displaced phase center antenna. It allows emulation of the Doppler sidelobe effects characteristic of an airborne radar. It does not require any changes to be made to the radar system and it causes an insignificant increase in the radar cost. The experimental results confirm that is a practical technique for emulating aircraft motion.

7. Sponsorship

This work was sponsored by the Advanced Research Projects Agency under Air Force Contract F19628-95-C-0002.

8. References

- [1] L.E. Brennan and I. S. Reed, "Theory of Adaptive Radar," IEEE Transactions on Aerospace and Electronic Systems, Vol. AES-9, March 1973, pp.237-252.
- [2] R. Klemm, " Adaptive Clutter Suppression for Airborne Phased Array Radars," IEE Proc. Pts. F and H, No. 1, Feb. 1983, pp. 125-132.
- [3] M. Skolnik, Radar Handbook, Second Edition, McGraw Hill, New York, New York, 1990, Chapter 16.
- [4] G. Tsandoulas, "Tolerance Control in Array Antenna," Microwave J., October 1977, pp. 24-25.
- [5] B. D. Carlson et al, "An Ultralow-Sidelobe Apdative Array Antenna," The Lincoln Laboratory Journal, Vol. 3, No.2, 1990, pp. 291-310.
- [6] H. M. Aumann, J. Ward, and F. G. Willwerth, " Inverse Displaced Phase Center Antenna for Aircraft Motion Emulation," Fourteenth Antenna Measurement and Techniques Conference, Columbus, Ohio, October 1992.

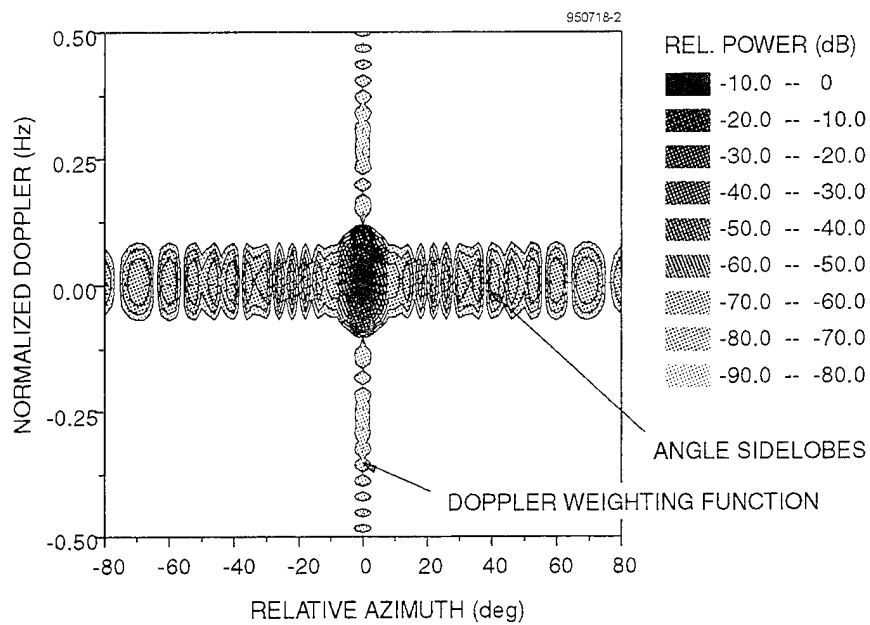


Fig. 1. Stationary Radar Azimuth-Doppler Clutter Map

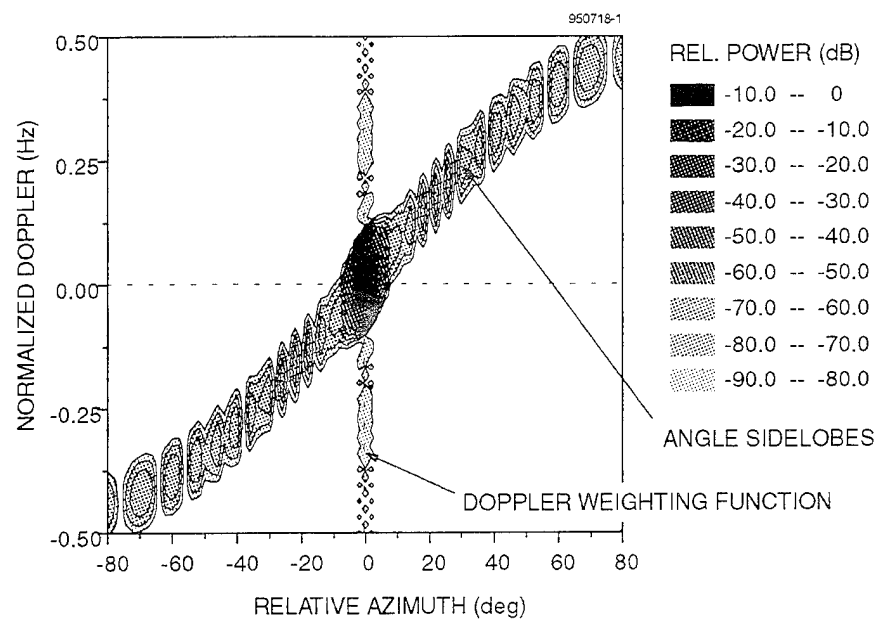


Fig. 2. Moving Radar Azimuth-Doppler Clutter Map

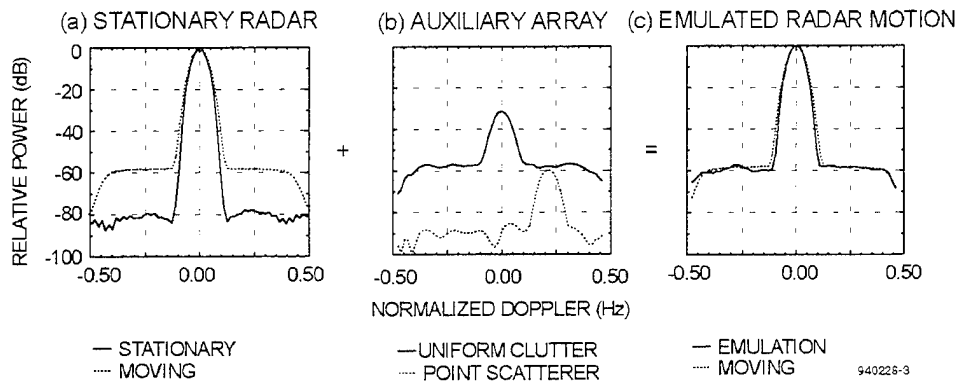


Fig. 3. Motion Emulation Concept

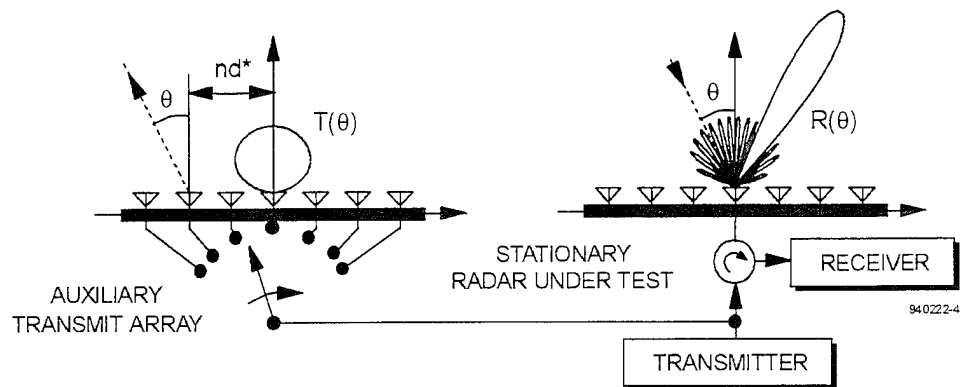


Fig. 4. Motion Emulation Implementation

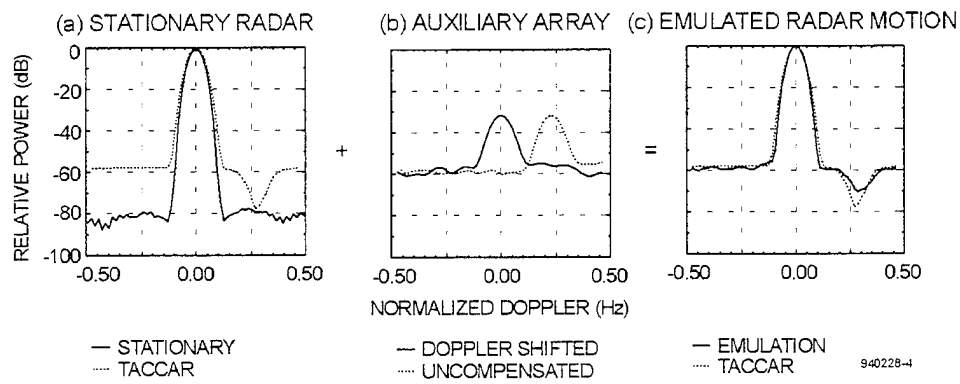
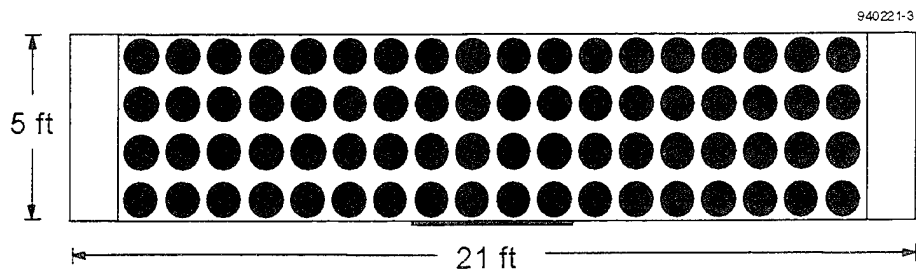


Fig. 5. Motion Emulation with Scan Compensation



- FREQUENCY 430 - 440 MHz
- 16-PULSE MOTION EMULATION
- ACTIVE, TRANSMIT AREA
 - 1-COLUMN SUBRAY, 800 WATTS PEAK
 - 3-COLUMN SUBARRAY, 2400 WATTS PEAK
- SEVERAL MODES OF OPERATION
- REAL-TIME PHASE CONTROL

Fig. 6. IDPCA Antenna Parameters

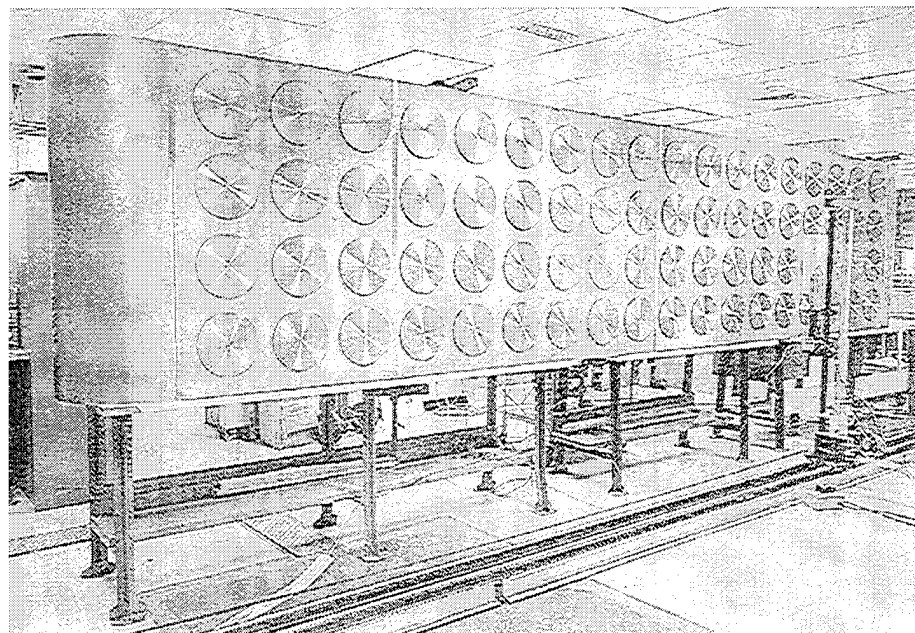


Fig. 7. IDPCA Antenna under Construction

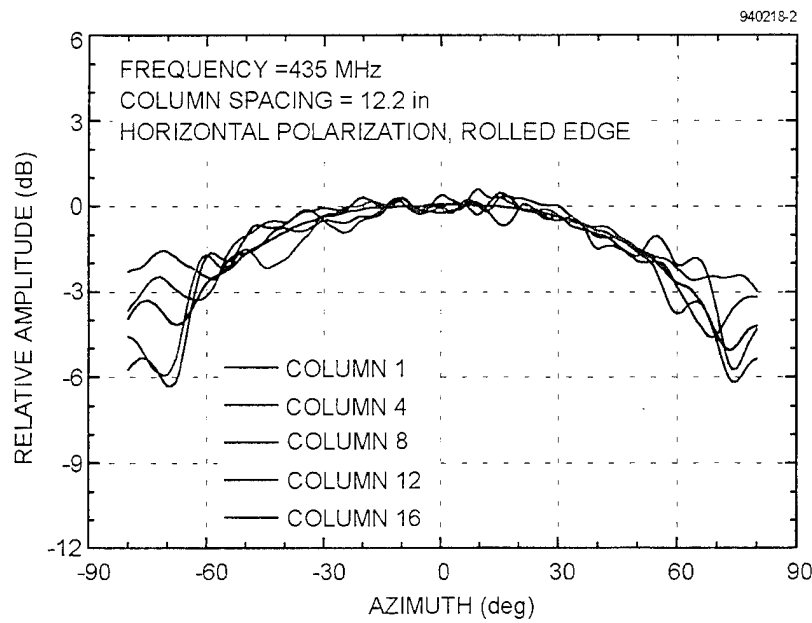


Fig. 8. Single Column Antenna Patterns

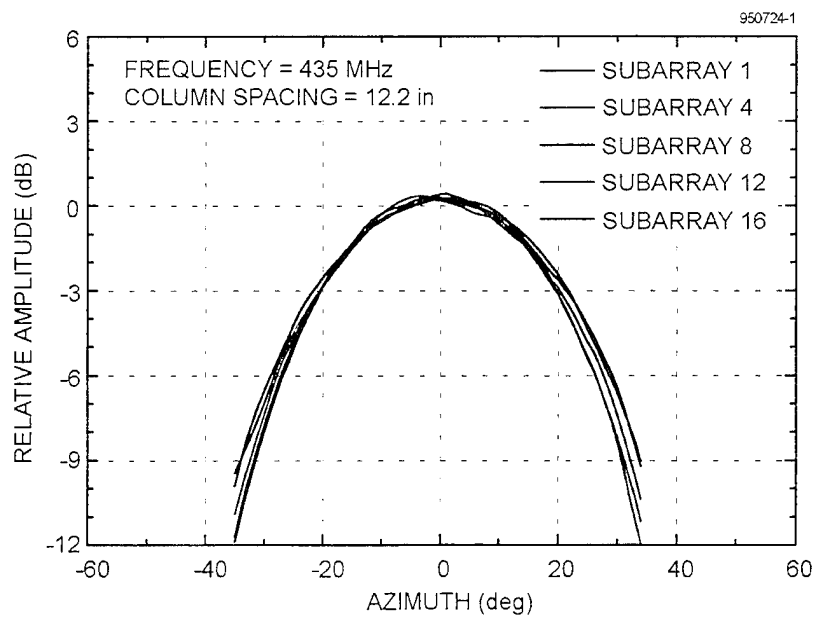


Fig. 9. Three-Column Subarray Antenna Patterns

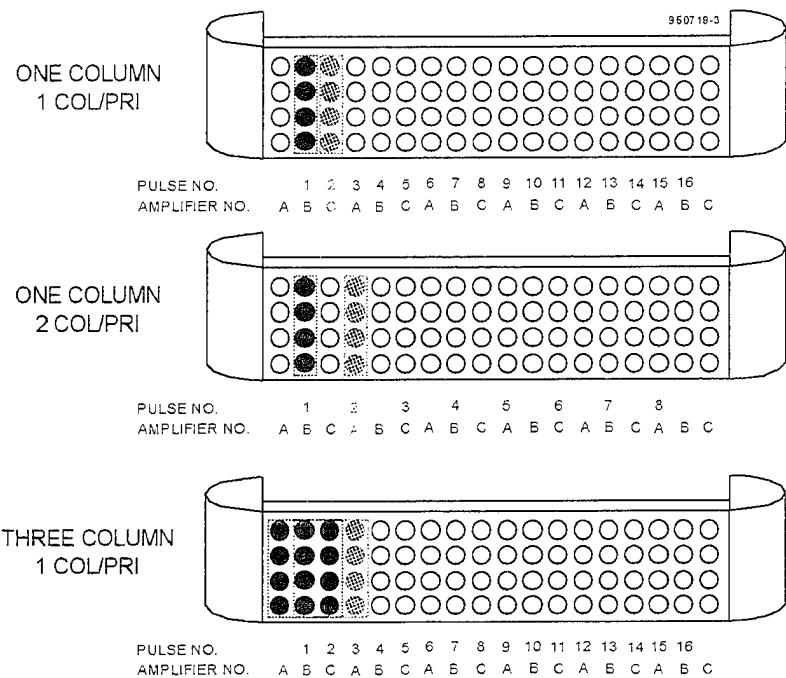


Fig. 10. IDPCA Operating Modes

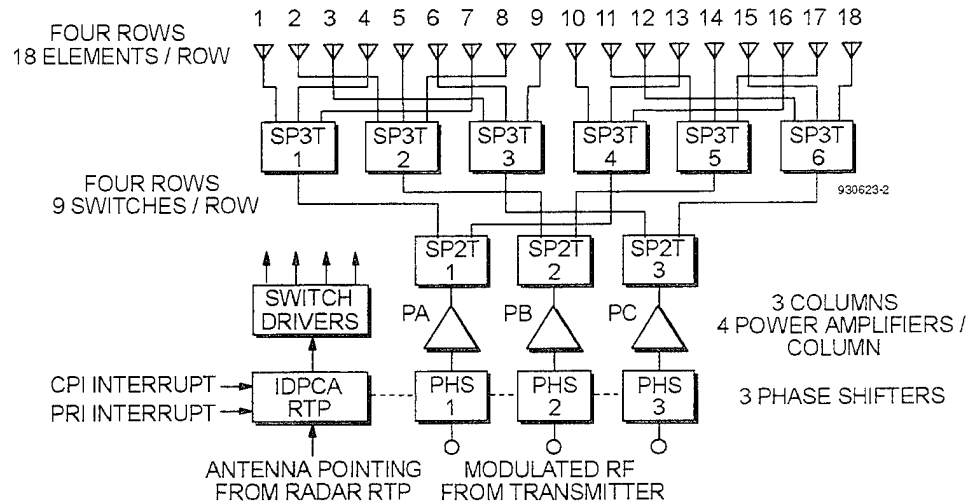


Fig. 11. IDPCA Antenna Block Diagram

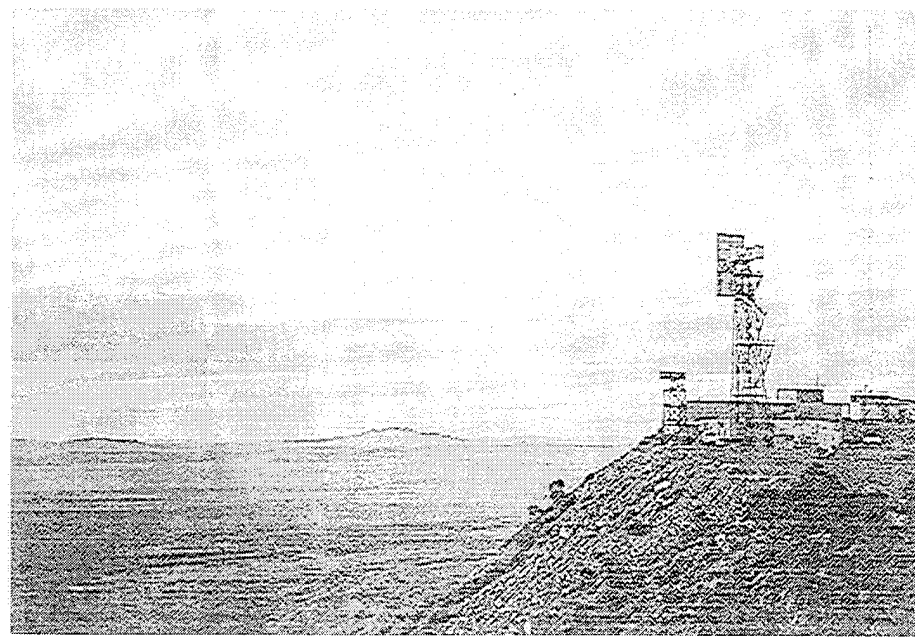


Fig. 12. Radar and IDPCA Antenna at White Sands, NM

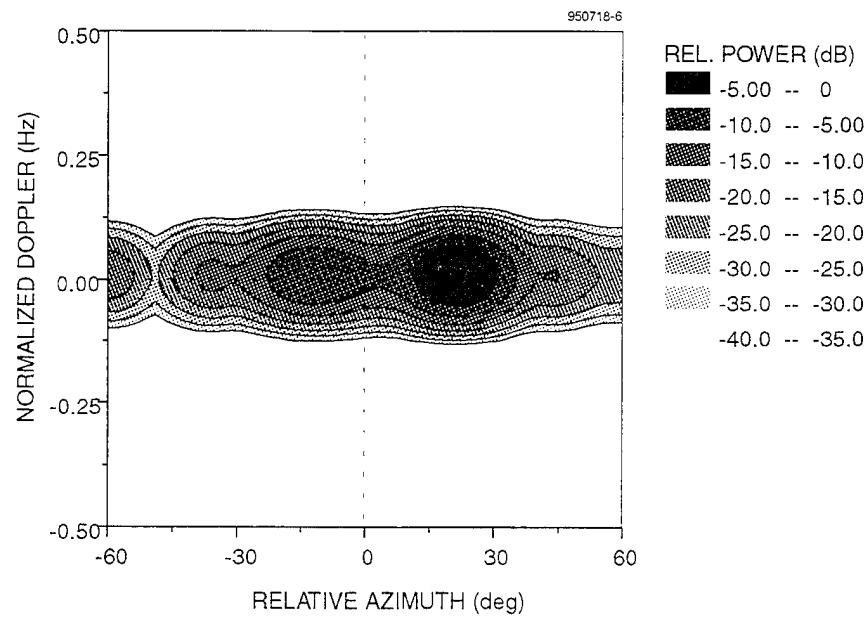


Fig. 13. Azimuth-Doppler Map of Stationary Clutter
Three-Column Mode, 1-Column / PRI, 16-Pulses / CPI

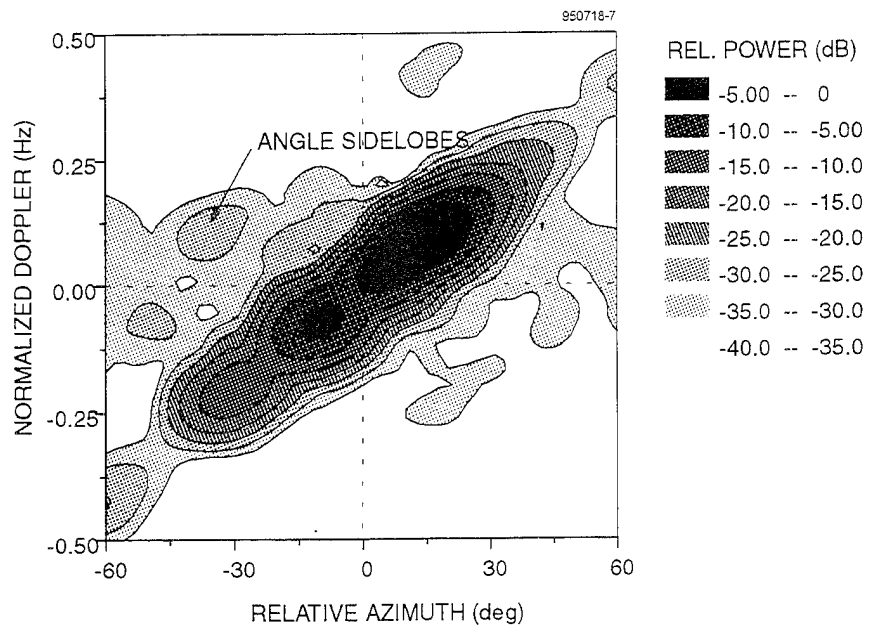


Fig. 14. Three-Column IDPCA Motion Emulation
1-Column / PRI, 16-Pulses / CPI

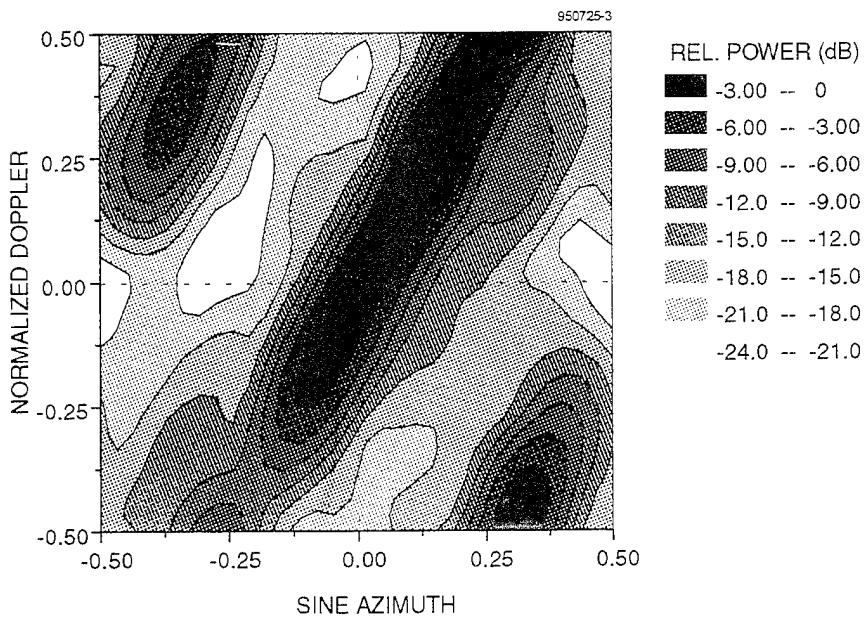


Fig. 15. One-Column IDPCA Motion Emulation
2-Columns / PRI, 8-Pulses / CPI

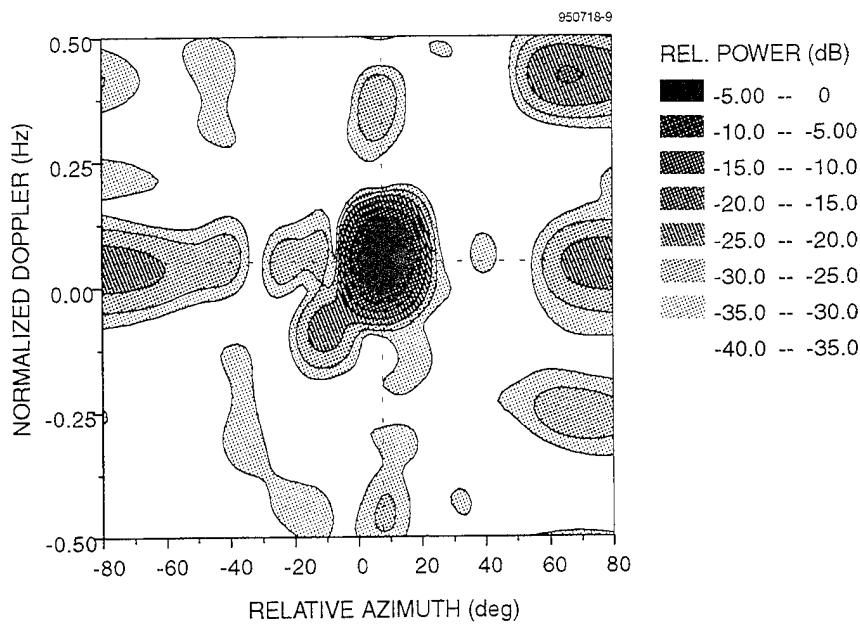


Fig. 16. Azimuth-Doppler Map of a Point Scatterer
One-Column IDPCA, 1-Column / PRI, 16-Pulses / CPI

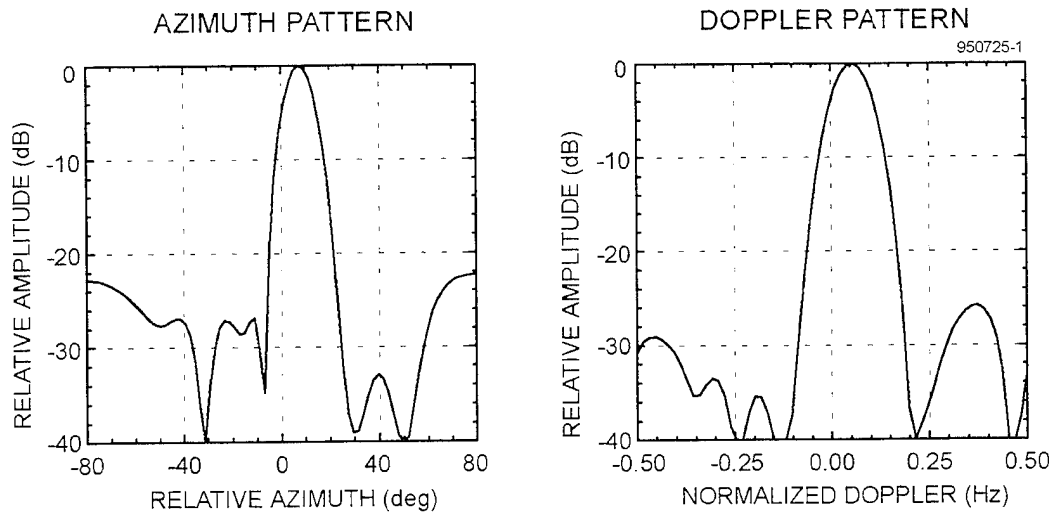


Fig. 17. Angle and Doppler Characteristics of a Point Scatterer

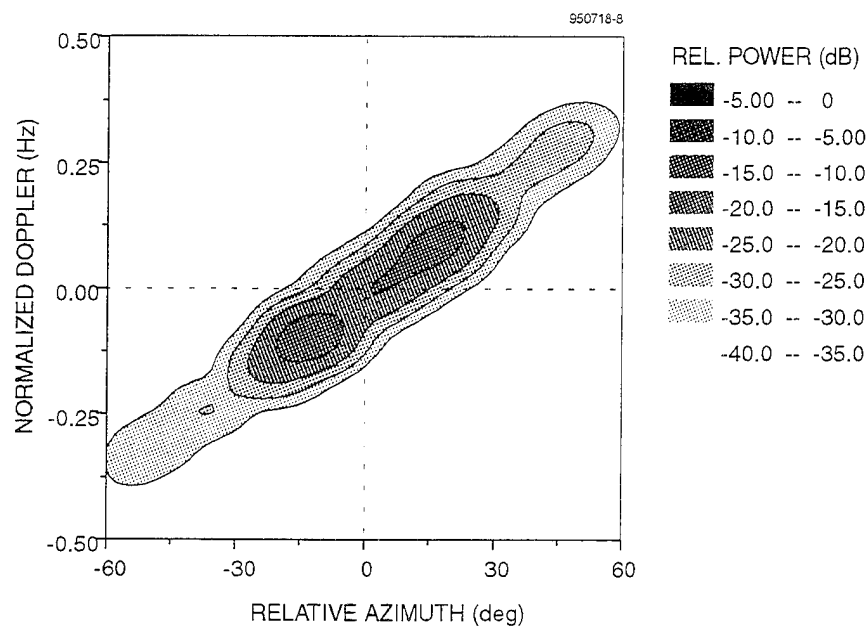


Fig. 18. Clutter Doppler Created by an Airborne Transmitter

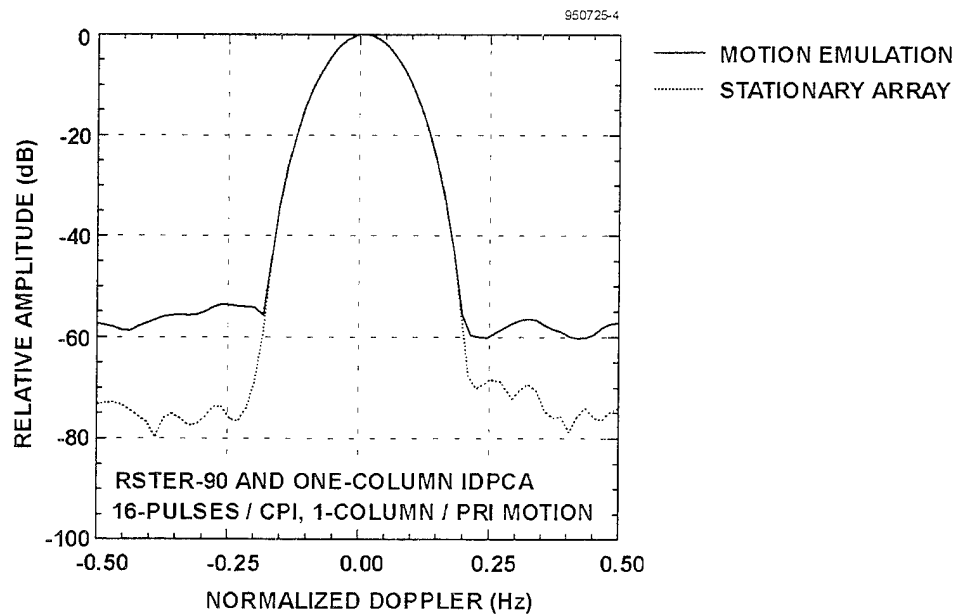


Fig. 19. Measured Emulated Clutter Doppler Spectrum

Leaky-Wave Scanning Antenna for W-Band

Vladimir A. Manasson, Lev S. Sadovnik, Paul I. Shnitser, Robert Mino,
Physical Optics Corporation, Torrance, California 90501
and
Long Q. Bui
Lear Astronics, Santa Monica, California 90406-0442

1.0 Introduction

Cost reduction is recognized as one of the most important considerations in MMW radar development. Hardware (especially phase-shifters) for electronic beam scanning in the millimeter-wave (MMW) band presents very complex fabrication challenges that dramatically arise the device cost. A typical mechanically scanning antenna contains one or more hinged parts (lenses, mirrors or feeds). In operation they experience strong mechanical accelerations and forces that sharply limit scanning speed. The authors have found a solution to this problem, using a new antenna architecture based on periodically loaded leaky-wave radiating elements. The paper presents a basic design and discusses some issues.

2.0 Basic Design

The antenna consists of the following components (see Figure 1): two dielectric waveguides, two parabolic mirrors, and a periodically varying metal grating that perturbs the propagation of the evanescent wave along the waveguide and thereby controls the diffraction of the MMW out of the waveguide. The cylindrical grating is mounted on the outer surface of a rotating drum.

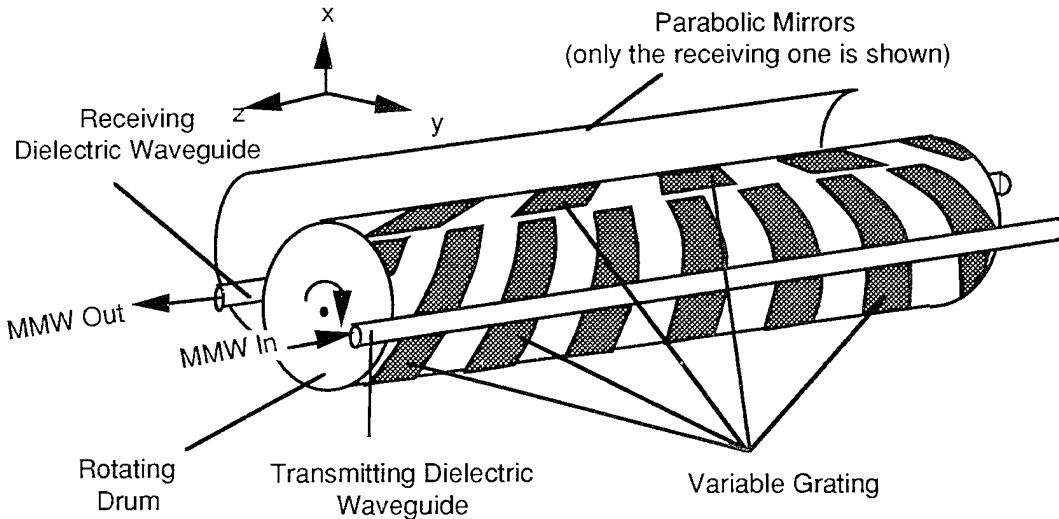


Figure 1
The variable grating consists of two identical semi-cylinders;
the grating periods in the immediate proximity of the two waveguides are exactly the same.

Beam tracing is shown in Figure 2 for the y-z plane and in Figure 3 for the x-y plane.

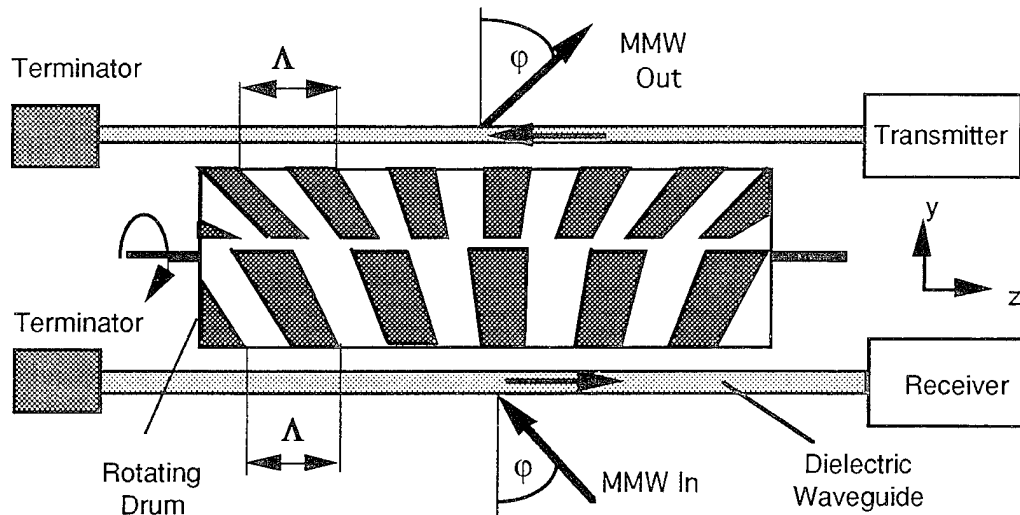


Figure 2

Beam tracing in the y-z plane. The angle φ of emission and of reception is determined by the instantaneous value of the grating period Λ , which varies along the circumference of the drum.

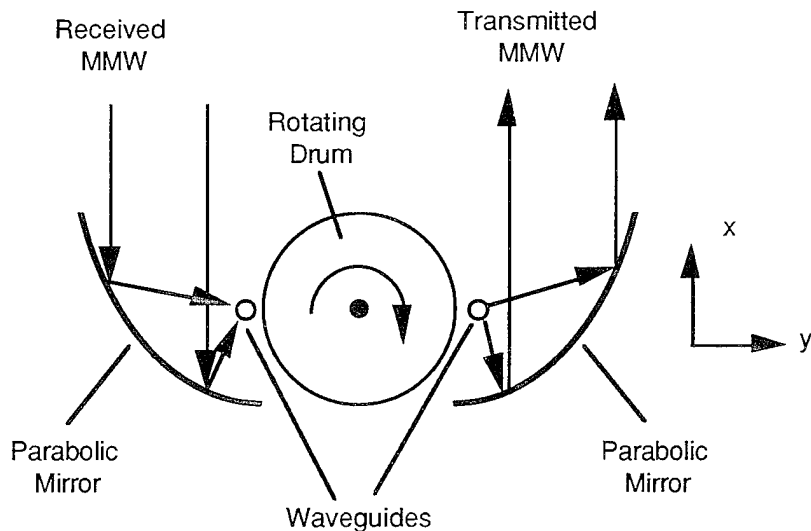


Figure 3
Parabolic mirrors direct and shape the beams in the x-y plane.

The period Λ of the grating close to the waveguide at any given time is a function of the angular position of the drum at that instant. The coupling angle φ is determined by Λ (see Figure 2). Drum rotation steers the beam. The cylindrical grating consists of two

identical semi-cylinders with identical grating patterns. The identical pattern on the two semi-cylinders where they are in close proximity to the waveguides ensures that the grating period Λ facing the waveguides will be the same in both waveguides, as will the coupling angles φ (in accordance with the reciprocity principle). Parabolic mirrors redirect the beams in x-direction (see Figure 3) and confine them in y-direction.

2.0 Principles of Operation

The unique feature of a dielectric waveguide is that it supports the propagation of electromagnetic waves not only inside the waveguide body but outside it as well (see Figure 4). The evanescent waves are perturbed by the presence of a metal grating. This perturbation excites a new radiant wave, which is radiated in free space.

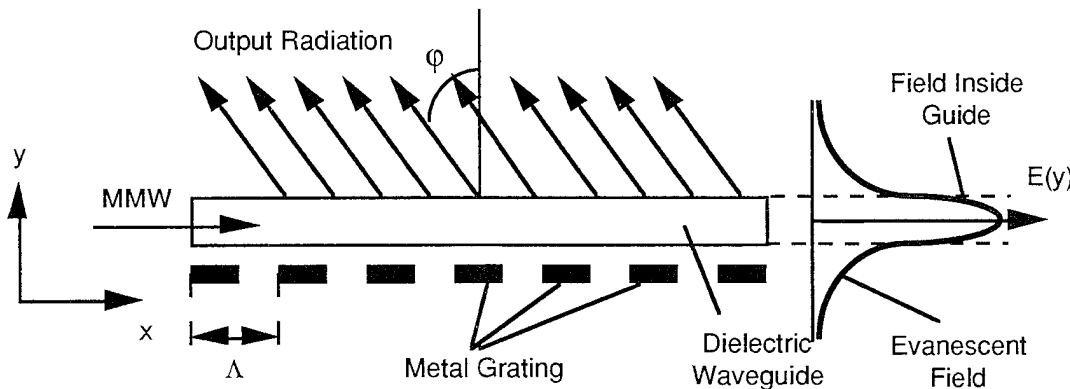


Figure 4
The proximity of the metal grating perturbs the evanescent electromagnetic waves.

The evanescent field decays exponentially with distance from the waveguide. Thus, when there is a metal grating on the outer surface of the cylinder (as shown in Figure 1), only the portion of the grating close to the waveguide will interact sufficiently with the electromagnetic waves to produce radiation.

The angle of the radiation φ is determined by the equation

$$\sin \varphi = \beta/k_0 - p\lambda/\Lambda, \quad (1)$$

where β is the propagation constant, λ and $k_0=2\pi/\lambda$ are the wavelength and the wave vector in free space, p is an integer, and Λ is the grating period. β depends on the waveguide material, its profile, size, and mode order. Eq. (1) indicates that φ depends on Λ . This dependence forms the basis for the scanning capability. In the proposed architecture, Λ varies continuously as the cylinder rotates.

3.0 Grating

The perturbing grating covers the outer surface of the rotating drum. This grating can be fabricated either of two ways. It can be formed as an entirely metal grating with a thick

profile, or as a thin metal grating on a dielectric substrate as shown in Figure 5. In the latter case it can be fabricated using printed circuit board technology.

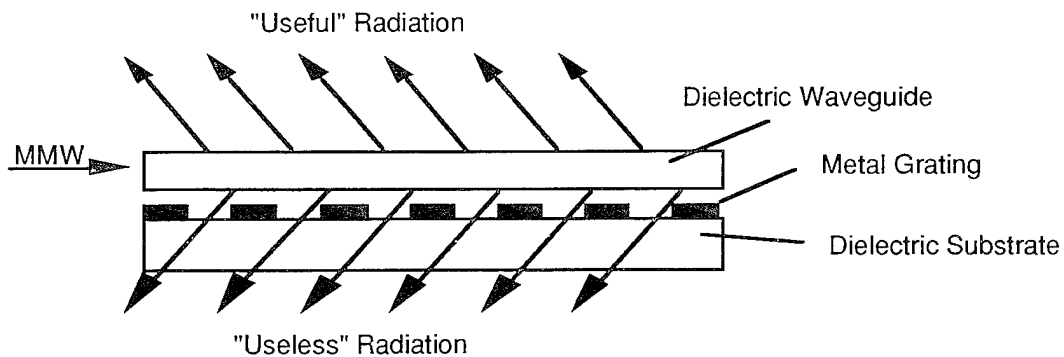


Figure 5

A metal grating on a dielectric surface causes MMW radiation to couple out of the waveguide in a controllable direction. However, a comparable portion of the MMW energy radiates in a parasitic direction.

A metal grating on a dielectric substrate would produce two beams propagating in opposite directions (see Figure 5). A substantial percentage of the radiation is then lost.

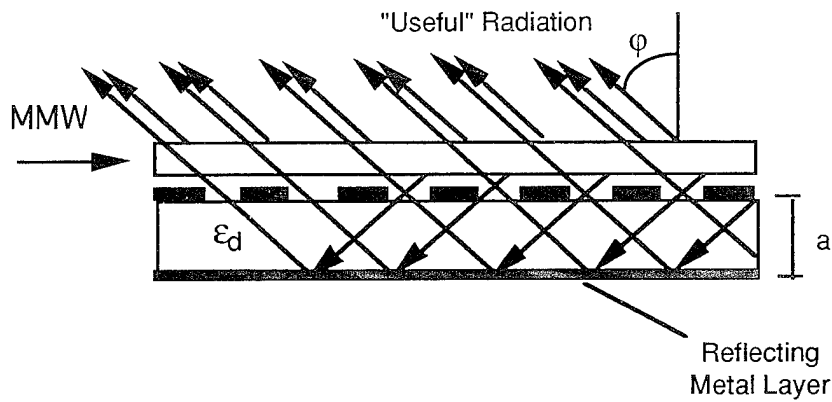


Figure 6
"Useless" radiation is redirected into the "useful" direction.

To redirect the "useless" radiation into the "useful" direction, we added a metal reflector as shown in Figure 6.

To make the interference between the "useful" MMW beam and the redirected beam constructive, the thickness of the dielectric layer is chosen based on the condition described by Eq. (2):

$$a = \lambda \cos \varphi / (4 \epsilon_d^{1/2}), \quad (2)$$

where φ is the central scanning angle, λ is the MMW wavelength in vacuum for the central frequency, and ϵ_d is the dielectric constant of the grating substrate material.

4.0 Experiment

For preliminary testing we fabricated a small antenna prototype. It consists of a quartz cylindrical rod and interchangeable metal gratings with different periods Λ and a choice of fill factors FF, $FF=(\text{metal strip width})/(\text{grating period})$. As a MMW source we used a 90 GHz Gunn oscillator with the standard WR10 metal waveguide output coupled to the quartz rod through a specially designed transition. The grating length was 1 inch and 3 inches. The detector was set at the distance of 6 feet ensuring far field measurements.

We tested gratings of both types of shown in Figures 5 and 6. The grating with the back-reflector, as we expected, radiates more efficiently in intended direction than the grating without a reflector (see Figure 7). We also found that for the two types of grating with the same period Λ the diffraction angles are different.

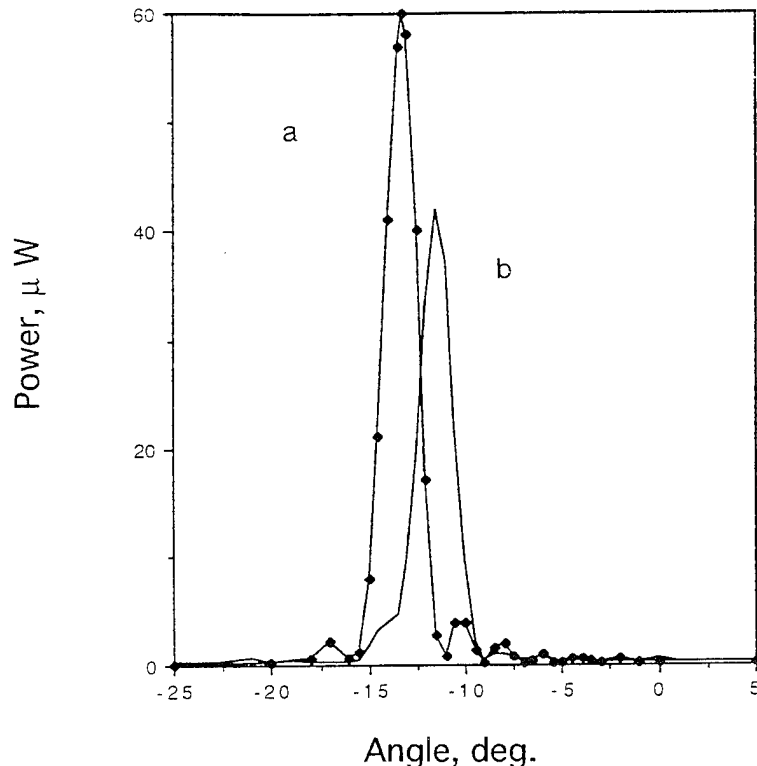


Figure 7
Beam pattern for grating with back-reflector (curve a) and without (curve b).
For both gratings $\Lambda=2.3$ mm.

One important design parameter is the gap δ between the dielectric rod and the grating. Radiated power depends on δ as shown in Figure 8 for the three gratings with fill factors of 0.3, 0.5, and 0.7. The maximum radiation occurred for FF=0.3. Curves have a bell shape with a few resonances. Their position and depth vary depending on the type of the grating, and on the fill factor.

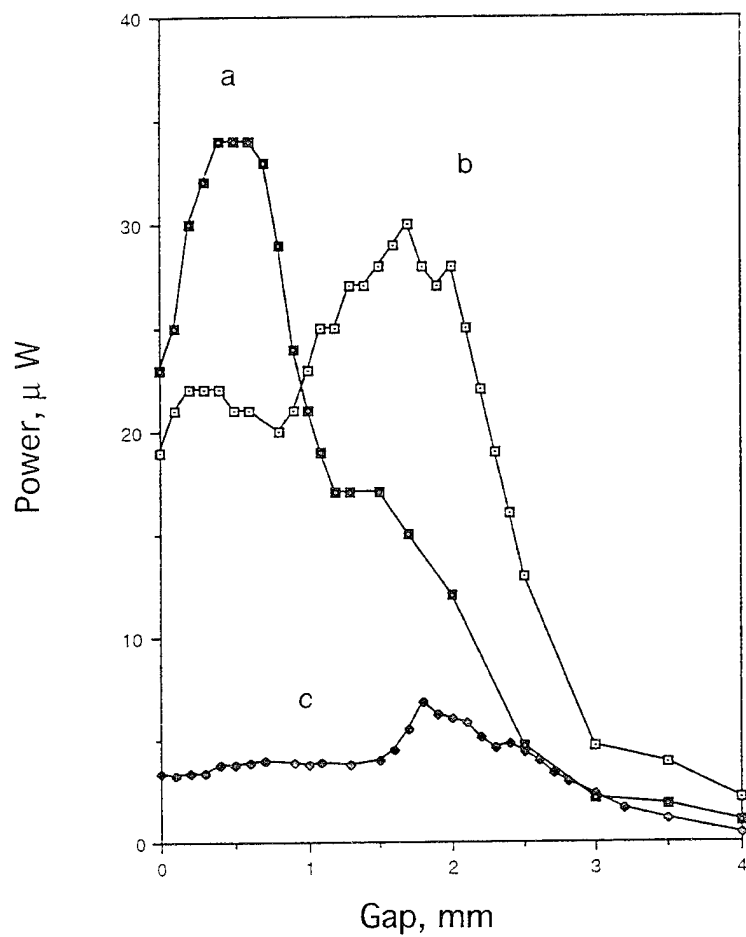


Figure 8
Dependence of radiated power on the gap size for three gratings with FF=0.3 (curve a), 0.5 (curve b), and 0.7 (curve c).

We also found that the diffraction angle ϕ depends on the gap size δ and the fill factor FF. The dependencies are shown in Figure 9. The diffraction angle ϕ grows with δ

when the grating is close to the waveguide, and depends weakly on the gap size at large distances.

According to the Eq.(1) at fixed parameters λ , Λ , and k_0 , the beam angle moves in the negative direction in response to a decrease in the propagation constant β . This decrease is in contrast to the expected Bloch slowing of the wave phase velocity (an increase in β) typical for wave propagation in a periodic media. Waves accelerate in metal waveguides. It is possible that the observed decrease in β results from the grating having the effect not of an periodic structure but of a metal wall. This hypothesis is qualitatively in agreement with the results shown in Figures 7 and 9.

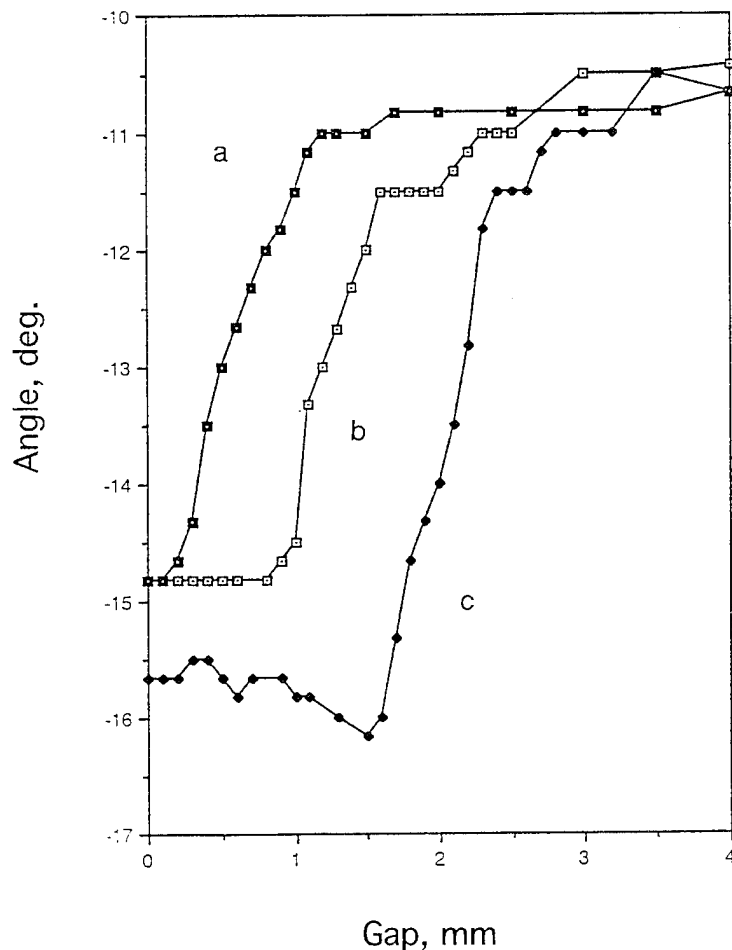


Figure 9
Dependence of radiation angle on gap dimension for three gratings with $FF=0.3$ (curve a), 0.5 (curve b), and 0.7 (curve c).

Beam patterns for the three grating of the same type but differing in period Λ are shown in Figure 10.

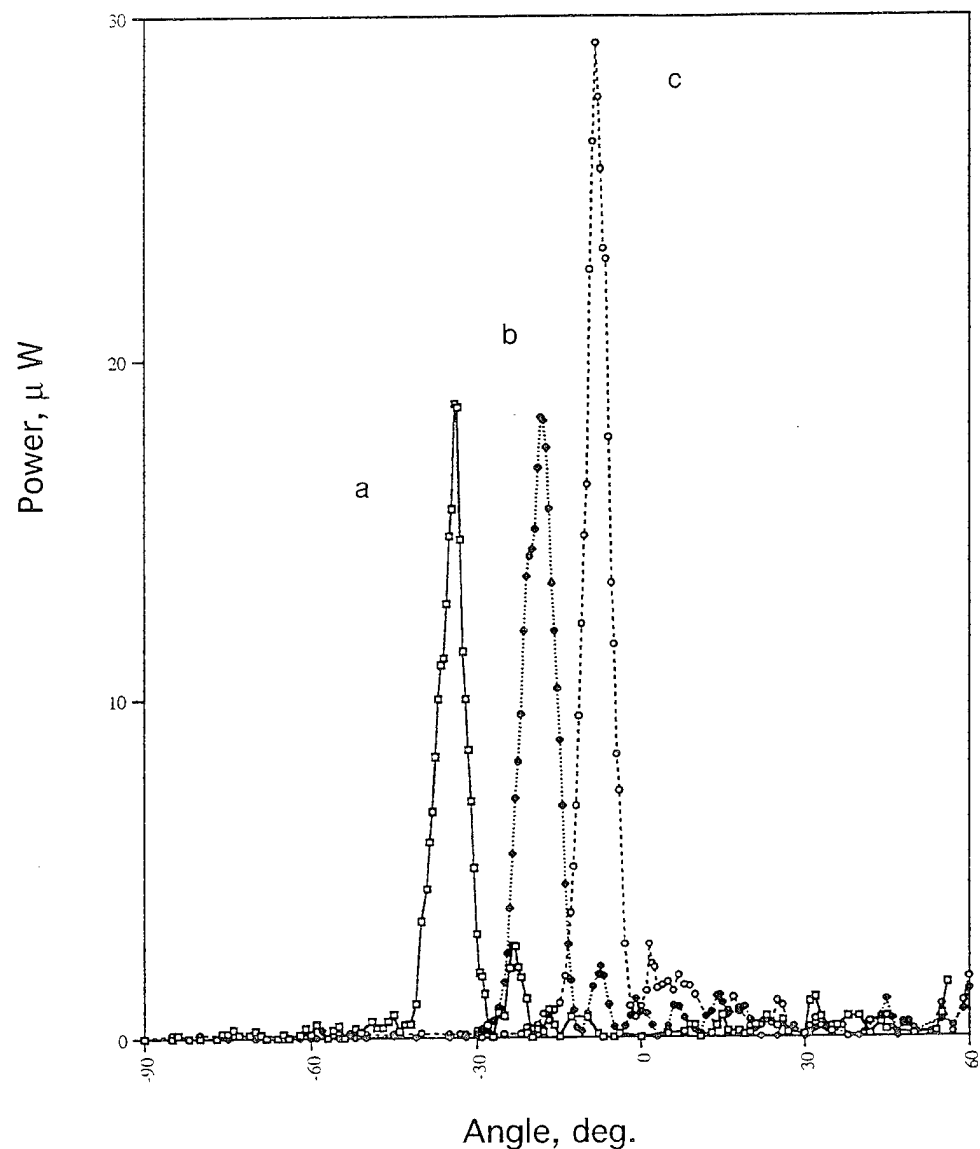


Figure 10
Beam-steering by varying the grating period.
 $\Lambda=2.0$ mm (a), 2.3 mm (b), and 2.7 mm (c).

5.0 Supports

For W-band single-mode operation, the rod diameter must be on the order of 1 mm. A narrow radiation angle such as 0.5 degree requires a rod length of as much as 50 cm. Without a mechanical support, such a long thin rod will bend and mechanically oscillate in a manner that will badly affect the antenna performance. It would be easy to use as a waveguide a composite metal/dielectric structure, such as an "image line" waveguide. The metal portion of the structure could be mounted directly to the antenna frame. Unfortunately, the metal in this long structure would insert excessive losses at W-band frequencies. An entirely dielectric waveguide inserts much lower losses but stiffening it is a more difficult problem. Metal supports for the dielectric rod would cause back-reflection. Dielectric supports would couple MMW out of the dielectric rod. At the same time, the support must insert minimal phase distortion so as to ensure that all antenna segments radiate in phase. Our solution is shown in Figure 11.

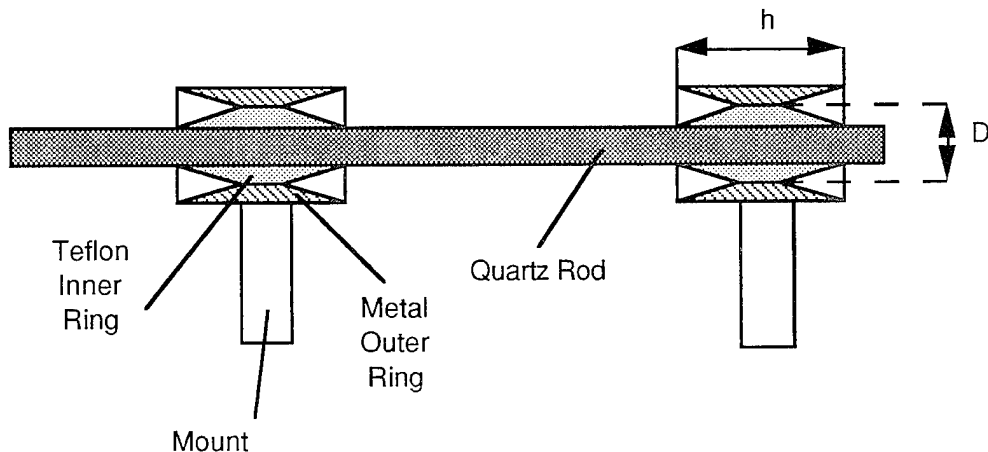


Figure 11
Dielectric rod waveguide with two supports.

The entirely quartz rod (dielectric waveguide) is supported on mounts. To electromagnetically isolate the rod from the mounts we used two tapered rings, the inner one made from the dielectric and the outer one of metal. The metal ring shields propagating millimeter waves from coupling to the mount. The short length h of the metal ring ensures that it introduces negligible absorption losses. The conical shape of the tapered ends of both metal and dielectric rings prevents undesired radiation and weakens the back reflection of MMW propagating along the rod. The hardest problem was to preserve the phase, i.e., to design a support that inserts the same phase shift $\Delta\theta$ as would be inserted by an unsupported quartz rod of the same length h . Our design seems to solve the problem. This is a simplified explanation. The dielectric ring surrounding the quartz rod decreases the effective propagation constant β of the MMW in the rod. In contrast, the presence of the metal outer ring increases the β . Both changes $\Delta\beta$ depends on the diameter D . If D is selected properly, the positive $\Delta\beta$ caused by the dielectric ring exactly compensates for the negative $\Delta\beta$ caused by the ring, and as a result the phase shift inserted by the support is the same as for an unsupported

piece of the rod of the same length h . The experimental study of $\Delta\theta$ as a function of the diameter D has confirmed this simple model. Phase distortion of less than 5 degrees per support was obtained experimentally.

6.0 Conclusions

The cost-effective, high-speed, compact, scanning antenna described here is very attractive for use in MMW radars and communication systems. Using the results presented above we have designed and fabricated a large antenna with an expected beamwidth of 0.5 degree, a scanning angle of 30 degrees, and a scanning speed 1500 degrees/second. This antenna shown in Figure 12, is currently under test.

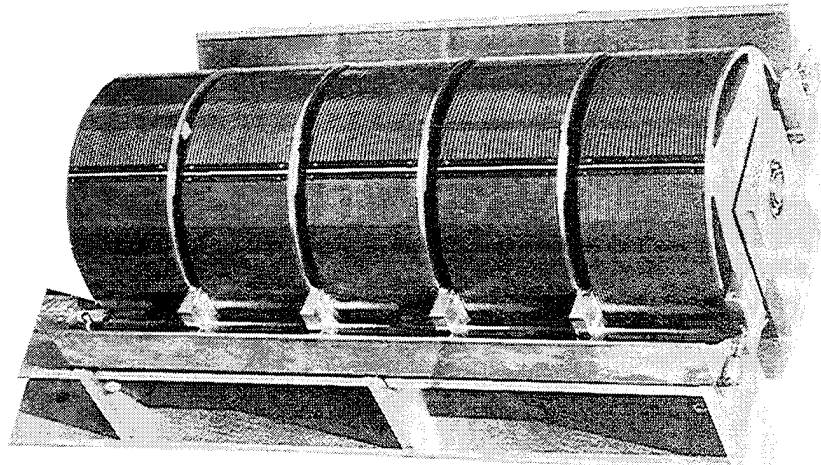


Figure 12
Mechanically scanning MMW antenna.

Octave Bandwidth Microwave Scanning Array

Paul G. Elliot
E-Systems, APTI Division
1250 24th Street NW, Suite 850
Washington, DC 20037

Abstract: A phased array design with test results are described which demonstrate more than one octave of bandwidth with scan. The array could be designed for any polarization and is scalable to any center frequency. A 7 element circularly polarized prototype array was fabricated for the frequency band from 750 to 1750 MHz. The tests on this prototype include array and element patterns and active impedance measurements. Computer models predict an active VSWR of less than 2:1 for one octave bandwidth with +/- 30 degree scan off broadside in any direction, and the test results obtained so far support this capability. The array is compact compared to other wideband scanning arrays: the printed circuit radiating elements lie approximately 1/4 wavelength in front of the ground plane, this could be reduced if dielectric were used. The elements are all etched on substrates that lie in the plane of the array, permitting several rows and columns of elements to be etched on the same board. The feed components behind the ground plane are of standard off-the-shelf stripline design. The array is suitable for electronic beam steering using phase shifters or for a multibeam antenna.

1. Introduction: This phased array uses radiating elements similar to turnstile antennas with some patented features to increase array bandwidth, and arranged in an equilateral triangular lattice. Figure 1 shows the front of a 7 element prototype array with printed circuit elements which was tested. The polarization of the array is determined by phasing in the array feed, so the array can be designed for any polarization. Circular polarization was chosen for the prototype through the use of 90 degree hybrids. The array frequency is scalable, in principle, to any center frequency by scaling the dimensions of the radiating portion of the array. The prototype array performs well from 750 MHz to 1750 MHz. Outside this frequency range the feed loss, polarization and pattern shape deteriorate. The interelement

spacing is one wavelength at 2170 MHz and 0.667 wavelengths at 1450 MHz which is close enough to permit +/- 30 degree scan off broadside in any direction with no grating lobes up to 1450 MHz, and +/- 20 degrees scan up to 1620 MHz.

A greater number of elements than the 7 used in the prototype would, of course, increase array gain, reduce beamwidth, and provide finer pattern control, but would require element phase shifts proportional to frequency (e.g. true time delay) to prevent beam squint problems for wideband signals.

2. Array Feed: Figure 2 shows a block diagram of the array feed. For the prototype it is a corporate feed providing uniform amplitude illumination. The prototype uses stripline components, with each component packaged in its own case and connected to other feed components by coaxial lines. This prototype feed demonstrates that the required feed bandwidth can be easily provided using stripline circuit techniques. Future versions of the feed could achieve manufacturing economies by placing more of the stripline feed components together on the same circuit board instead of in separate cases. Plots of the feed loss over the array bandwidth will be shown. This array can be used for transmit and receive.

3. Element Size and Manufacturability: The elements are compact compared with most other types of ultra-wideband phased array elements since the depth of the element above the ground plane is approximately one quarter wavelength near the center frequency, less if dielectrics are used. The elements are etched on substrates that lie in the plane of the array, permitting several rows and columns of elements to be etched on the same board, an economical feature which also contrasts favorably with most ultra-wideband array elements.

4. Impedance Measurements: Figures 3 and 4 show the measured VSWR at the input port to the corporate feed which feeds the entire 7 element array. All elements are excited with uniform forward power. In Figure 3 the array was phased for broadside. In Figure 4 the array was scanned to 20 degrees off broadside in azimuth which is the only scan direction measured so far. The VSWR in both figures is below 2.1:1 from 730 MHZ to 2 GHz, and is below 1.7:1 from 900 MHZ to 2 GHz. Phase shifters were not available yet for these measurements so scanning was accomplished for the tests by inserting short lengths of coaxial line. The use of phase shifters would add some insertion loss which would actually improve the VSWR but otherwise have a negligible effect on these test results. Other scan directions and scan angles have not been measured yet, but computer simulations of the array predict an active element VSWR of below 2:1 for all planes of scan at all scan angles less than +/- 30 degrees off broadside for all frequencies from 750 MHz to 1450 MHz.

Figure 5 shows the VSWR at the input to the center element with the other 6 elements not driven but terminated in their matching feed networks. The VSWR is, as expected, somewhat higher than in Figures 3 and 4 since the matching circuit was designed for the active impedance with all elements excited, not the case where only one element is driven. Also, some of the power dividers in the feed are bypassed to reach a single element, the slightly lower feed loss contributing a little to the increase in VSWR.

5. Pattern Measurements: Figures 6 through 9 show broadside patterns for the prototype array elevation and azimuth cuts. The array was also scanned twenty degrees in one plane as shown in Figures 10 and 11. All the patterns at frequencies between 750 and 1750 MHz show a well formed main beam pointed in the correct

directions and sidelobes that are close to the expected levels. Some pattern degradation is seen for the 500 MHz and 2000 MHz curves.

Figure 12 plots the broadside gain measured on the peak of the beam at each frequency and compares it with the approximate theoretical directivity. The difference between directivity and gain is the total loss in the antenna feed, which is also plotted in Figure 12. This loss is due to the mismatch loss at the radiating elements plus loss in all the feed components (baluns, 90 degree hybrids, power dividers, and coax). The feed components, excluding mismatch loss at the elements, could contribute up to 3.5 dB of loss in the worst case which is the sum of their individual insertion loss specifications. It can be seen in Figure 12 that the total loss is below 3.5 dB over most of the frequency range between 750 MHZ and 1400 MHZ, and rises only slightly above this from 1400 MHZ to 1750 MHz. This establishes the important result that there are no major loss mechanisms that are not accounted for, and that the radiating elements are well matched to the feed network over a very wide bandwidth. The low array VSWRs shown in Figures 3 and 4 also support the conclusion that the elements are well matched over one octave or more.

Figures 13 through 16 show the center element principal plane patterns in the terminated array environment. These are typical element patterns, showing a directive pattern in the forward direction with no deep nulls. The cross-polarization level (LHCP) was also checked and is usually about 10 dB below the co-polarized element pattern on broadside.

6. Acknowledgements: The author wishes to acknowledge valuable guidance and suggestions from Dr. Leon Susman of E-Systems, APTI Division and from Dr. Walter Kahn of ANRO Inc., Sarasota, FL.

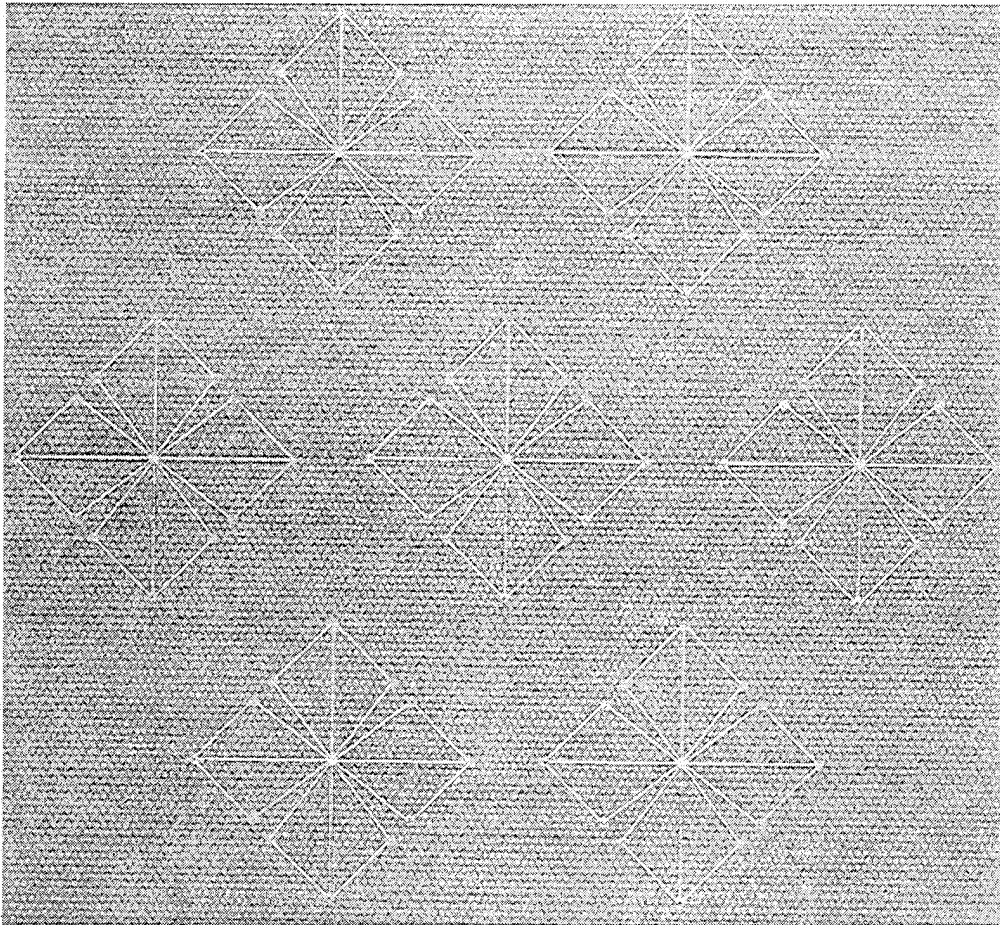


Figure 1. Photo of 7 Element Prototype Array

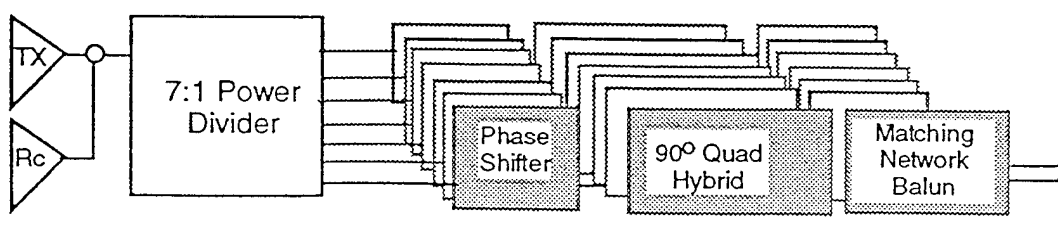


Figure 2. Feed Block Diagram

Measured VSWR for Full 7 Element Feed Input, Broadside Beam

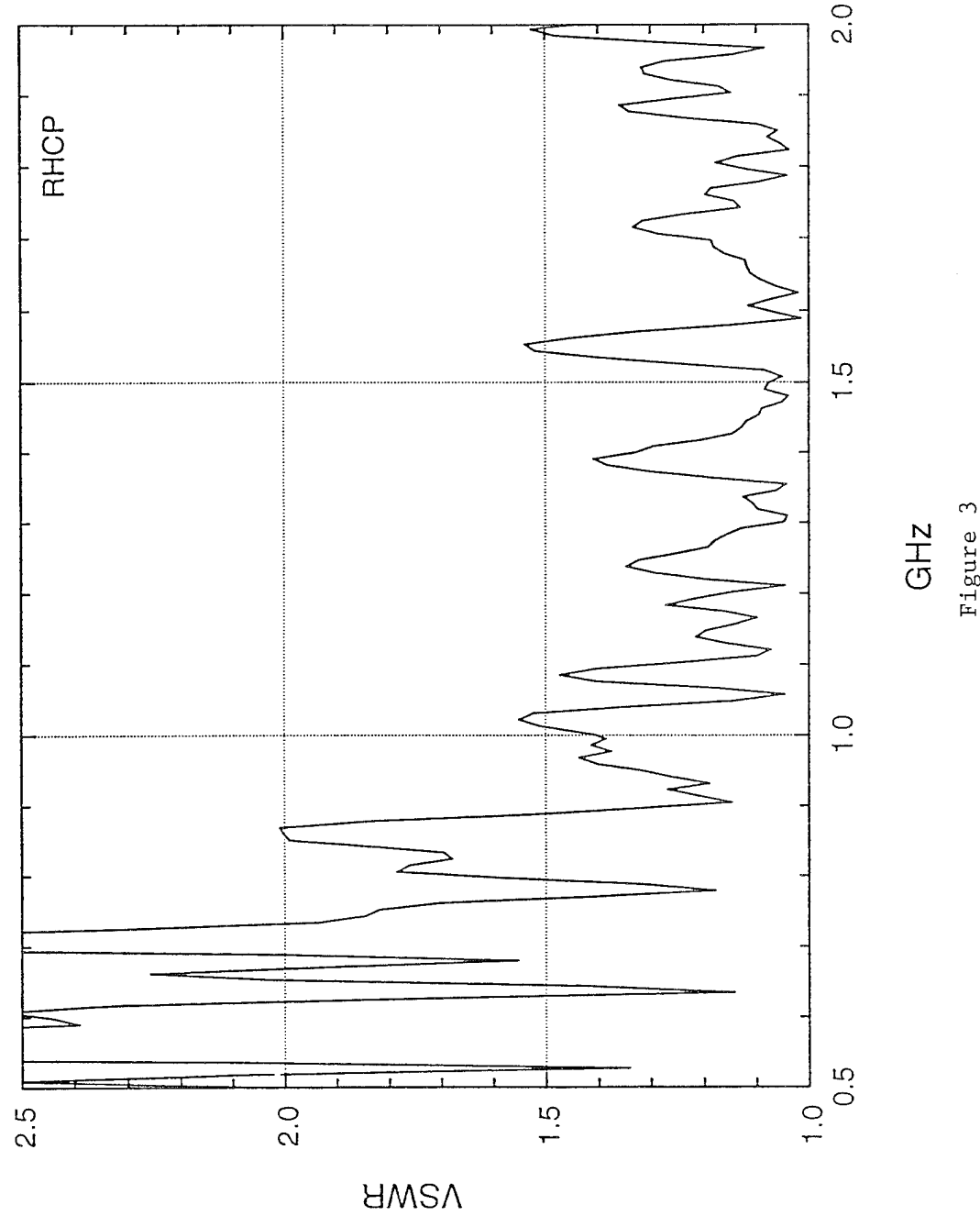


Figure 3

Measured VSWR for Full 7 Element Feed Input, Beam Scanned
Scan to 20 degrees off Broadside in $\Phi = 90$ plane (az)

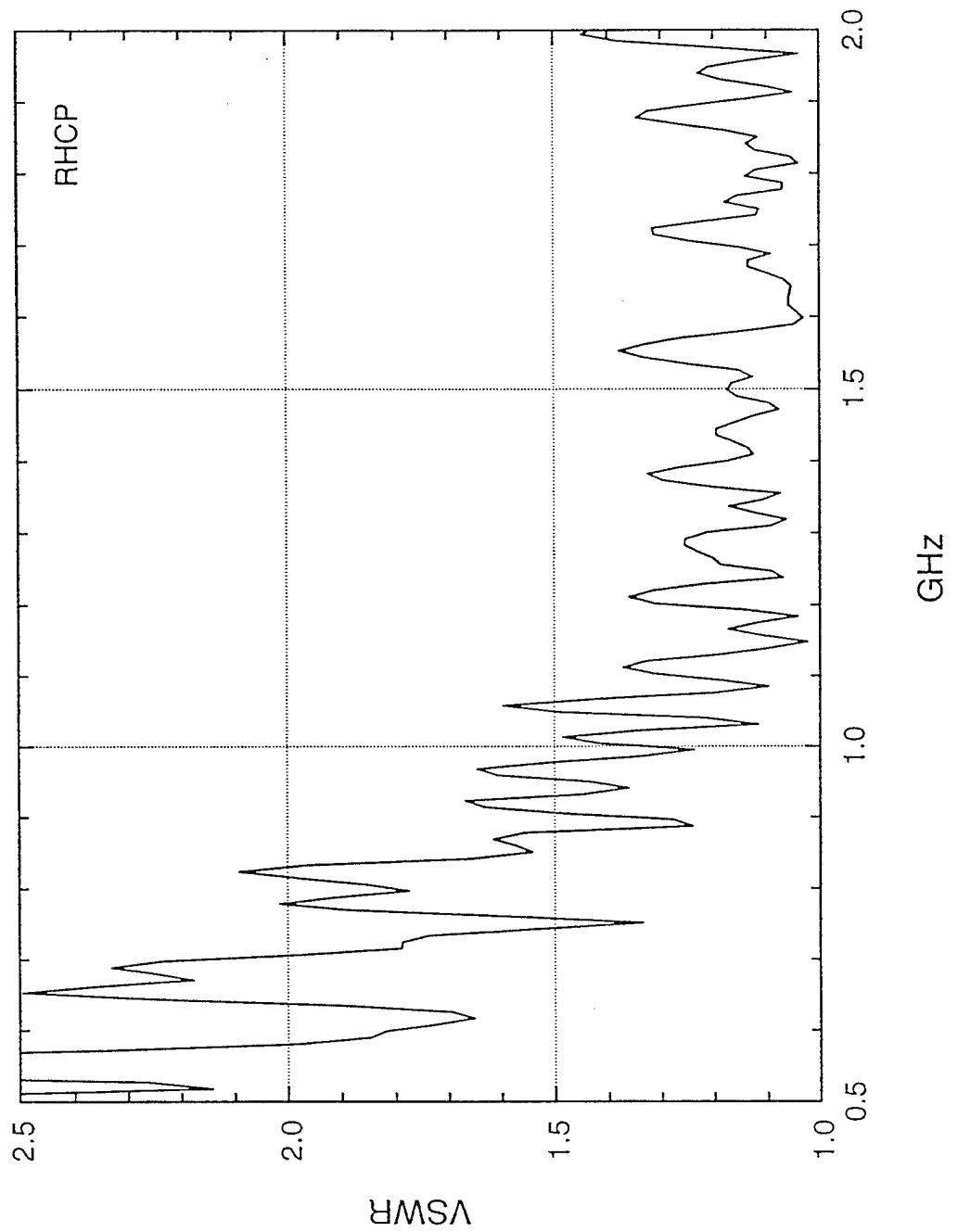


Figure 4

Measured VSWR for Central Element with Other 6 Elements Terminated

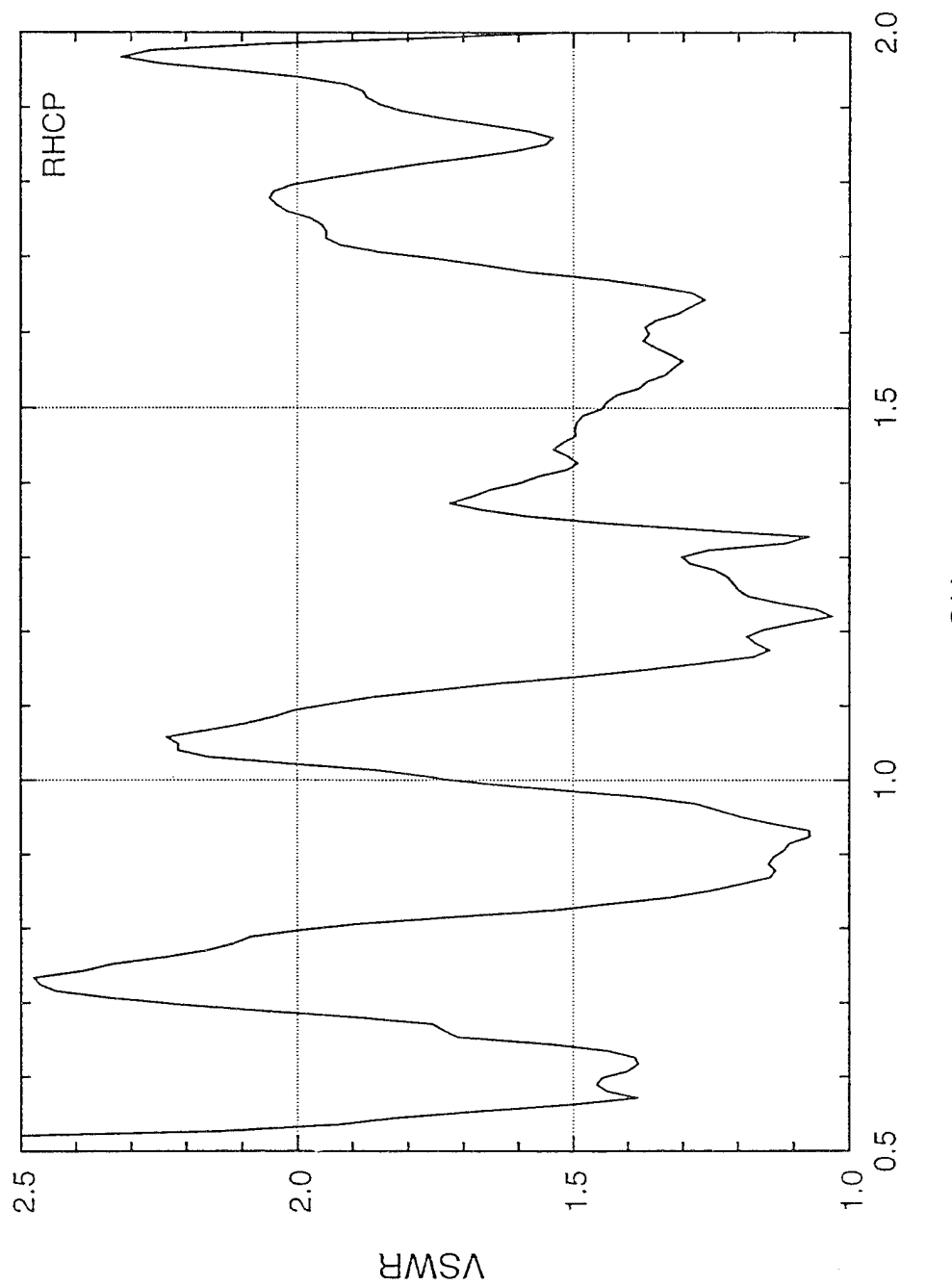


Figure 5

Wideband Microwave Phased Array Broadside Measured Pattern
Mismatch and Feed Loss included but not Phase Shifters

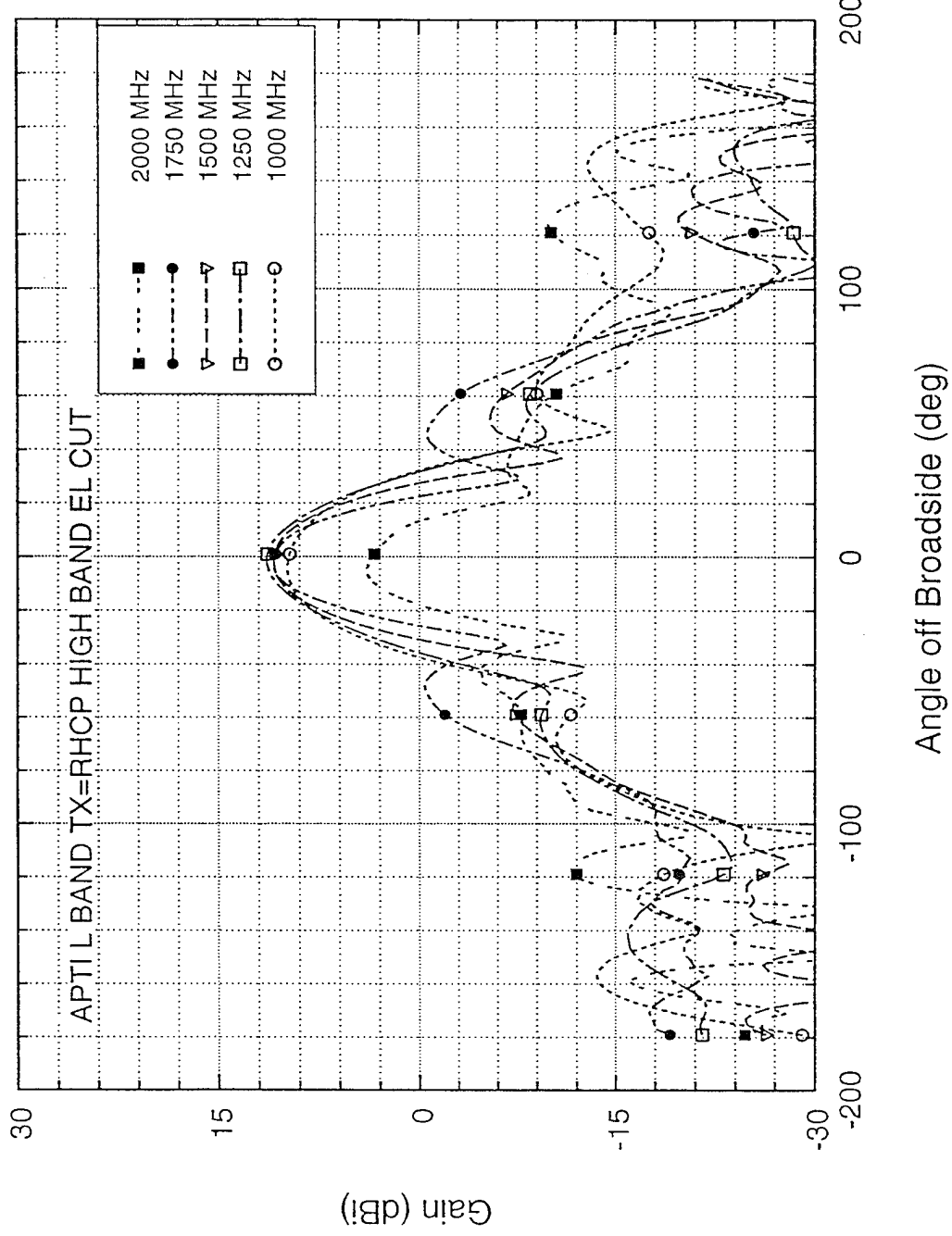


Figure 6

Wideband Microwave Phased Array Broadside Measured Pattern
Mismatch and Feed Loss included but not Phase Shifters

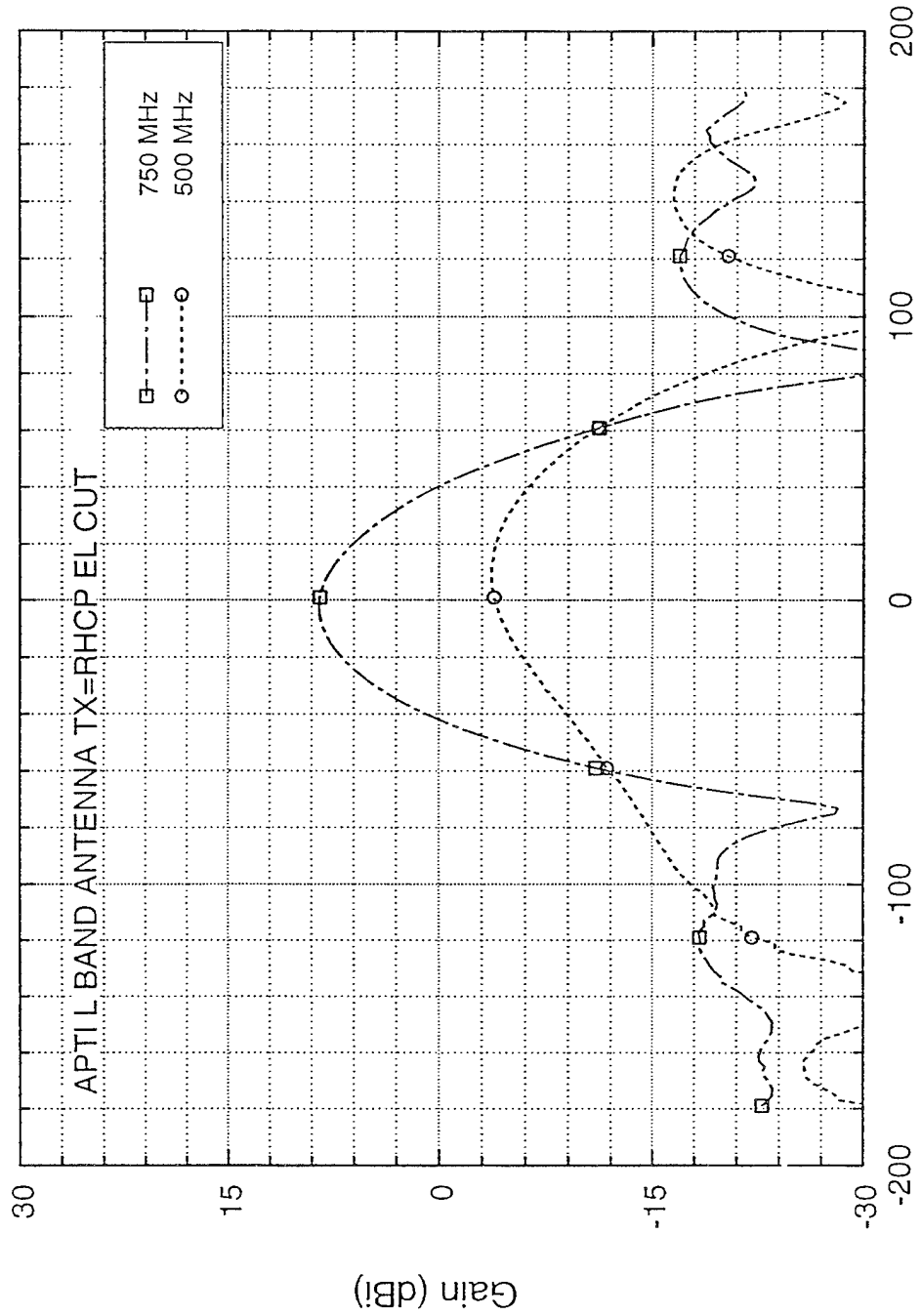


Figure 7

Wideband Microwave Phased Array Broadside Measured Pattern
Mismatch and Feed Loss included but not Phase Shifters

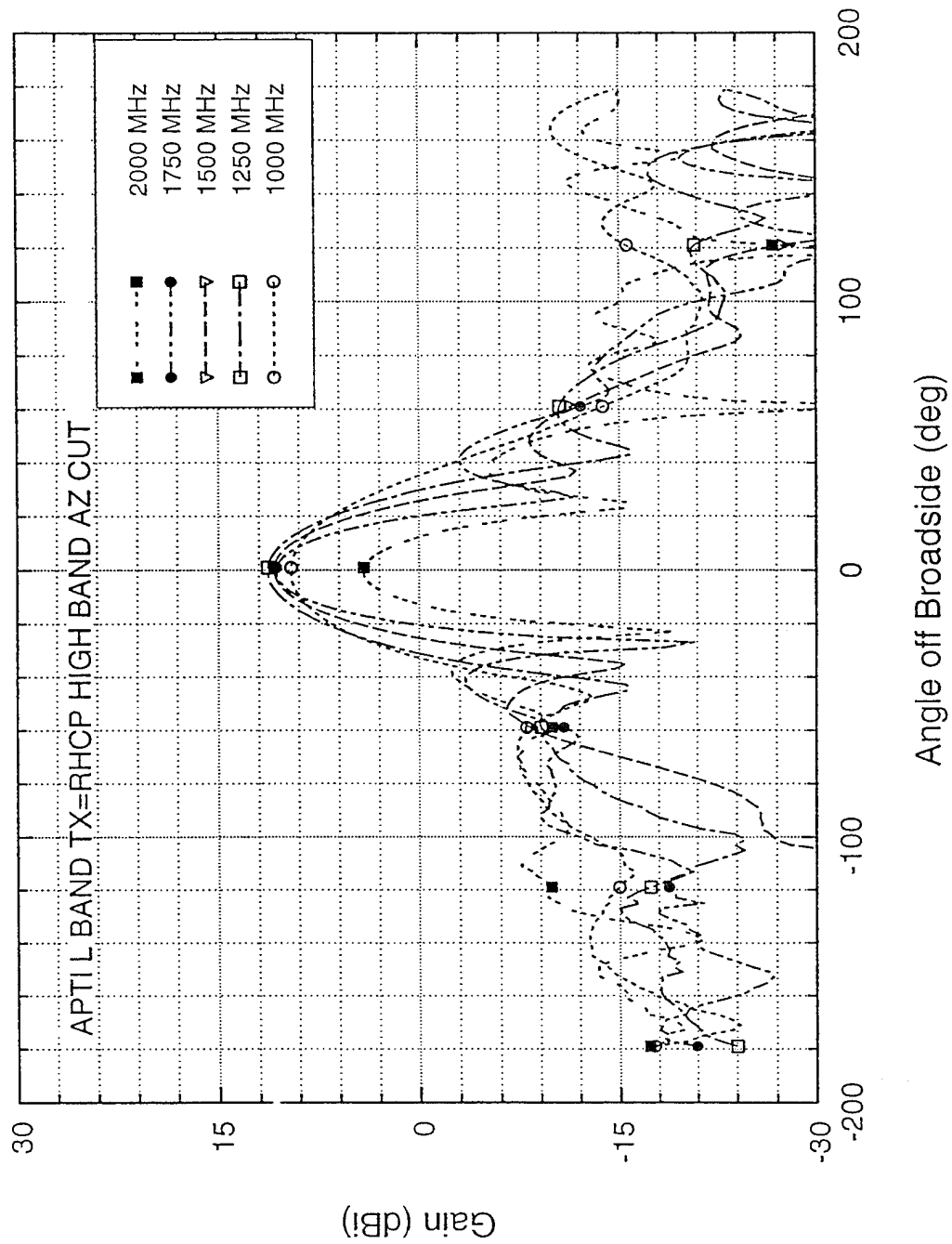


Figure 8

Wideband Microwave Phased Array Broadside Measured Pattern
Mismatch and Feed Loss included but not Phase Shifters

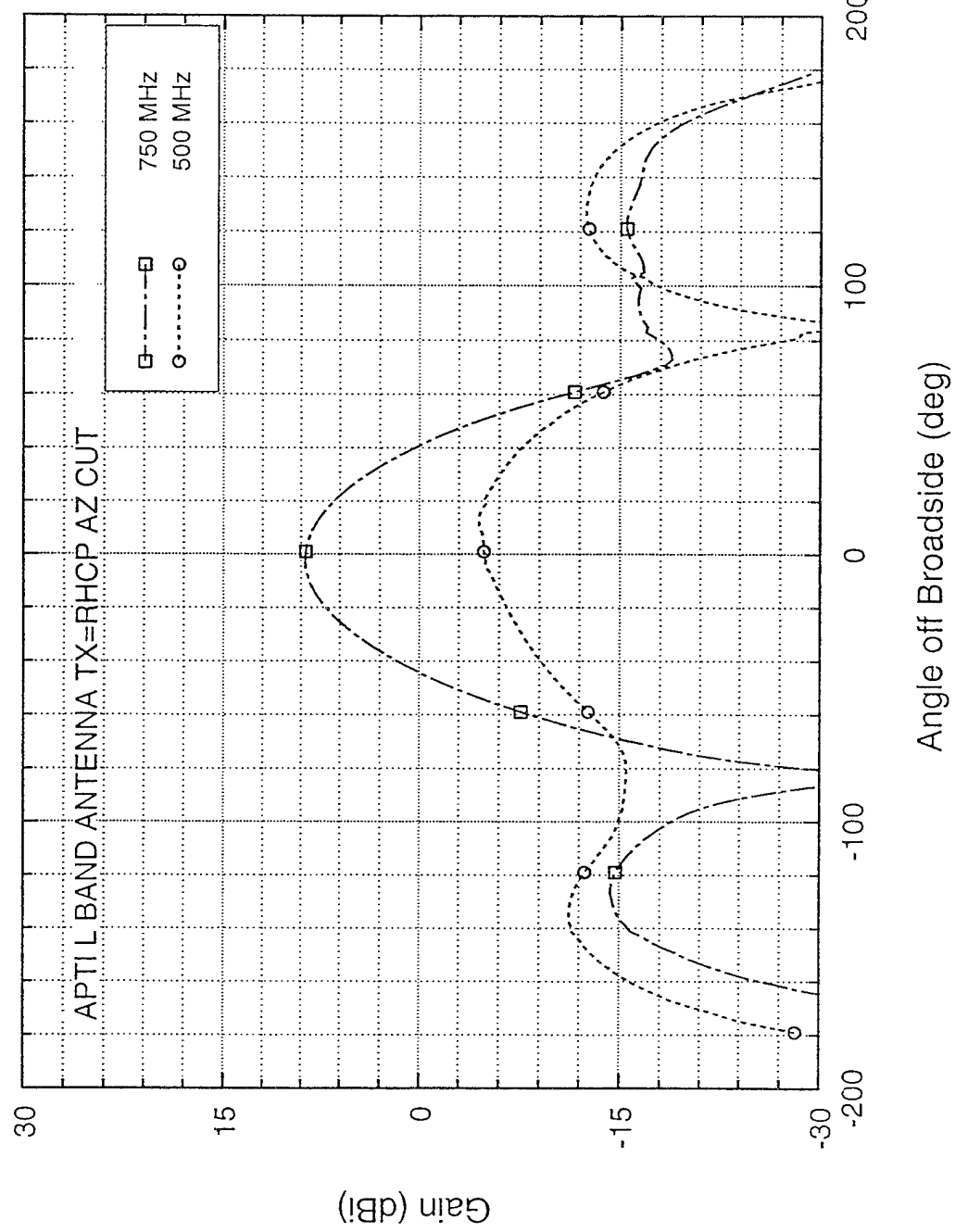


Figure 9

Wideband Microwave Phased Array Scanned Measured Pattern
Mismatch and Feed Loss included but not Phase Shifters

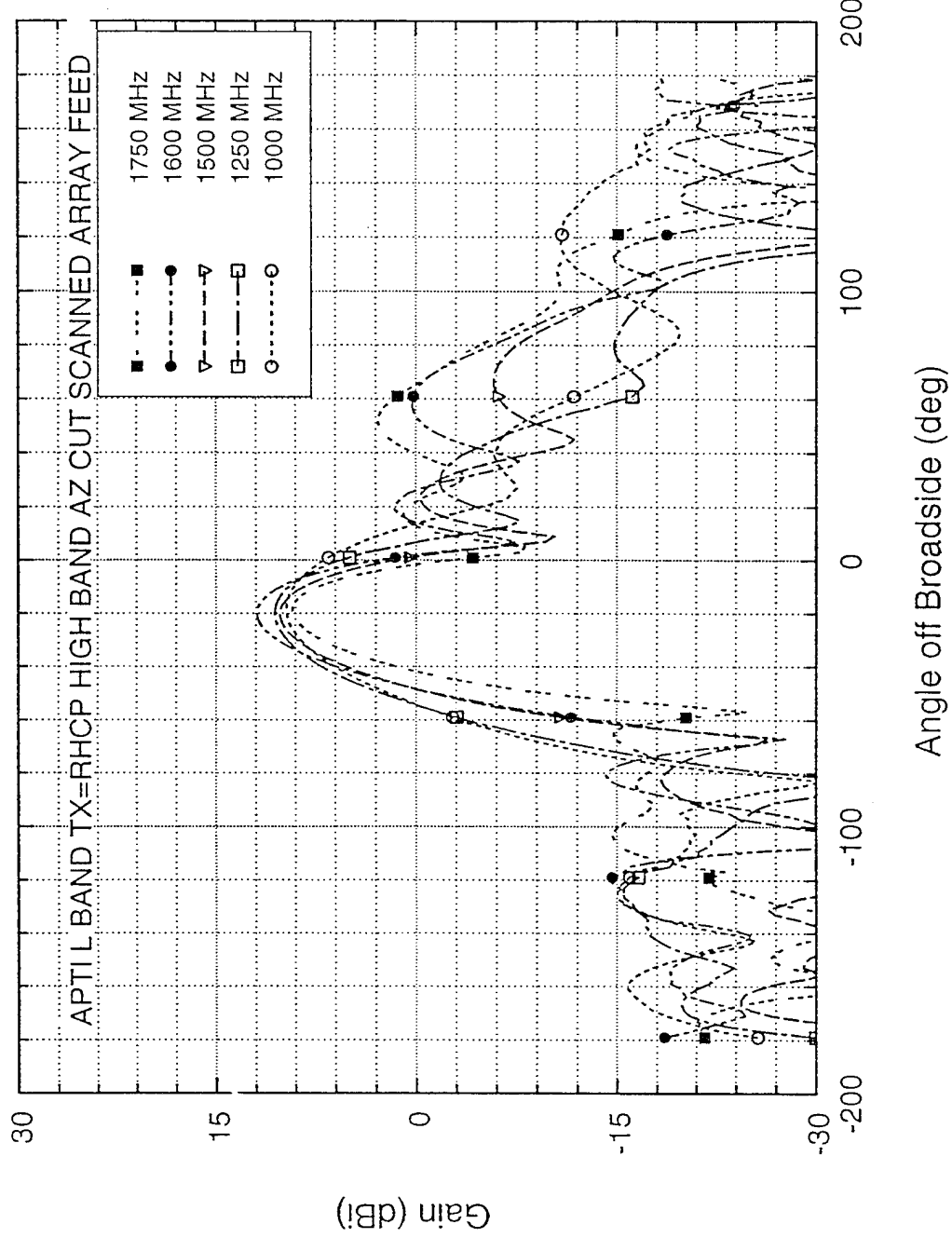


Figure 10

Wideband Microwave Phased Array Scanned Measured Pattern
Mismatch and Feed Loss included but not Phase Shifters

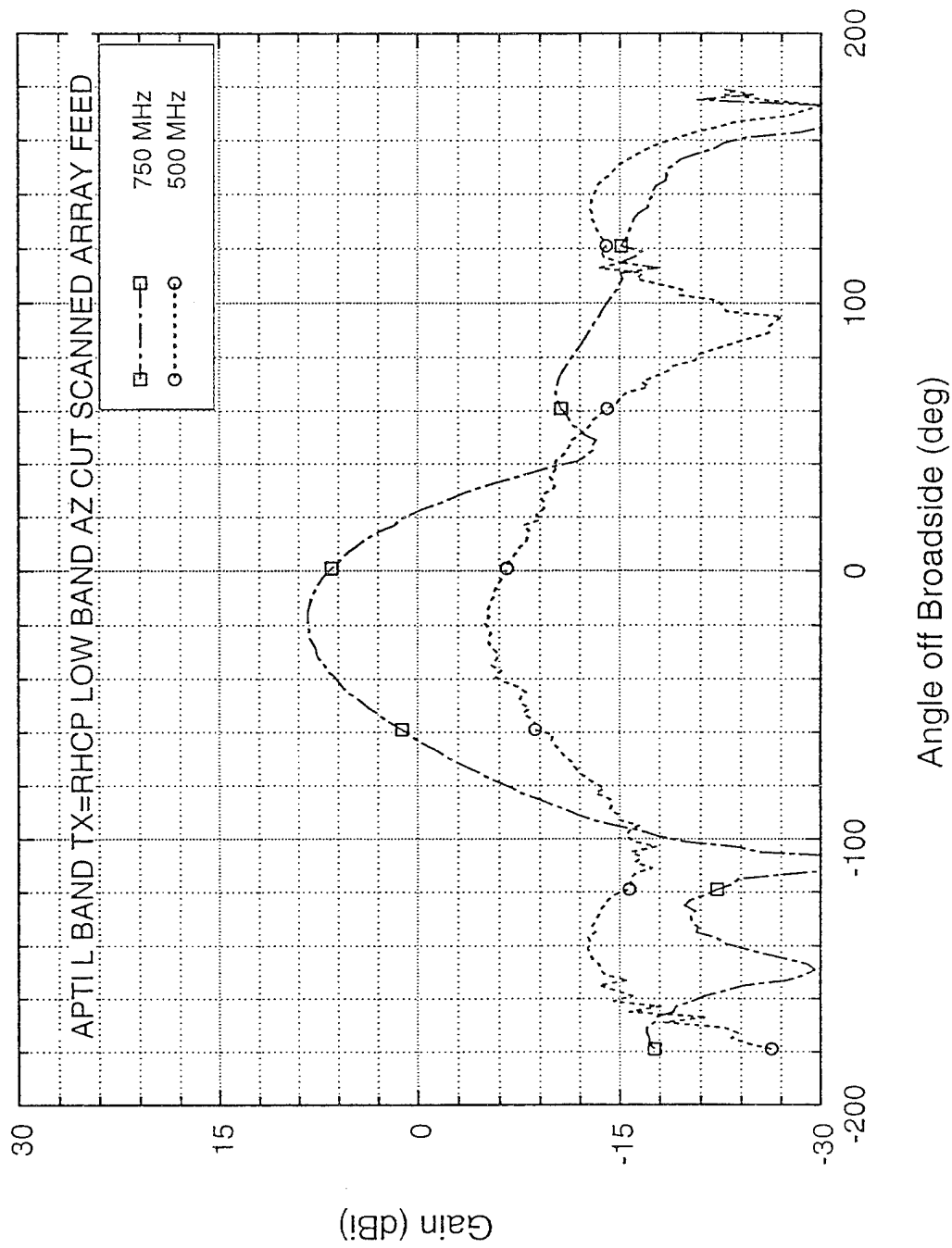


Figure 11

Array Gain, Directivity, and Loss for 7 Element Broadside Array

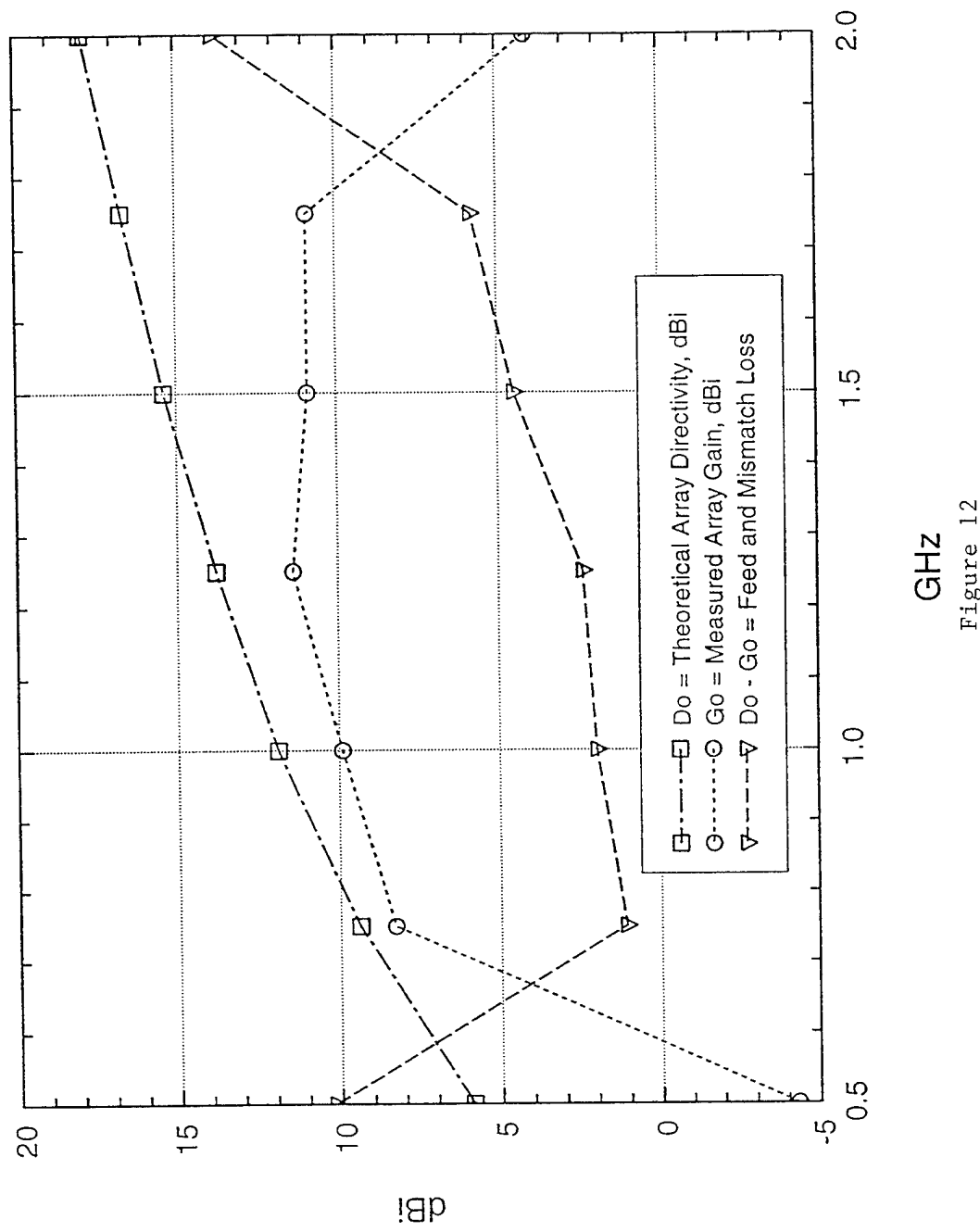


Figure 12
GHz

Wideband Microwave Phased Array Center Element Measured Pattern
Mismatch and Feed Loss included but not Phase Shifters

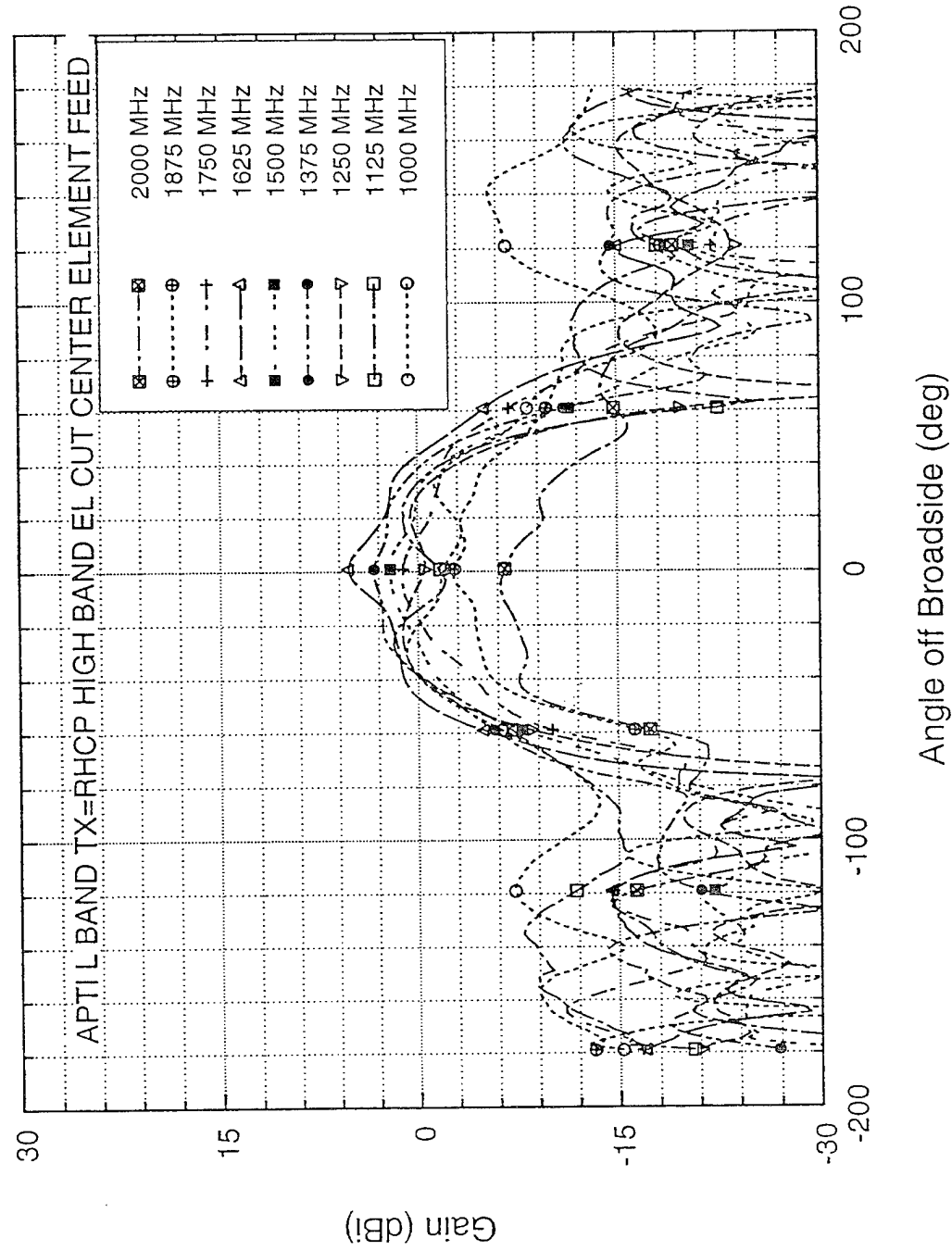


Figure 13

Wideband Microwave Phased Array Center Element Measured Pattern
Mismatch and Feed Loss included but not Phase Shifters

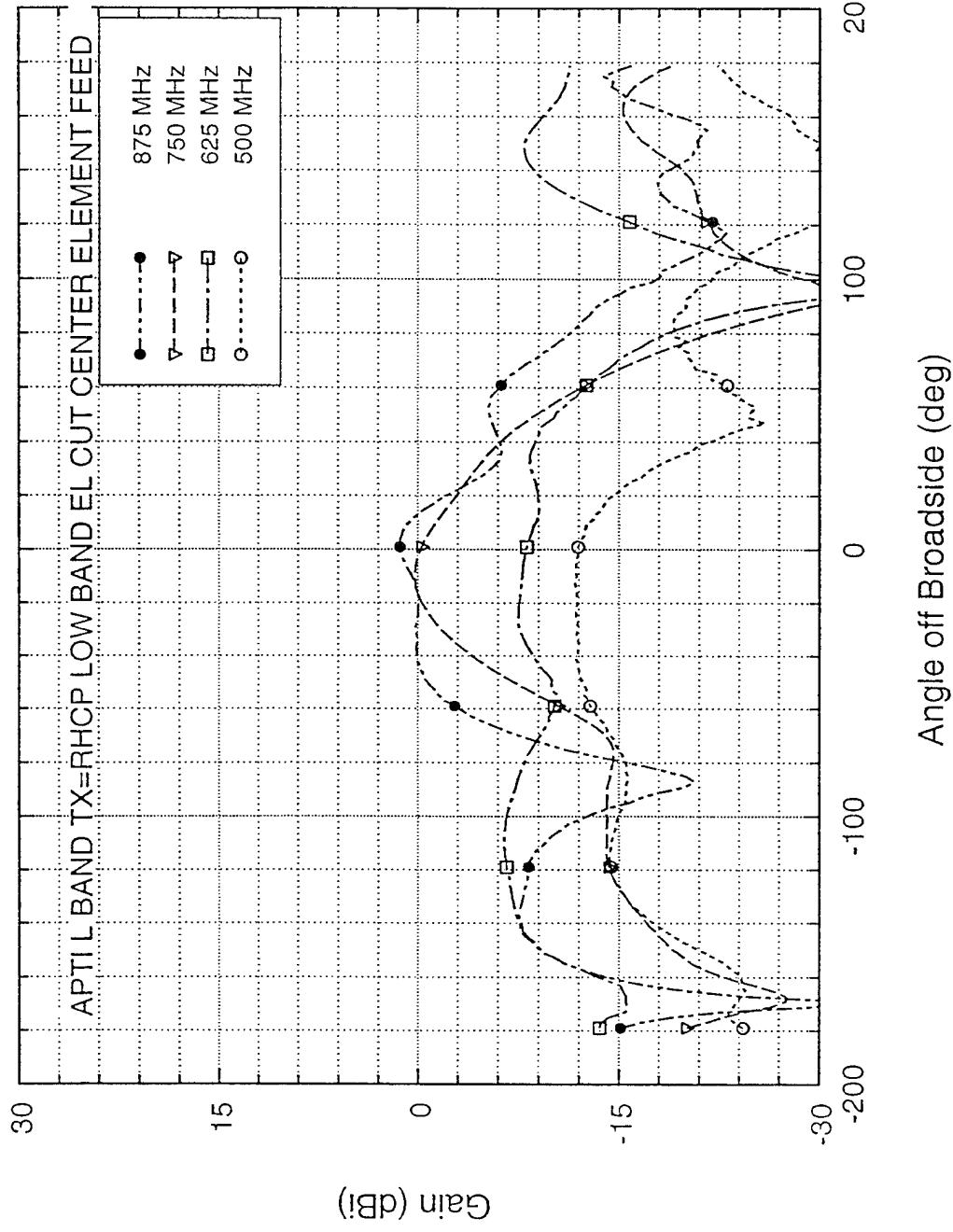


Figure 14

Wideband Microwave Phased Array Center Element Measured Pattern
Mismatch and Feed Loss included but not Phase Shifters

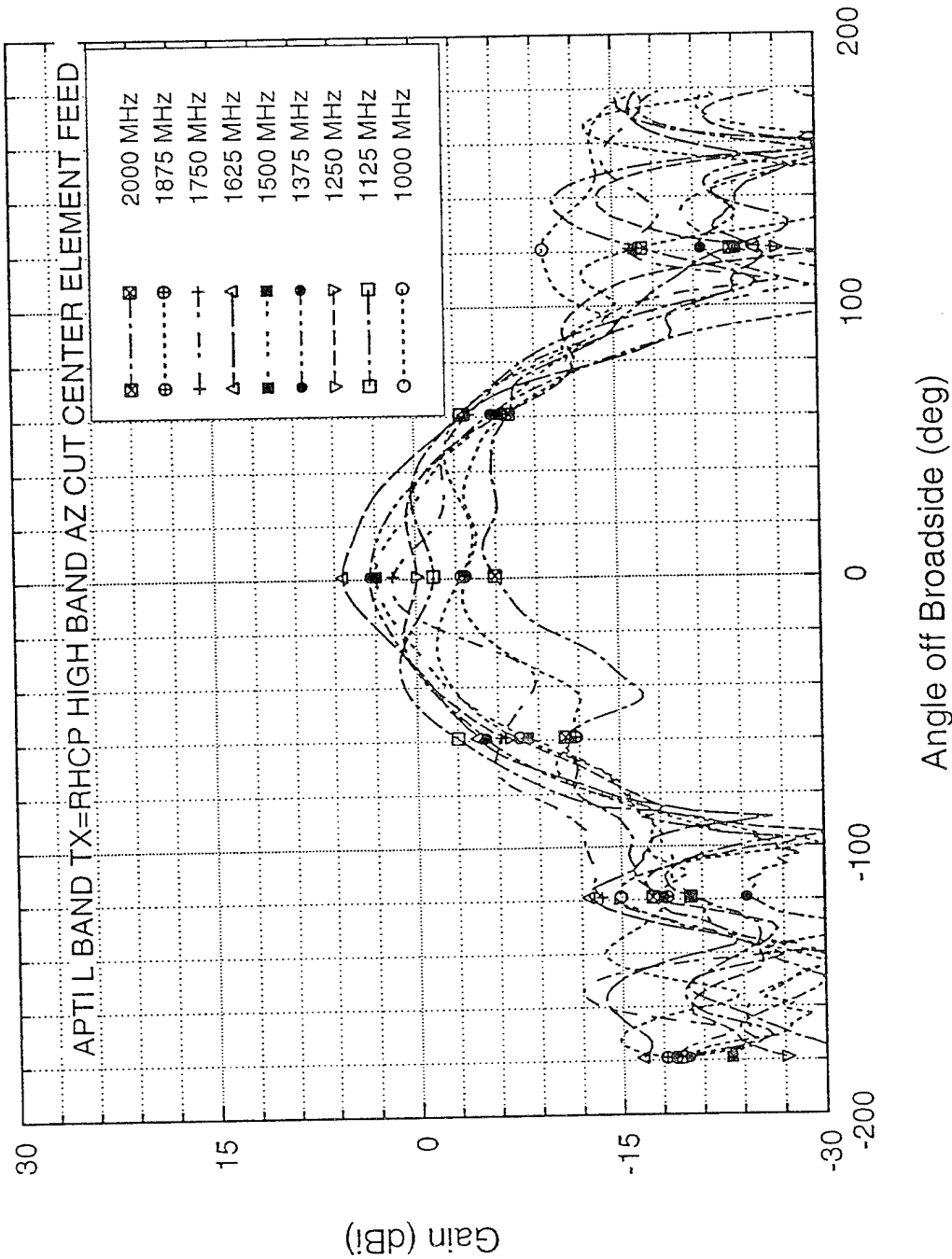


Figure 15

Wideband Microwave Phased Array Center Element Measured Pattern
Mismatch and Feed Loss included but not Phase Shifters

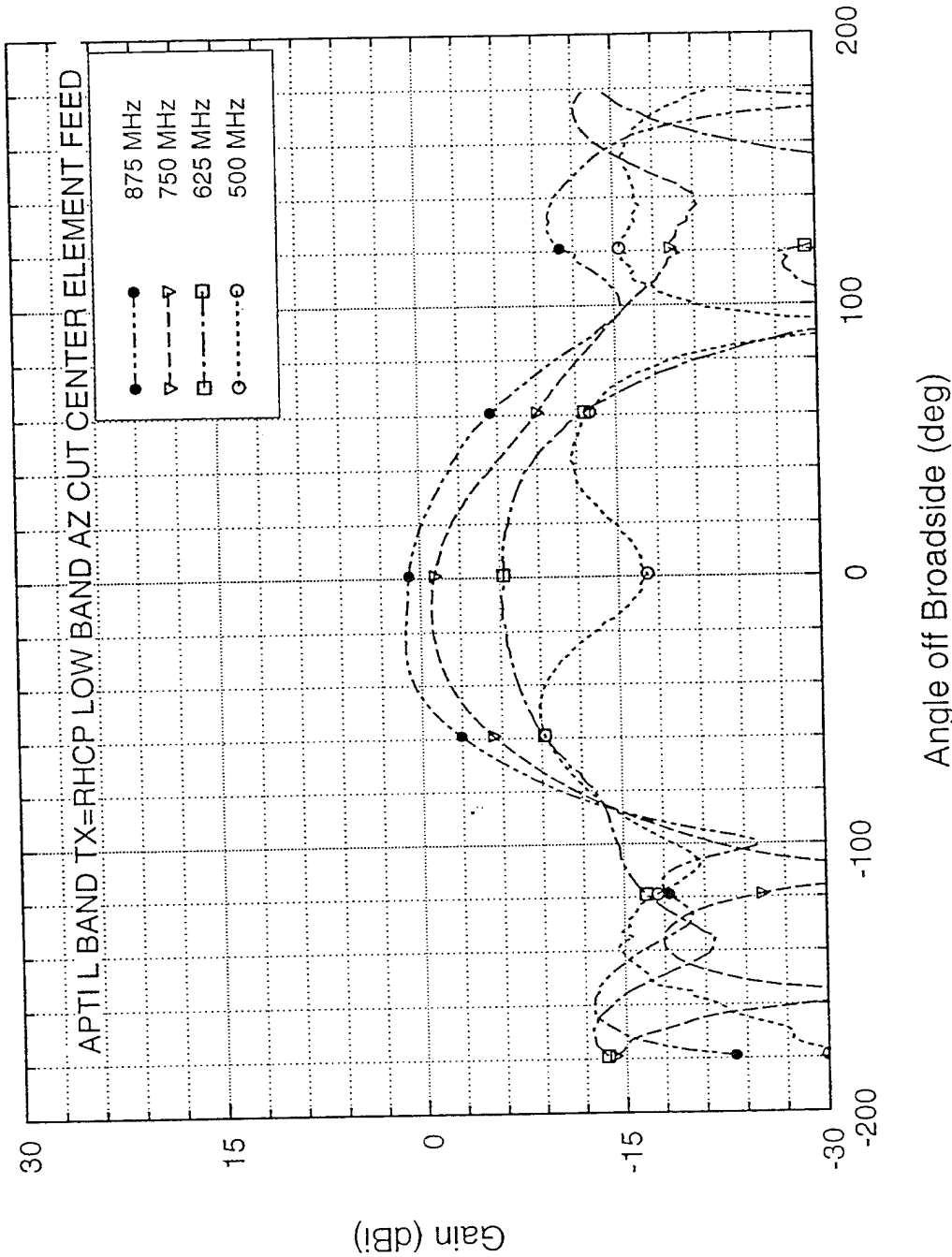


Figure 16

TOWARD A BETTER UNDERSTANDING OF WIDEBAND VIVALDI NOTCH ANTENNA ARRAYS

J. Shin and D.H. Schaubert

Antenna Laboratory

Department of Electrical and Computer Engineering

University of Massachusetts

Amherst, MA 01003

Abstract: A moderately thorough parameter study has been conducted to determine the relationships between several design parameters of Vivaldi notch antenna arrays and their wide-band, wide-scan performance. The results indicate promising starting points for designers wishing to develop new arrays for wide-band applications and they provide guidance to improve the performance of existing designs. The SWR of infinite, single-polarized, stripline-fed antenna arrays has been evaluated by using a full-wave method of moments analysis. The antennas typically exhibit a high SWR at the upper and lower limits of their frequency range. Between these limits, the SWR oscillates. The results show how the upper and lower limits and the inband oscillations change as the antenna parameters(exponential taper, grid spacings, stripline stub, slotline cavity, etc.) are varied. The undesirable effects of one parameter change can be compensated by changing a second parameter in most cases. The upper frequency limit for H-plane scanning is restricted by a scan blindness, which depends strongly on array grid spacings. Adjustment of antenna parameters has led to a design with $\text{SWR} < 2$ over a bandwidth of 4.7:1 and a scan volume of ± 45 degrees in the E- and H-planes.

1. Introduction

The use of Vivaldi notch antennas for wide-band/wide-scan phased arrays was proposed more than two decades ago[1]. Although a number of successful arrays have been demonstrated, the fundamental operation of these antennas is not yet well understood, nor can designers reliably create new arrays fulfilling specified requirements without a great deal of design iteration. The advent of accurate numerical simulations for these antennas has made it possible to replace many of the empirical iterations with numerical analysis, but rapid convergence to a good design is still highly dependent upon the experience

of the designer and few results have been published to aid designers in the best choice of starting points or in the most fruitful areas to explore when a design needs improvement. The intent of this paper is to present a summary of numerous studies that were undertaken to ascertain the effects of various design parameters on the performance of wide-band/wide-scan Vivaldi notch antenna arrays. The studies have focused on successful designs and, although they are not exhaustive, they yield insights into what is needed for a successful design and how to improve a design that is nearly good enough.

The studies have been performed by using a full-wave numerical analysis that has been fully validated by comparison to other analyses and to experimental data. The algorithm treats infinite phased arrays, so the results are useful for large scanning arrays. This paper considers only single-polarized arrays. Additional work is commencing to study dual-polarized arrays. The paper presents SWR versus frequency for numerous parameter variations and identifies trends that are useful in designing arrays. Section 2 describes the parameters of the antenna arrays. Section 3 briefly describes the methods used in the study, and section 4 contains the results and discussions.

2. Parameters of a Vivaldi Notch Antenna Array

The parameters of a Vivaldi notch antenna array are defined in Figs. 1 and 2. They can be classified into the substrate parameters(relative dielectric constant, ϵ_r , and thickness, t), the array grid dimension parameters(H-plane spacing, a , and E-plane spacing, b), and the antenna element parameters, which can be subdivided into the stripline/slotline transition, the taper section, and the stripline stub and slotline cavity. The stripline/slotline transition is specified by W_{ST} (stripline width) and W_{SL} (slotline width). The exponential taper profile is defined by the opening rate R and two points $P_1(z_1, y_1)$ and $P_2(z_2, y_2)$

$$y = c_1 e^{Rz} + c_2$$

where

$$c_1 = \frac{y_2 - y_1}{e^{Rz_2} - e^{Rz_1}}$$

$$c_2 = \frac{y_1 e^{Rz_2} - y_2 e^{Rz_1}}{e^{Rz_2} - e^{Rz_1}}.$$

The taper length L is $z_2 - z_1$ and the aperture height H is $2(y_2 - y_1) + W_{SL}$. The parameters related to the stripline stub and slotline cavity shown in Fig.2 are as follows:

- L_C : length of rectangular slotline cavity,
- H_C : height of rectangular slotline cavity,
- L_G : offset of rectangular slotline cavity from the ground plane,
- D_{SL} : diameter of circular slotline cavity,
- L_{STB} : length of uniform stripline stub,
- R_R : radius of radial stripline stub,
- A_R : angle of radial stripline stub,
- D_{ST} : diameter of circular stripline stub,
- L_{TC} : distance from the transition to the slotline cavity,
- L_{TA} : distance from the transition to the taper.

3. Method of the Parameter Study

In this parameter study, we are interested in the impedance bandwidth of the arrays. The program used for computing the active input impedance of the arrays is based on the Green's Function–Moment Method formulation[2]. It treats infinite phased arrays by analyzing the unit cell in detail. Triangular basis functions[3] have been added to improve the modeling capability for exponentially flared slots. Impedance matrix interpolation[4] has been used to speed up the overall computations over a given frequency band.

For a given set of parameters, the MoM analysis and the interpolation produces the active input impedance, $Z_{in}(f)$, from which the impedance band-

width ($\text{SWR} < 2.0$) is calculated. Generally, Z_c , the characteristic impedance of the stripline which gives good coupling to slotline is different from the system impedance, which is usually 50Ω . Two kinds of transitions from Z_c to 50Ω can be used; a tapered one of Fig.3(a) and a stepped one of Fig.3(b). The former is used when the $Z_{in}(f)$ shows a wideband match to Z_c and the latter is used for the cases of wideband match to 50Ω . The resultant bandwidths are defined as BW_{Zc} and BW_{50} , respectively. There are cases where a wider impedance bandwidth can be achieved, even though both BW_{Zc} and BW_{50} are not satisfactory. By using transmission line theory, $Z_{in}(x, f)$, the input impedance along the stripline is computed from $Z_{in}(f)$ and the position where widest impedance match to 50Ω occurs can be determined. The use of the stepped transition at an appropriate position as shown in Fig.3(c) results in the maximum bandwidth, MBW_{50} .

Initially, the array grid dimensions are fixed to $a = 3.45$ cm and $b = 3.2$ cm for studying the effects of antenna element parameters. With these dimensions, the upper frequency is limited to about 5 GHz to ensure no grating lobes over $\pm 45^\circ$ scan volume in both E- and H- planes. Later, the array grid dimensions are reduced and the upper limit of the computation frequency increases accordingly. The introductory stage of the parameter study has been focused to broadside scan performance. After narrowing down to some good sets of parameters, the scan performance has been studied by computing the SWR's of broadside, H-plane 45° , and E-plane 45° scan. The relative dielectric constant of the substrate is fixed to 2.2 for studying the effects of antenna element parameters and array grid dimensions. Dielectric thicknesses of 0.144 cm, 0.288 cm, and 0.4 cm have been studied.

4. Results and Discussions

4.1 Antenna Element Parameters

Intuitively, one suspects that the design of the basic radiating element must be reasonably “good” if wideband array performance is to be achieved. The parameter studies that follow are not thorough because there are too many parameters to fully explore all combinations in a single effort. However, based upon much more data that also have been evaluated, many of the trends exhibited here will be observed for other values of the fixed parameters. Furthermore, these studies emphasize successful designs, so the trends displayed here may be especially useful in optimizing an array that is performing reasonably well.

4.1.1 stripline/Slotline Transition

The transition from stripline to slotline is important, so various values of W_{ST} and W_{SL} have been studied for the three dielectric thicknesses. The parameter study was conducted by varying R from 0.01 to 0.7 to find the maximum usable bandwidth with fixed values of W_{ST} and W_{SL} . All other parameters are fixed to $H = 2.2$ cm, $L = 4.5$ cm, $L_C = 0.5$ cm, $H_C = 1.2$ cm, $L_G = 0$ cm, $L_{STB} = 1.4$ cm, and $L_{TC} = L_{TA} = 0.25$ cm. The shape of the antenna is shown in the inset of Fig.4.

Tables 1 – 3 show broadside scan BW_{Zc} and MBW_{50} for the dielectric thicknesses of $t = 0.144$ cm, 0.288 cm, and 0.4 cm, respectively. In Table 1 the data for $W_{ST}=0.025$ cm are available only for $W_{SL}=0.05$ cm, because for such narrow stripline width the results of the computations converge very slowly and we didn’t compute for other slot widths. From the tables it can be observed that

1. In most cases, MBW_{50} is greater than BW_{Zc} ,

Table 1. Broadside impedance bandwidth: substrate thickness = 0.144 cm.

W_{ST} (Z_C)	BW_{ZC}		MBW_{50}					
	1.0 GHz	5.0 GHz	1.0 GHz	5.0 GHz				
0.025 cm (109 Ω)								
0.05 cm (81 Ω)	1.30 1.23	5+ 4.05	1.35 1.15	5+ 5+	1.30 1.22	4.89 4.65	1.39 1.43	2.80 2.82
0.1 cm (56 Ω)	2.05 1.91	3.35 5+	1.96 1.18	5+ 5+	2.16 2.02	3.45 3.61	1.23 1.23	2.52 2.61

2. There are many stripline/slotline combinations which result in bandwidths of about 4:1. The limit of the lower operating frequency end(f_L) is about 1.2 GHz and that of the upper end(f_U) extends up to 6 GHz in some cases but is set to 5 GHz to ensure no grating lobes in $\pm 45^\circ$ scan volume.

3. For wide slot width of 0.2 cm, the operating bandwidths are very narrow except a few cases.

4. For the same stripline width and dielectric constant, f_L decreases slightly as W_{SL} decreases, ignoring a few cases where f_L is determined by the first in-band hump. This might be due to the effectively longer stub length when measured from the top edge of the slotline instead of the center.

4.1.2 Tapered Section

The typical frequency response of a wideband design using a uniform stripline stub and rectangular slotline cavity shows two or three in-band humps, a very steep increase in SWR below f_L , and a less steep increase above f_U . Fig.4 shows the effects of the exponential opening rate R for a typical case where $t = 0.144$ cm, $W_{ST} = 0.05$ cm, $W_{SL} = 0.05$ cm. As shown in Fig.4, f_L

Table 2. Broadside impedance bandwidth: substrate thickness = 0.288 cm.

W_{SL} (Z_C)	BW_{Zc}		MBW_{50}	
	1.0 GHz	5.0 GHz	1.0 GHz	5.0 GHz
0.025 cm				
0.05 cm (109 Ω)	1.47 3.45		1.53 5+	
	1.36 3.66		1.38 3.77	
0.1 cm (81 Ω)	1.33 4.65		1.33 5+	
	1.32 4.06		1.28 4.01	
0.2 cm (56 Ω)	1.94 5+		1.21 5+	
	1.18 5+		1.2 5+	
0.24 cm (50 Ω)	2.07 5+		1.99 5+	
			1.21 2.74	
			1.22 2.53	

Table 3. Broadside impedance bandwidth: substrate thickness = 0.4 cm.

W_{SL} (Z_C)	BW_{Zc}		MBW_{50}	
	1.0 GHz	5.0 GHz	1.0 GHz	5.0 GHz
0.025 cm				
0.1 cm (94 Ω)	1.46 3.48		1.50 4.16	
	2.7 3.83		1.41 3.89	
0.2 cm (68 Ω)	1.34 5+		1.36 5+	
	1.22 4.53		1.23 5+	
0.24 cm (61 Ω)	1.30 5+		1.30 5+	
	1.20 5+		1.22 5+	
			1.29 4.79	
			1.21 4.90	
			1.31 2.68	
			1.31 4.58	

decreases as R increases and the in-band humps can be controlled by varying R . The small discontinuities in the SWR plots are caused by the matrix interpolation scheme[4]. Smooth results can be obtained at the expense of increased computer time, but these results will not yield additional information.

Fig.5 shows a significant band broadening using the simple step transition for a case of Fig.4($R = 0.6$). This band-broadening technique often works when the SWR referred to Z_C of the in-band humps are less than about 2.5 and the real part of the impedances there are less than 50Ω . It is also possible to find the optimum position of the step transition for several scan conditions simultaneously, for example, broadside scan, H-plane 45° scan, and E-plane 45° scan.

To see the effects of taper length L , the maximum usable bandwidth is determined by varying the opening rate R with fixed values of $L=2.5\text{-}6.5$ cm in 1 cm steps. All other parameters are set as above except $t = 0.4$ cm, $W_{ST} = 0.2$ cm, and $W_{SL} = 0.05$ cm to get the results of Table 4. It was found that the bandwidth diminishes for $L \leq 3.5$ cm and that increasing L beyond 4.5 cm is of little value. Thus $L=4.5$ cm can be considered as the optimum taper length for the range of parameters studied here. As L increases, f_L decreases slightly but the first in-band hump gets larger, which limits the performances in the lower frequency range for longer tapers. It also has been noted that the number of the in-band humps increases as L increases, implying the reflection at the antenna aperture causes the in-band humps, at least partially.

The effects of the aperture height H have been studied for $H=1.7$, 2.2, and 3.2 cm with L fixed to 4.5cm. From the results in Table 5, f_L decreases as H decreases.

Table 4. Effects of the taper length, L . Unit:GHz

	$L = 3.5$ cm	$L = 4.5$ cm	$L = 5.5$ cm
BW_{Zc}	2.35 – 4.42	1.21 – 5.0 ⁺	1.76 – 5.0 ⁺
MBW_{50}	2.22 – 4.20	1.20 – 5.0 ⁺	1.17 – 5.0 ⁺

Table 5. Effects of the aperture height, H . Unit:GHz

	$H = 1.7$ cm	$H = 2.2$ cm	$H = 3.2$ cm
BW_{Zc}	1.98 – 4.76	1.21 – 5.0 ⁺	2.11 – 5.0 ⁺
MBW_{50}	1.15 – 5.0 ⁺	1.20 – 5.0 ⁺	1.28 – 5.0 ⁺

4.1.3 stripline/Slotline Cavities

Although Tables 1 – 3 show several cases in which the BW_{Zc} and/or MBW_{50} are greater than 3.5:1, in most cases the SWR of the in-band humps are close to 2.0 and in most cases the H-plane scan has a larger hump in the frequency ranges of 1.2 – 2.5 GHz. The case where $t = 0.288$ cm and $W_{ST} = W_{SL} = 0.1$ cm has shown the widest band over which the SWR's referred to Z_C are less than about 1.5 for the broadside scan, resulting in wider overall bandwidth in the $\pm 45^\circ$ scan volume than any other stripline/slotline combination. So in most of the following parameter studies, this transition is exploited to search for a wider operating frequency bandwidth.

Increasing the stub length, L_{STB} , decreases f_L a little, but the reduction of f_U is more severe than the benefit at the lower frequency. From the results shown in Fig.6, it can be concluded that the steep change of SWR in the lower frequency band is dominated by the imperfect performance of the “open circuit” provided by the slot cavity, whereas the the less steep change of SWR at the upper end is due to the imperfect performance of the “short circuit” provided by the stripline stub. The increases of SWR at higher frequencies in

Fig.6 correspond approximately to half-wavelength resonances at 5.5 GHz, 6.2 GHz, and 7.05 GHz for $L = 1.8$ cm, 1.6 cm, and 1.4 cm, respectively.

Fig.7 shows the effects of the backwall offset, $L_G=1$, 2, and 3cm. The lower end of the frequency band is reduced, but the enlarged in-band hump limits the wideband performance. It is also noticed that increasing L_G from 0 to 1 cm introduces a significant difference in the SWR performance below 2.5 GHz, but additional increments of L_G do not change the performance so much.

Fig.8 shows the effects of using a radial stripline stub and a circular slotline cavity. The radial stripline stub not only improves f_L further but also improves the first in-band hump and the higher end of the frequency band. Although it is not shown in Fig.8, a circular stripline stub of 0.9-cm diameter showed similar results as the radial stub of $R_R=0.8$ cm and $A_R=80^\circ$. In Fig.8, the circular slot cavity shows similar performance as the rectangular slot cavity. It is found that circular and rectangular slot cavities of approximately the same area result in similar SWR response.

Fig.9 shows the effects of the size of the radial stripline stub. The in-band humps change a little, but the overall performance does not change very much for the changes of $R_R=0.6$ cm to 0.8 cm.

Fig.10 shows the effects of the size of the circular slot cavity. For larger cavities, f_L decreases significantly, but the first in-band hump gets large to limit the overall wideband operation. For excessively large cavities, the first in-band hump cannot be compensated by changing other parameters.

The results presented so far have been limited to the broadside scan. Fig.11 shows the scan performances of broadside, H-plane 45° , and E-plane 45° for the same antenna array as in Fig.7 with $L_G= 1$ cm. The very large in-band hump around 1.8 GHz in broadside scan and H-plane 45° scan can be significantly improved by using a radial stub instead of the uniform stripline stub

as shown in Fig.12. The very sharp anomalies around 3.5 GHz and 4.73 GHz in H-plane scan have been verified by finite array measurements[5]. All other Vivaldi antenna arrays analyzed showed similar scan-blindness anomalies in H-plane scan, which limit the overall wideband and wide-scan performance of the arrays. The frequencies of the H-plane scan anomalies are independent of the slot cavity and the stripline stub, but decrease somewhat as the taper length L increases or the opening rate R increases. In the next section, it will be shown that the frequencies of the H-plane scan anomalies can be controlled by varying the array grid spacings.

4.2 Array Grid Dimensions a and b

Generally, the SWR performances of the broadside scan and E-plane scan are better than those of the H-plane scan and, thus, overall bandwidth is mainly determined by the H-plane scan performance, especially the first in-band hump and the first H-plane scan anomaly. The frequencies of the H-plane scan anomalies move upward significantly when the E-plane grid spacing b is reduced. The magnitudes of the in-band humps also change as the array grid spacing varies. Fig.13 shows plots of SWR in H-plane 45° scan for $b=1.7$ cm, 2.0 cm, 2.5 cm, and 3.2 cm with $a=2.5$ cm, $R=0.3$, and $H=1.7$ cm. All other dimensions are same as the array of Fig.12. The first in-band hump reduces as the b decreases. The frequency of the first H-plane scan anomaly is shifted from about 3.5 GHz to about 5.5 GHz as b decreases from 3.2 cm to 1.7 cm. The net effect of the reduced in-band hump and the increased frequency of the scan anomaly is an operating bandwidth of 4.7:1.

Fig.14 shows the effects of the H-plane spacing, a , on the frequency of the H-plane scan anomaly. The frequency of the first H-plane scan anomaly is shifted from about 4.8 GHz to about 6.0 GHz by varying a from 3.45 cm to 1.7 cm with b fixed to 1.7 cm. The magnitude of the first in-band hump

increases as a decreases, which is the opposite trend to the case of the E-plane spacing, b .

The amount of the frequency shift of the first H-plane scan anomaly due to the change of the grid spacing a or b also depends upon the value of the orthogonal grid spacing b or a , respectively, as shown in Fig.15. For $a=1.7$ cm, the frequency of the first H-plane anomaly is shifted from 3.65 GHz to 6 GHz as b is reduced from 3.2 cm to 1.7 cm, whereas it is shifted from 3.45 GHz to 4.77 GHz for the same change of b when $a=3.45$ cm. Similarly, for $b=1.7$ cm, the frequency of the first H-plane anomaly is shifted from 4.77 GHz to 6 GHz as a is reduced from 3.45 cm to 1.7 cm, whereas it is shifted from 3.45 GHz to 3.65 GHz for the same change of a when $b=3.2$ cm.

Thus it can be concluded that the frequency of the first H-plane scan anomaly is shifted upward as the grid spacing a or b is reduced. The frequency of the H-plane scan depends on a less sensitively than on b . The smaller is a , the larger is the frequency shift due to same change of b , and the smaller is b , the larger is the frequency shift due to same change of a .

The scan performances shown in Fig.16 for the broadside scan, H-plane 45°, and E-plane 45° scan exhibit about 4.7:1 bandwidth over a 45° scan volume. The grid spacings of the arrays are $a=2.5$ cm and $b=1.7$ cm, and all other parameters are the same as in Figs. 13 and 14.

4.3 Dielectric Constant ϵ_r

To see the effects of the dielectric constant of the substrate, ϵ_r is varied from 2.2 to 4 and 10 for the array of Fig.16. The main effect of high dielectric constant is the significant shift downward the frequencies of the H-plane scan anomalies as shown in Fig.17. It is also observed that the in-band humps get larger in size and move downward in frequency, which is the result of reduced wavelength λ_g due to the high dielectric constant. Thus, for Vivaldi antenna

arrays, lower dielectric constant appears to be better for wideband/widescan operation.

5. Conclusions

A moderately extensive parameter study of wideband Vivaldi notch antenna arrays has been performed by using a full-wave method of moments analysis. The study divided the antenna parameters into three broad categories: array grid, element metalization patterns, and dielectric substrate. The bulk of the parameter study was devoted to various aspects of the element metalization pattern. These include the stripline-to-slotline transition, the stripline stub and slotline cavity, and the exponential antenna taper. It was relatively easy to obtain $\text{SWR} < 2$ up to the maximum frequency for operation free of grating lobes in E-plane scan. Extending the lower operating frequency limit downward toward 1 GHz was difficult, but the use of radial stubs and properly chosen antenna tapers provides reasonably good performance. In-band humps in the SWR can be controlled by varying many of the antenna parameters, so that the adverse effects of some changes can be offset by other parameter changes. Extending the upper frequency limit for H-plane scan requires reduced E-plane spacing to move the scan anomaly to higher frequencies. The best design so far achieves $\text{SWR} < 2$ over a bandwidth of 4.7:1 and a scan volume of ± 45 degrees around broadside. Based on a limited amount of data, it appears that the antennas perform better when a lower permittivity substrate is used. Further studies of substrate permittivity are needed to explore the effects of several antenna parameters on high-permittivity substrates.

6. Acknowledgement

This work was supported in part by the US Army Research Office under contract DAAL03-92-G-0295.

References

- [1] L.R.Lewis, M.Fasset, and J.Hunt, "A broadband stripline array element," *Digest of 1974 IEEE Symp. Antennas Propagat.*, pp.335-337, 1974.
- [2] D.H.Schaubert, J.A.Aas, M.E.Cooley, and N.E.Buris, "Moment method analysis of infinite stripline-fed tapered slot antenna arrays with a ground plane," *IEEE Trans. Antennas Propagat.* vol.AP-42, no.8, pp.1161-1166, Aug. 1994.
- [3] S.M.Rao, D.R.Wilton, and A.W.Glisson, "Electromagnetic scattering by surfaces of arbitrary shape," *IEEE Trans. Antennas Propagat.* vol.AP-30, no.3, pp.409-418, May 1982.
- [4] E.H.Newman, "Generation of wide-band data from the method of moments by interpolating the impedance matrix," *IEEE Trans. Antennas Propagat.* vol.AP-36, no.12, pp.1820-1824, Dec. 1988.
- [5] D.H. Schaubert, W.C. Chang, and G.J. Wunsch, "Measurement of phased array performance at arbitrary scan angles," *Proc. of 1994 Antenna Applications Symp.*, Allerton Park, Monticello, Illinois, Sep. 21-23, 1994.

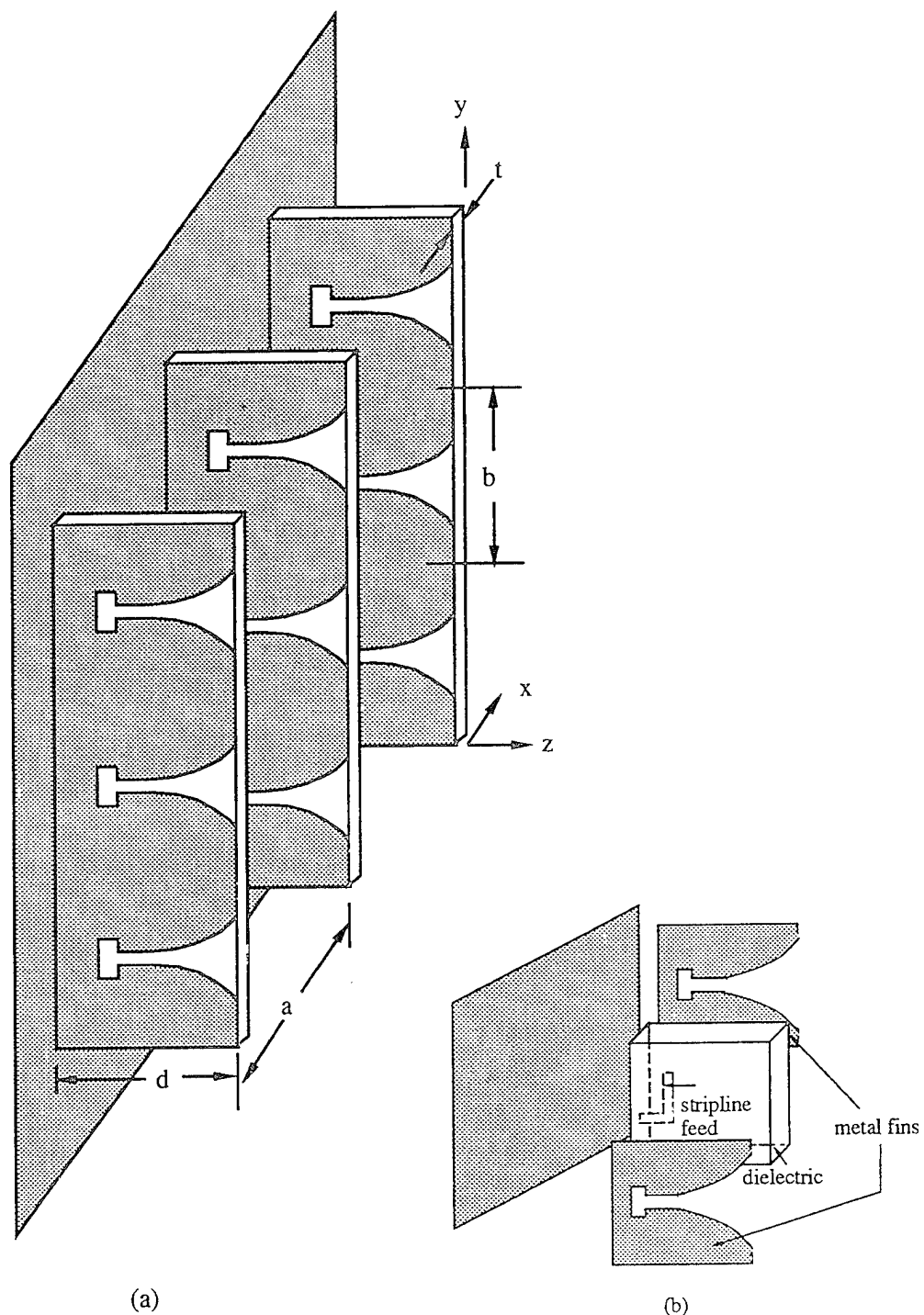
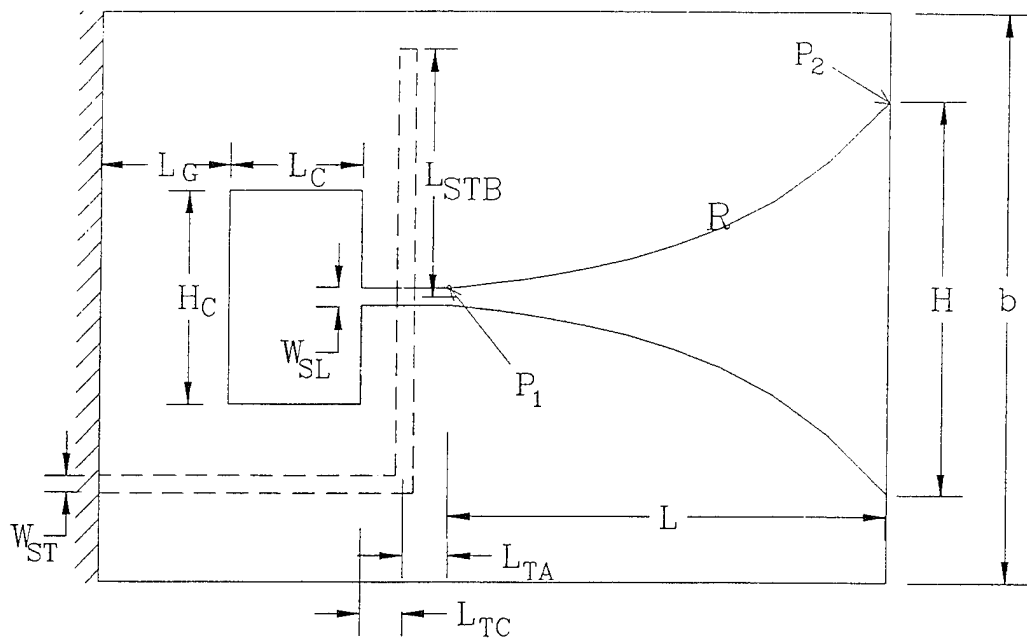
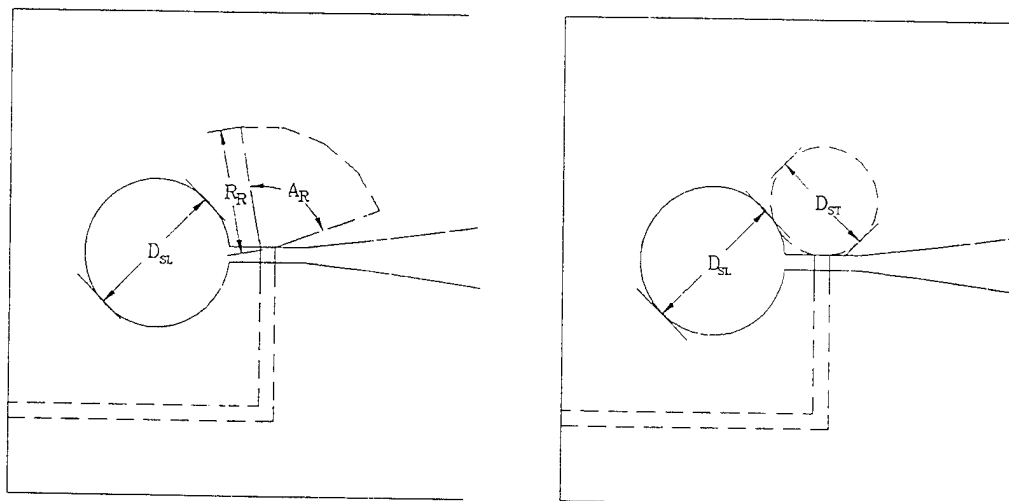


Figure 1. Stripline-fed Vivaldi notch antenna array: (a) portion of infinite array, (b) exploded view of antenna element showing stripline feed.



(a)



(b)

(c)

Figure 2. Definition of parameters of Vivaldi notch antenna element: (a) rectangular cavity and uniform stub, (b) circular cavity and radial stub, (c) circular cavity and circular stub.

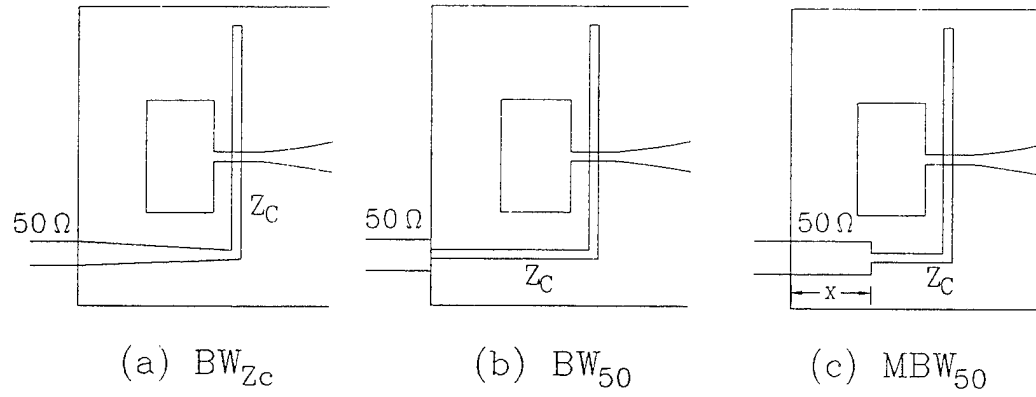


Figure 3. Transitions for various definitions of bandwidth.

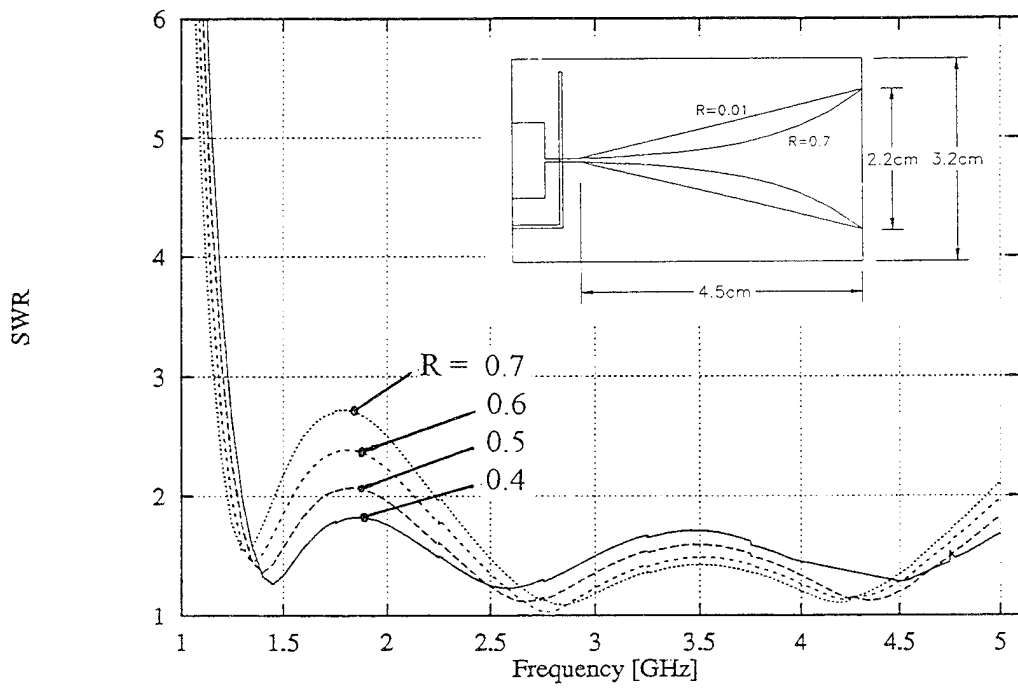


Figure 4. Effects of opening rate R . (BW_{Zc} , broadside scan, $\epsilon_r = 2.2$, $t = 0.144$ cm, $W_{ST} = 0.05$ cm, $W_{SL} = 0.05$ cm, $a = 3.45$ cm, $b = 3.2$ cm, $H = 2.2$ cm, $L = 4.5$ cm, $L_{STB} = 1.4$ cm, $L_C = 0.5$ cm, $H_C = 1.2$ cm, $L_{TC} = L_{TA} = 0.25$ cm, $d = 5.5$ cm)

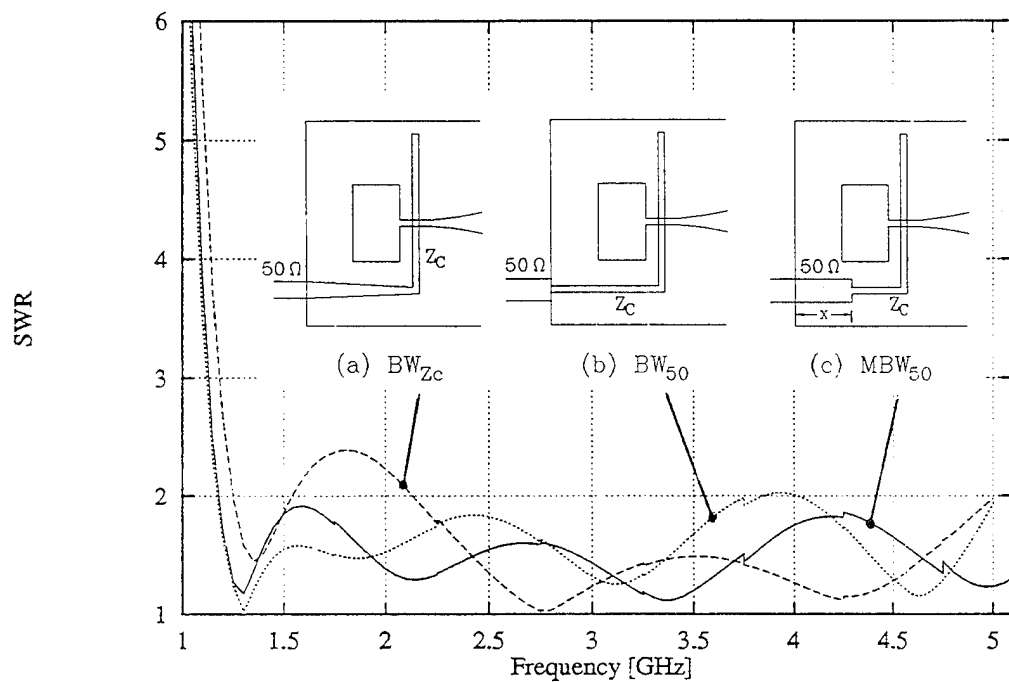


Figure 5. Band broadening effect of using a simple step transition. ($R = 0.6$ and all other parameters are same as in Fig.4)

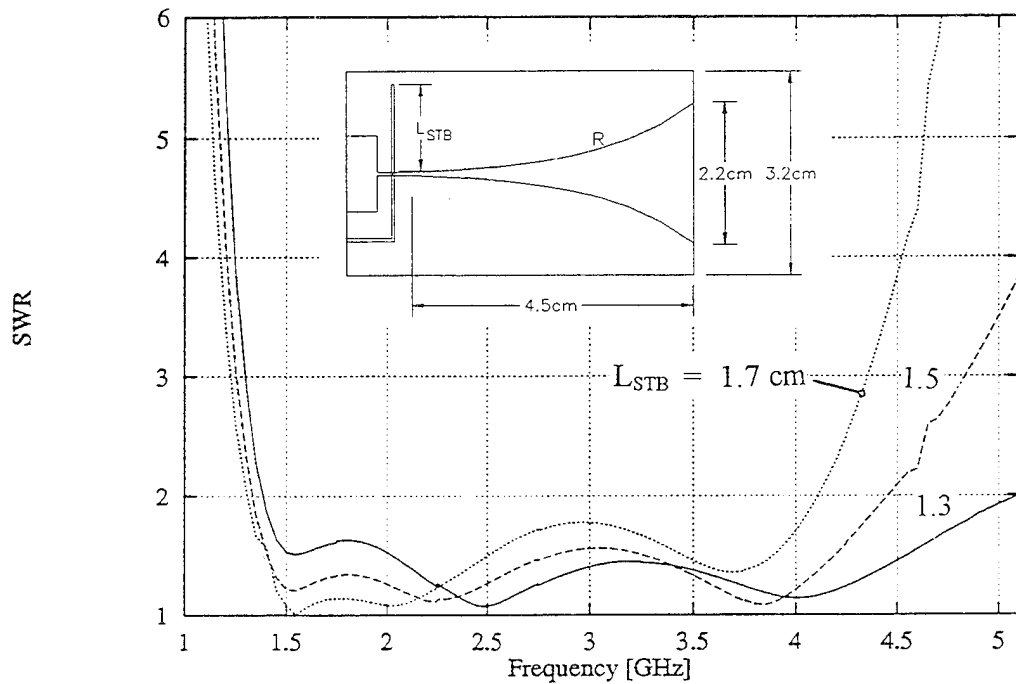


Figure 6. Effects of stripline stub length, L_{STB} . (BW_{Zc} , broadside scan, $\epsilon_r = 2.2$, $t = 0.288$ cm, $W_{ST} = 0.1$ cm, $W_{SL} = 0.1$ cm, $a = 3.45$ cm, $b = 3.2$ cm, $R = 0.3$, $H = 2.2$ cm, $L = 4.5$ cm, $L_C = 0.5$ cm, $H_C = 1.2$ cm, $L_{TC} = L_{TA} = 0.25$ cm, $d = 5.5$ cm)

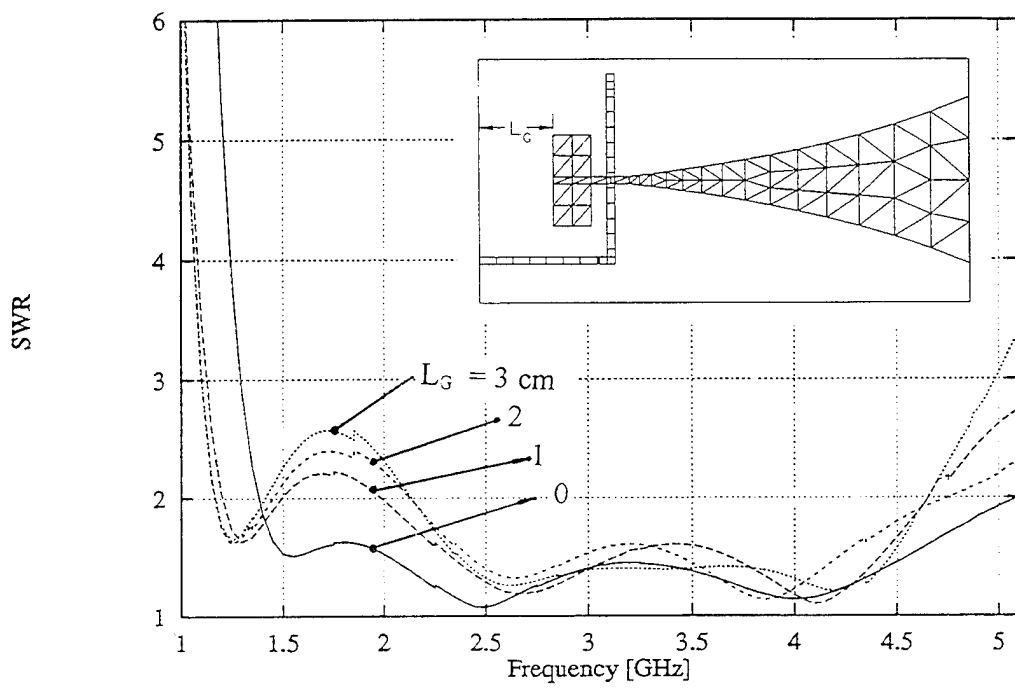


Figure 7. Effects the backwall offset, L_G . (BW_{Zc} , broadside scan, $\epsilon_r = 2.2$, $t = 0.288$ cm, $W_{ST} = 0.1$ cm, $W_{SL} = 0.1$ cm, $a = 3.45$ cm, $b = 3.2$ cm, $R = 0.3$, $H = 2.2$ cm, $L = 4.5$ cm, $L_{STB} = 1.4$ cm, $L_C = 0.5$ cm, $H_C = 1.2$ cm, $L_{TC} = L_{TA} = 0.25$ cm)

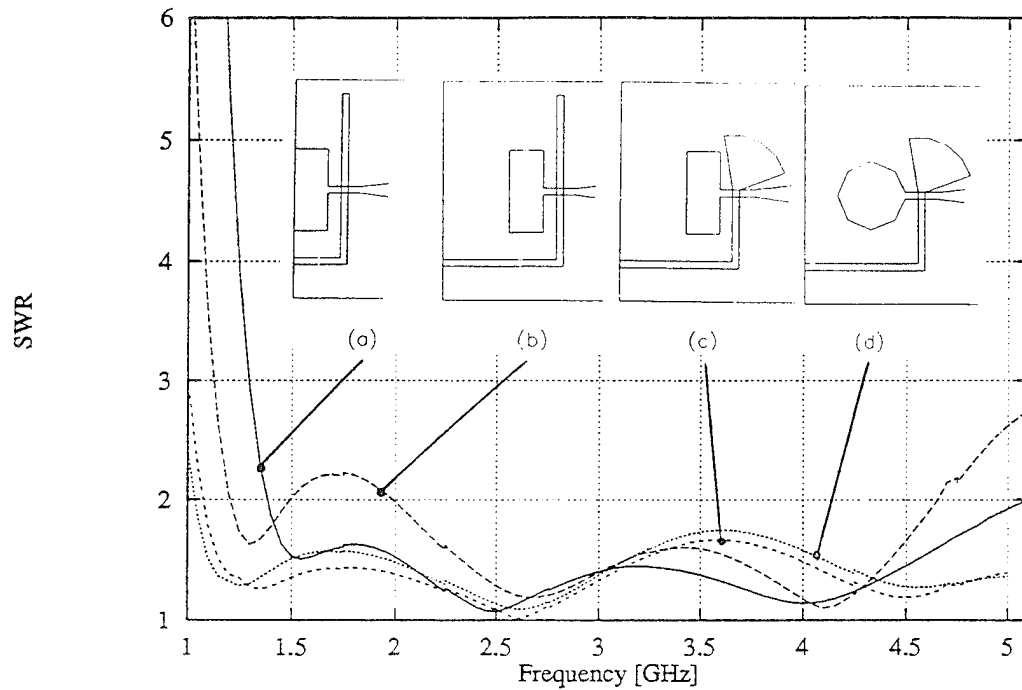


Figure 8. Effects of radial stripline stub and circular stub. (BW_{Zc} , broadside scan, All parameters are same as Fig.7 except as otherwise mentioned.): (a) rectangular slot cavity and uniform stripline stub, (b) 1-cm offset backwall (c) radial stripline stub($R_R=0.8$ cm and $A_R=80^\circ$) with 1-cm offset backwall (d) circular slot cavity($D_{SL}=1.0$ cm) and radial stripline stub.

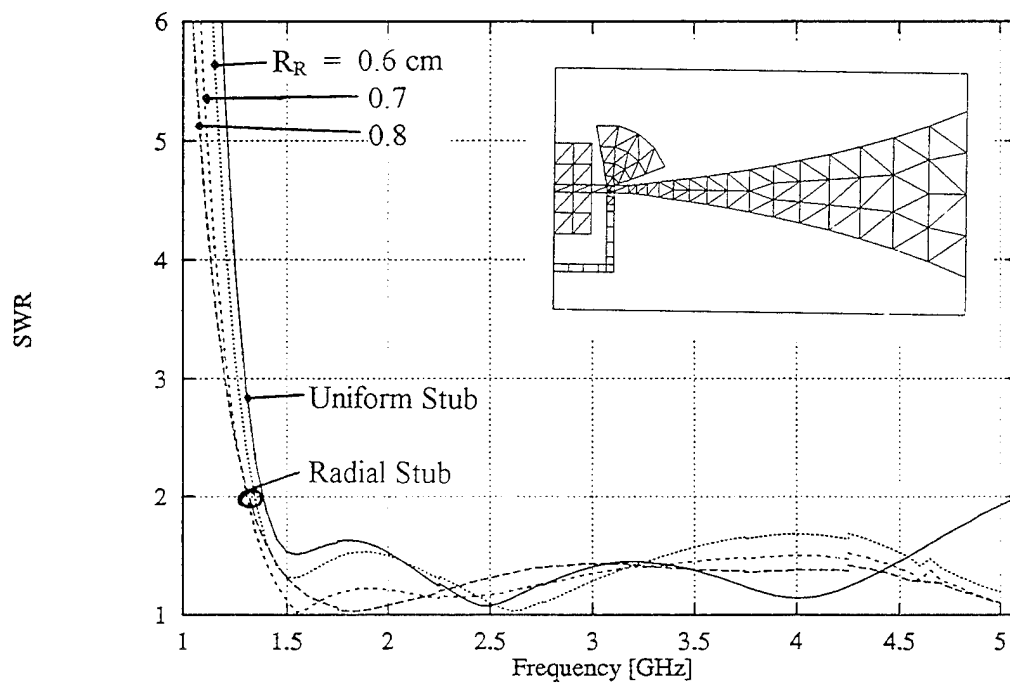


Figure 9. Effects of size of radial stripline stub. (BW_{Zc} , broadside scan, All parameters are same as Fig.8 (c) except $L_G = 0 \text{ cm}$ and varying R_R .)

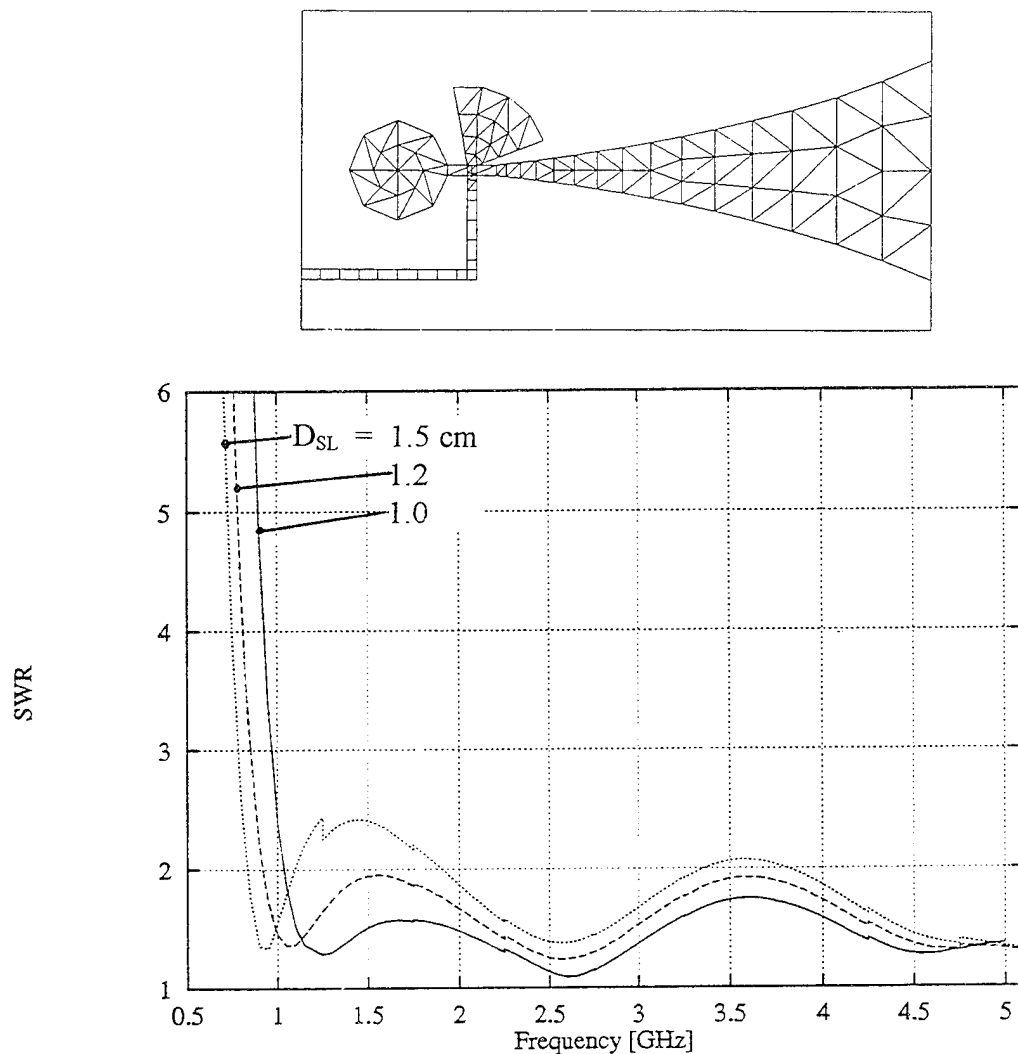


Figure 10. Effects of size of circular slot cavity. (BW_{Zc} , broadside scan, All parameters are same as Fig.8 (d) except varying D_{SL} .)

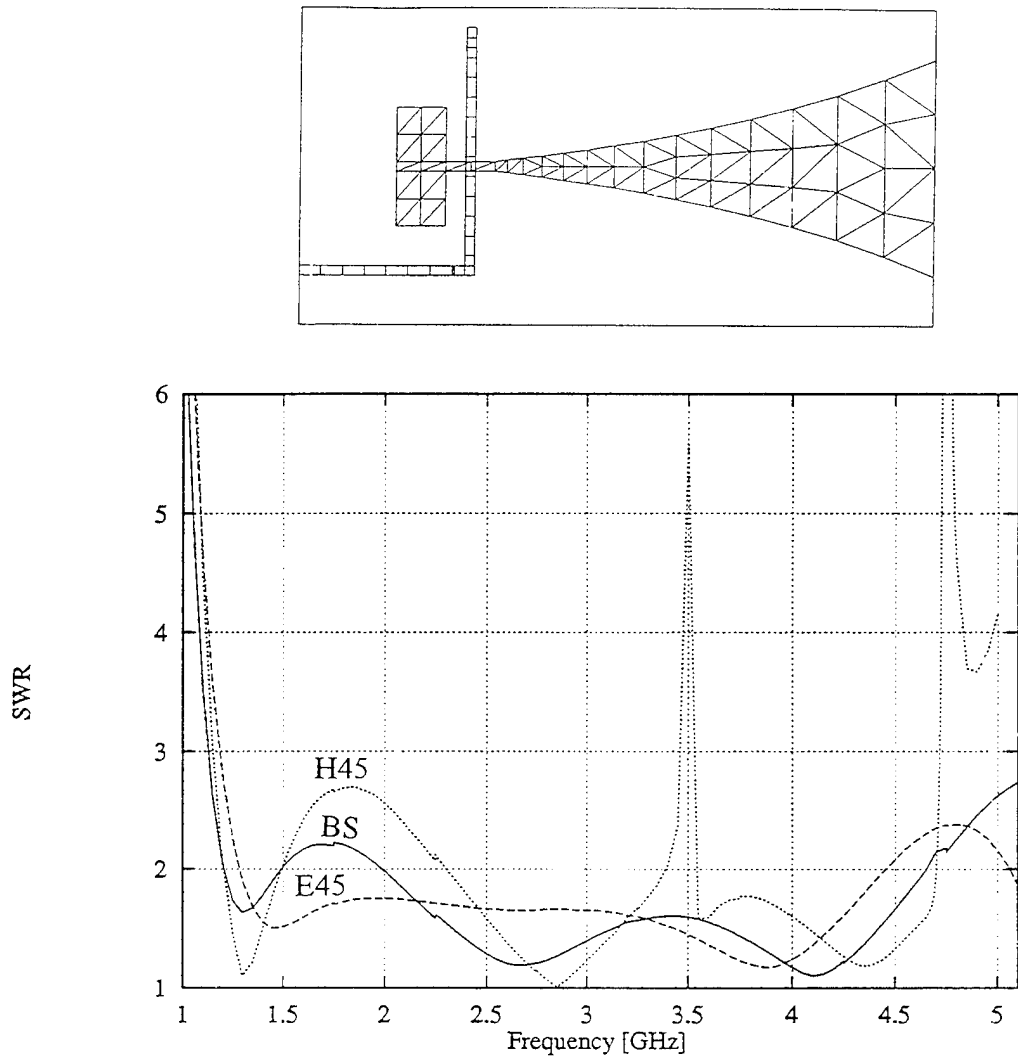


Figure 11. Scan performance of antenna array having rectangular slot cavity and uniform stripline stub. (BW_{Zc} , All parameters are same as array of Fig.7 with $L_G = 1$ cm.)

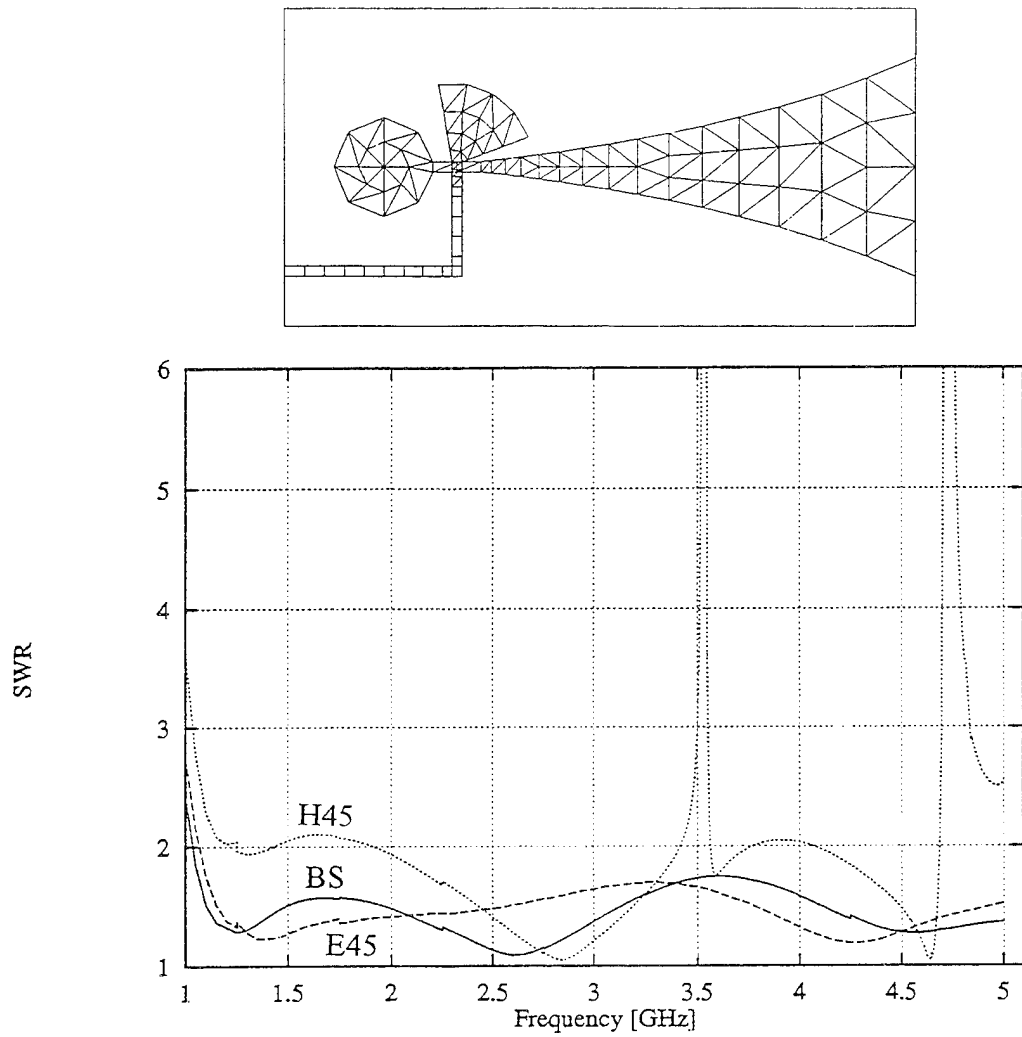


Figure 12. Scan performance of antenna array having circular slot cavity and radial stripline stub. (BW_{Zc} , All parameters are same as array of Fig.8 (d).)

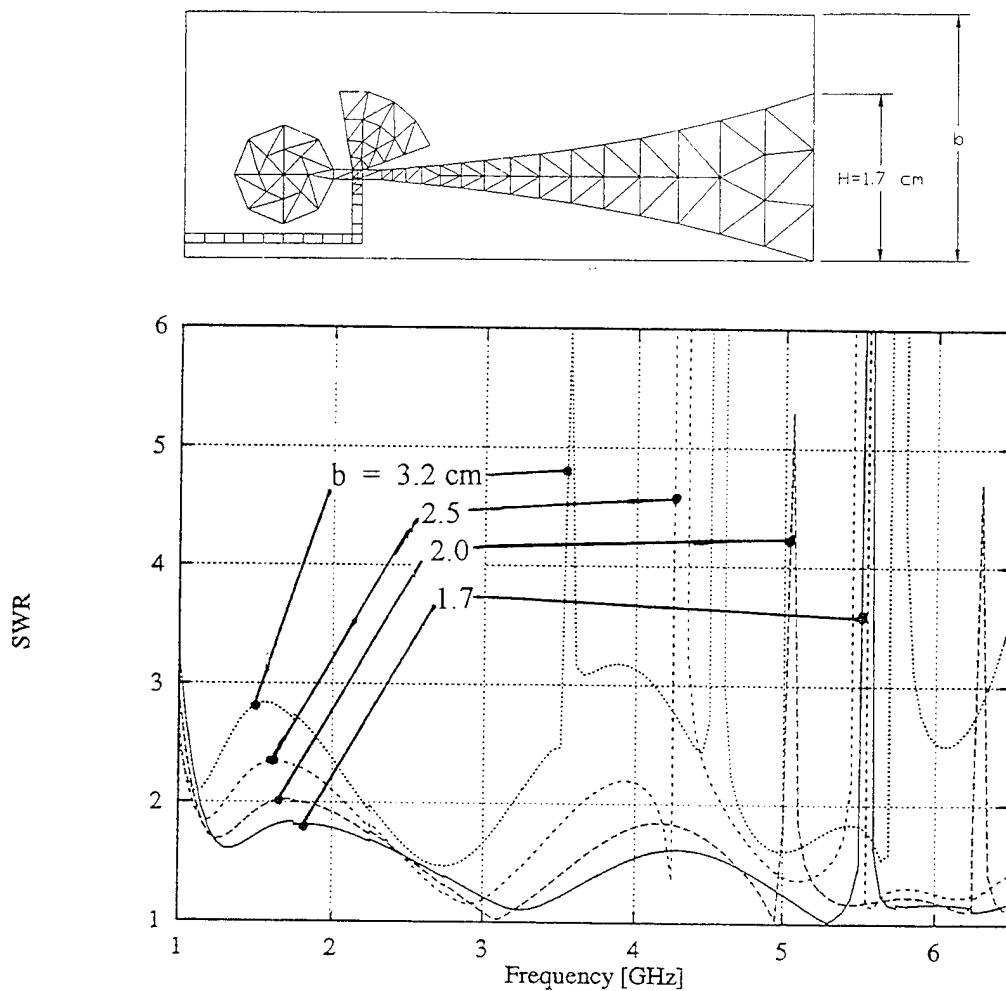


Figure 13. Effects of E-plane grid spacing, b . (BW_{Zc} , H-plane 45° scan, All parameters are same as array of Fig.8 (d) except different H , a , and varying b , i.e. $\epsilon_r = 2.2$, $t = 0.288$ cm, $W_{ST} = 0.1$ cm, $W_{SL} = 0.1$ cm, $a = 2.5$ cm, $R = 0.3$, $H = 1.7$ cm, $L = 4.5$ cm, $R_R = 0.8$ cm, $A_R = 80^\circ$, $D_{SL} = 1.0$ cm, $L_{TC} = L_{TA} = 0.25$ cm, and $d = 6.5$ cm.)

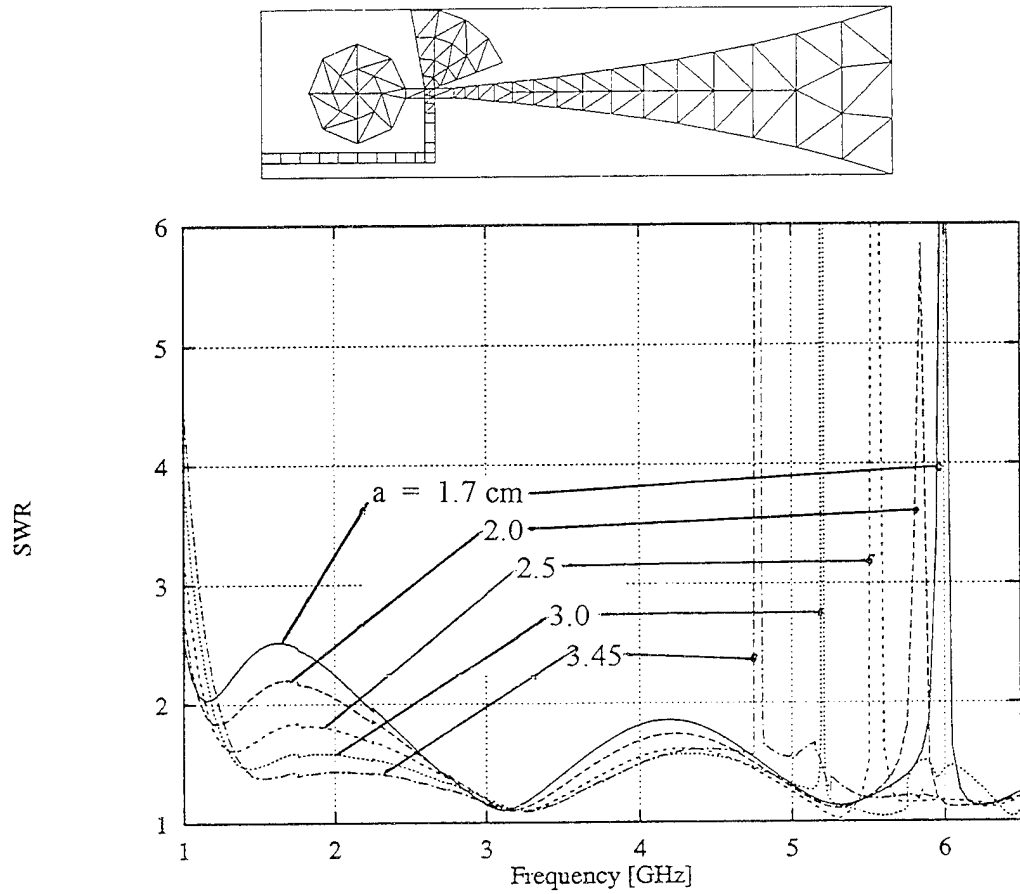


Figure 14. Effects of H-plane grid spacing, a . (BW_{Zc} , H-plane 45° scan, All parameters are same as array of Fig.13 except $b=1.7$ cm and varying a .)

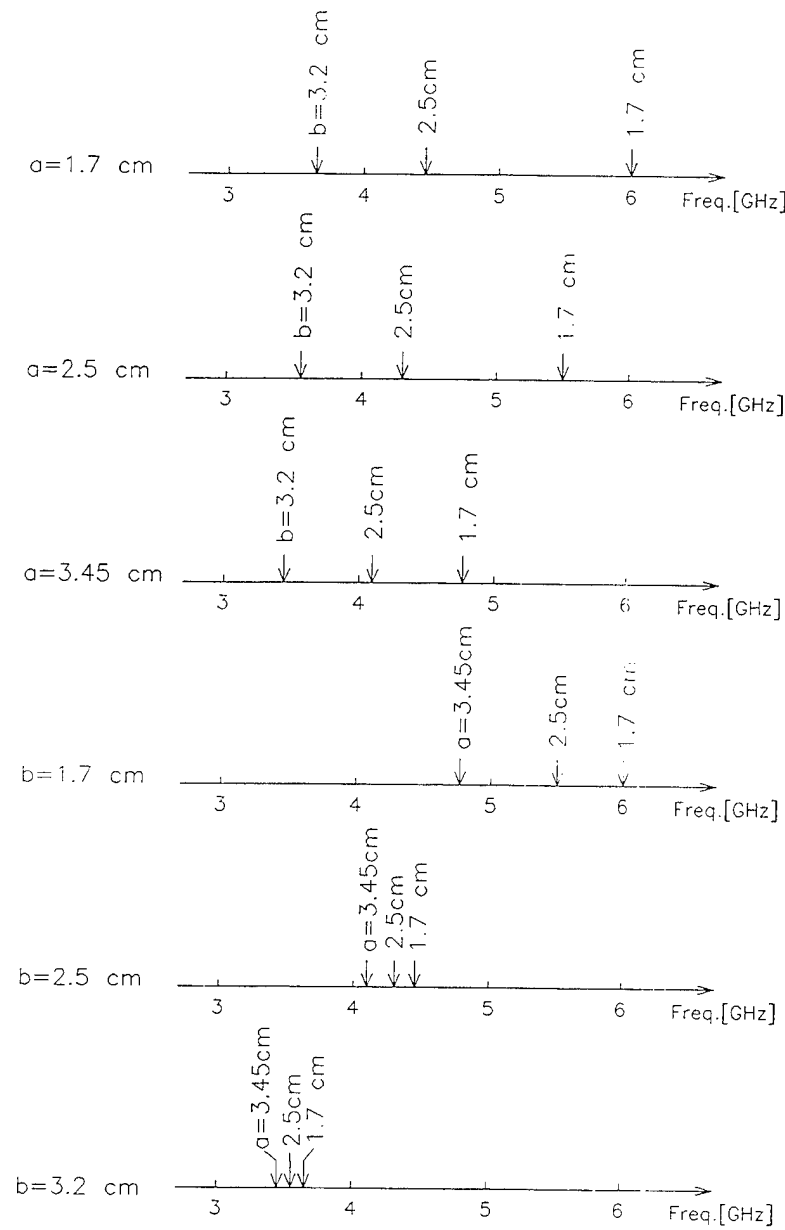


Figure 15. Frequencies of the first H-plane scan anomaly for various grid spacings a and b . (All parameters are same as array of Fig.13 except varying a and b .)

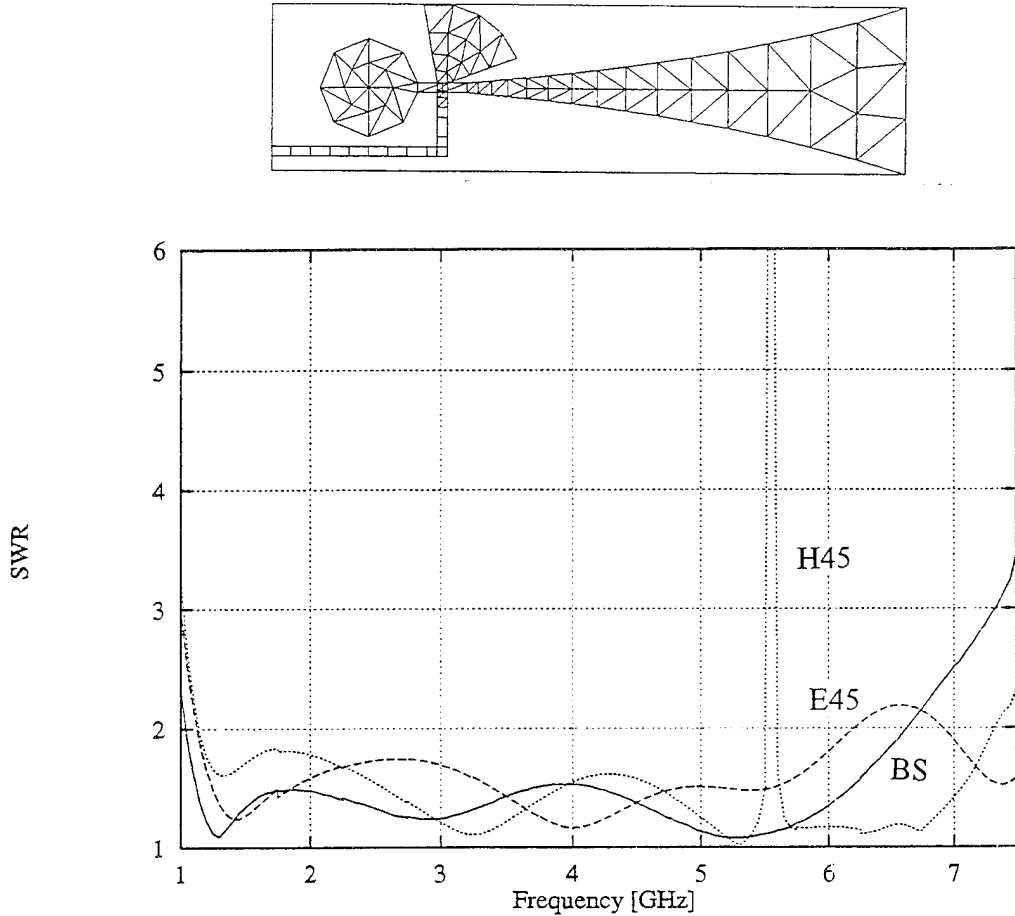


Figure 16. Scan performance of antenna array having 4.7:1 bandwidth over 45° scan volume. (BW_{Zc} , All parameters are same as array of Fig.13 with $b=1.7$ cm.)

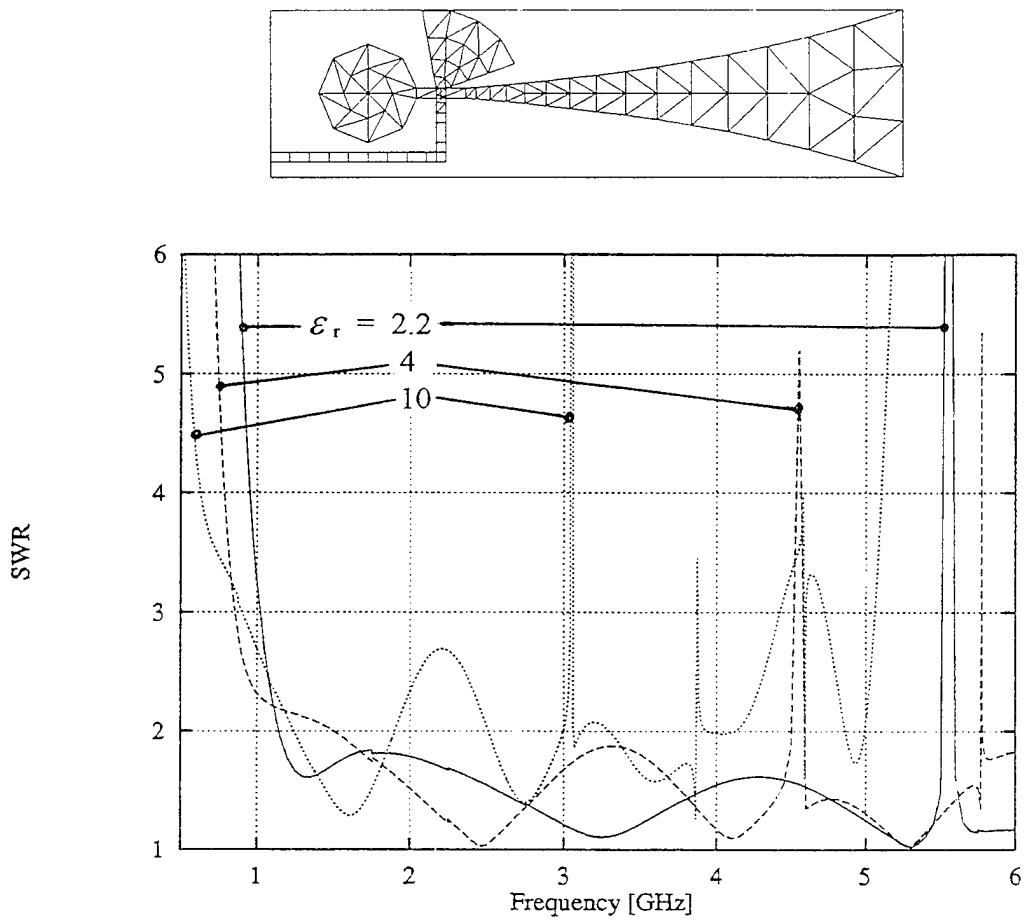


Figure 17. Effects of dielectric constant. (BW_{Zc} , H-plane 45° scan, All parameters are same as array of Fig.15 except varying ϵ_r .)

ADDITION OF A POLARIMETRIC CAPABILITY TO A TACTICAL SAR SYSTEM

by

Don Collier

Marshall Greenspan

Larry Orwig

Harold Shnitkin

Westinghouse Norden Systems, Inc.

P.O. Box 5300

Norwalk, CT 06856, USA

Abstract:

Under a recent program sponsored by the U. S. Air Force's Wright Laboratory/AARM (F33615-92-C-1045, Elton Hopper, Technical Manager), the function of a conventional, vertically polarized airborne monopulse radar system was expanded to include a polarization diversity capability. A unique, light-weight, meanderline polarizer lens configuration was added to the flatplate array antenna, enabling it to receive simultaneous horizontally and vertically polarized target returns while transmitting a vertically polarized signal. An alternative RF switch position permits transmission of right-hand circular and reception simultaneously of right- and left-hand circularly polarized returns. Either configuration detects two weakly correlated polarization scattering states. Such data are potentially useful in automatic target identification (ATR), either through partial polarization whitening of the image or by supplying dual polarimetric feature information for matching against a target model. The system design also provides for the addition of a high speed RF switch to support interleaved transmission of orthogonal polarization states for measurement of the full coherent polarization scattering matrix .

The radar system's partial polarization matrix capability was flight tested at Eglin Air Force Base by Wright Laboratory in Florida in February, 1995. Polarimetric performance was verified by scattering data from an in-scene array of corner reflectors of known reflection characteristics. This paper describes the polarimetric calibration methodology and shows preliminary flight test results, including real-time radar scope displays as well as synthetic aperture ground map images.

1.0 THE MULTIFUNCTION, FLATPLATE ARRAY ANTENNA

1.1 Background

The radar used on this project is the AN/APG-76, an airborne system which was developed by Westinghouse Norden Systems. The APG-76 antenna is a fully gimbaled and mechanically scanned Ku-band multiple aperture slotted flatplate array comprising an elliptical monopulse aperture, three azimuth interferometers and a guard antenna. The full array consists of 60 subarrays whose short waveguide runs permit them to achieve a 3% operating bandwidth. The pencil beam monopulse pattern has elevation sidelobes at -23 dB and azimuth sidelobes at -25 dB below the main beam peak. Gain in the pencil beam mode exceeds 34 dB. A shaped or CSC² beam mode is also available with a 31 dB maximum gain. For the experiment reported here, the radar was nose-mounted in a Gulfstream-II aircraft based at the Westinghouse facility in Baltimore, Maryland.

1.2 Modes of Operation

The multiple aperture APG-76 supports many modes of operation including scanning, spotlight, or strip map synthetic aperture radar (SAR) ground imaging. Other modes supported by the large monopulse array pencil beam include long range target location, monopulse air-to-air tracking, target identification and track, terrain clearance, and air-to-ground ranging. Both along-track (radial velocity measurement) and cross-track (elevation mapping) interferometry are supported. The alternative CSC² elevation pattern is generated by means of a patented technique which 1) switches power to only the upper half of the radiating aperture and 2) introduces a fixed phase shift into the lowest row of that half-aperture [1]. Shaped beam operation facilitates ground and ship target location, and has been used in conjunction with the interferometers to generate wide area topographic strip maps under an earlier program sponsored by ARPA for the U.S. Army/TEC [2].

Power switching for the shaped beam is accomplished by means of an RF switch in the feed manifold as shown in Figure 1. In the switch position illustrated here, transmission is through the full monopulse sum aperture. In the other position, transmission is through the upper half array only. (Isolation in this switch has been measured to be better than -55 dB.) This choice of configurations, used with the polarized array described in the following section, makes possible a choice between linear and circular polarization bases. In the polarimetric system, however, the phase shifters are disabled so both polarization types are generated as a pencil beam.

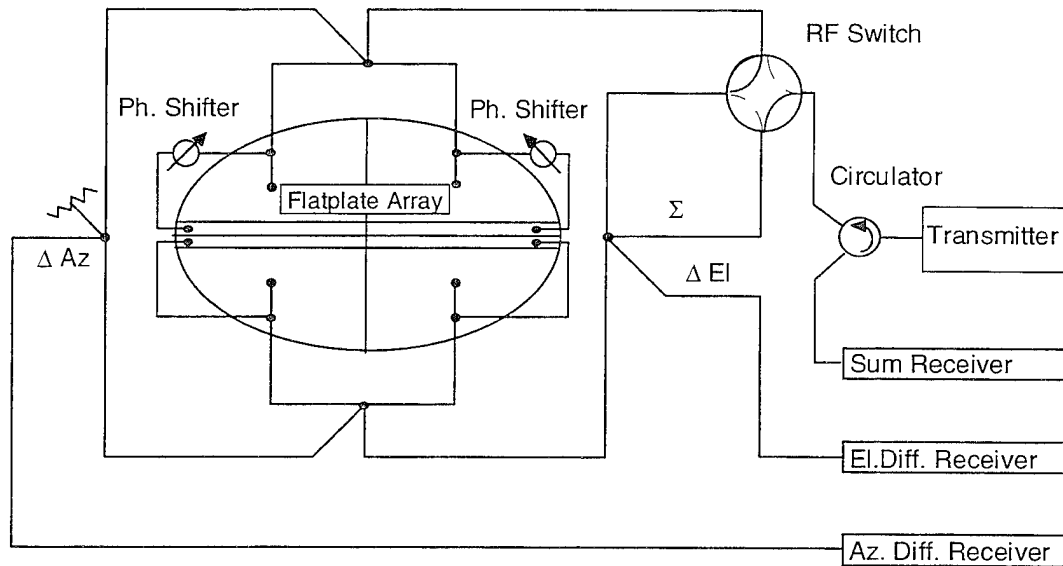


Figure 1. Simplified Electrical Schematic of Monopulse Aperture

2.0 THE POLARIMETRIC LENS CONCEPT

The polarimetric response of a scattering cell to incident radiation can be a valuable input for SAR-based terrain cover analysis or automatic target classification. To obtain such data, polarized RF energy is transmitted and the co-polarized and cross-polarized target echoes are measured simultaneously. In a dual polarization system, a single polarization state is transmitted. In a fully polarimetric system, orthogonal polarization states are transmitted on alternate pulses.

Until recently, polarimetric SAR has been practical only when separate antennas were employed for the two received polarization states. The configuration applied in this program uses the vertically polarized APG-76 antenna described in the preceding section, to which oppositely-sensed, circularly polarized coverings have been installed on the upper and lower half apertures. For brevity, we refer to these coverings as lenses although they play no role in focusing radiation. The arrangement is illustrated schematically in Figure 2, where the RF switch is set for upper half-aperture transmission. Note that, for simplicity, the azimuth difference receiver and associated microwave hybrid comparators, shown in figure 1, have been deleted from figure 2 and subsequent array aperture diagrams.

Together with state-of-the-art radar control and signal processing techniques, this design has produced a variety of high quality polarimetric SAR data. For the first time, it has been possible to incorporate polarimetric SAR modes into an airborne system that employs a single slotted flatplate antenna.

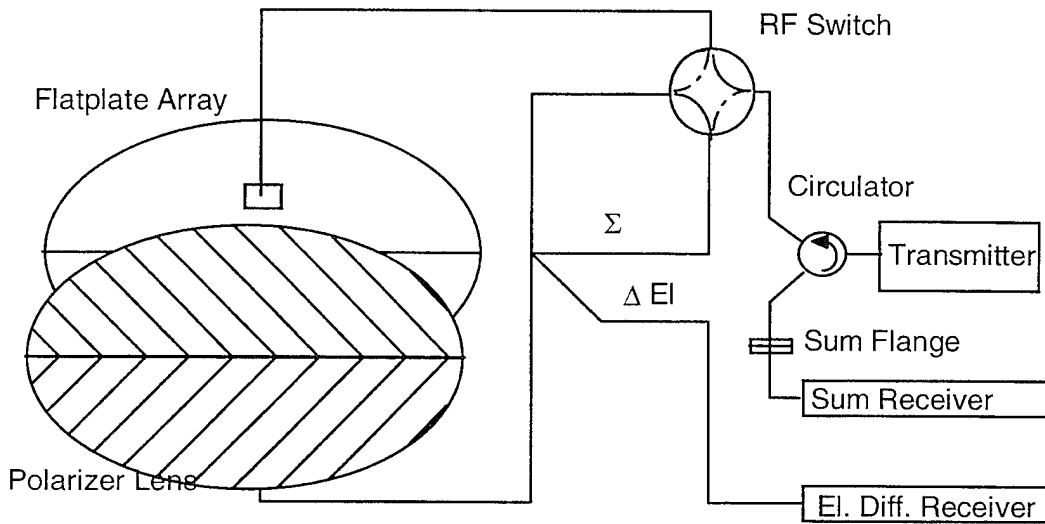


Figure 2. Flatplate Array With Polarizer Lenses Covering Aperture

2.1 The Polarizer Lens

Polarization modifying gratings or lenses were designed and built in the 1940's, and were described by Marcuvitz [3]. The meanderline lens used in this application is similar to the design outlined by Young, Robinson and Hacking in 1973 [4] and refined by Montgomery in 1981 [5]. The layout is shown in Figure 3, in which microstrip meanderlines set at a 45 degree angle are etched into copperclad dielectric sheets.

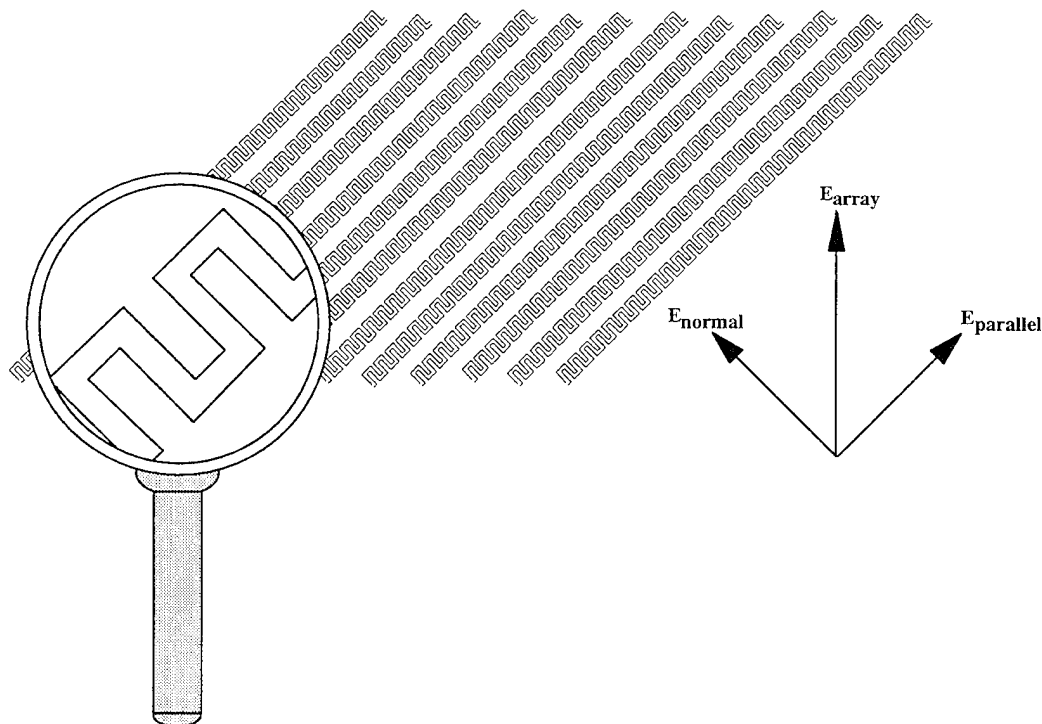


Figure 3. Microstrip Meanderline Layout of Polarizer Lens

Vertically polarized RF energy emitted from the array slots impinges on the polarizer sheet, located approximately 0.5 inches in front of the antenna aperture. The radiated voltage vector E_{array} consists of two components or legs, one parallel to the meanderline strips, $E_{parallel}$, and one perpendicular to the meanderline strips, E_{normal} . As E_{normal} passes through the lens, it undergoes a phase delay, since the lens acts as a capacitive reactance to this leg of the RF signal. In similar manner, the vector $E_{parallel}$ undergoes a phase advance, since the lens acts as an inductive reactance to this leg of the RF vector.

The full 90 degree phase differential between legs required for circular polarization is not normally achieved with a single layer. The structure must be matched to free space to minimize RF reflections. Consequently, three or more layers are used in the manner of spatial filters, each one shifting the RF phase a fraction of the desired total. When the 90 degree separation between vector components has been obtained, the linearly polarized energy becomes circular by definition.

2.2 Antenna Polarization Modes

Two polarization modes are possible with the array illustrated in Figure 2. With the switch in the position shown, RF energy is transmitted through the upper half aperture only. The orientation selected for the meanderlines in the upper lens converts the vertically polarized energy emerging from the array into righthand circularly polarized energy (RCP). The lower lens converts vertically polarized energy to lefthand circular polarization (LCP), but with the switch set as shown there is nominally no transmission through the lower half aperture. By the principle of reciprocity, RCP and LCP signals returning through the upper and lower lenses, respectively, are converted back to linear vertical polarization. These orthogonal returns may then be routed to separate receivers for detection. But any LCP and RCP returns at the upper and lower lenses, respectively, are converted to horizontal polarization and are rejected by the waveguide slots.

If the RF switch is rotated 90 degrees, the entire sum aperture radiates: RCP is transmitted from the upper lens and LCP from the lower lens. It can be shown [6][7] that when RF from contrary-sensed circularly polarized antennas combines in the far field, the result is linearly polarized energy. The orientation of the linear polarization vector depends on the phase relation between the two circular components. With the present system design, on elevation boresight the net polarization vector is vertical. Off boresight, it is linear with an orientation which varies slowly with the elevation monopulse phase. The combined vectors in the far field are always linearly polarized, even though each half aperture is circularly polarized. On receive, the sum channel is sensitive to the same polarization it has transmitted. RF energy returned through the Elevation

Delta port is also linear and is always orthogonally polarized relative to the energy returned through the Sum Port.

2.3 Achieving a Full Polarization Matrix

With the addition of a second high power RF switch as shown in Figure 4, this one capable of switching at the transmitter pulse repetition rate (PRF), the same antenna may achieve pulse-to-pulse interleave of orthogonal polarization transmit states. In that case, the full polarization scattering matrix could be measured. Switch 1, the slow switch present in the current radar, would continue to select between circular and linear polarization bases. Switch 2, the fast switch, would provide the pulse-to-pulse switching between orthogonal transmit states in the basis chosen by switch 1. Details of this design have been discussed elsewhere [7],[8],[9].

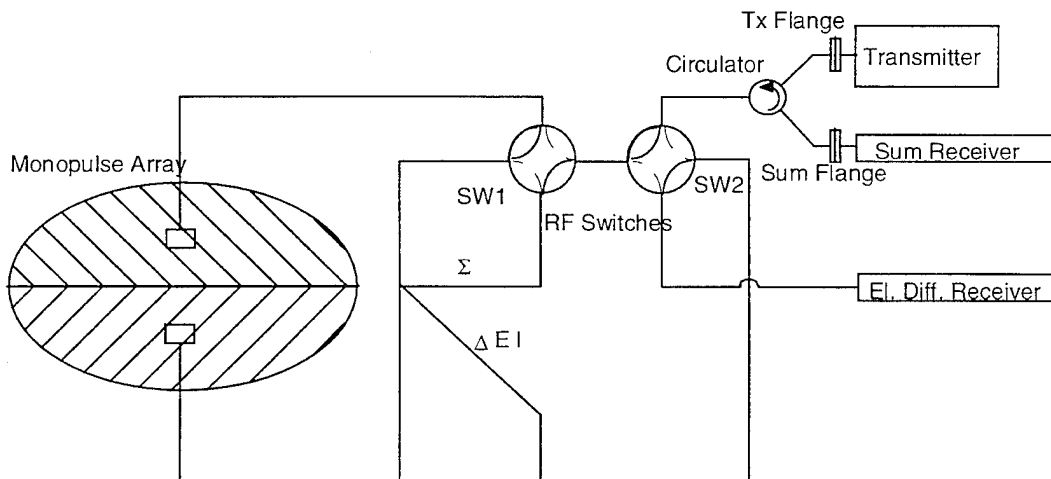


Figure 4. Simplified Electrical Schematic of Fully Polarimetric Monopulse Aperture

3.0 SYSTEM EVALUATION AND CALIBRATION

A comprehensive evaluation program was conducted which encompassed both laboratory and flight test phases. In this section we present the empirically-determined performance characteristics of the lensed system, and discuss the procedures that were used to calibrate the polarimetric SAR imagery.

3.1 Range Test Results

The lens was manufactured and installed on the APG-76 array by Rantec Corporation of Calabasas, California. Pattern tests were conducted at Rantec to verify that the beam shape continued to meet the antenna specifications. At Norden Systems, extensive high voltage and real beam isolation tests were carried out at various frequencies across the radar pass band. In the linear mode, isolation between sum and difference channels at boresight was found to be

excellent, averaging -39.1 dB within the high resolution field of view. Isolation between upper and lower half apertures in the circular mode averaged -23.3 dB. No high voltage transmission problems were encountered. Insertion loss in the lens was determined to be less than 0.2 dB one way.

3.2 Polarimetric Calibration Methodology

Polarimetric data must be calibrated before they can be applied to a practical ATR algorithm suite. Removal of polarimetric crosstalk and complex gain imbalance from the SAR imagery allows the polarimetric signature to be more readily compared with the predictions of target models and makes the signature stable across a set of similar radar antennas.

Full calibration of polarimetric data requires measurement of the full polarimetric scattering matrix. Calibration based on such measurements has been thoroughly discussed in the literature (*e.g.*, [10]-[14] for SAR systems; [15] contains similar considerations for a ground-based radar). However, as our radar transmits only a single polarization state during a given SAR interval, we are able to measure only half of the scattering matrix coherently. Therefore, we can perform only a partial calibration. In this section we will outline the calibration method used and discuss its limitations. Toward this end, we will take the radar to be operating with the circular polarization basis selected.

3.2.1 Restriction to Two Polarimetric Channels

In the general (four-channel) case, the polarimetric signal at the receivers may be written as

$$\mathcal{S} = \begin{bmatrix} \mathbf{u}_1 & \mathbf{v}_1 \\ \mathbf{u}_2 & \mathbf{v}_2 \end{bmatrix} = \begin{bmatrix} \mathbf{R}_{1R} & \mathbf{R}_{1L} \\ \mathbf{R}_{2R} & \mathbf{R}_{2L} \end{bmatrix} \begin{bmatrix} \mathbf{S}_{RR} & \mathbf{S}_{RL} \\ \mathbf{S}_{LR} & \mathbf{S}_{LL} \end{bmatrix} \begin{bmatrix} \mathbf{T}_{R1} & \mathbf{T}_{R2} \\ \mathbf{T}_{L1} & \mathbf{T}_{L2} \end{bmatrix} \begin{bmatrix} \mathbf{x}_1 & \mathbf{y}_1 \\ \mathbf{x}_2 & \mathbf{y}_2 \end{bmatrix} \quad (1)$$

where \mathbf{T} and \mathbf{R} are the transmit and receive system distortion matrices, \mathbf{S} is the true polarimetric scattering matrix of the target or clutter cell, \mathbf{x} and \mathbf{y} are the polarization states transmitted in two successive pulses, represented in a convenient basis, and \mathbf{u} and \mathbf{v} are the corresponding detected returns. Now for the transmit-receive basis let us choose the two positions of switch 2 in Figure 4; the two states of this switch are then represented by $[1 \ 0]^t$ and $[0 \ 1]^t$. Nominally these states are right- and left-handed circular or vertical and horizontal linear polarization, depending on the position of switch 1. The return signal is then simply $\mathcal{S} = \mathbf{R} \mathbf{S} \mathbf{T}$ and, after \mathbf{R} and \mathbf{T} have been found, the calibrated result is just

$$\mathbf{S} = \mathbf{R}^{-1} \mathcal{S} \mathbf{T}^{-1} \quad (2)$$

and the usual full polarimetric calibration may be achieved. In the present experiment, however, switch 2 is absent so all pulses are in the same state, $\mathbf{x} = \mathbf{y} = [1 \ 0]^t$. Equation (1) degenerates to

$$\mathcal{S} = \begin{bmatrix} \mathbf{u}_1 & \mathbf{u}_1 \\ \mathbf{u}_2 & \mathbf{u}_2 \end{bmatrix} = \begin{bmatrix} \mathbf{R}_{1R} & \mathbf{R}_{1L} \\ \mathbf{R}_{2R} & \mathbf{R}_{2L} \end{bmatrix} \begin{bmatrix} \mathbf{S}_{RR} & \mathbf{S}_{RL} \\ \mathbf{S}_{LR} & \mathbf{S}_{LL} \end{bmatrix} \begin{bmatrix} \mathbf{T}_{R1} & \mathbf{T}_{R2} \\ \mathbf{T}_{L1} & \mathbf{T}_{L2} \end{bmatrix} \begin{bmatrix} 1 & 1 \\ 0 & 0 \end{bmatrix}$$

or, rather

$$\begin{bmatrix} \mathbf{u}_1 \\ \mathbf{u}_2 \end{bmatrix} = \begin{bmatrix} \mathbf{R}_{1R} & \mathbf{R}_{1L} \\ \mathbf{R}_{2R} & \mathbf{R}_{2L} \end{bmatrix} \begin{bmatrix} \mathbf{S}_{RR} & \mathbf{S}_{RL} \\ \mathbf{S}_{LR} & \mathbf{S}_{LL} \end{bmatrix} \begin{bmatrix} \mathbf{T}_{R1} \\ \mathbf{T}_{L1} \end{bmatrix} \quad (3)$$

in which the right inverse \mathbf{T}^{-1} does not exist. As a result, even given \mathbf{R} and \mathbf{T} we cannot solve completely for \mathbf{S} , as crosstalk terms due to \mathbf{T}_{L1} will remain. We may, however, remove the errors due to \mathbf{R} and estimate the remaining errors due to \mathbf{T} .

3.2.2 Experimental Considerations

Before proceeding, we make several observations pertaining to the radar and to the experiment as it was performed:

- Nominally, \mathbf{x}_1 is transmitted through the upper half aperture and is RCP with the lens in place, but in practice it is mixed by \mathbf{T}_{L1} into a combination of RCP and LCP. The crosstalk can be due both to imperfections in the lens and to incomplete isolation in the RF switch but we expect it to be dominated by the former; the switch isolation has been measured to be below -55 dB while lab and range tests place the lens crosstalk between -20 dB and -25 dB.
- The co-pol (RCP) return pathway from the lens to the RF switch is identical to the transmit pathway, and this path contains no active elements, so crosstalk in this channel should be the same on transmit as on receive. As a result, if the gains are normalized so that $\mathbf{R}_{1R} = \mathbf{T}_{R1}$, then we expect $\mathbf{R}_{1L} = \mathbf{T}_{L1}$.
- The cross-pol (LCP) return pathway is independent of the RCP transmit pathway, so there is no necessary relation between \mathbf{R}_{2R} and \mathbf{T}_{R2} .

For the data collection flights, a line of dihedral and trihedral reflectors was laid out adjacent to the target area, with a spacing between reflectors of 12 m. All reflectors were within 30 m of the ground position of the planned radar boresight, or between 1.1 and 0.4 mrad off boresight at our data collection ranges of 27.5 to 74 km in this experiment. Corner reflector azimuth alignments were controlled with a precision of $\pm 0.1^\circ$ to sighting stakes surveyed by Optometrics Corp. of Dayton, Ohio. The reflectors were provided for the occasion by MIT Lincoln Laboratory, and comprised one of their two sets of calibration quality corner reflectors. Both sets were designed

for use at Ka-band, however. The APG-76 is a Ku-band radar and the relative reduction in the scattering cross section of the reflectors, combined with the long range at which the target area was imaged, meant that the accuracy of the calibration was somewhat compromised by clutter. We will discuss this issue after we examine the general approach used for a partial calibration.

3.2.3 Solution Method

Given the single transmitted state (RCP), each measurement used in the calibration is the *ratio* of the cross-polarized return to the co-polarized return from a given reflector. The mathematics is therefore insensitive to an overall complex amplitude, so we may remove a common factor from all elements of \mathbf{R} and another from \mathbf{T} . We choose these two factors to be \mathbf{R}_{1R} and \mathbf{T}_{R1} , and rewrite equation (3) as

$$\delta' = \begin{bmatrix} s_1 \\ s_2 \end{bmatrix} = \begin{bmatrix} 1 & \delta_1 \\ \delta_2 & f \end{bmatrix} \begin{bmatrix} S_{RR} & S_{RL} \\ S_{LR} & S_{LL} \end{bmatrix} \begin{bmatrix} 1 \\ \varepsilon_1 \end{bmatrix} \quad (4)$$

where $\delta' = \delta / (\mathbf{R}_{1R} \mathbf{T}_{R1})$, $s_1 = \mathbf{u}_1 / (\mathbf{R}_{1R} \mathbf{T}_{R1})$, $\delta_1 = \mathbf{R}_{1L} / \mathbf{R}_{1R}$, etc.

With this normalization, pursuant to the known transmit-receive symmetry in this system as described in section 3.2.2, we have $\delta_1 = \varepsilon_1$ so there are only three independent quantities to solve for: δ_2 , ε_1 and f . We therefore require three reflectors to calibrate the data. This minimum set was taken to be a trihedral, a dihedral with crease horizontal (0 degrees), and a dihedral with crease rolled 45 degrees clockwise about the reflector boresight. This choice supported calibration in both the circular and the linear polarization bases used in the experiment. In fact we deployed a total of five reflectors, including a dihedral rolled 45 degrees counterclockwise and a redundant second trihedral. The boresight axis of each reflector was aligned in azimuth and elevation to the planned radar line of sight at the middle of each data run (range 53.7 km).

The scattering matrices for the three reflectors are expressed in a circular basis as:

$$S(\text{tri}) = \begin{bmatrix} 0 & 1 \\ 1 & 0 \end{bmatrix} \quad S(\text{di}) = \begin{bmatrix} e^{-j2\alpha} & 0 \\ 0 & -e^{+j2\alpha} \end{bmatrix}, \quad (\alpha = \text{roll angle}, j = \sqrt{-1}) \quad (5)$$

and this leads via equation (4) to the measurement vectors:

$$\delta'(\text{tri}) = \begin{bmatrix} 2\epsilon \\ \mathbf{f} + \epsilon\delta \end{bmatrix} \quad \delta'(\mathbf{0}^\circ \mathbf{di}) = \begin{bmatrix} 1 - \epsilon^2 \\ \delta - \epsilon\mathbf{f} \end{bmatrix} \quad \delta'(\pm 45^\circ \mathbf{di}) = \pm \mathbf{j} \begin{bmatrix} 1 + \epsilon^2 \\ \delta + \epsilon\mathbf{f} \end{bmatrix} \quad (6)$$

where to minimize the use of subscripts we have denoted $\epsilon \equiv \epsilon_1 = \delta_1$ and $\delta \equiv \delta_2$. By forming ratios of the two components of each measurement vector, we obtain a set of complex equations in the unknown parameters δ , ϵ and \mathbf{f} . We denote by μ the ratio of the cross-polarized to the co-polarized return:

$$\mu(\text{tri}) \equiv \mu_T = \frac{\mathbf{f} + \epsilon\delta}{2\epsilon}, \quad \mu(\mathbf{0}^\circ \mathbf{di}) \equiv \mu_0 = \frac{\delta - \epsilon\mathbf{f}}{1 - \epsilon^2}, \quad \mu(\pm 45^\circ \mathbf{di}) \equiv \mu_{45} = \frac{\delta + \epsilon\mathbf{f}}{1 + \epsilon^2} \quad (7)$$

The two complex ratios μ_{45} are identical, so that the five reflectors used in the experiment provided redundant (backup) information both in the trihedrals and in the rolled dihedrals.

Equations (7) comprise three independent complex equations sufficient to find the three quantities \mathbf{f} , ϵ and δ . By casting (7) in terms of the three parameters δ , $\epsilon\mathbf{f}$ and ϵ^2 , one readily obtains a quadratic equation for ϵ^2 and equations for δ and $\epsilon\mathbf{f}$ as separate functions of ϵ^2 . The solutions reduce to:

$$\epsilon^2 = b \pm \sqrt{b^2 - 1} \quad \text{where} \quad b = \frac{\mu_0 + \mu_{45} - 2\mu_T}{\mu_0 - \mu_{45}} \quad (8a)$$

and

$$\delta = \frac{1}{2} [\epsilon^2 (\mu_{45} - \mu_0) + (\mu_{45} + \mu_0)], \quad \mathbf{f} = \frac{1}{2\epsilon} [\epsilon^2 (\mu_{45} + \mu_0) + (\mu_{45} - \mu_0)] \quad (8b)$$

This solves the problem up to the choices of root for ϵ^2 and then ϵ . The requirements $|\epsilon| < 1.0$, $|\delta| < 1.0$ reduce the selection to a 180° phase ambiguity on \mathbf{f} and ϵ , which is resolved by assuming the phase of \mathbf{f} to be close to 0° .

3.2.4 Properties of the Distortion Matrix Solution

If the gains are balanced in the two receiver channels then we expect: $|\mathbf{f}| \cong 1.0$. (9a)

If the upper and lower lenses are electrically identical except for the 90° difference in orientation of their meanderlines, then we expect balanced crosstalk: $|\epsilon\mathbf{f}| \cong |\delta|$. (9b)

The polarimetric isolation of the system is estimated by ϵ and δ/\mathbf{f} .

If $|\epsilon^2| \ll 1.0$ then one can show that relation (9b) holds if and only if:

$$|\text{phase}(\epsilon\mathbf{f}) - \text{phase}(\delta)| \cong |\text{phase}(\mu_0) - \text{phase}(\mu_{45})| \cong 90^\circ. \quad (9c)$$

If relation (9b) holds and $|\varepsilon^2|, |\varepsilon\delta| \ll 1.0$ then approximate expressions for the magnitudes of the crosstalk parameters are:

$$|\epsilon f|^2 \equiv |\delta|^2 \equiv \frac{1}{4}(|\mu_0|^2 + |\mu_{45}|^2) \quad (9d)$$

$$\text{while the gain imbalance is: } |f|^4 \equiv |\mu_T|^2 (|\mu_0|^2 + |\mu_{45}|^2) \quad (9e)$$

$$\text{and if (9a) also holds then: } |\mu_T|^2 \equiv (|\mu_0|^2 + |\mu_{45}|^2)^{-1} \quad (9f)$$

3.2.5 Residual Errors in the Partial Calibration

The matrix product $S' = R^{-1} \begin{bmatrix} f & -\varepsilon \\ -\delta & 1 \end{bmatrix} \begin{bmatrix} 1 \\ \varepsilon \end{bmatrix} = S \begin{bmatrix} 1 \\ \varepsilon \end{bmatrix}$ leaves crosstalk errors of

order ε . In particular, if we remeasure the error ratios μ after calibration of the image, we expect to find:

$$\mu'_T = 1/\varepsilon, \quad \mu'_0 = -\varepsilon, \quad \mu'_{45} = \varepsilon \quad (10)$$

which are to be compared with the precalibration ratios (7). For the general scatterer we expect:

$$S'_{RR} = S_{RR} + \varepsilon S_{RL}, \quad S'_{LR} = S_{LR} + \varepsilon S_{LL} \quad (11)$$

with the crosstalk (error) terms arising in the upper polarizer lens during transmission. For small ε , the magnitude of the ratio $\mu = S'_{LR} / S'_{RR}$ is bounded by $|1/\varepsilon|$ and $|\varepsilon|$ for pure odd-bounce and even-bounce scatterers, respectively, and is in the order of unity for resolution cells with general mixed properties. At high enough resolution, and given $|\varepsilon|$ reasonably small, this sort of behavior should be helpful for distinguishing different types of scattering centers on man-made objects, and therefore is of potential benefit for automatic target recognition. Note that the ratio $\mu(\text{odd-bounce}) / \mu(\text{even-bounce}) \sim |\varepsilon^2|$. If $|\varepsilon| < -20$ dB, for example, then the two μ types are separated by 40 dB or more.

3.3 Polarimetric Calibration Results from Flight Data

Following laboratory and compact range tests, the array with the polarizing lenses installed was mounted on the APG-76 pedestal in the nose of a Gulfstream-II aircraft which is owned by Westinghouse Norden Systems and operated out of Baltimore, Maryland. The system was flight tested locally in February 1995, imaging the Aberdeen area and the calibration reflectors as set up on a Westinghouse test range. It was then flown to Eglin Air Force Base, Florida, where the reflectors were again installed and flight data were collected against the reflectors and a number of interesting targets. In this section we summarize the results of a typical calibration run.

To calibrate the data, a SAR image was formed of the target area in each polarization channel when the radar line of sight was parallel to the corner reflector boresight alignment. During the

motion compensation and autofocus processes, the same phase corrections were applied to each receiver channel, both to ensure that the images remained coregistered and to preserve the polarimetric phase relation between channels. Then, since the two polarimetric phase centers were separated by their elevation monopulse baseline, a range-dependent phase offset was applied to one channel to compensate for the elevation monopulse phase. For each corner reflector, the brightest pixel in the channel of the nominal return was identified; this was the co-polarized channel (RR) for the dihedrals and the cross-polarized channel (RL) for the trihedrals. We will refer to this channel as the *direct channel* in this section; the other channel is the *error channel*. The complex amplitude was sampled at the same pixel in both channels, an adjustment was made for clutter, and the ratio of the adjusted amplitudes defined the error ratio μ for that reflector. The distortion parameters were then estimated using the equations of the preceding section, the images were calibrated, and the residual errors were checked against equations (10).

The accuracy of the calibration was restricted by the clutter content of the images. For the two trihedrals (rated at 20 dBsm and 30 dBsm at Ka-band), the signal in the direct channel was 32 dB and 42 dB above mean clutter, respectively. However, the signal in the error channel was only 9 dB above mean clutter for the smaller trihedral. Similarly, the dihedrals were 24-27 dB above clutter in the direct channel, but only 9-13 dB above clutter in the error channel. The standard deviation of the clutter in small regions near the corner reflectors was typically 2-3 dB relative to the region mean, while the means of nearby regions varied over about 3 dB. For all reflectors except the larger trihedral, the uncertainty of the clutter level was thus a significant fraction of the error signal itself, and the adjusted error signal level was sometimes in doubt by several dB.

Table 1 lists typical values for $\mu = | \mathbf{RL} / \mathbf{RR} |$, taken directly from the clutter-adjusted data as discussed above. (The order of the reflectors in the table matches their sequence on the ground in 12 m spacing from far range to near.) The uncertainty in the clutter estimate (performed locally near each reflector) may be partly responsible for the 2.4 dB difference in the values for μ for the $\pm 45^\circ$ dihedrals. Ground clutter also contaminates the phase of μ . This is shown both by the 3.4° difference between $\text{phase}(\mu)$ for the two $\pm 45^\circ$ dihedrals, and by the fact that the difference between these phases and $\text{phase}(\mu)$ for the 0° dihedral misses the 90° expectation (eqn. 9c) by an average of 5° .

	$\mu = RL / RR $	phase(RL conjg(RR))
1. Trihedral (30 dBsm)	+ 26.3 dB	+ 171.8°
2. Dihedral, -45° roll	- 17.6 dB	- 107.9°
3. Dihedral, 0° roll	- 12.8 dB	- 24.2°
4. Dihedral, $+45^\circ$ roll	- 14.2 dB	- 110.3°
5. Trihedral (20 dBsm)	+ 27.0 dB	+ 173.3°

Table 1. Sample Calibration Inputs

Table 2 shows the calibration solution using the -45° dihedral together with the 0° dihedral and the larger trihedral. The results for ϵ and δ/f justify the small-value approximation made in (9b)-(9f) for the second-order terms. They are slightly better than the real beam isolation estimates derived from laboratory and compact range data for circular polarization (-23.3 dB). However, the crosstalk terms in Table 2 imply an asymmetry in the isolation between the upper and lower lenses of $|\delta| - |\epsilon f| = 0.8$ dB. This much asymmetry does not seem physically reasonable given the straightforward nature of the lens design and fabrication technology. In fact, it originates mathematically in the 6.3° phase discrepancy between the dihedral μ and (9c). (The large value for $|f|$ results from the fact that the experimental configuration bypassed paired attenuators and amplifiers in the monopulse channels which are normally used to balance the gains.)

	Magnitude	dB(magnitude)	Phase
f	2.29	+ 7.2 dB	- 1.1°
ϵ	0.0553	-25.2 dB	+ 8.2°
δ	0.138	-17.2 dB	+127.2°

Table 2. Sample Calibration Outputs Using Reflectors 1, 2, 3

	$\mu = \mathbf{RL} / \mathbf{RR} $	phase($\mathbf{RL} \text{ conjg}(\mathbf{RR})$)
1. Trihedral (30 dBsm)	+ 25.1 dB	- 24.7°
2. Dihedral, -45° roll	- 27.0 dB	+ 26.3°
3. Dihedral, 0° roll	- 26.1 dB	+179.2°
4. Dihedral, +45° roll	- 23.4 dB	+ 36.1°
5. Trihedral (20 dBsm)	+ 26.9 dB	- 2.6°

Table 3. Sample Post-Calibration Residuals

Table 3 shows the residual μ values at the reflectors after we used this solution to calibrate the complex SAR images. These are all similar to the ideal residuals as constrained by ε (eqns. 10), although – as with the input data – interpretation of the values is compromised by clutter in the error channel. Also, we do not expect complete adherence to (10) because the values in Tables 1 and 2 depart from expectations (eqns. 9b). Finally, we observe from Tables 1 and 3 that the +45° dihedral responded to the calibration by a similar amount to the -45° dihedral (9.2 dB vs. 9.4 dB change in $|\mu_{45}|$); only the latter was used to obtain the calibration solution.

To illustrate the degree of sensitivity of the calibration to errors in the clutter-adjusted input μ , we consider two alternative calibrations. For the magnitude of μ_{45} , alternative (A) uses the mean of the ±45° dihedral values in Table 1 (-15.7 dB). Alternative (B) supposes that half the power level in the adjusted dihedral error channel is clutter, and therefore offsets both μ_{45} and μ_0 by -3 dB. In both alternatives we increase the phase separation of μ_{45} and μ_0 by 6° so that their difference is close to 90° as expected from (9c). The results are summarized in Tables 4 and 5.

	Magnitude		dB(magnitude)		Phase	
	A	B	A	B	A	B
f	2.41	1.97	+ 7.7	+ 5.9	+ 2.5°	- 0.47°
ε	0.0554	0.0475	-24.7	-26.5	+ 11.8°	+ 8.8°
δ	0.141	0.0934	-17.0	-20.6	+122.9°	+129.0°

Table 4. Sensitivity of Calibration Outputs to Corner Reflector Data

	dB(RL / RR)		phase(RL conjg(RR))	
	A	B	A	B
1. Trihedral (30 dBsm)	+ 24.6	+ 26.3	- 28.3°	- 25.3°
2. Dihedral, -45° roll	- 28.4	- 25.7	+ 20.9°	+ 42.1°
3. Dihedral, 0° roll	- 26.0	- 22.7	+178.3°	+168.2°
4. Dihedral, +45° roll	- 24.5	- 21.7	+ 31.6°	+ 48.1°
5. Trihedral (20 dBsm)	+ 26.4	+ 28.1	- 6.2°	- 3.1°

Table 5. Sensitivity of Calibration Residuals to Corner Reflector Data

The alternative results (B) seem to be unlikely because the relative phase of the μ_{45} and μ_0 residuals should be near 180°. There is little basis for preference between (A) and the nominal results in Tables 2 and 3.

From the standpoint of ATR applications, the key result here is that, even beginning with clutter-contaminated data which were also strained by a severe gain imbalance due to a hardware fault, *it was possible to calibrate two-channel polarimetric data well enough to separate dihedral-like from trihedral-like scatterers by 48 dB to 54 dB*, which is to say, at least by order $|\varepsilon^{-2}|$. This represents about a 10 dB improvement over the uncalibrated data. To the extent that man-made objects can be characterized by their distributions of even- and odd-bounce scattering centers, these results suggest that a dual polarimetric system based on a meanderline lens has sufficient isolation to provide useful inputs to the target classification process.

Uncertainty in the clutter content of the pixels containing the corner reflectors does mean that the calibration solution is imprecise. However, *~50 dB separation of the even- and odd-bounce scatterers persists over a significant range of possible calibration solutions*. Furthermore, the small clutter regions near the five reflectors had calibrated ratios μ near -5 dB, so that separation of both reflector types from nearby mean clutter was ~20 dB purely on the basis of μ without regard to total power. Thus, a lensed radar may also be useful at the target detection stage of an ATR algorithm suite.

4.0 EXAMPLE IMAGES

This section presents sample SAR imagery in the two polarimetric channels, and photographs of some of the ground environment in the target area. In all radar images, the line of sight is from bottom to top.

Figure 5 shows the -45° triangular dihedral, with the 30 dBsm trihedral in the background. Ground clutter consists of dry powder/clay with sparse dry grass and similar vegetation. Figure 6 pictures the long vehicle which is parked parallel to the road in the radar images. It has been decorated with scatterers of various shapes to provide a particularly interesting target.

Figure 7 is a frame grabbed from the video playback of the realtime radar display. This image was processed from circular cross-polar (RL) data collected at a range of 77.8 km. The pixel size is 3 ft \times 3 ft. The two calibration trihedrals form a vertical pair just to the right of the cross. The three dihedrals lie along the line joining the trihedrals, but are not visible in this polarization channel at this range. The three bright scatterers in a vertical line to the right of the calibration trihedrals are additional trihedrals placed by Optimetrics Corp. The vehicle shown in Figure 6 appears to the right of the lowest Optimetrics trihedral.

Figure 8 is a composite of four images, showing the target area in RR, RL, VV, and VH polarimetric channels. (The linear and circular polarization scenes were recorded on separate passes by the target area.) All four images were processed to 3 ft square pixels.

5.0 SUMMARY AND CONCLUSIONS

Meanderline polarizing lenses developed by Westinghouse Norden Systems have been installed on an AN/APG-76 antenna array. Following laboratory and flight tests, the capabilities of this dual-polarimetric system were exercised in an Air Force Wright Laboratory data collection flight at Eglin AFB. We have calibrated the polarimetric SAR imagery to the extent allowed by the two-channel data. The calibration solution obtained from the SAR data suggests that the polarimetric isolation of this system is near -24 dB to -25 dB in the circular polarization mode. This result corroborates earlier ground-based (real beam) tests which found an average isolation of -23.3 dB over a limited set of field positions and frequencies.

It has been found that, given a lensed system with reasonable polarimetric purity (isolation), one can calibrate the imagery well enough to achieve separation of even- and odd-bounce scatterers by order $|\varepsilon^{-2}|$ where ε characterizes the isolation, even when the error channel target returns are uncertain by several dB due to clutter. For the lensed APG-76, this separation exceeds +45 dB. It is suggested that this capability, exercised at ranges in excess of 50 km, is potentially useful in

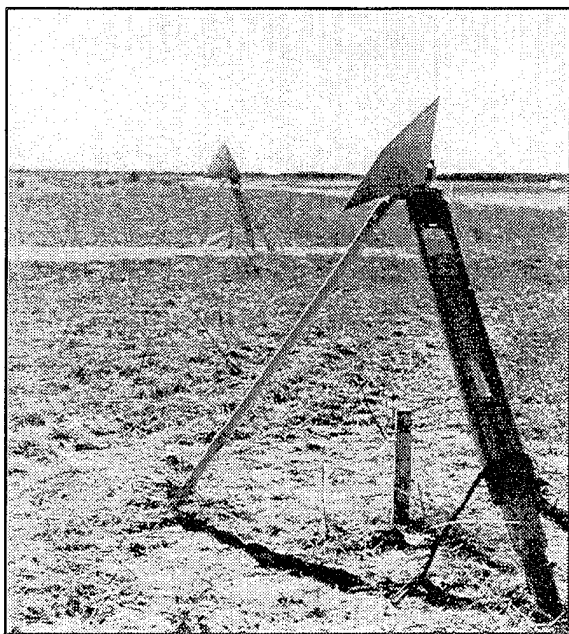


Figure 5. Dihedral on Tripod at Eglin AFB Test Range

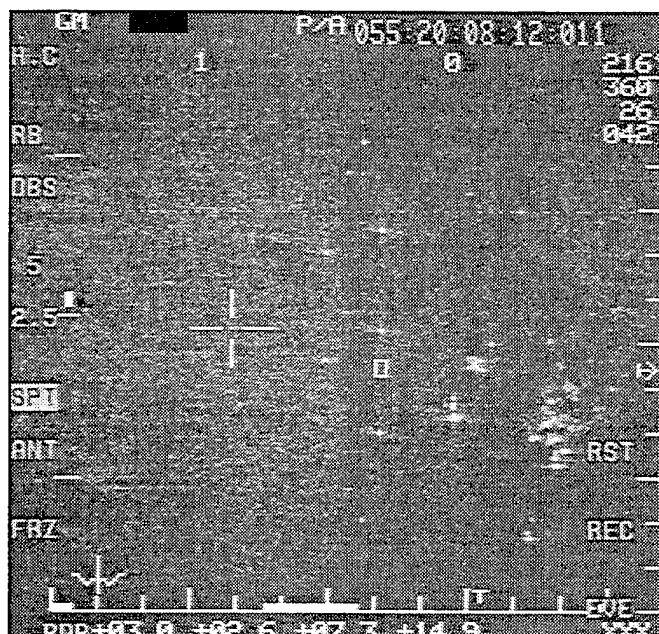


Figure 7. Real-time 3 x 3 ft Image of Target Area from APG-76 Display

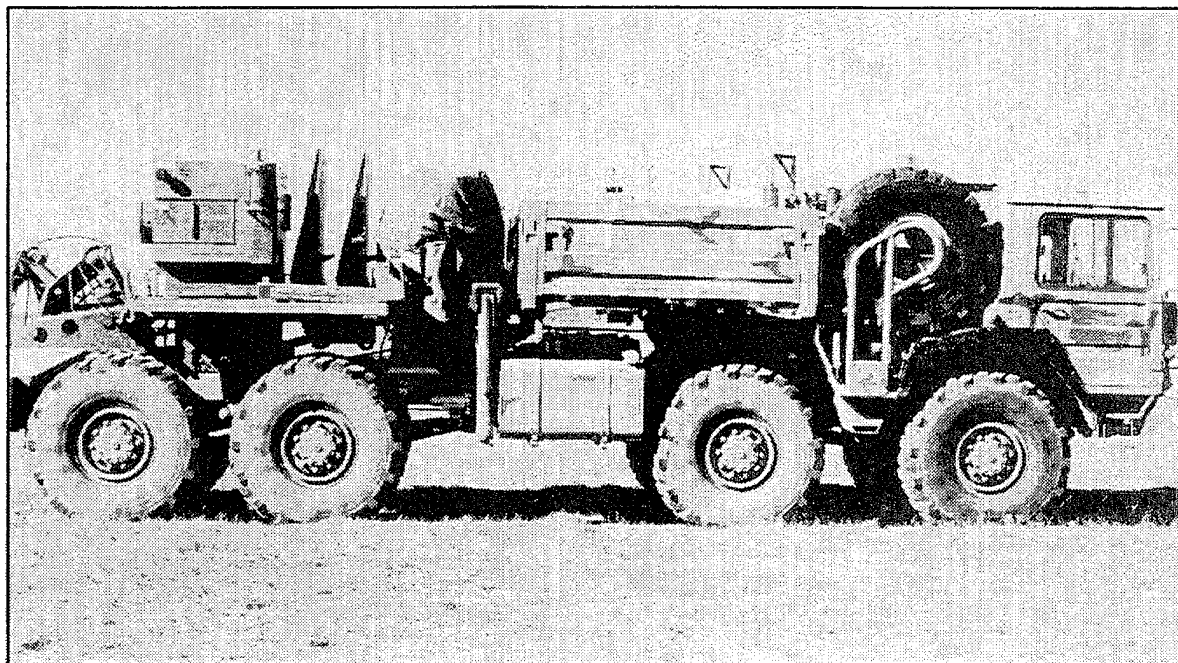


Figure 6. "Decorated" Target Vehicle at Eglin AFB Test Range

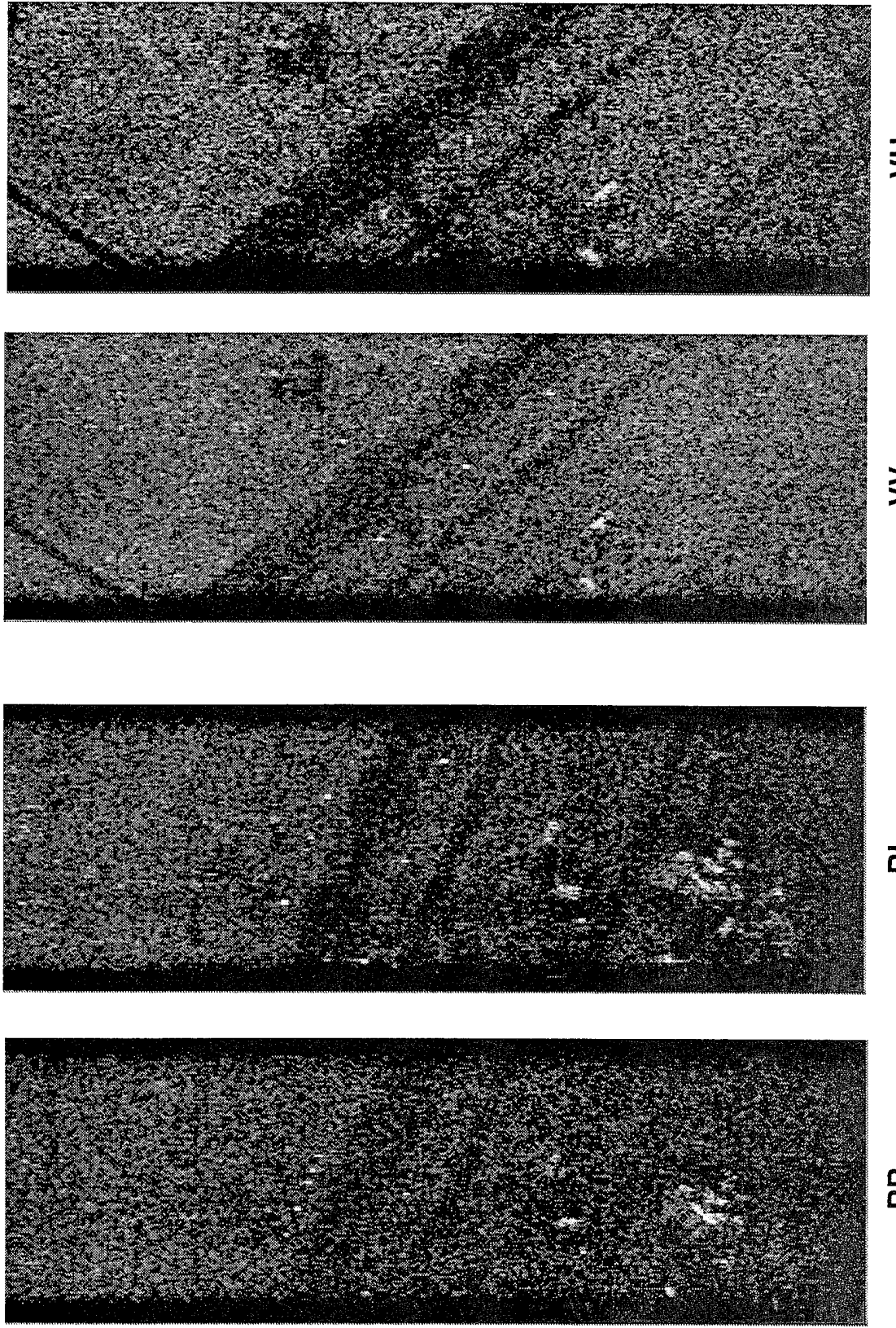


Figure 8. APG-76 Multi-Polarimetric Imagery of Eglin AFB Target Area (3x3 ft resolution, degraded from 1x1 ft)

feature-based ATR in a tactical environment. Work is ongoing to analyze significant amounts of data for the dual polarimetric responses of several vehicle types under these conditions.

6.0 ACKNOWLEDGEMENTS

Major portions of this program were funded under SLIN 4 of Georgia Tech Research Institute Subcontract A-9428-S3/Air Force Contract F33615-92-C-1045 (Mr. Elton Hopper, Technical Manager).

7.0 REFERENCES:

- [1] P. W. Smith , "Multimode antenna array", U.S. Patent No. 4,376,281 (1983).
- [2] Advanced Research Projects Agency / U.S. Army Topographic Engineering Center contract DACA 76-92-C-0028.
- [3] N. Marcuvitz, ed., *Waveguide Handbook*, Dover Publications, Inc., 1951, pp. 280-285.
- [4] Leo Young, Lloyd A. Robinson and Colin A. Hacking, "Meander-line Polarizer", *IEEE Transactions on Antennas and Propagation*, May 1973.
- [5] J. P. Montgomery, "Broadband K-band polarizer", *AFWAL Technical Report-81-1063*, April 1981.
- [6] John D. Kraus, *Antennas*, McGraw-Hill Book Co., 1950, pp 465-478.
- [7] D. C. Collier, M. Greenspan, D. MacFadyen, L. Orwig, "Application of a polarizing lens to a multimode flatplate array antenna", *Proceedings of the 1994 Antenna Applications Symposium*, Monticello, IL, September 1994.
- [8] D. Collier, "An RF switch and polarizer lens to enhance aperture SAR performance", Patent Application N-1262, 18 February 1994, Patent Pending.
- [9] D. Collier, M. Greenspan, D. MacFadyen, L. Orwig, "RF propagation from a flatplate array with polarizing lenses," *Proc IEEE 1995 Internat Radar Conf*, Alexandria, VA, May 1995.
- [10] R. N. Barnes, "Polarimetric calibration using in-scene reflectors," MIT Lincoln Laboratory, Lexington, MA, Proj. Rep. TT-65, Sept. 1986.
- [11] D. R. Sheen, A. Freeman, and E. S. Kasischke, "Phase calibration of polarimetric radar images", *IEEE Trans Geosci Remote Sensing*, vol 27, pp 719-731, Nov. 1989.
- [12] H. A. Zebker and Y. Lou, "Phase calibration of imaging radar polarimeter Stokes matrices," *IEEE Trans Geosci Remote Sensing*, vol 28, pp 246-252, March 1990.
- [13] J. J. van Zyl, "Calibration of polarimetric radar images using only image parameters and trihedral corner reflector responses," *IEEE Trans Geosci Remote Sensing*, vol 28, pp 337-348, May 1990.
- [14] K. Sarabandi, L. E. Pierce and F. T. Ulaby, "Calibration of a polarimetric imaging SAR," *IEEE Trans Geosci Remote Sensing*, vol 30, pp 540-549, May 1992.
- [15] C. M. H. Unal, R. J. Niemeijer, J. S. van Sinttruyen and L. P. Ligthart, "Calibration of a polarimetric radar using a rotatable dihedral corner reflector," *IEEE Trans Geosci Remote Sensing*, vol 32, pp 837-845, July 1994.

MEASUREMENT OF ISOLATION BETWEEN TWO ELLIPTICALLY POLARIZED ANTENNAS

H. Shnitkin & D. Collier
Westinghouse Norden Systems
Norwalk, CT

ABSTRACT :

This paper presents the technical analysis and the measurement technique for isolation measurement between two elliptically polarized antennas in support of the companion paper, entitled "Addition of a Polarimetric Capability to a Tactical SAR System" by D. Collier, M. Greenspan, L. Orwig and H. Shnitkin. An equivalent circuit of a two-antenna system is presented together with a derivation of input/output transfer coupling, using S-parameter analysis. The concluding coupling equation is a function of : (1) sense of rotation, (2) major axis orientation and (3) ellipticity of both transmit and receive antennas. A computer program and table of typical transfer coupling values are included. Subsequently, a definition of antenna orthogonality is presented and justified. Finally, the methods for measuring the above three parameters of the transmit and receive polarization ellipses are detailed and measured sample data is compared to computed sample data to demonstrate the antenna system isolation.

PURPOSE

Some of the latest radars are attempting to improve their target signature information by the use of both, right-hand circular and left-hand circular, polarized antennas. A companion paper (by D. Collier et al) addresses this circular polarization / target recognition technique and furthermore explains that the quality of target recognition depends upon the ability to accurately control and measure the polarization parameters of these radar antennas. For best target recognition performance, the two radar antennas used should possess

orthogonal polarizations in order to obtain the needed isolation . Since, in practice, all C.P. antennas possess small errors in symmetry, which results in *elliptical* polarization, this paper presents an analysis and measurement technique for evaluating the isolation between two *elliptically* polarized antennas.

THE PROBLEM

It is easy to recognize that maximum coupling between two elliptically polarized antennas occurs when they both possess the same sense of rotation, the same axial ratio, and the same orientation of the major axis of the polarization ellipse. Not so obvious is the condition of maximum isolation (or no coupling) between the two antennas, which is also called *orthogonality*. The problem to be addressed here is how to measure the two antennas and how to compute their degree of isolation (or orthogonality) in order to predict the resulting effect on the quality of radar target recognition .

EQUIVALENT CIRCUIT

An equivalent circuit model is the preferred approach to the full understanding of the coupling between two elliptically polarized antennas. Each antenna is represented by a 90-degree phase type of directional coupler with arbitrary coupling value, with one coupler output connected to a vertically (linear) polarized antenna and the other to a horizontally polarized one. These are shown in Figure 1 .

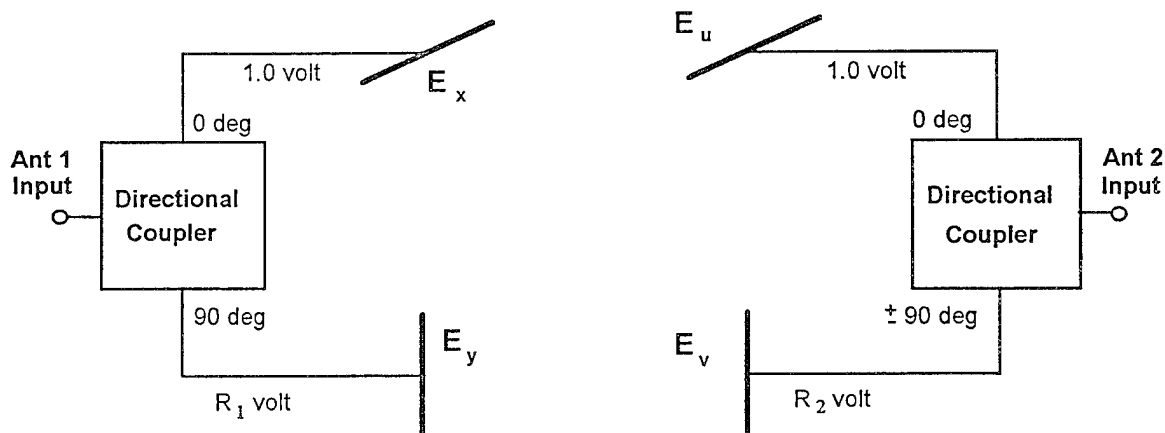


Figure 1 , Equivalent Circuit of Two Elliptically Polarized Antennas

Antenna 1, on the left, is oriented in the X-Y coordinate system, while antenna 2, on the right, is at an inclined angle in the U-V coordinate system. Furthermore, the positive X-axis forms an angle α with the positive U-axis, as shown in Figure 2.

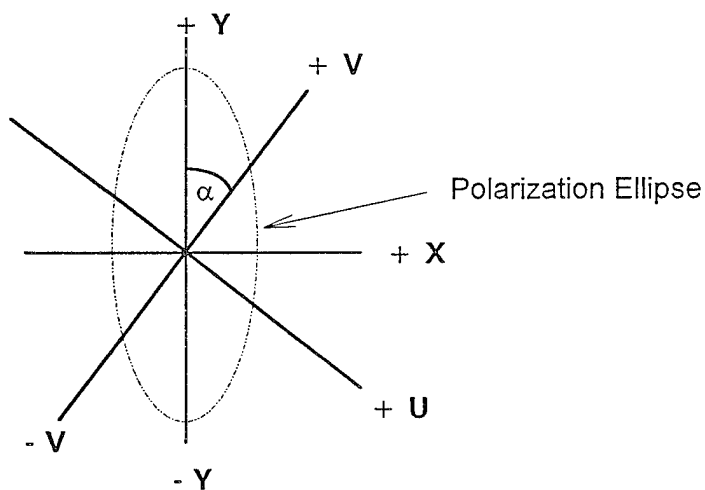


Figure 2 , Coordinate Axes

The circuit configuration for antenna 1, as shown in Figure 1, yields an elliptical polarization with an axial ratio of R_1 volts and the major axis of the polarization ellipse in the Y-direction, since R_1 volts are delivered to the E_y antenna and one volt to the E_x antenna. Similarly, for antenna 2, the axial ratio is R_2 volts and the major axis is in the V-direction. If both antennas are of the same sense of rotation, the -90-degree phase to E_v applies; for opposite sense of rotation, the +90-degree applies. The above can be demonstrated for the case of $\alpha = 0$ and circular polarization ($R_1 = R_2 = 1$) by comparing the total transmission phase through the upper branch to that through the lower branch in Figure 1. Because +90-phase of antenna 2 produces a 180-degree total phase through the lower branch, compared to zero phase through the upper branch, the coupled signal through the upper branch will cancel that through the lower branch and thus produce isolation !

S-PARAMETER DERIVATION

For the purpose of deriving S-parameters, the equivalent circuit of Figure 1 is subdivided into three sections, namely antenna 1, conversion from the X-Y to the U-V coordinates, and antenna 2. These are now designated as S1, SC, and S2, respectively, as shown in Figure 3.

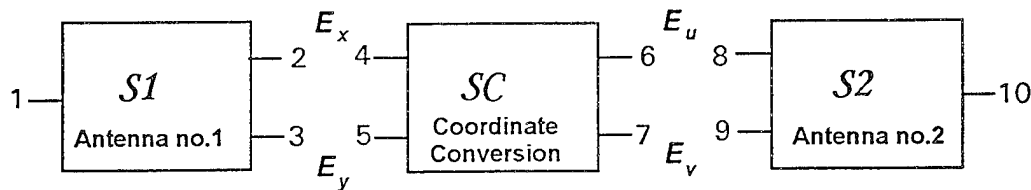


Figure 3 , S - Parameter Block Diagram

The complex transfer S-parameters for these three cascaded and assumed to be loss-less networks of Figure 3 can now be evaluated. The results are tabulated below.

TABLE 1 , Transfer S-Parameters of Two-Antenna System

$$S1_{2,1} = R_1 / \sqrt{R_1^2 + 1} \quad SC_{6,4} = \cos \alpha$$

$$S1_{3,1} = j / \sqrt{R_1^2 + 1} \quad SC_{7,4} = \sin \alpha$$

$$SC_{6,5} = -\sin \alpha$$

$$SC_{7,5} = \cos \alpha$$

$$S2_{10,8} = R_2 / \sqrt{R_2^2 + 1}$$

$$S2_{10,9} = -j / \sqrt{R_2^2 + 1} \quad (\text{same sense of rotation})$$

$$S2_{10,9} = j / \sqrt{R_2^2 + 1} \quad (\text{opposite sense of rotation})$$

Using the coordinate axes diagram of Figure 2, the SC network parameters above can be verified with equations [1] and [2], as shown.

$$E_v = E_x \sin \alpha + E_y \cos \alpha \quad [1]$$

$$E_u = E_x \cos \alpha - E_y \sin \alpha \quad [2]$$

Now the total voltage transfer characteristic of the combined three networks, namely, $S_{10,1}$, can be computed. For this purpose the same sense of rotation of the polarization vector was assumed for both, the left and the right antennas. Considering the four possible signal paths , the combined transfer function is :

$$S_{10,1} = (S_{2,1})(S_{6,4})(S_{10,8}) + (S_{2,1})(S_{4,7})(S_{10,9}) + (S_{3,1})(S_{7,5})(S_{10,9}) + (S_{3,1})(S_{6,5})(S_{10,8})$$

Substituting the appropriate values from Table 1 , yields [3]

Same sense :

$$S_{10,1} = \frac{1}{\sqrt{R_1^2 + 1}} \cdot \frac{1}{\sqrt{R_2^2 + 1}} \cdot [(R_1 R_2 + 1) \cos \alpha + j \cdot (R_1 + R_2) \sin \alpha] \quad [4]$$

This results in a power coupling factor of

$$P_{10,1} = \frac{1}{(R_1^2 + 1)(R_2^2 + 1)} \cdot [(R_1 R_2 + 1)^2 \cos^2 \alpha + (R_1 + R_2)^2 \sin^2 \alpha] \quad [5]$$

Opposite sense :

$$S_{10,1} = \frac{1}{\sqrt{R_1^2 + 1}} \cdot \frac{1}{\sqrt{R_2^2 + 1}} \cdot [(R_1 R_2 - 1) \cos \alpha + j \cdot (R_1 - R_2) \sin \alpha] \quad [6]$$

This results in a power coupling factor of

$$P_{10,1} = \frac{1}{(R_1^2 + 1)(R_2^2 + 1)} \cdot [(R_1 R_2 - 1)^2 \cos^2 \alpha + (R_1 - R_2)^2 \sin^2 \alpha] \quad [7]$$

For the same sense [of rotation] maximum coupling is achieved if the two antennas possess equal axial ratio and the major axes of their polarization ellipses are co-linear. This can now be proven with equation [5]; the first condition makes $R_1 = R_2$, while the second makes $\alpha = 0$. Substituting these relations in equation [5] yields $P_{10,1} = 1.0$ or 100 % coupling.

VERIFICATION OF THE ORTHOGONALITY CRITERION

Two elliptically polarized antennas are considered orthogonal, i.e., they are completely decoupled, if the following three conditions are met :

1. Their sense of rotation must be opposite.
2. Their axial ratios must be equal.
3. The major axes of their polarization ellipses must be orthogonal.

This can now be proven through equation [7] , when $R_1 = R_2$ and when $\alpha = 90$ degrees. This causes $\cos \alpha = 0$ and $(R_1 - R_2) = 0$, thus forcing $P_{10,1}$ to be zero. [NO coupling !]

COMPUTATIONS

By means of a simple computer program written around equations [5] and [7] , a set of possible polarizations have been evaluated for their orthogonality or lack thereof . The computed results , shown in Table 2 , show that only a small discrepancy between the axial ratios of the two antennas or a minor deviation of α from the 90-degree value causes isolation to fall above the -30 dB value. For most practical conditions, however, -20 dB of isolation appears achievable.

TABLE 2 , Sample Coupling Computations between Two Antennas

<u>Axial Ratio 1</u>	<u>Axial Ratio 2</u>	<u>Angle Between Axes</u>	<u>Sense</u>	<u>Coupling</u>
0 dB	1 dB	90 deg.	opposite	-24.8 dB
1 dB	2 dB	90 deg.	opposite	-24.9 dB
1 dB	1 dB	90 deg.	opposite	-24.8 dB
3 dB	3 dB	90 deg.	opposite	-80.3 dB
1 dB	1 dB	70 deg.	opposite	-28.1 dB
1 dB	3 dB	70 deg.	opposite	-17.7 dB
1 dB	1 dB	50 deg.	opposite	-22.7 dB
1 dB	2 dB	50 deg.	opposite	-18.6 dB
2 dB	2 dB	50 deg.	opposite	-16.7 dB
1 dB	3 dB	50 deg.	opposite	-15.5 dB
3 dB	3 dB	90 deg.	opposite	- 0.3 dB
0 dB	2 dB	30 deg.	same	- 0.1 dB
3 dB	3 dB	50 deg.	same	- 0.3 dB
3 dB	3 dB	90 deg.	same	- 0.5 dB

MEASUREMENTS

Before equation [7] can be used to predict antenna coupling (or isolation) between two actual antennas, their axial ratios, their major axis orientation angles and their sense of circularity must first be measured. The first two parameters are most easily ascertained on an antenna range with a rotating horn as the transmitting source. Axial ratio measurement simply requires a

minimum and a maximum signal measurement while rotating the above horn. However, the major axis orientation is most accurately determined by measuring two angular orientations at about 45 degrees on both sides of the major axis angle , which produce equal received signals; then compute the angle half-way between these two orientation angles. In other words, the major axis angle is the angle bi-sector of the two measured angles. The difference between the two major axis orientation angles of the **two** antennas is the angle α . Finally, for determining the sense of rotation one must either transmit using a C.P. antenna or physically examine the antenna design for clues .

Actual measurements were performed on a radar antenna, whose aperture was equally divided between right-hand and left-hand circular polarization. Isolation was predicted for various azimuth and elevation angles within the main beam, using range measurements of axial ratio and ellipse orientation. These results are shown in Table 3.

TABLE 3 , Predicted Isolation Between LHCP & RHCP Radar Antenna From Measurements

<u>AZIMUTH</u>	<u>E L E V A T I O N</u>				
	<u>-2 deg.</u>	<u>-0.7 deg.</u>	<u>0 deg.</u>	<u>+0.7 deg.</u>	<u>+2 deg.</u>
-1 deg	-23.3 dB	-24.5 dB	-22.5 dB	-23.2 dB	-24.8 dB
0 deg	-20.3 dB	-19.9 dB	-24.3 dB	-31.4 dB	-26.5 dB
+1 deg	-24.4 dB	-20.1 dB	-17.3 dB	-19.4 dB	-19.4 dB

**AN ACCURATE PHASE ALIGNMENT PROCEDURE
FOR ULTRA LOW SIDELOBE ANTENNAS
USING APERTURE COUPLED
FIELD PROBE TECHNIQUES**

**G. E. EVANS
D. T. HOTOPP
G. L. KEMPIC
D. P. PARRISH
K. G. RAMSEY**

**WESTINGHOUSE ELECTRIC CORPORATION
ELECTRONIC SYSTEMS GROUP
BALTIMORE, MARYLAND**

ABSTRACT

This paper will discuss a unique and extremely accurate phase alignment procedure for ultra low sidelobe, slotted waveguide, single axis scanned phased arrays. The procedure is not only very accurate, but can be performed without removing the antenna in question or its radome from their operational platform, which saves significant time and money in general periodic antenna performance "tune-ups" and mid life antenna system refurbishments and/or performance upgrades.

INTRODUCTION

The Phase Alignment Procedure was conceived and successfully implemented on an array of 28 horizontally running slotted waveguide radiators. Each of which were many wavelengths in extent, and which were manifolded and electrically scanned in the elevation plane. However, the procedure has the flexibility to be employed on other array antenna types including fixed beam and two axis scanned phased arrays.

The Phase Alignment Procedure discussed herein employs a matched stripline probe assembly to sample a very small part of the energy from each of the slots whose phase is being measured and subsequently aligned.

The combination of minimum aperture field disturbance and phase data averaging to counteract the effects of measurement noise and manufacturing tolerance induced phase errors results in a phase alignment procedure which is extremely accurate and economical in terms of depot level equipment maintenance.

TECHNICAL DISCUSSION

The use of an aperture coupled probe to tune a low sidelobe waveguide slotted array evolved from a task on a Westinghouse antenna problem in which it was desired to perform a mid-life performance check on the antenna while the antenna was installed on its platform aircraft with the radome in place. The

specific information which was desired for the performance check was the scanned plan phase flatness.

Given the imposed restrictions described above, the use of a far field range or a compact range was not possible since any relative phase data obtained on the radiating elements in question would be degraded by the presence of the radome and the effect of multipath produced by the surrounding environment.

The inability to employ conventional antenna range procedures for the aperture phase flatness check motivated Westinghouse engineers to investigate aperture probing techniques as a way to measure the flatness of the scan plane aperture phase. Aperture phase probing techniques which scanned a plane directly in front of and parallel to the aperture were quickly ruled out because of position registration difficulties. This left directly coupled aperture probe techniques as the remaining viable alternative for investigation.

Several directly coupled aperture phase sensing probes were investigated. The first was a waveguide cap which fit over the center slot of the slotted waveguide radiator whose phase was being measured. The array geometry of the antenna being measured is shown in Figure 1 and the waveguide slot cap probe is shown in Figure 2.

It was found that the waveguide cap probe took an extremely long time to move around the aperture in the process of measuring the required phases and

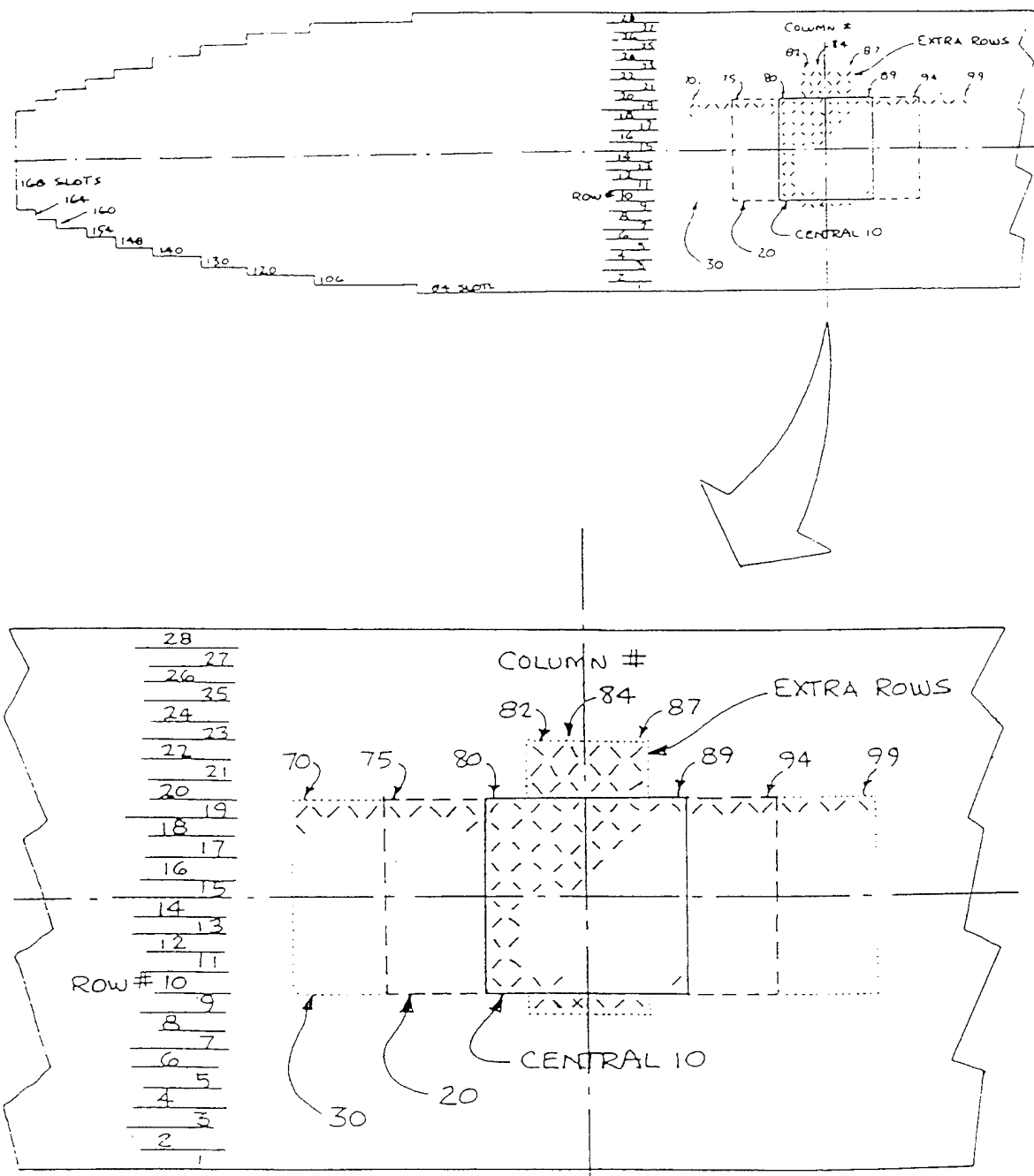


Figure 1
Array Geometry

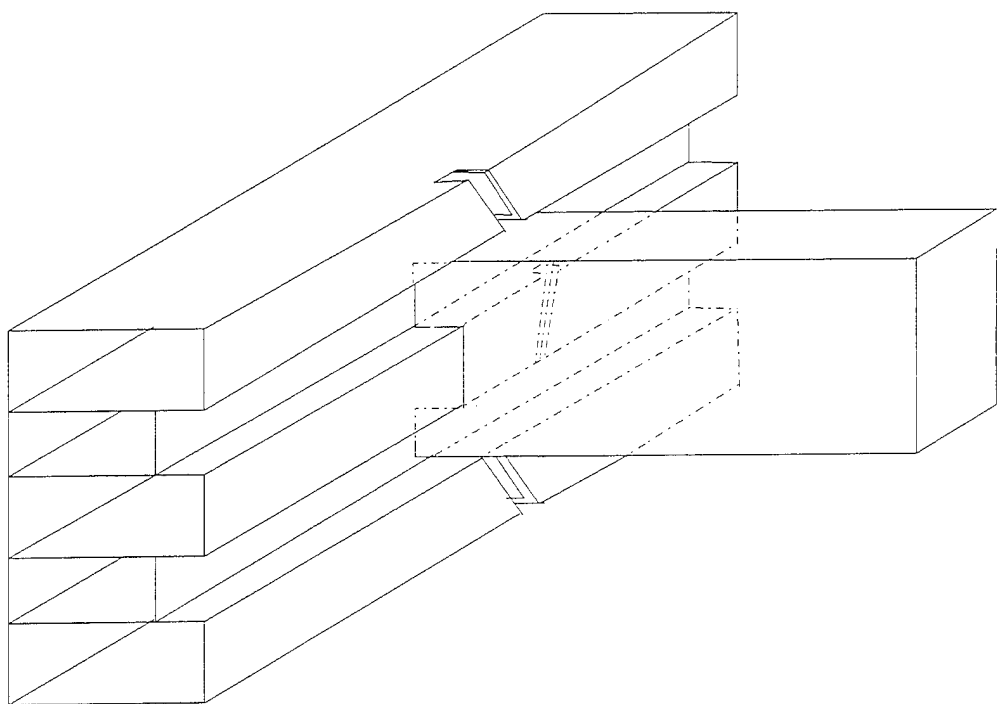


Figure 2
Wave Tee Coupler Probe

that, in order to obtain repeatable measurements, that the cap had to be mounted to the array face in such a way that permanent deformation of the antenna in the location of the cap attachment points was incurred. In addition to the foregoing, the effect of the waveguide cap probe on mutual coupling among the slot being measured and neighboring slots was a concern. All factors considered, the waveguide cap probe was finally eliminated as a candidate for all the foregoing reasons.

The most promising probe configuration and the one which was finally selected for the phase measurement task was a stripline probe which was directly coupled to the slot being measured. This configuration is shown in Figure 3. The advantages of this configuration were that the probe could be "lightly" coupled to the slot being measured by tapping off energy from the slot in a region where the fields are minimal, thus causing minimal perturbation to the slot radiation characteristics during the phase measurement. Furthermore, the probe and the coax transmission line connecting the probe and the network analyzer used to measure radiator phases could be tucked between radiators in such a way as to minimize mutual coupling perturbations due to R. F. scattering from the probe structure.

During the mid-life aperture phase checkout, it was recognized that the phase measurement procedure discussed above could easily be extended to be

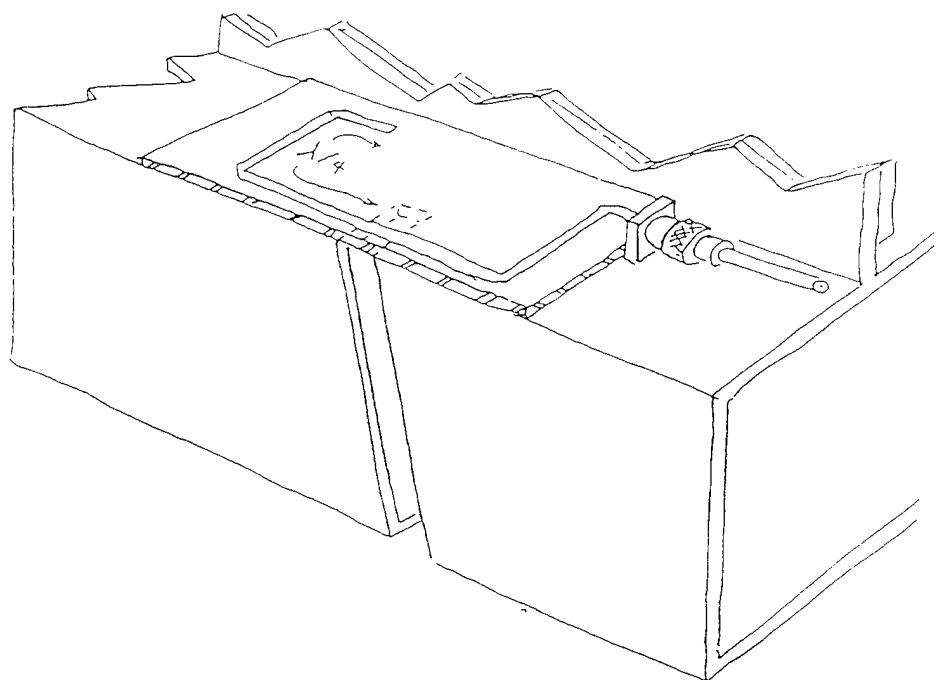


Figure 3
Stripline Probe

used as a on aircraft phase alignment procedure as well.

The phase alignment procedure, using the stripline probe of Figure 3, needed a number of refinements before it was optimized to the point where it was accurate enough to be used to tune phase well enough to obtain very low scan plane sidelobes.

In order to obtain maximum power transfer between the probe and a radiating slot, it was necessary to tune the probe in the presence of the slot being measured. This was done by judiciously trimming a stripline matching circuit, which was part of the transmission line feeding the probe, until a match of better than 1.25:1 was obtained. This was a one time operation. Details of the matching are shown in Figure 4 and a photograph of the probe shown in Figure 5.

It was also found (see Figure 6) that the coax transmission line feeding the probe through a channel between two slotted sticks required mode suppressors to avoid exciting spurious TEM through modes between the sticks when the feeding transmission line was present. The mode suppressors simply shorted the feeding transmission line to waveguide walls of the stick channels and were moved with the feed transmission line/probe combination as each stick was measured.

The problem of mechanically registering the probe at the same distance from the array face for each slot phase measurement was solved by providing

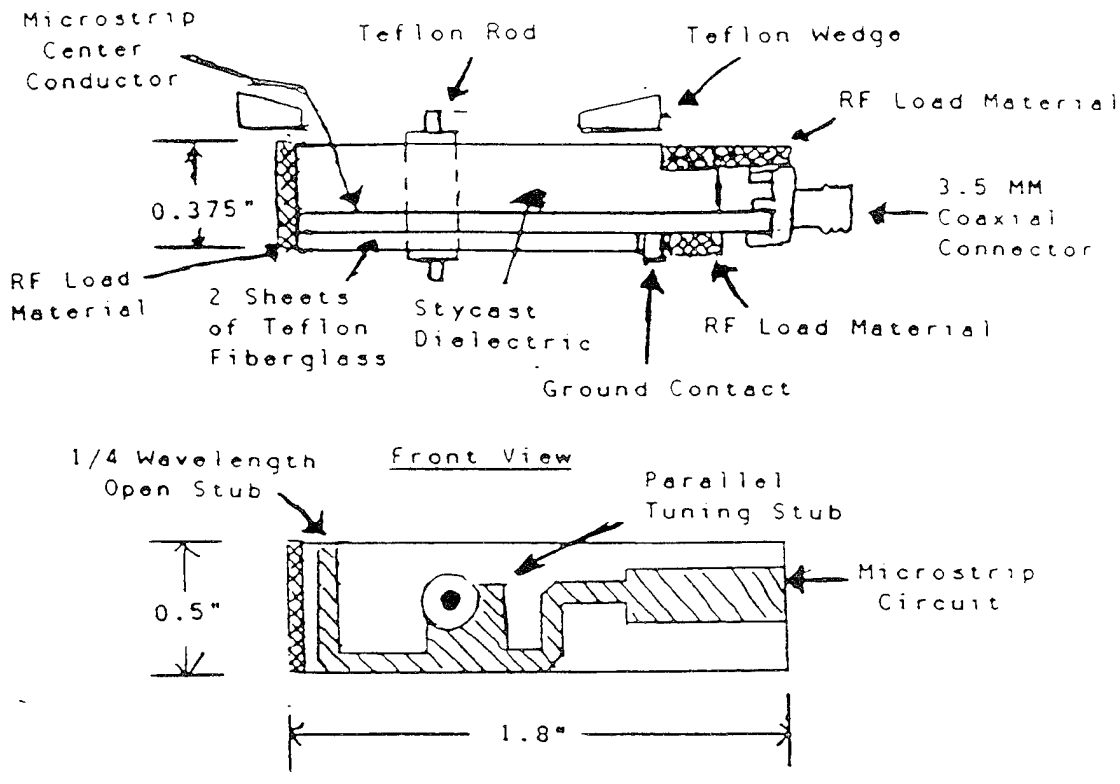


Figure 4
Stripline Probe Matching
and Mechanical Details

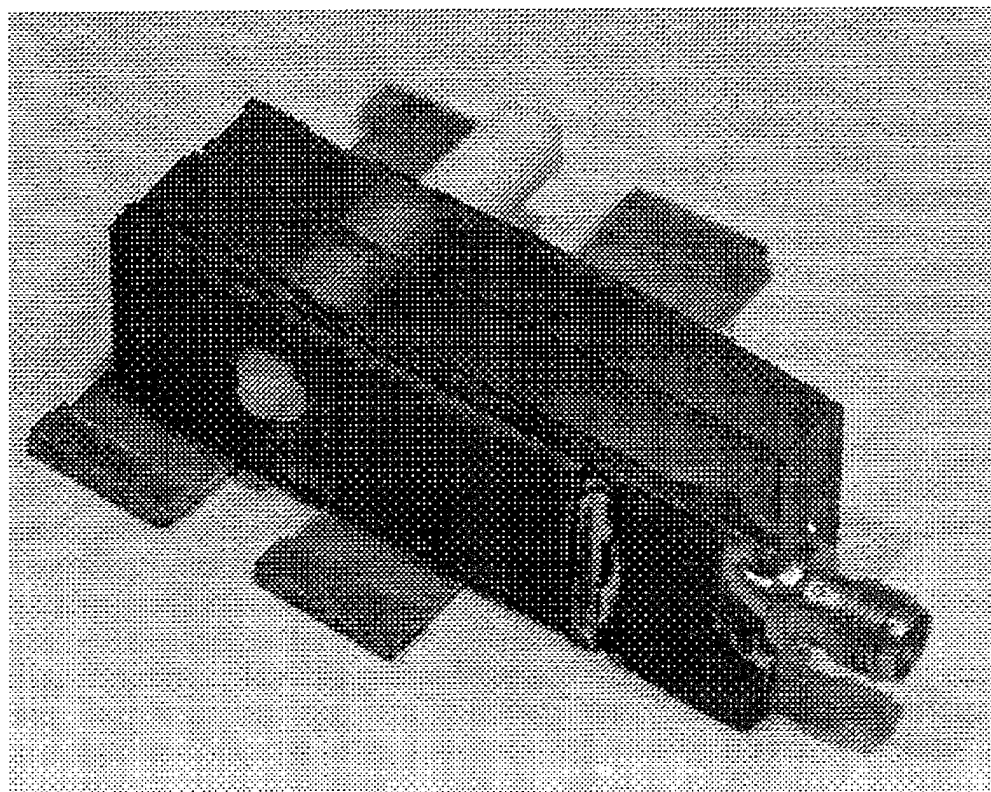


Figure 5
Stripline Probe

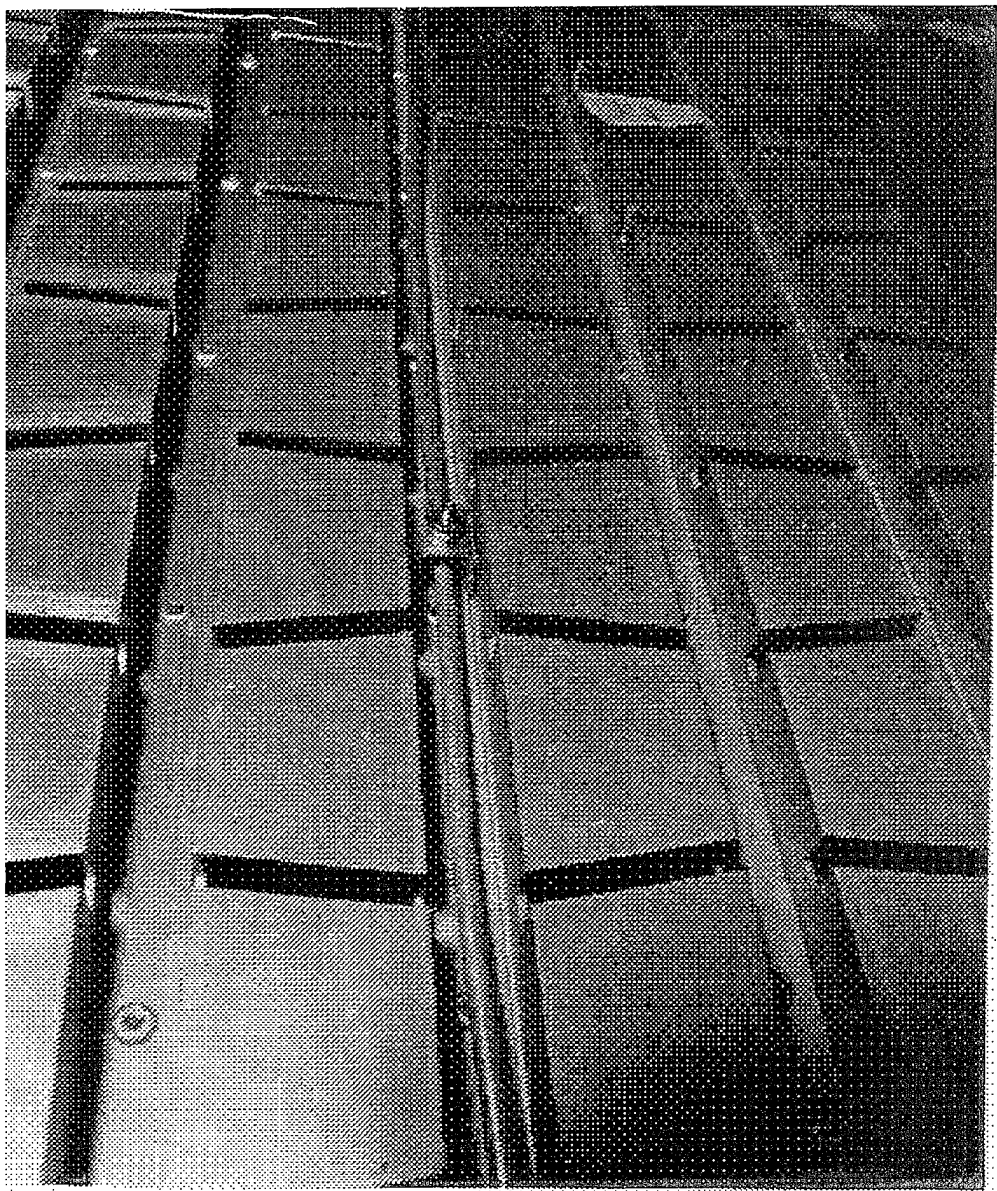


Figure 6
Probe Feed Coax and Mode Suppressors

teflon self locating buttons (see Figures 4 and 5) which provided "X" and "Y" registrations (see Figure 7) and a fiberglass stop on the probe (Figure 8) which provided "Z" direction registration. This feature of the probe was extremely crucial to the success of the phase alignment scheme since it gave probe location repeatability with a tolerance that was equivalent to fractions of a degree. Figure 9 shows a complete view of an array face, probe and feeding transmission line. Figure 6 also shows details of the coax mode suppression devices.

Figure 10 shows a block diagram of the antenna phase alignment test equipment setup.

Originally, phase measurements were made at only one slot on each of the slotted waveguide radiating elements. Measurement accuracy and repeatability were found to be unsatisfactory. Since each slotted waveguide radiator had at least 84 slots and in most cases many more than this, it was decided to measure more slots on each stick in order to obtain more measurement accuracy via data averaging. It was found that for the center sticks of the array that measuring 20 slots and averaging the data to obtain results gave the same performance as obtained for thirty slots per stick averaging and slightly better results than for ten slots per stick phase data averaging. From that point on data was taken on twenty slots per stick for the array ten center sticks. Since there was an amplitude taper in the scan plane, for sticks outside the ten center stick area, ten slot averaging

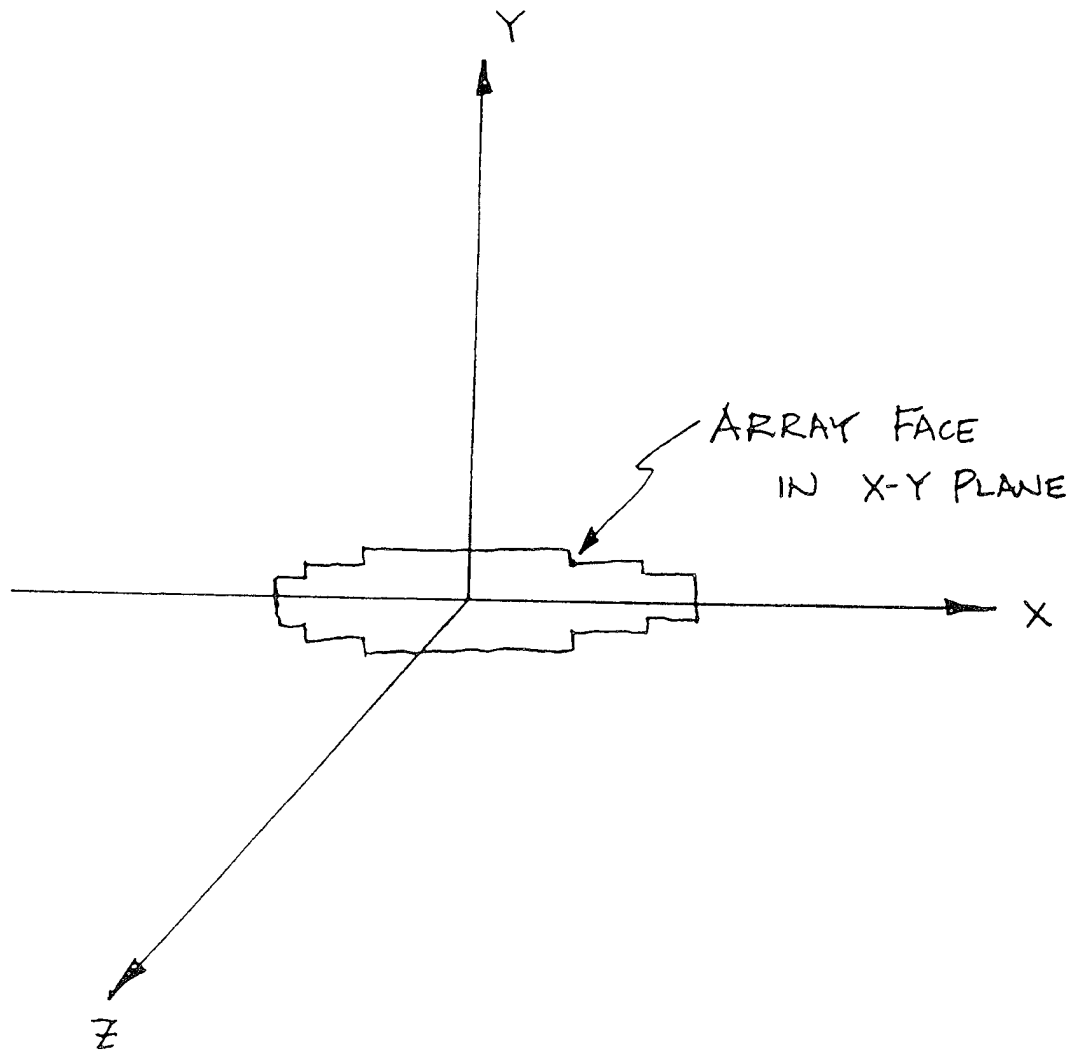


Figure 7
Array Coordinate System

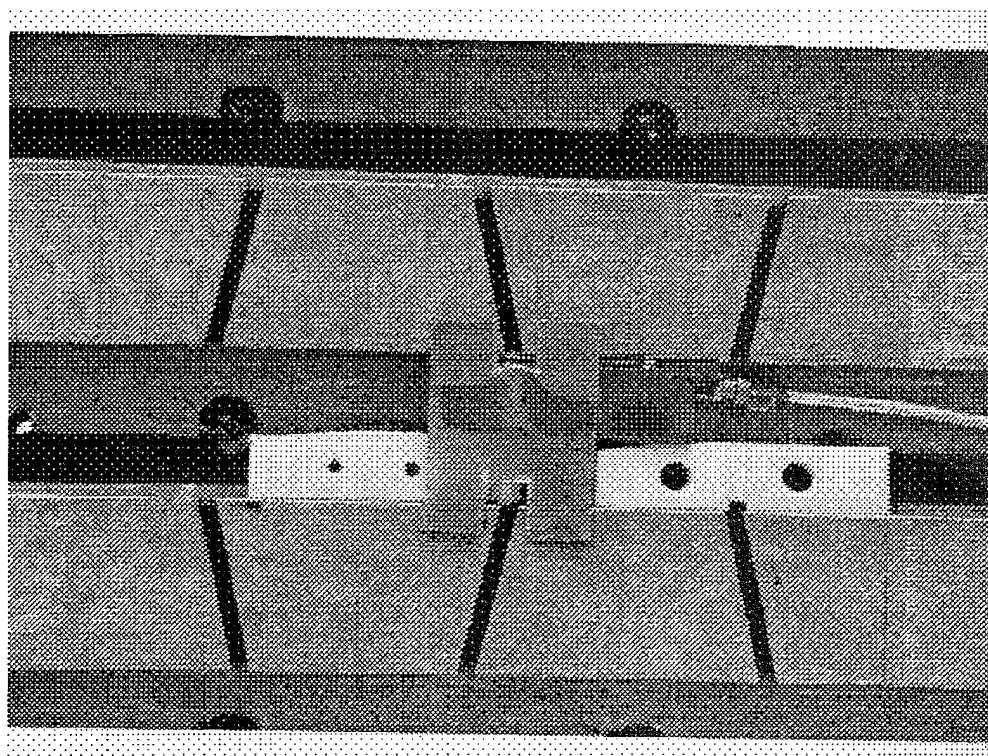


Figure 8
Probe and Position Registration Details

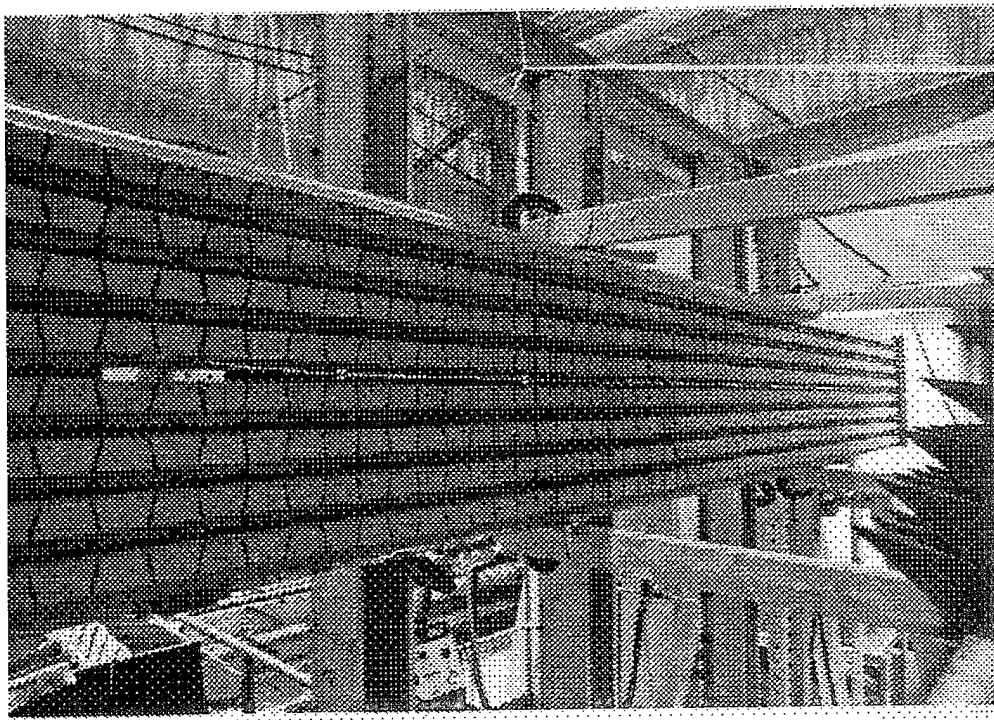


Figure 9
Entire Probe Measurement Setup

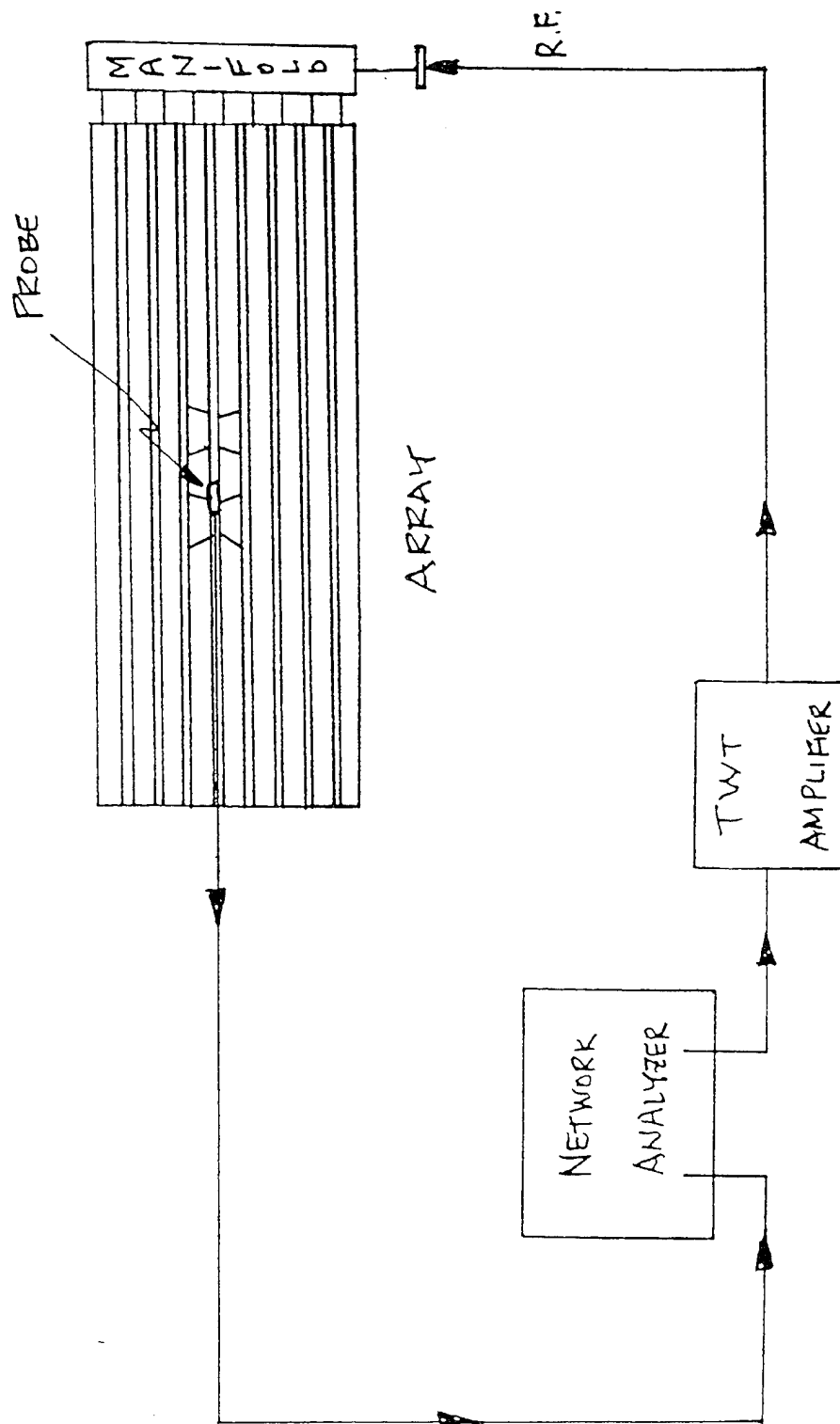


Figure 10
Test Equipment Setup

was employed since phase errors on these outer sticks did not affect the antenna pattern as much as the center sticks.

Phase measurements taken on the array in question produced the relative values shown in Figure 11. These were values measured on an already tuned array so that by further adjusting these values by tuning the array electronic phase shifters, the tester would have extended the measurement process to an even more accurate tuning process. The pattern associated with the aperture distribution phases of Figure 11 is shown in Figure 12. The theoretical pattern of the measured antenna is shown in Figure 13. A pattern of the same antenna taken on a far field range is shown in Figure 14. The quality of the pattern of Figure 12 demonstrates that the "On Aircraft" tuning procedure provides an excellent method of phase tuning or checking the aperture phase of a low sidelobe antenna in the field and in the presence of its radome.

Amplitude errors are not included in the computed pattern of Figure 12 since they could not be adjusted during the process in question and it can be seen that the computed pattern of Figure 12 and the measured pattern of Figure 14 are very similar in terms in performance. This was to be expected due to the extremely accurate mechanical tolerances obtained in the numerically controlled machining of the antenna feed network couplers which allow very tight tolerance control of feed network amplitude tolerances (on the order of .05 dB RMS).

<u>STICK NO.</u>	<u>MEASURED PHASE (DEG.)</u>	<u>STICK NUMBER</u>	<u>MEASURED PHASE (DEG.)</u>
1	-9.41*	15	-0.01
2	-9.41*	16	0.91
3	-9.41	17	-0.02
4	-7.51	18	-0.30
5	-7.51	19	0.06
6	-6.42	20	-1.10
7	-6.09	21	-1.92
8	-3.14	22	-1.65
9	-3.81	23	-3.12
10	-3.00	24	-4.33
11	-2.60	25	-4.80
12	-1.28	26	-6.25
13	-1.98	27	-6.25*
14	0.00	28	-6.25*

Figure 11
Measured Aperture Distribution Phases

28 ELEMENT LINEAR ARRAY PATTERN
ELEVATION PATTERN
MEASURED PATTERN FINAL PHASE ERRORS
 $\cos(\theta)^{**2}$ ELEMENT FACTOR

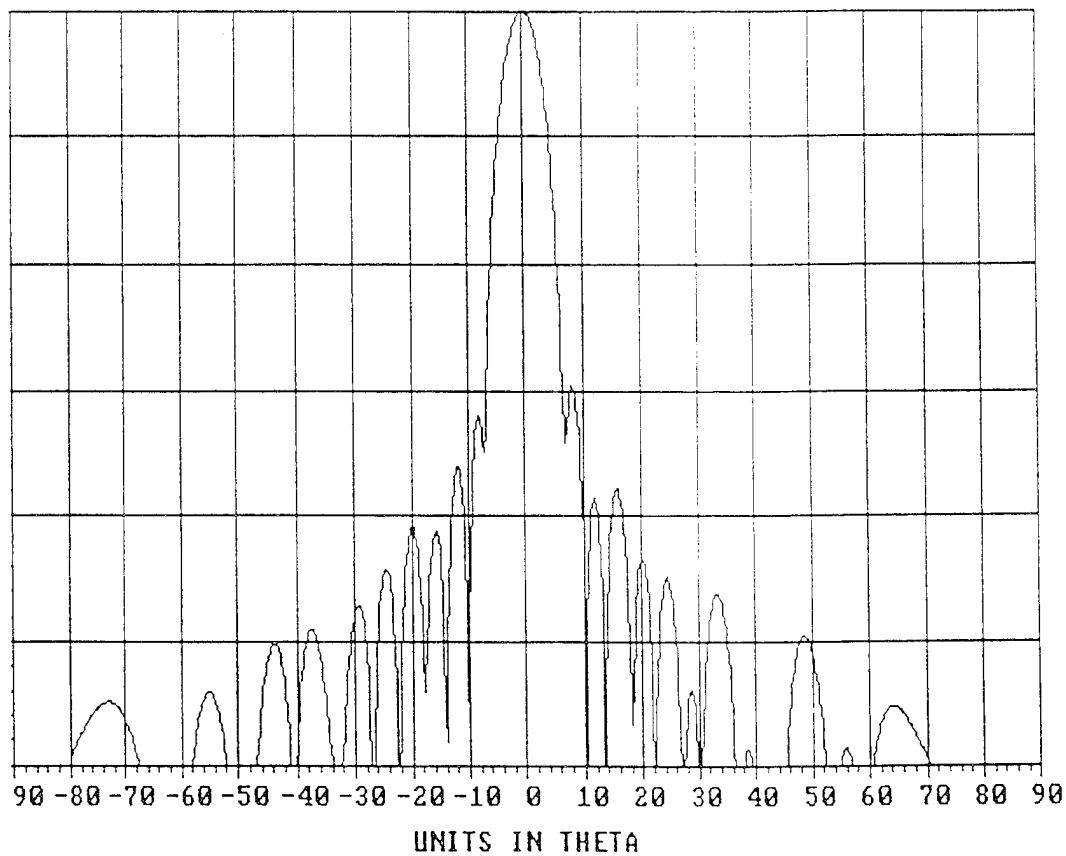


Figure 12
Computed Pattern Using
Phases from Figure 11

28 ELEMENT LINEAR ARRAY PATTERN
ELEVATION PATTERN
THEORETICAL PATTERN NO PHASE ERRORS
 $\cos(\theta)^{**2}$ ELEMENT FACTOR

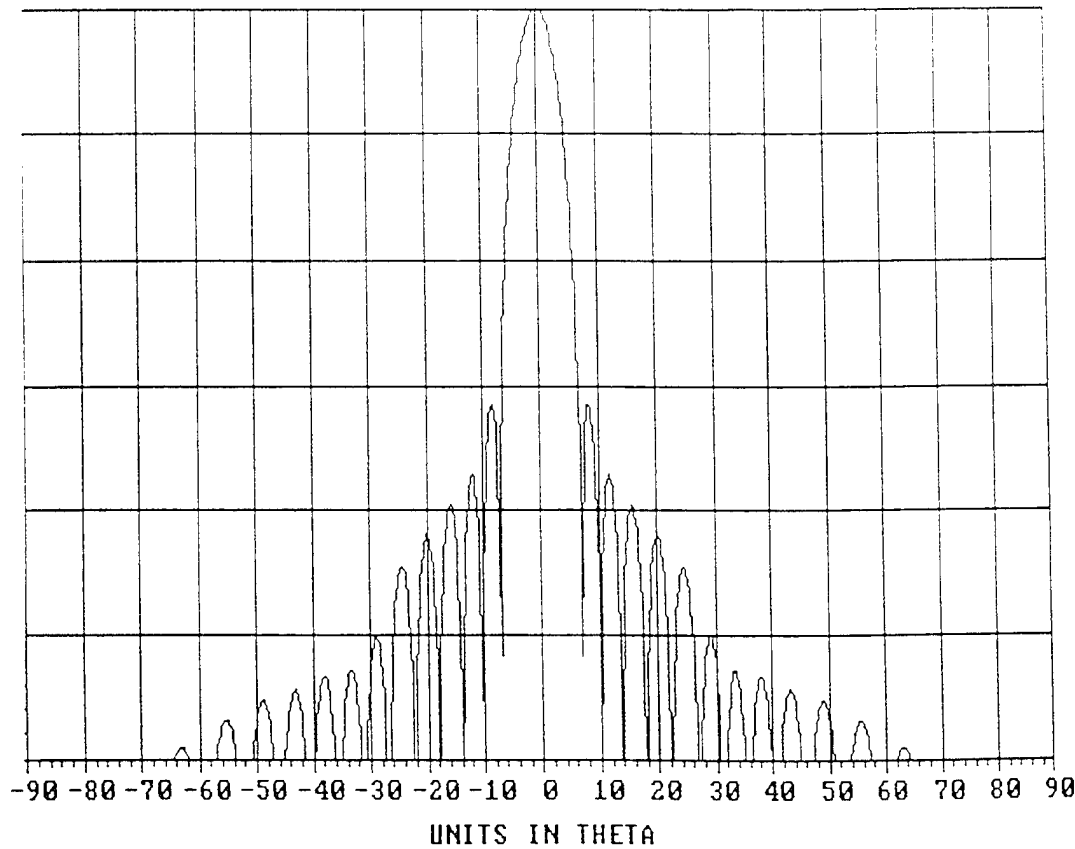


Figure 13
Theoretical Array Pattern

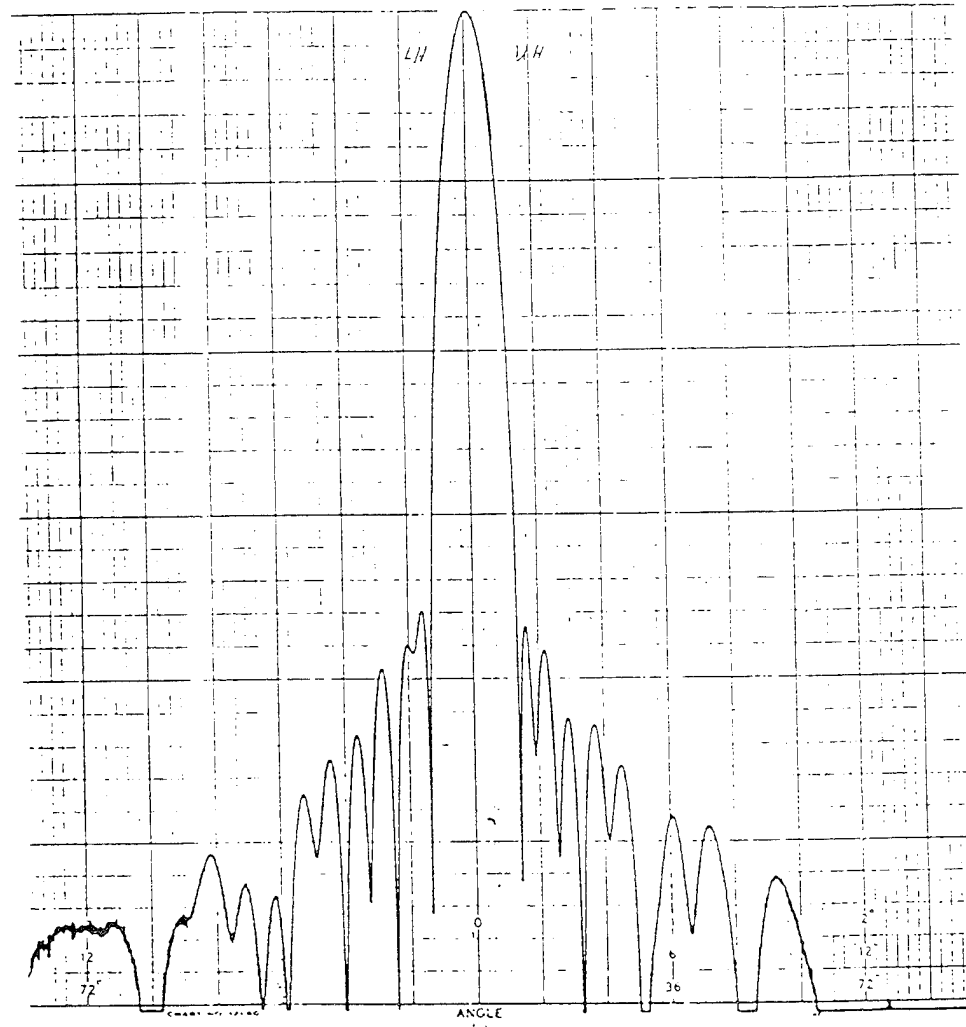


Figure 14
Angle Measured Array Pattern

CONCLUSION

The foregoing discussion provides a detailed outline of an extremely accurate array aperture phase alignment procedure which was derived from an accurate aperture phase measurement procedure on a single axis scan low sidelobe phased array. The procedure allows the phase tuning to be done on the associated platform with radome in place. This last feature saves significant time and money by virtue of providing the maintenance flexibility to virtually allow flight line/forward deployment "Depot" antenna performance update and/or refurbishment capability. The procedure, however is not restricted to single axis scan antenna arrays but can be just as useful for fixed beam arrays or two axis electronically scanned arrays.

E-3A REFLECTIONLESS MANIFOLD
PERFORMANCE IN THE PRESENCE OF
MISMATCHED RADIATING ELEMENTS

D. P. PARRISH
J. M. VEZMAR
K. G. RAMSEY

WESTINGHOUSE ELECTRIC CORPORATION
ELECTRONIC SYSTEMS GROUP
BALTIMORE, MARYLAND

ABSTRACT

This paper will discuss the performance of an E-3A Antenna type transmit elevation feed network (manifold) in the presence of mismatched phase shifters and mismatched fourth port terminations. The effect of these mismatches on the elevation pattern performance and the amount of spurious power delivered to transmit feed network "isolated" ports will be evaluated.

INTRODUCTION

In designing the E-3A Antenna Elevation Manifold (feed network), matched radiating elements are assumed. This is done because of the lack of any "A Priori" knowledge of the actual radiator input admittance and because it has been found, in practice, that the antenna gain and pattern performance results obtained in this manner have been more than satisfactory.

However, when the question of manifold power handling is addressed, it is important to know how the power is distributed to the various components which comprise the manifold assembly in order to assess predicted component average power induced overheating conditions, if any. This can be accomplished by a computer aided analysis of the manifold assembly which includes the effects of feed network component mismatch, and hence mutual coupling, among the various feed network components. The analysis determines not only the actual power delivered to the radiating aperture of the antenna, but also the error power present at any "fourth port" termination in the manifold assembly due to tolerance induced manifold circuit imbalances and finite component reflections. Recent analysis of proposed E-3A system performance upgrades has highlighted the need to closely examine the power handling capability of any and all manifold components and its effect upon overall antenna performance.

TECHNICAL DISCUSSION

A block diagram of the E-3A Antenna transmit elevation manifold is shown in Figure 1. The manifold is a balanced waveguide microwave circuit consisting of a branchguide 3 dB coupler feeding a pair of "identical" travelling wave reactive tee (three port) series feed slotted waveguide coupling assemblies. Figure 2 shows a slotted waveguide reactive tee coupler similar to those discussed immediately above. Figure 3 shows the microwave equivalent circuit of the waveguide reactive tee coupler shown in Figure 2.

For the E-3A manifold, the effect of component tolerance errors and component mismatch interaction induced errors is manifested to a very small degree in elevation pattern and antenna gain performance. However, the primary effect of these errors manifests itself in the unwanted power delivered to "fourth port" loads, in particular, unwanted power delivered to the transmit hybrid loads of Figure 1.

The following analysis assesses the effects of the aforementioned error sources on antenna pattern performance and upon the unwanted R. F. energy delivered to any manifold "fourth port" or travelling wave feed assembly end terminations.

A more complete schematic of the E-3A transmit elevation manifold is shown in Figure 4. To properly assess the performance of the manifold shown

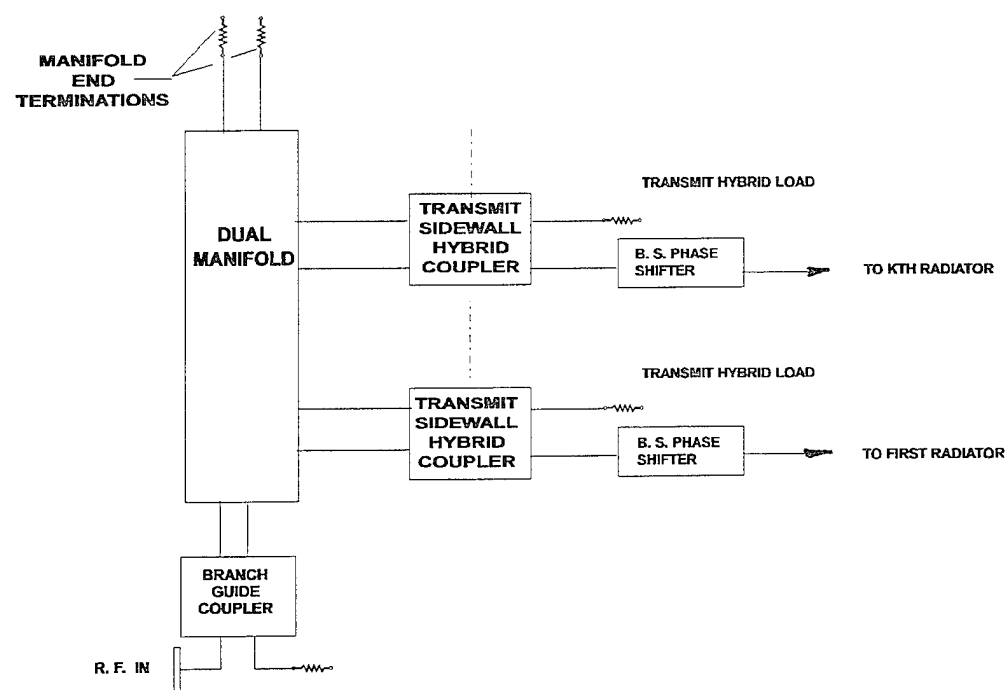


Figure 1
E-3A Antenna Transmit Manifold Block Diagram

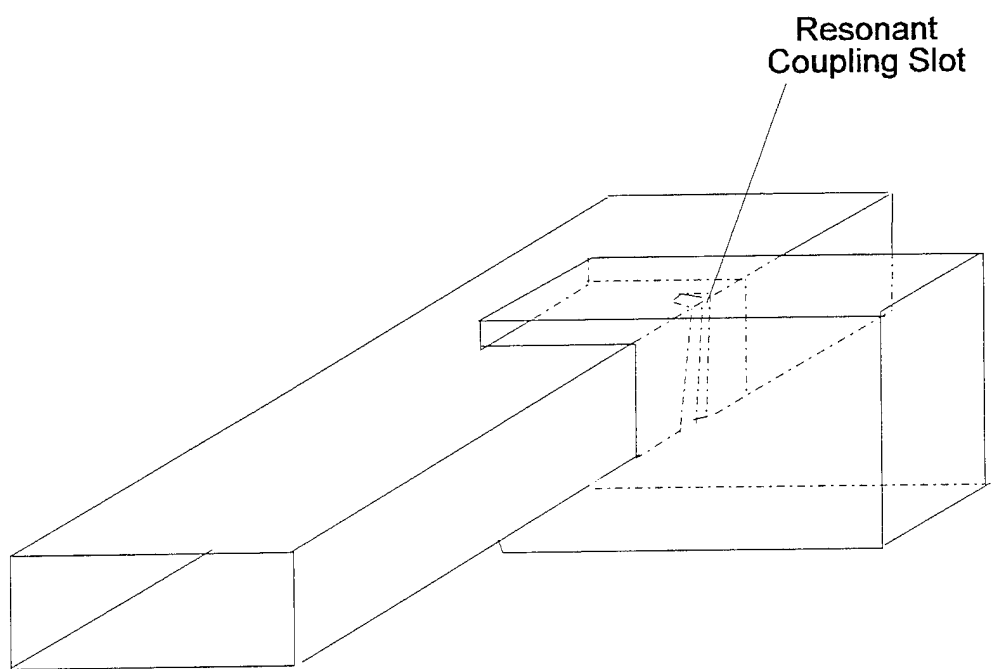


Figure 2
Waveguide Three Port Reactive Tee Coupler

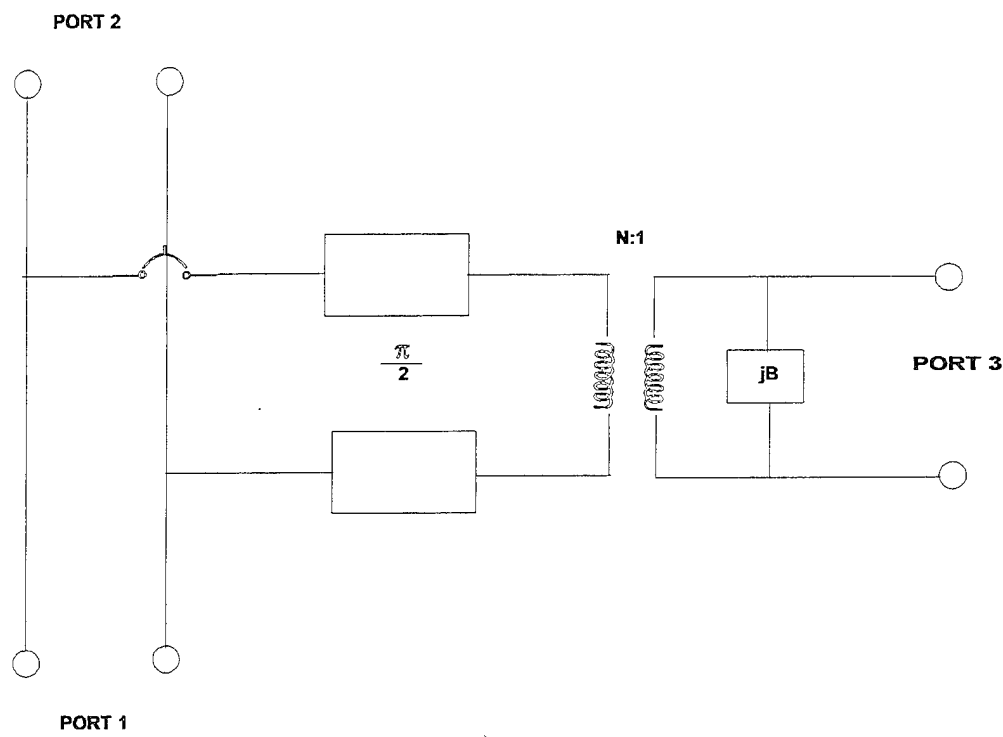


Figure 3
Equivalent Circuit of Three Port Reactive Tee

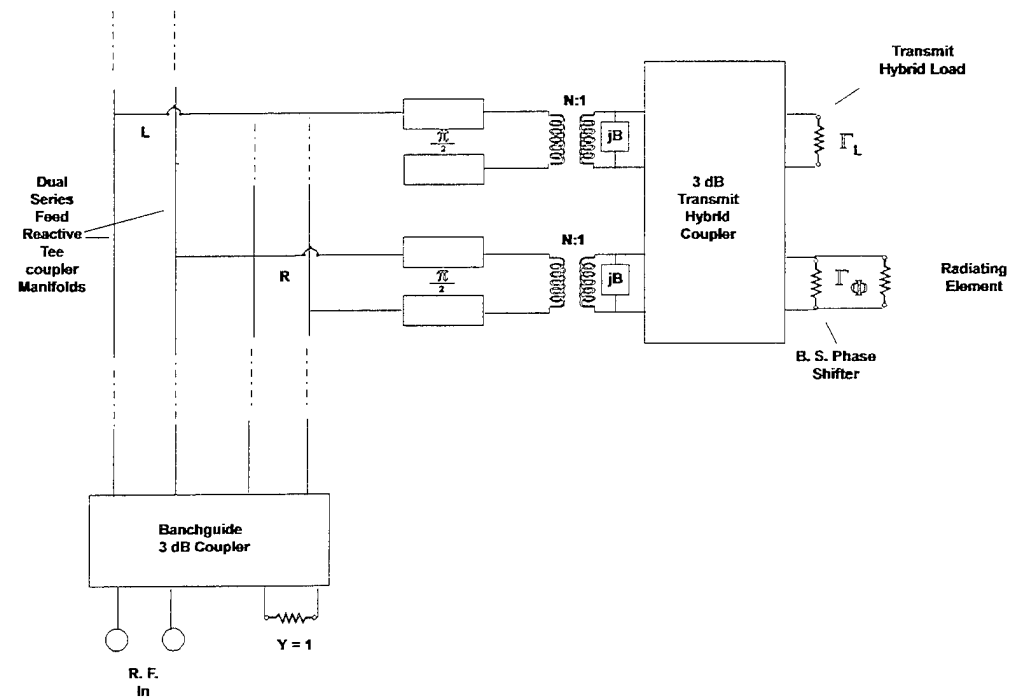


Figure 4
E-3A Transmit Manifold Schematic

in Figure 4, it is necessary to use a combination of scattering parameter and manifold microwave equivalent circuit analysis and combine the results to obtain the desired information.

The E-3A Elevation Transmit Manifold shown in Figure 4 has 28 pairs of branch tee coupling ports; a pair for each of the 28 radiating elements. Each radiating element is fed by a pair of slotted waveguide reactive (branch) tee couplers (see Figure 2) through a 3 dB sidewall coupler and a beam steering phase shifter. The two 28 port travelling wave reactive tee couplers of Figure 4 are fed, in quadrature, at their inputs by a 3 dB waveguide branch line coupler. This manifold geometry is very easy to package and provides a balanced microwave circuit that is very elevation pattern insensitive to the phase and amplitude errors of the two slotted waveguide travelling wave reactive tee coupler assemblies of Figure 4.

Primary manifold R. F. signal error sources are:

1. Phase errors between branch coupling terminal pairs "R" and "L" (see Figure 4), feeding a particular radiating element, due to R. F. propagation velocity differences between slotted waveguide manifolds "R" and "L".
2. Beam steering phase shifter reflections which contribute significantly to the amount of power reaching the transmit hybrid

load of the same radiator feed transmission line in which the phase shifter is located.

3. Amplitude errors in the branchguide coupler and the transmit couplers in each radiator feed transmission line.
4. Mutual coupling between radiator feed lines; i.e., R. F. energy reflected from a phase shifter and transmit hybrid load in a particular radiator feed line which is delivered to the transmit hybrid load of other radiator feed lines.

The performance of the manifold assembly of Figure 4 is assessed by first determining the input admittance at branch tap terminal inputs "R" and "L" for each of the 28 radiating element feed lines of the elevation manifold and then analyzing the microwave equivalent circuit of each of the two travelling wave reactive tee coupler assemblies of Figure 4 to obtain the voltage at the two input ports of the transmit hybrid of each manifold radiator feed line. These input voltages are then combined (in each of the 28 feedline transmit hybrids) to evaluate the voltage present at the two transmit hybrid output ports which feed the phase shifter (and radiating element) and transmit hybrid load as shown in Figure 4.

The relative value of these two transmit hybrid output voltages gives the desired information about the power to each of the twenty eight transmit hybrid

loads of Figure 4.

Since the transmit hybrid of Figure 4 does not have a microwave equivalent circuit, it is necessary to represent all 28 branch tap pairs of the "reflectionless" manifold assembly of Figure 4 with scattering matrices in order to fully quantify manifold performance.

The use of scattering matrices to evaluate theoretical E-3A elevation manifold performance is illustrated in Figure 5. Using scattering matrices for this problem avoids difficulties associated with the lack of a microwave equivalent circuit for the 3 dB transmit hybrid coupler, and enables the analyst to determine the actual input impedances of the two input ports of the "black box" of Figure 5 so that the manifold performance can be evaluated analytically.

The use of the "black box" of Figure 5 allows the conceptually straightforward determination of the manifold performance in terms of elevation pattern quality and the relative power to each of the transmit hybrid loads.

Since the E-3A patterns are classified, the actual analysis for the E-3A manifold, though now completed, will not be shown herein, instead, very similar analytical results for a 28 port unclassified low sidelobe pattern producing feed network will be shown with no loss of useful information or reduction of problem solution scope.

The scattering behavior of the black box of Figure 5 is derived by taking

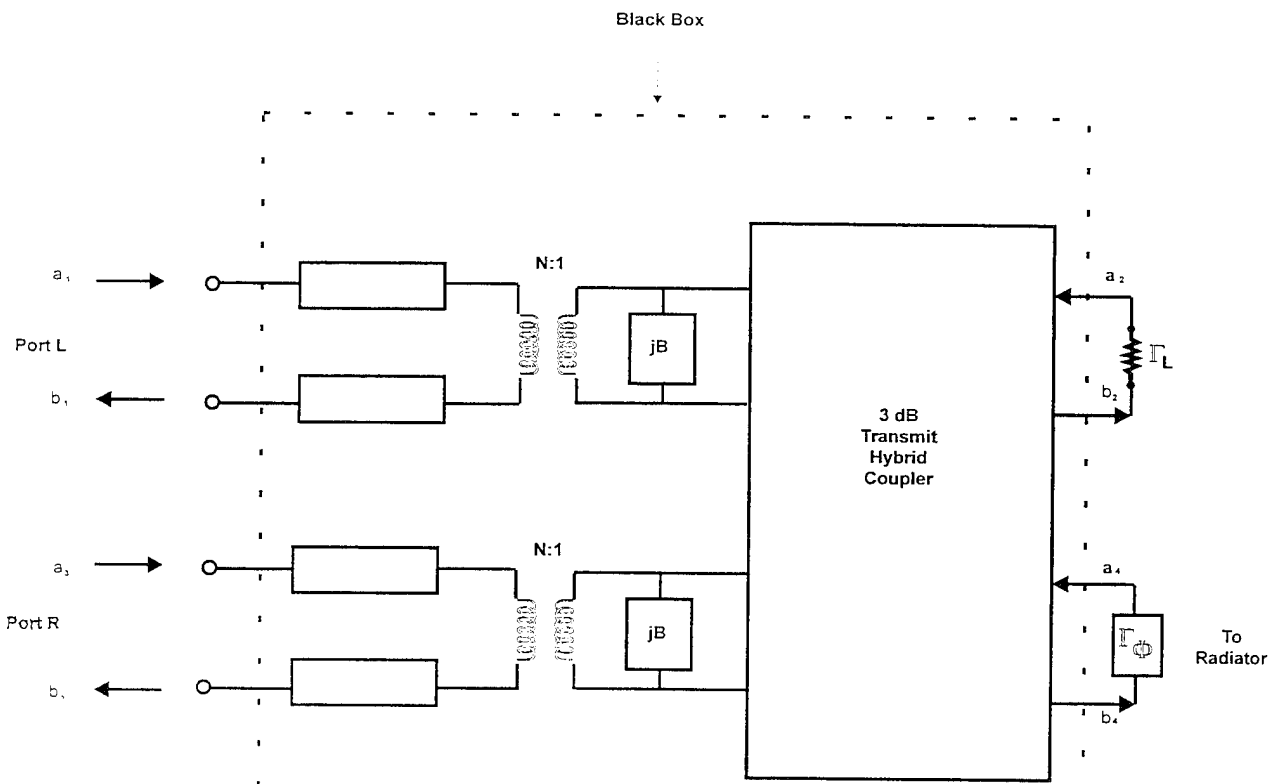


Figure 5
Scattering Parameter Black Box
Treatment of Coupling Slots & ϕ -Shifter Module

the individual scattering matrices of the transmission line components of Figures 6 through 9, transforming them to "C" matrices, as shown in Figure 10, and cascading them from left to right (see Figure 5) to obtain an overall "C" matrix for the black box of Figure 5 from which the reflection coefficients, and hence the input admittances of Ports L and R of the black box of Figure 5 can be obtained.

The determination of the Port L and Port R input admittances for each manifold branch, combined with L and R manifold half signal superposition, now allow the transmit manifold performance to be ascertained with simple microwave equivalent circuit analysis.

Using the foregoing approach for the E-3A type manifold, performance results as shown in Figures 11 through 20 are obtained.

Figure 11 shows the power delivered to the transmit hybrid load "isolated" ports and the intended phase shifter signal "through" ports of the antenna feed network relative to the antenna input power. Figure 12 shows the associated theoretical and realized elevation patterns for the case where both the transmit hybrid loads (THL) and phase shifters (phasers) are perfectly matched. Note the perfect agreement between the theoretical and itemized elevation patterns and the extremely low power to the THLS.

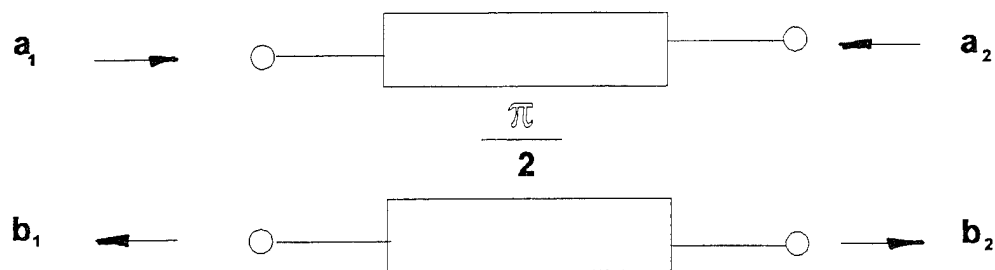
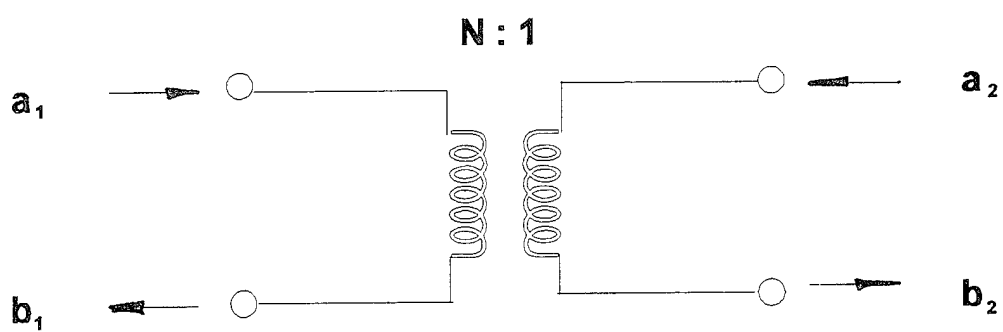
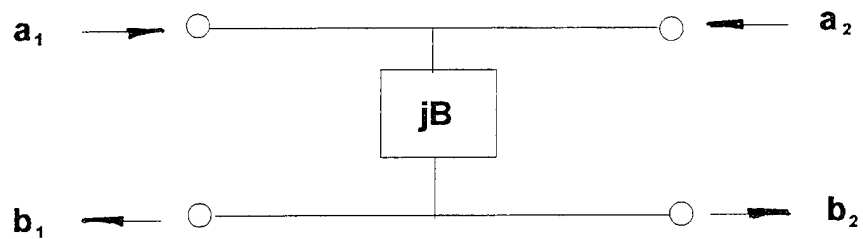


Figure 6
Scattering Matrix of a 90°
Transmission Line Section



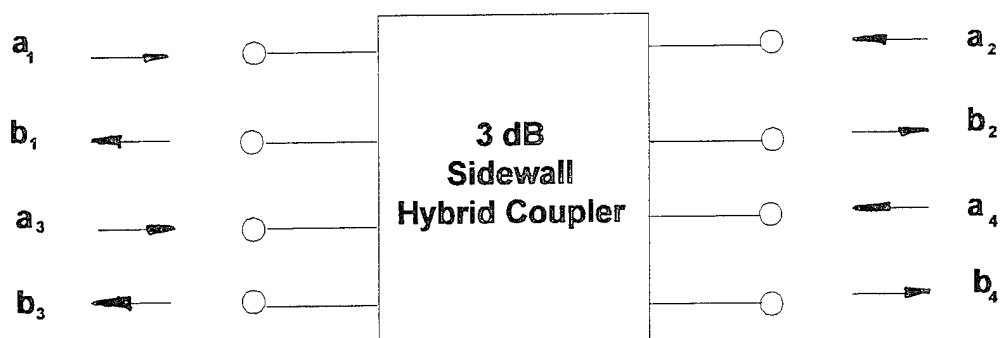
$$S = \begin{bmatrix} \frac{N^2 - 1}{N^2 + 1} & \frac{2N}{N^2 + 1} \\ \frac{2N}{N^2 + 1} & \frac{1 - N^2}{1 + N^2} \end{bmatrix}$$

Figure 7
Scattering Matrix for
An Ideal Transformer



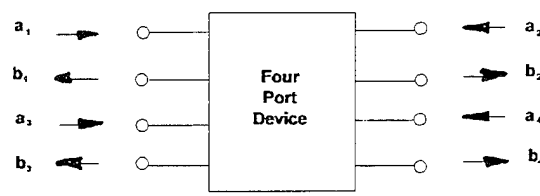
$$S = \begin{bmatrix} \frac{-jB}{2+jB} & \sqrt{\frac{2}{B^2+4}} e^{j \tan^{-1}(-\frac{B}{2})} \\ \sqrt{\frac{2}{B^2+4}} e^{j \tan^{-1}(-\frac{B}{2})} & \frac{-jB}{2+jB} \end{bmatrix}$$

Figure 8
Scattering Matrix of a Pure
Shunt Susceptance



$$S = \begin{bmatrix} 0 & .707 & 0 & -j.707 \\ .707 & 0 & -j.707 & 0 \\ 0 & -j.707 & 0 & .707 \\ -j.707 & 0 & .707 & 0 \end{bmatrix}$$

Figure 9
Scattering Matrix of a 3 dB Hybrid Coupler



$$\begin{bmatrix} b_1 \\ b_2 \\ b_3 \\ b_4 \end{bmatrix} = \mathbf{S} \begin{bmatrix} a_1 \\ a_2 \\ a_3 \\ a_4 \end{bmatrix} \quad \begin{bmatrix} a_1 \\ a_2 \\ a_3 \\ a_4 \end{bmatrix} = \mathbf{C} \begin{bmatrix} a_2 \\ b_2 \\ a_4 \\ b_4 \end{bmatrix}$$

Figure 10
S and C Matrix Relationships

K	HYBRID LOAD		PHASE SHIFTER	
	VOLTAGE	dB	VOLTAGE	dB
1	0.000	-151.531	0.015	-36.588
2	0.000	-147.718	0.022	-33.158
3	0.000	-144.213	0.036	-28.758
4	0.000	-142.013	0.055	-25.138
5	0.000	-139.306	0.079	-22.098
6	0.000	-137.601	0.106	-19.518
7	0.000	-139.975	0.136	-17.348
8	0.000	-143.054	0.168	-15.508
9	0.000	-140.585	0.200	-13.988
10	0.000	-140.268	0.230	-12.748
11	0.000	-144.840	0.258	-11.778
12	0.000	-155.136	0.280	-11.058
13	0.000	-144.037	0.296	-10.588
14	0.000	-142.040	0.303	-10.358
15	0.000	-149.191	0.303	-10.358
16	0.000	-141.498	0.296	-10.588
17	0.000	-144.167	0.280	-11.058
18	0.000	-150.096	0.258	-11.778
19	0.000	-160.875	0.230	-12.748
20	0.000	-155.299	0.200	-13.988
21	0.000	-151.427	0.168	-15.508
22	0.000	-153.336	0.136	-17.348
23	0.000	-163.134	0.106	-19.518
24	0.000	-128.304	0.079	-22.098
25	0.000	-163.410	0.055	-25.138
26	0.000	-169.891	0.036	-28.758
27	0.000	-177.146	0.022	-33.158
28	0.000	-117.713	0.015	-36.589

Figure 11
Relative Phaser and Load Voltages

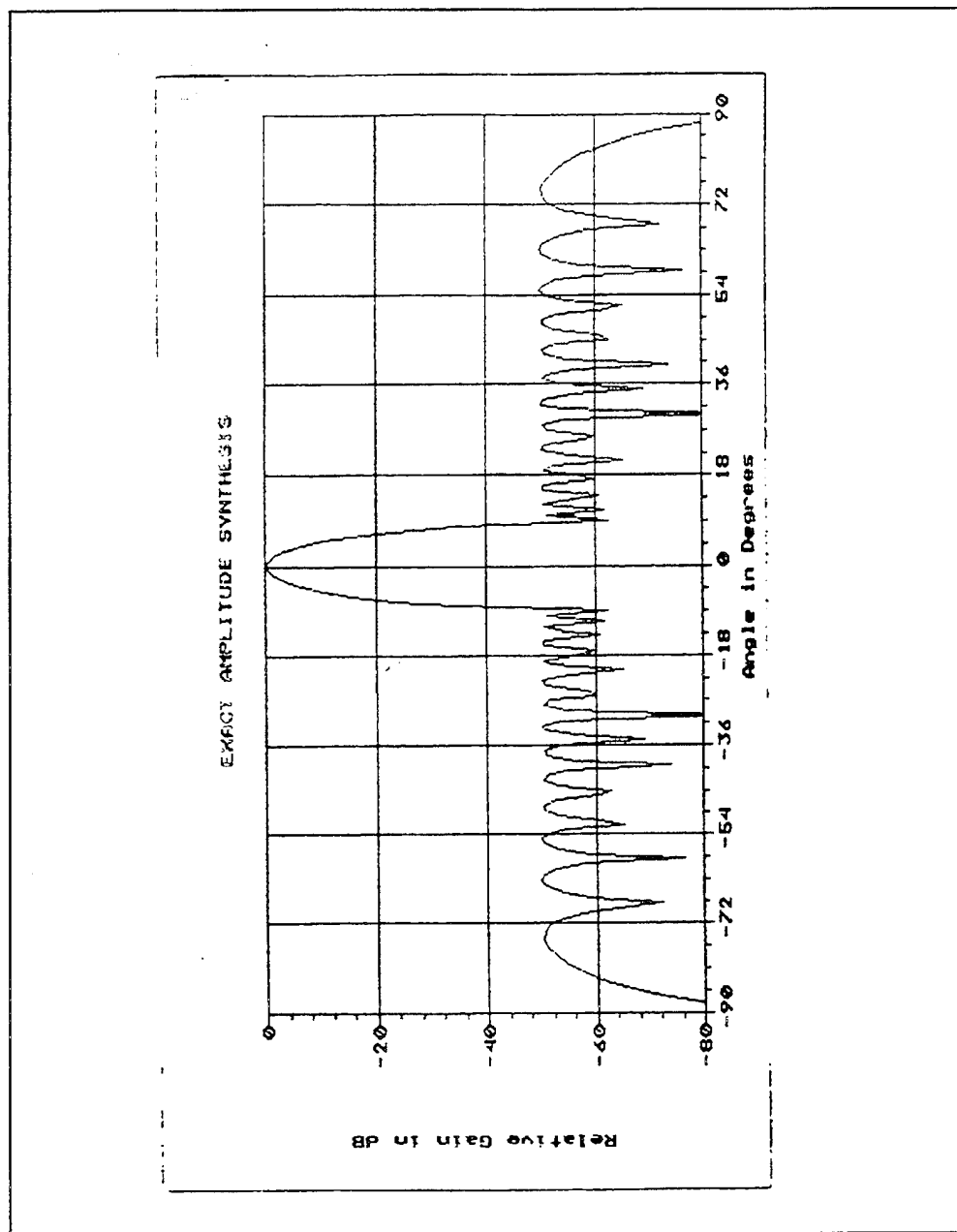


Figure 12
Matched Phasers and Loads
Exact Amplitude Synthesis

Figures 13 through 14 show the same comparison for the case where the phasers are matched and the THLS are mismatched. Note that the relative THL ports are truly "isolated" as long as the phasers are perfectly matched.

Figures 15 and 16 demonstrate the effects of mismatched phasers. The phaser and THL mismatches have statistically independent, rayleigh distributed, reflection coefficient amplitudes with a "3 SIGMA" value equal to .14 and random phases uniformly distributed between 0 and 360 degrees. Small, but discernable differences between the theoretical and realized elevation patterns are now evident and the THL power is no longer negligible since the circuit inside the black box of Figure 5 is no longer perfectly balanced.

Figures 17 and 18 demonstrate antenna performance under the more realistic conditions wherein both the THL and phaser have mismatches whose statistics are described in the paragraph above. The THL mismatches cause the pattern to worsen slightly relative to the case where only the phasers are mismatched. This is because phaser reflections are now not completely absorbed by the THLS and the THL reflections now radiate from the aperture in an uncontrolled fashion. Note in Figure 17 that the power delivered to the THLS is approximately the same as in Figure 15.

Figures 19 and 20 demonstrate the drastic effects of replacing the THLS with short circuits. Under these conditions, all phaser reflection energy which

HYBRID LOAD			PHASE SHIFTER		
K	VOLTAGE	dB	VOLTAGE	dB	
1	0.000	-151.544	0.015	-36.588	
2	0.000	-147.708	0.022	-33.158	
3	0.000	-144.215	0.036	-28.758	
4	0.000	-142.002	0.055	-25.138	
5	0.000	-139.312	0.079	-22.098	
6	0.000	-137.653	0.106	-19.518	
7	0.000	-139.977	0.136	-17.348	
8	0.000	-143.054	0.168	-15.508	
9	0.000	-140.518	0.200	-13.988	
10	0.000	-140.263	0.230	-12.748	
11	0.000	-144.859	0.258	-11.778	
12	0.000	-155.443	0.280	-11.058	
13	0.000	-144.047	0.296	-10.588	
14	0.000	-142.037	0.303	-10.358	
15	0.000	-149.207	0.303	-10.358	
16	0.000	-141.487	0.296	-10.588	
17	0.000	-144.165	0.280	-11.058	
18	0.000	-150.108	0.258	-11.778	
19	0.000	-160.902	0.230	-12.748	
20	0.000	-155.337	0.200	-13.988	
21	0.000	-151.420	0.168	-15.508	
22	0.000	-153.299	0.136	-17.348	
23	0.000	-163.148	0.106	-19.518	
24	0.000	-128.303	0.079	-22.098	
25	0.000	-163.436	0.055	-25.138	
26	0.000	-169.892	0.036	-28.758	
27	0.000	-177.138	0.022	-33.158	
28	0.000	-117.715	0.015	-36.589	

Figure 13
Relative Phaser And Load Voltages

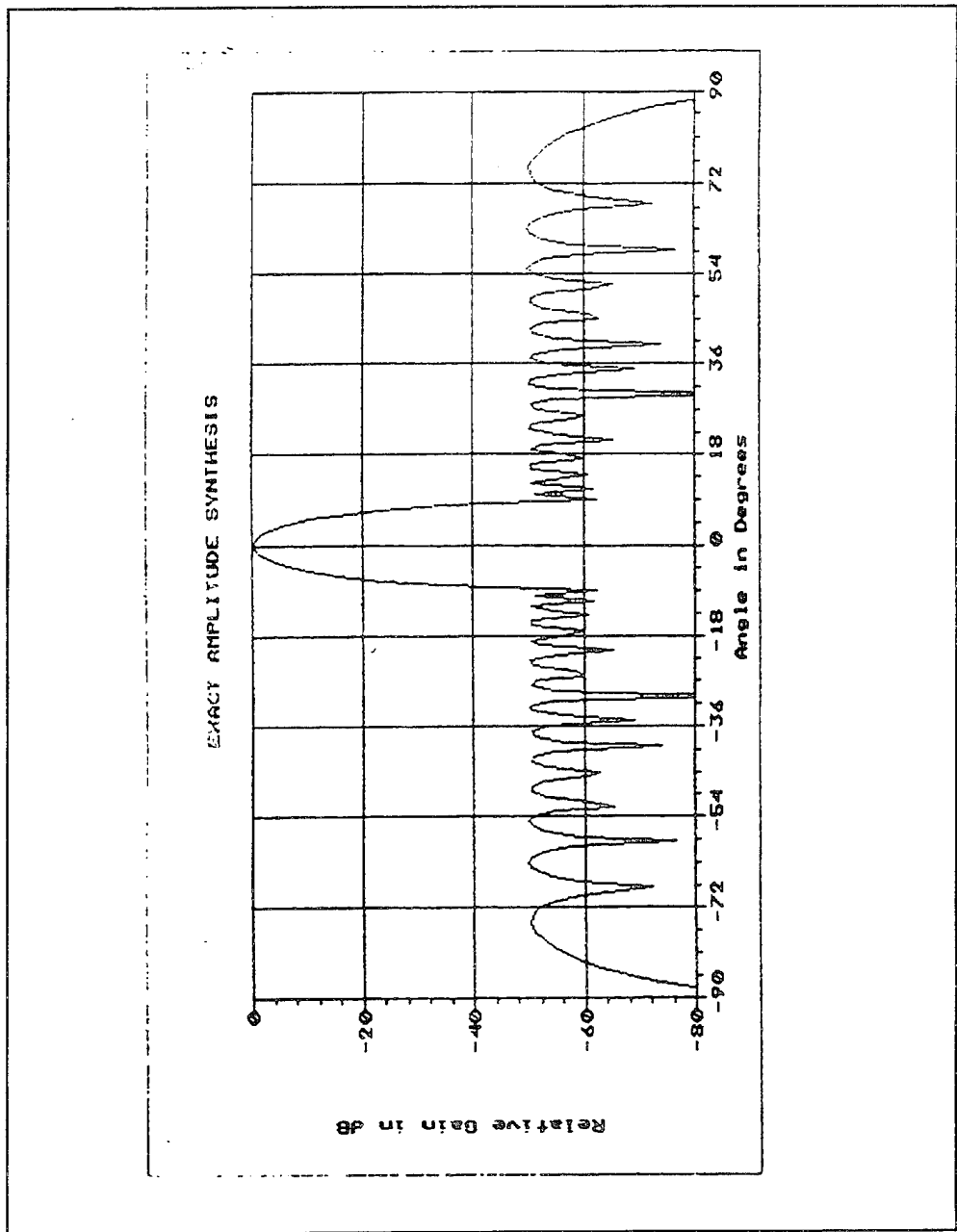


Figure 14
Matched Phasers and Mismatched Loads
Exact Amplitude Synthesis

K	HYBRID LOAD		PHASE SHIFTER	
	VOLTAGE	dB	VOLTAGE	dB
1	0.000	-69.018	0.015	-36.601
2	0.003	-51.940	0.022	-33.175
3	0.008	-42.323	0.036	-28.780
4	0.011	-39.401	0.055	-25.159
5	0.004	-48.822	0.078	-22.105
6	0.008	-42.056	0.106	-19.531
7	0.009	-40.656	0.136	-17.361
8	0.029	-30.675	0.169	-15.462
9	0.014	-36.824	0.200	-13.994
10	0.018	-34.905	0.231	-12.737
11	0.025	-32.117	0.259	-11.748
12	0.013	-37.889	0.279	-11.073
13	0.026	-31.748	0.295	-10.609
14	0.029	-30.801	0.303	-10.367
15	0.026	-31.805	0.303	-10.361
16	0.009	-41.367	0.295	-10.592
17	0.023	-32.932	0.280	-11.057
18	0.029	-30.717	0.258	-11.784
19	0.017	-35.151	0.230	-12.753
20	0.014	-37.091	0.200	-13.996
21	0.007	-42.894	0.168	-15.507
22	0.014	-37.156	0.136	-17.349
23	0.001	-58.738	0.106	-19.518
24	0.010	-40.088	0.079	-22.098
25	0.005	-45.988	0.055	-25.140
26	0.002	-52.801	0.037	-28.753
27	0.002	-56.349	0.022	-33.156
28	0.001	-59.417	0.015	-36.743

Figure 15
Relative Phaser And Load Voltages

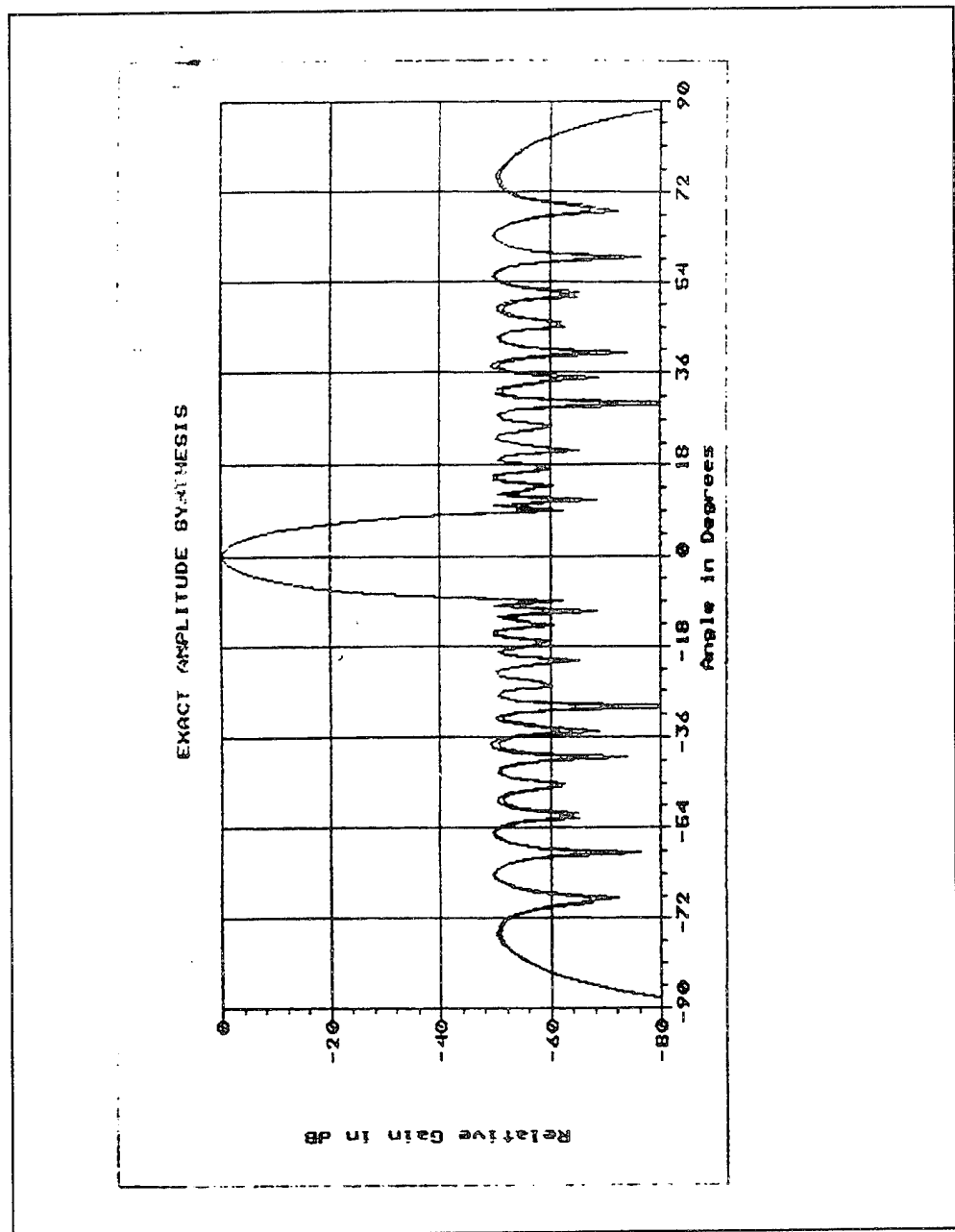


Figure 16
Mismatched Phasers And Matched Loads
Exact Amplitude Synthesis

HYBRID LOAD			PHASE SHIFTER		
K	VOLTAGE	dB	VOLTAGE	dB	
1	0.000	-69.073	0.015	-36.620	
2	0.003	-51.909	0.022	-33.127	
3	0.008	-42.348	0.036	-28.812	
4	0.011	-39.407	0.055	-25.173	
5	0.004	-48.832	0.078	-22.132	
6	0.008	-42.117	0.106	-19.527	
7	0.009	-40.661	0.136	-17.360	
8	0.029	-30.681	0.168	-15.468	
9	0.015	-36.736	0.200	-13.969	
10	0.018	-34.903	0.230	-12.747	
11	0.025	-32.146	0.258	-11.757	
12	0.013	-37.899	0.279	-11.077	
13	0.026	-31.741	0.296	-10.570	
14	0.029	-30.763	0.305	-10.307	
15	0.026	-31.839	0.302	-10.399	
16	0.009	-41.352	0.295	-10.592	
17	0.023	-32.923	0.280	-11.047	
18	0.029	-30.755	0.256	-11.830	
19	0.017	-35.179	0.230	-12.762	
20	0.014	-37.156	0.198	-14.050	
21	0.007	-42.872	0.168	-15.486	
22	0.014	-37.088	0.137	-17.275	
23	0.001	-58.735	0.106	-19.512	
24	0.010	-40.114	0.078	-22.149	
25	0.005	-46.046	0.055	-25.200	
26	0.002	-52.799	0.037	-28.744	
27	0.002	-56.323	0.022	-33.132	
28	0.001	-58.996	0.015	-36.726	

Figure 17
Relative Phaser And Load Voltages

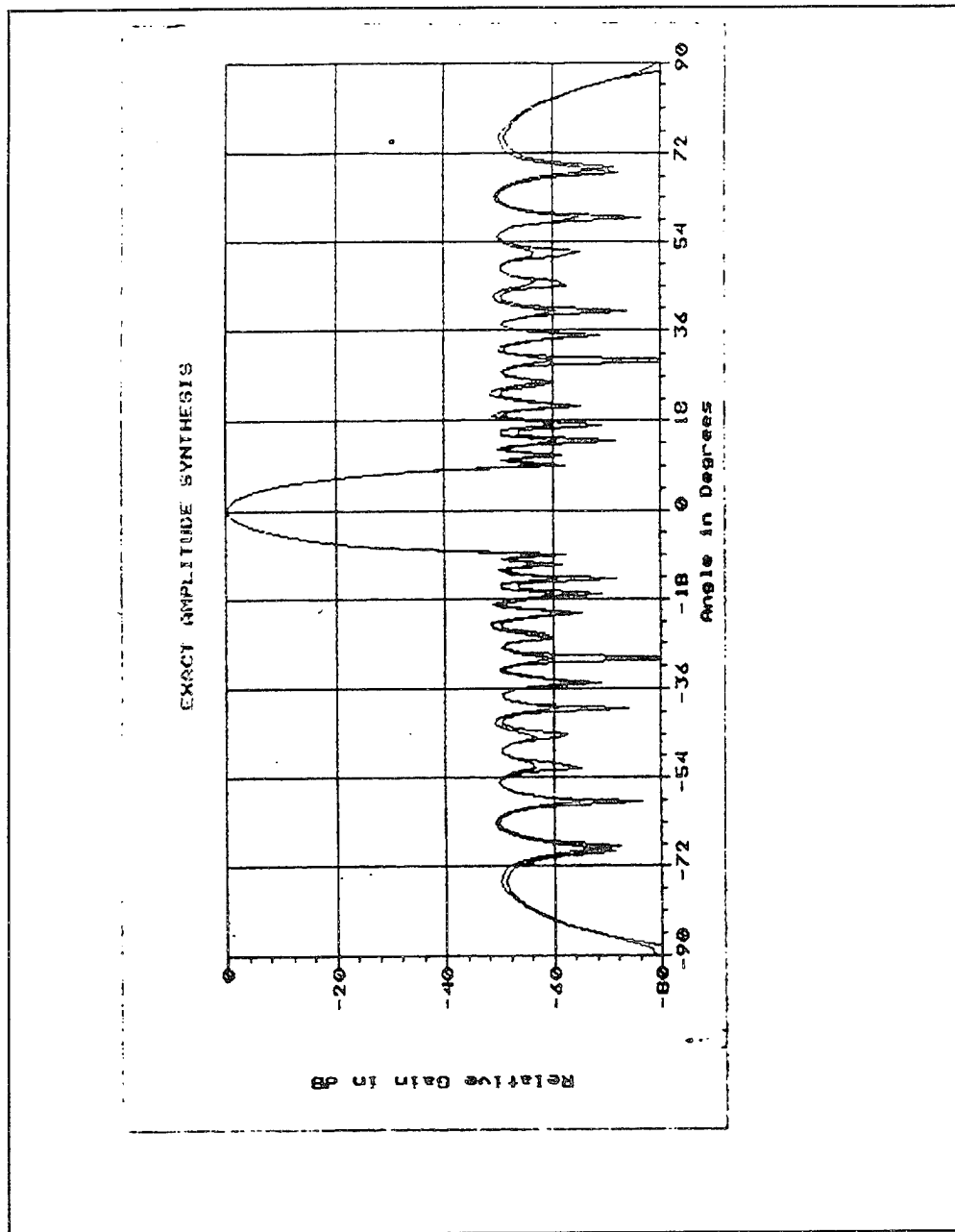


Figure 18
Mismatched Phasers And Loads
Exact Amplitude Synthesis

HYBRID LOAD			PHASE SHIFTER		
K	VOLTAGE	dB	VOLTAGE	dB	
1	0.000	-105.884	0.014	-36.796	
2	0.000	-88.876	0.022	-33.116	
3	0.000	-78.777	0.040	-27.969	
4	0.000	-75.811	0.064	-23.880	
5	0.000	-85.423	0.082	-21.710	
6	0.000	-79.068	0.104	-19.678	
7	0.000	-77.507	0.136	-17.308	
8	0.000	-67.974	0.158	-16.010	
9	0.000	-73.559	0.199	-14.041	
10	0.000	-71.986	0.227	-12.889	
11	0.000	-69.024	0.261	-11.654	
12	0.000	-75.056	0.286	-10.882	
13	0.000	-69.029	0.275	-11.217	
14	0.000	-67.510	0.325	-9.764	
15	0.000	-69.167	0.284	-10.923	
16	0.000	-78.357	0.299	-10.487	
17	0.000	-69.929	0.279	-11.085	
18	0.000	-67.365	0.281	-11.030	
19	0.000	-72.013	0.237	-12.495	
20	0.000	-74.314	0.189	-14.479	
21	0.000	-79.692	0.171	-15.335	
22	0.000	-73.942	0.146	-16.726	
23	0.000	-95.518	0.106	-19.530	
24	0.000	-76.514	0.088	-21.131	
25	0.000	-82.557	0.060	-24.433	
26	0.000	-90.123	0.034	-29.288	
27	0.000	-93.541	0.021	-33.628	
28	0.000	-113.761	0.015	-36.497	

Figure 19
Relative Phaser And Load Voltages

does not couple to the main manifold feed lines radiates from the aperture in uncontrolled fashion again. The elevation pattern results are much worse in this case since none of the reflected phaser energy is absorbed by the THLS and the uncontrolled radiation is much stronger than it is in Figure 18.

Figure 21 shows the schematic of a series fed manifold employing three port reactive tee couplers. This type of feed network is very sensitive to the admittances which each tee coupler branch arm sees. The elevation patterns of Figures 22 and 23 illustrate this in dramatic fashion. Figure 22 shows that the theoretical and realized patterns are identical when the phasers of Figure 21 are matched. Figure 23 shows that the elevation pattern is badly degraded when phaser mismatches, having the same statistical nature as those described for the pattern of Figure 16 are present in the feed network schematic of Figure 21. It is interesting to note the similarity of the realized patterns of Figures 20 and 23. By replacing the THLS of Figure 4 with short circuits, we force the phaser reflections at each stick in the antenna to radiate in an uncontrolled fashion in a manner similar to the situation shown in Figure 21 when phaser mismatches are present.

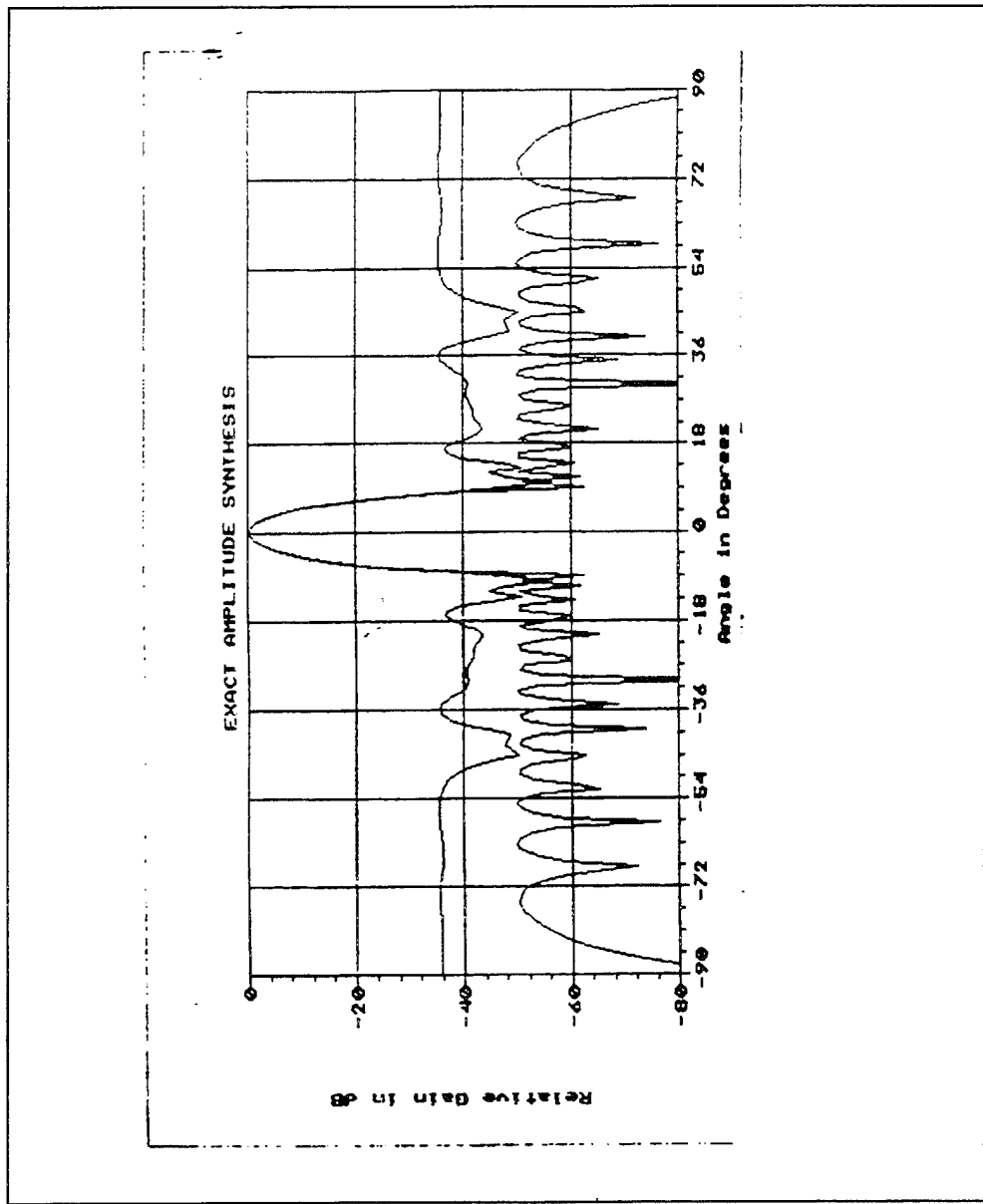


Figure 20
 Dual Manifold in Which
 Hybrid Loads Have Reflection
 Coefficients of 0.9999
 Exact Amplitude Synthesis

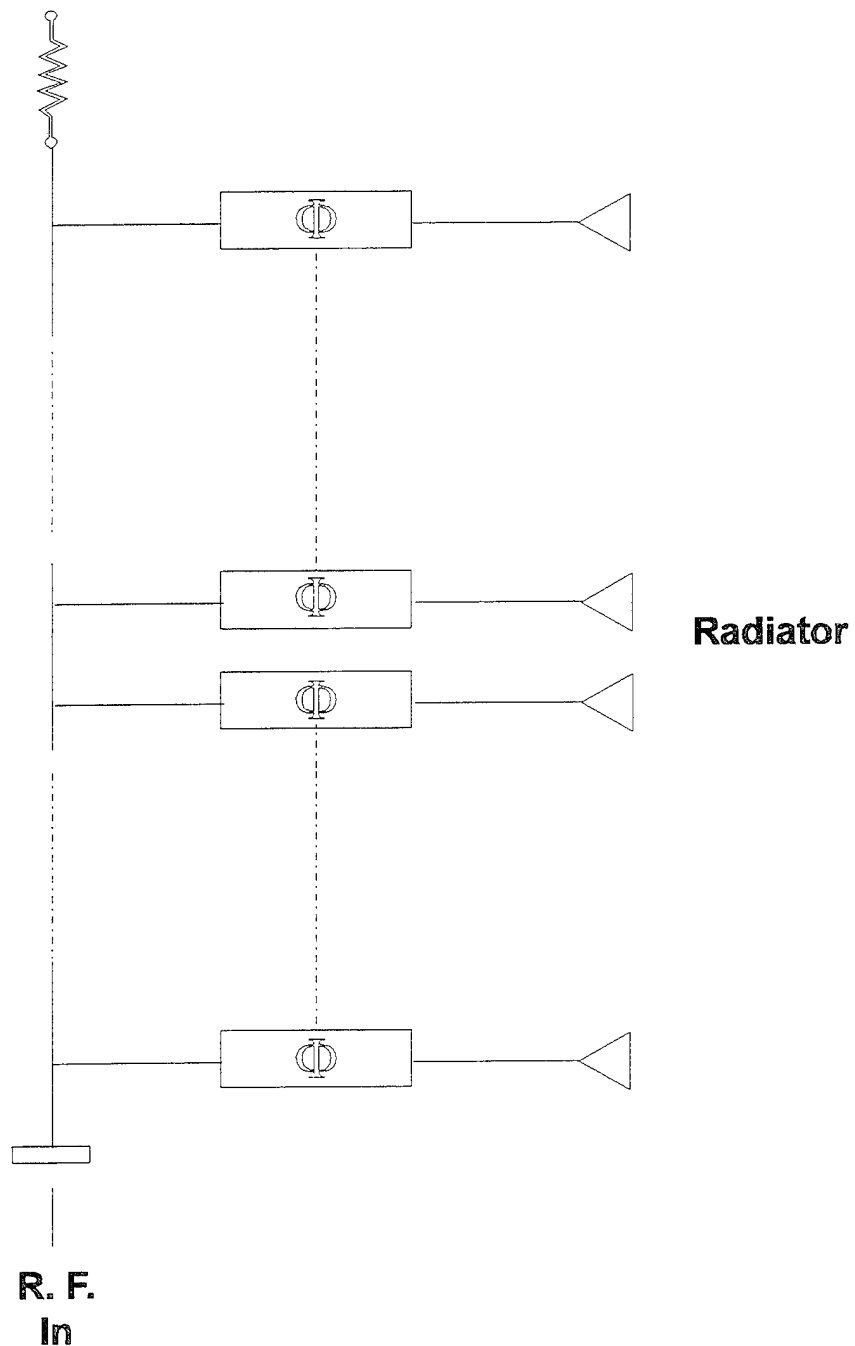


Figure 21
Single Line Series Fed
3 Port Reactive Tee Feed Network

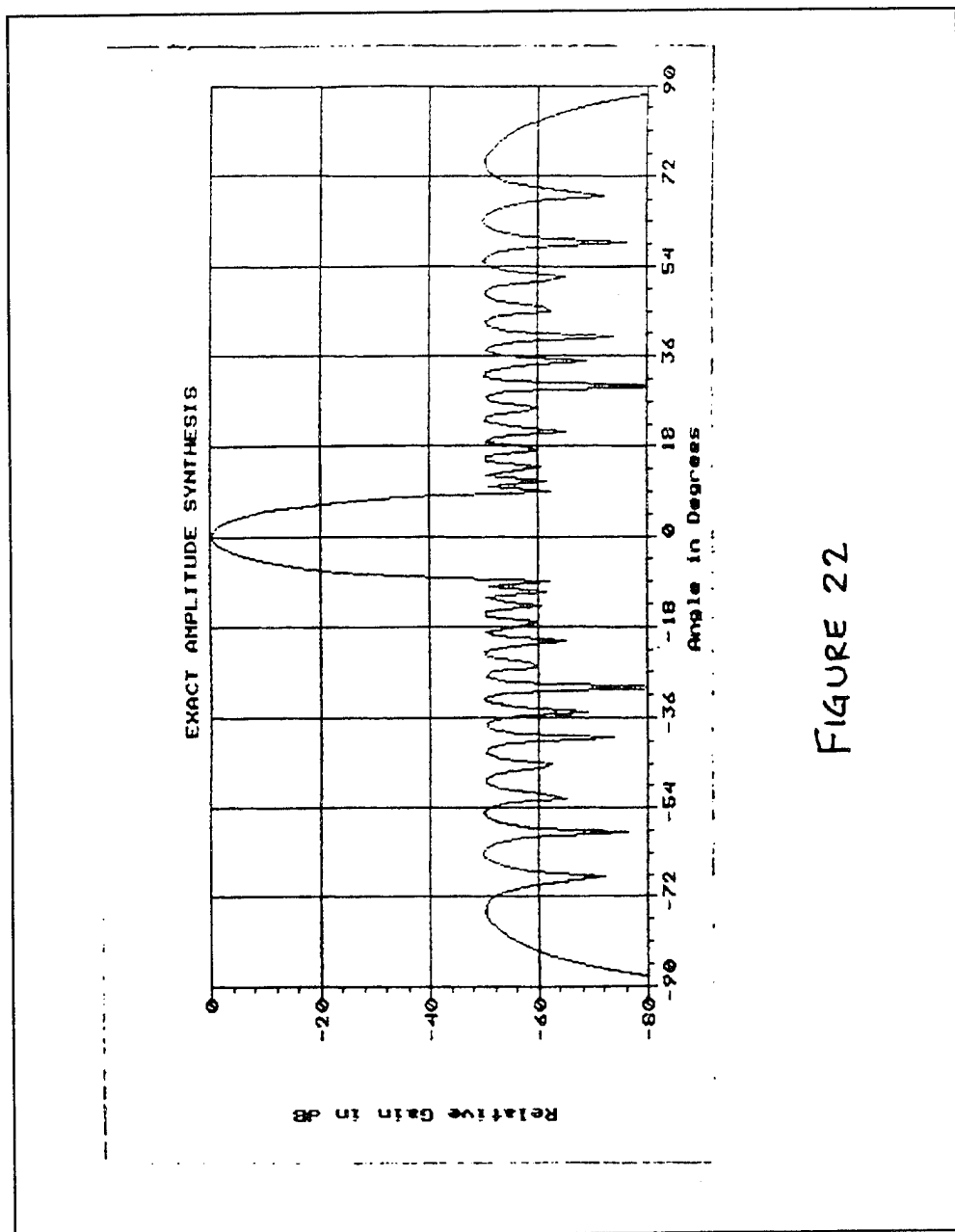


FIGURE 22

Figure 22
Single Reactive T Manifold
With Matched Thru Port

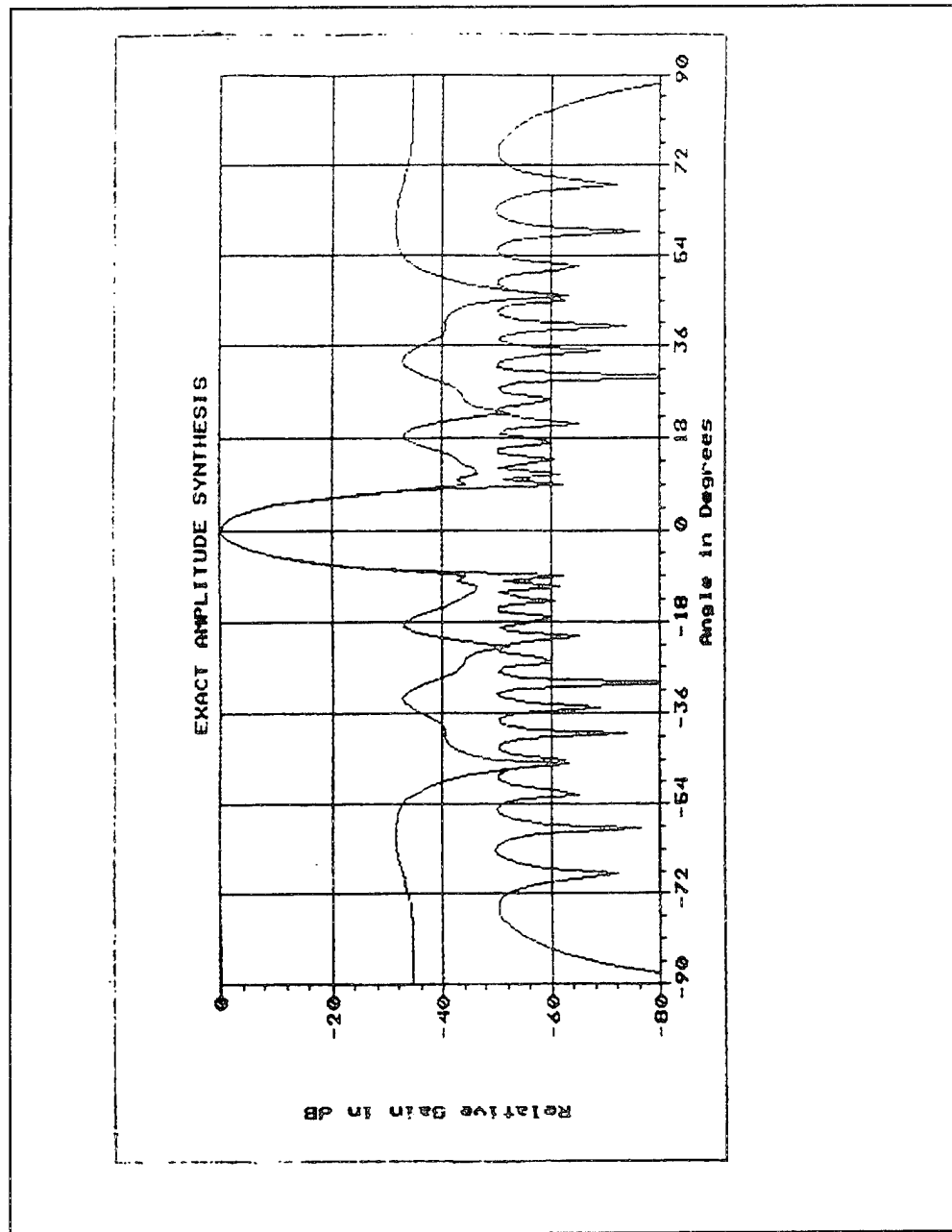


Figure 23
Single Reactive T Manifold
With Mismatched Thru Port

CONCLUSION

The foregoing computer aided analysis has employed the combination of scattering matrix theory and equivalent circuit analysis of a complicated microwave transmission line feed network, of the type used on the E-3A antenna system, to determine feed network performance as a function of both primary antenna component and "isolated" component mismatch tolerance effects.

The significance of this is that previously neglected component tolerance effects (such as "isolated" port termination mismatches) is now exactly accounted for in the analysis of antenna feed network performance and its consequent effect on overall antenna performance.

***MISSION
OF
ROME LABORATORY***

Mission. The mission of Rome Laboratory is to advance the science and technologies of command, control, communications and intelligence and to transition them into systems to meet customer needs. To achieve this, Rome Lab:

- a. Conducts vigorous research, development and test programs in all applicable technologies;
- b. Transitions technology to current and future systems to improve operational capability, readiness, and supportability;
- c. Provides a full range of technical support to Air Force Material Command product centers and other Air Force organizations;
- d. Promotes transfer of technology to the private sector;
- e. Maintains leading edge technological expertise in the areas of surveillance, communications, command and control, intelligence, reliability science, electro-magnetic technology, photonics, signal processing, and computational science.

The thrust areas of technical competence include: Surveillance, Communications, Command and Control, Intelligence, Signal Processing, Computer Science and Technology, Electromagnetic Technology, Photonics and Reliability Sciences.